Nanoparticules d'or thermosensibles : propriétés optiques en solution et comportement à l'interface

Cynthia Said-Mohamed

THÈSE DE DOCTORAT

DE L'UNIVERSITÉ PARIS-SUD XI

(UNIVERSITÉ D'ORSAY)

Présentée par

Cynthia Sourayat SAID-MOHAMED

Pour obtenir le titre de

Docteur de l'Université Paris-Sud XI

THERMOSENSITIVE GOLD NANOPARTICLES:

SOLUTION OPTICAL PROPERTIES AND INTERFACIAL BEHAVIOR

Thèse soutenue le 14 novembre 2011, devant le jury composé de:

Bernard Cabane	Emérite - CNRS, ESPCI Paris	Invité
Mohamed Daoud	Chercheur HDR - CEA, SPEC-Saclay	Examinateur
Dominique Hourdet	Professeur, Université Pierre et Marie Curie Paris VI	Rapporteur
Liliane Léger	Professeur, Université Paris-Sud XI	Présidente
Lay-Theng Lee	Directeur de Recherche - CNRS, LLB-Saclay	Directrice de thèse
Olivier Spalla	Chercheur HDR - CEA, LIONS-Saclay	Rapporteur
Heikki Tenhu	Professeur, Université Helsinki, Finlande	Examinateur
Fabrice Vallée	Directeur de Recherche - CNRS, Université Lyon-1	Examinateur

A ma grand-mère Zalhata,

Tsina paro ou dioiza !

Remerciements

Cette thèse a été réalisée au Laboratoire Léon Brillouin. Je souhaiterais donc remercier Philippe Mangin et Christiane Alba-Simionesco (directeurs successifs), Susana Gota-Goldmann et Jean-Paul Visticot (sous-directeurs successifs) et Alain Menelle pour m'avoir accueilli au sein de leur laboratoire.

Je suis très reconnaissante à Dominique Hourdet et Olivier Spalla d'avoir accepté d'être les rapporteurs de cette thèse. Je tiens également à remercier Liliane Léger d'avoir assuré le rôle de présidente de mon jury de thèse, ainsi que Heikki Tenhu, Fabrice Vallée, Mohamed Daoud et Bernard Cabane, qui ont accepté de participer à ce jury.

Je tiens à exprimer ma plus sincère gratitude à ma directrice de thèse Lay-Theng Lee. Je ne la remercierai jamais assez pour tout ce qu'elle m'a apporté et son soutient. A ses côtés, j'ai énormément appris au niveau scientifique mais aussi au niveau personnel. Elle a toujours été disponible et a fait preuve envers moi d'une extrême gentillesse et générosité, ce que je ne pourrai jamais oublier.

I would like to express my greatest gratitude to Heikki Tenhu for welcoming me in his Laboratory of Polymer Chemistry and for his teaching in polymer and nanoparticles synthesis. Thank you for caring for me during my stay in Helsinki. I will never forget your kindness and your great sense of humour. I also would like to thank his students Petri and Mikko for helping me with my synthesis and Adina for her kindness. A special thank to Jukka who helped me all throughout this thesis. Not only he taught me about polymer and nanoparticles synthesis but he also always took time to help with my experiments and answer my questions (and with a smile). I wish you all the best!

Je tiens également à remercier les personnes avec qui j'ai collaboré durant cette thèse : Gilbert Zalczer (Transmission), Didier Lairez (DNPA et Latex), Frédéric Ott (Réflectivité de X), Alan Braslau, Fabrice Vallée, Natalia Del Fatti et Paolo Maioli (modélisation). Je remercie aussi Francis Gibert pour son aide pour le montage des manips de réflectivité.

Je remercie tous les doctorants et post-doctorants que j'ai rencontré au LLB durant ces trois années de thèse. Merci à Anne-Sophie pour sa gentillesse et sa bonne humeur. Merci à Christophe, François, Sindhu, Anne-Laure, Clémence, Nicolas J., Vincent, Aurélie, Claire, Zineb, Nicolas G., Weiqing, Adrien, Caroline, Alexandros, Prexilia, Li, Emilie. Je tiens également à remercier Stéphanie pour son agréable compagnie lors des trajets au CEA et les nombreux fous rires. Je remercie aussi les

chercheurs du laboratoire : Giulia, Jean-Marc, José, Fabrice, François B., François M., Stéphane, Natalie, Jacques, Annie. J'en profite pour remercier Chantal Marais, Aurore verdier, Claude Rousse, Mireille Noiran et Anne Mostefaoui pour leur aide en ce qui concerne le domaine administratif. Je remercie Bernard Mailleret pour avoir participé à la préparation de ma soutenance et veillé à son bon déroulement.

Je remercie la famille et amis qui sont venus de loin pour assister à ma soutenance. Un grand merci à Tonton Ahamada d'avoir toujours été présent aux moments importants de ma vie. Merci beaucoup à Tata Roukia pour son soutien un-conditionnel depuis ma tendre enfance et son honnêteté, à mon petit correcteur en herbe Shahid à qui je souhaite beaucoup de réussite dans la vie. Merci à Tata Ourango et Tonton Omar pour leur sympathie et pour avoir toujours pris soin de ma grand-mère Zalhata. Je tiens à remercie la famille et les amis qui m'ont soutenu (notamment Elarif, Sidney, Said, Abdou, Fatima…). Je tiens à exprimer ma plus sincère reconnaissance à Mme Grigis pour m'avoir enseigné l'anglais et avoir toujours été de bon conseil. Merci pour votre extrême gentillesse et votre soutient.

Au premier homme de ma vie : Hachim. C'est drôle, je me rappelle toujours du jour de ta naissance. Maman nous a dit : c'est votre petit frère, il faut en prendre soin. Quand je te vois aujourd'hui, je suis fier de l'homme que tu es devenu. Tu es si gentil et tu as le don de me redonner le sourire quand je n'ai pas le moral. Je te souhaite de tout mon cœur de réussir et surtout d'être heureux dans la vie! Je ne serai jamais loin pour t'apporter mon soutient quelque soient les circonstances...

Enfin, je remercie ma mère. Je me suis toujours sentie privilégiée car tu m'a toujours laisser libre de faire mes propres choix et apporter toute ta confiance et ton soutient en toute circonstance. Quelque soient les difficultés, tu as toujours su relever les obstacles avec un tel courage et sans jamais te plaindre. Je ne te remercierai jamais assez pour tout ce que tu as fais. Ngamhandzo hane roho yahangwou !

Chapter 1

Introduction

Nanoparticles in the 1-100 nm range can be said to bridge the gap between small molecules and bulk material as they offer a variety of opportunities to investigate the evolution of material properties with particle dimension [1]. Metal nanoparticles such as gold, silver and copper nanoparticles exhibit unique electronic, optical and catalytic properties [2], [3], [4], [5] that, unlike bulk metals and molecular compounds, strongly depend on the particle size and shape, the nature of the protecting organic shell and the interparticle distance [6].

Their most interesting characteristic is the Surface Plasmon Resonance (SPR) in the visible spectrum which gives them the particularity of exhibiting bright colors. When light interacts with the metal nanoparticle, it creates an oscillating electric field responsible for the oscillation of conduction band electrons. The collective oscillation of these conduction band electrons gives rise to the SPR for nanoparticles that results in an absorption band in the visible spectrum. The optical properties of metal nanoparticles depend upon size and shape of particles [7], [8] and their local environment [9], [10], [11], [12], as well as the charging state of the metal cores [13]. However, for very small particles (D $<$ 20-25 nm, for gold), the Mie theory [14] predicts that the SPR peak position is independent of particle size and is only governed by the dielectric properties of the surrounding medium (protecting shell and solvent). When the particles are close to each other, an electronic dipole-dipole interaction between the plasmons of neighboring particles takes place. In that case, the SPR also depends on the interparticle distance. Based on the SPR physical phenomenon, particles have potential applications in decorating, coatings, biosensors, optical and electronic devices. In fact, they were initially used for decorative purposes. The most famous example showing the intriguing optical properties of these nanoparticles is the Lycurgus Cup (British Museum) dating back to Roman times, where gold and silver nanoparticles were incorporated into the glass to impart brilliant colors and, more fascinating, to create an optical illusion of changing colors depending on whether it is viewed by transmitted (ruby red) or reflected (yellowish green) light. Later, in the Middle Age, nanoparticles were used as decorative pigments for vitraux that we commonly see in Cathedrals.

Gold plays a special role in nanotechnology as it presents additional advantages. To begin with, it is the most stable noble metal. Therefore designers of any nano-scale objects requiring metallic components preferably use gold instead of other less noble metal that can be altered by oxidation. Then, gold is a far better electron conductor than silicon. The third advantage of gold is that it offers a unique surface chemistry. In fact, gold nanoparticles grafted

with organic molecules (usually via the sulfur atom) have the ability to self-assemble into two or three-dimensional ordered structures that can have potential applications in biomedical and chemical detection and optical and microelectronics devices. For the assembling of gold and other metal nanoparticles, the "bottom-up" approach (assembling of single atoms and molecules into larger nanostructures) is most commonly used compared to "top-down" approach (breaking down of large pieces of material to generate the required nanostructures from them). Certain ligand-protected gold nanoparticles can form stable thin film at the air-water interface that have the particularity of also exhibiting optical properties in the UV-range. Then, the optical properties of the interfacial gold particles may be controlled by manipulating the interparticle distance in the thin film and the structural properties of the adsorbed layer with surface compression.

Gold nanoparticles are colloidally unstable and are susceptible to irreversible aggregation. To stabilize them, they can be coated with small organic molecules such as citrates, surfactants, ligands or polymers. Most of the reported synthesis involve wet chemistry techniques based on reactions in solution that yield metal nanoparticles with a wide range of sizes, shapes and dielectric environment [15]. Faraday reported the first controlled synthesis of colloidal gold in 1857 [16], [17]. Colloidal dispersions of gold were prepared by reducing an aqueous solution of a gold salt $HAuCl_4$ with a solution of phosphorous in carbon disulphide. The most popular method of preparing gold particles in water is the reduction of $HAuCl_4$ in a boiling sodium citrate solution [18], [19]. Gold particles ranging from 10 to 100 nm are obtained depending on the $HAuCl_4$:sodium citrate molar ratio. Recent work by Abecassis [20] focused on assessing the formation mecanism of gold nanoparticles in situ in liquid media (homogeneous or in microemulsion) by small angle scattering techniques. The studied gold particles were prepared using the same principle of salt exchange (reduction of $HAuCl_4$ by sodium salt). Gold particles can also be coated with a monolayer. Schiffrin and coworkers [21] reported the two-phase reduction method to produce alkanethiolate-protected gold nanoparticles with tunable particle size between 1 to 10 nm depending on the ratio of the Au salt and the alkanethiol ligand.

Functional ligands can also be attached to the nanoparticle surface to provide an additional tool to design surface architecture and to modulate physico-chemical properties for compatibility and detection. To this end, polymeric ligands have proved to be a popular choice due to their flexibility for tailoring specific uses and also for their greater long-term stabilizing properties compared to small molecules such as citrates. Notable examples include polysaccharides [22], DNA [23], [24], [25], [26], [27], and a category of "smart" polymers [28] that possesses stimuli-responsive attributes. In particular, pH, salinity and temperature-sensitive polymers have been widely studied due to their potential applications in biomedical and delivery systems [29], [30], [31], [32], [33]. Two ways of polymeric stabilization are distinguished. The "grafting-to" technique requires pre-synthesized polymers end-capped with a thiol [34],[35], [36], or dithioester [37], and polymers with disulphide unit [38], [39]. In "grafting-from" method [40], [41], monomers are polymerized from the surfaces carrying polymerization-initiating species. Both methods preferably involve controlled/living radical polymerization techniques such as ATRP [42], [43] and RAFT [44], [45],[46], [47], [48],[49],[50], [51] ,[52] to obtain a monodisperse and dense polymeric shell around the gold cores. We can cite a few examples of gold [53], [54] and silver [55] nanoparticles grafted with RAFT thermosensitive polymers. Recent advances on synthesis and applications of

polymer-protected gold nanoparticles can be found in a comprehensive review by Shan et al [56].

The objective of this thesis is to control the gold nanoparticles optical properties by tuning the protecting shell dielectric constant ϵ_s. ϵ_s can be modulated by varying the stabilizing shell structural properties. We choose to stabilize the gold particles with a thermosensitive polymer layer in order to thermally induce a change in the polymer shell conformation that can result in significant variation of ϵ_s. A thermosensitive polymer exhibits a coil-globule transition at a critical temperature T_c. Our approach is to graft onto gold nanoparticles PNIPAM-based polymers with a large range of molecular mass and different degrees of hydrophobicity to obtain particles with varying shell thickness and hydrophobicity. Thus the coating shell conformational changes can be induced at a wide range of temperature.

In this thesis, the first chapter describes detailed synthesis and chemical characterizations of the protecting polymers, followed by those of the polymer-protected gold nanoparticles. We discuss the methods to control: (i) the graft polymer molecular mass and hydrophobicity and (ii) the polymer-protected gold nanoparticles size. We also report the free polymers thermal properties. In the following chapter, we study the bulk structural properties of polymer-gold nanocomposites by Small Angle Neutron Scattering (SANS). We observe the polymer molecular mass and temperature effects on the coating shell conformation. The experimental scattering curves are modelled to obtain information about the shell property (thickness of shell). The third chapter consists of measuring the bulk gold nanoparticles optical properties by UV-visible spectroscopy. We concentrate on two principal aspects: (i) the effect of molecular chainlength on the optical sensitivity of the gold nanoparticle to the surrounding dielectric constant, and (ii) the SPR response to temperature-induced conformational changes in the polymer shell. The extinction spectra are also modelled in order to extract valuable information about the protecting shell properties (ϵ, ϕ_p). These results are then combined with the results obtained from different techniques (TEM, SANS) to rationalize and consolidate the data from the different samples with different characteristics. The fourth chapter is dedicated to the polymer-protected gold nanoparticles behaviour at the air-water interface. We discuss the graft polymer chain length and the temperature influences on the tuning of the interparticle distance. Then, we report efforts made to optimize the thin film stability for a better interparticle distance manipulation. The gold monolayer structural properties and stability are determined by the Neutron and X-ray reflectivities. In the last chapter, we focus on the thin film optical properties by transmission. The compression and temperature effects on the SPR are studied. Combining these last results with those obtained from the reflectivity study enable us to correlate the thin film structural properties (polymer conformation and gold core organization) with the optical properties.

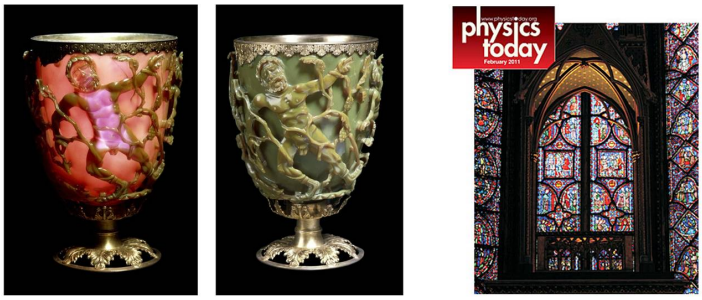

Figure 1.1: Pictures of the Lycurgus Cup (British Museum) showing the color change depending upon the direction of light illuminating it, and the Sainte Chapelle Cathedral (Paris).

Chapter 2

Synthesis of polymer-protected gold nanoparticles

In this chapter, we describe in detail the preparation techniques for the thermoresponsive polymers and the polymer-protected gold nanoparticles. Although we follow the synthesis routes employed by Shan [57] for Au-PNIPAM nanoparticles, important adjustments are made to obtain larger gold nanoparticles that are grafted with longer polymer chain lengths. Therefore, we also discuss parameters that are changed from the original recipes in order to control the graft polymer molecular mass and the gold nanoparticle size. At the same time, we report the synthesis of a new copolymer Cpa-PNIPAM-co-NPAM that is also used to coat the particles.

All syntheses and characterizations of polymers and polymer-coated gold nanoparticles were carried out at the University of Helsinki (4+2 months in the laboratory of Prof. H. Tenhu, visit funded by a grant from the Center for International Mobility, Finland). Some polymers were also synthesized at LLB prior to grafting onto the nanoparticles.

2.1 Synthesis of thermoresponsive polymers

This section describes the synthesis methods and the characterization of thermoresponsive and amphiphilic polymers that are used to protect the gold nanoparticles. Poly(N-isopropylacrylamide) and poly(N-isopropylacrylamide-co-N-propylacrylamide) with wide range of molecular mass and different degrees of hydrophobicity are synthesized by Reversible Addition-Fragmentation Chain Transfer (RAFT) polymerization. The resulting PNIPAM-based polymers are characterized in terms of their chemical composition, molecular characteristics and thermal properties.

2.1.1 The Reversible Addition-Fragmentation Chain Transfer (RAFT) polymerization

The RAFT polymerization [45],[46], [47], is a living polymerization that is performed on monomers (eg. acrylamides, styrenes) capable of radical polymerization in the presence of a reversible chain transfer reagent and an initiator. It generally yields various well-defined

molecular mass polymers with low polydispersities depending on the [Monomer]: [RAFT-agent] and the [RAFT-agent]:[Initiator] ratios.The RAFT-agent is a thiocarbonylthio species [58] possessing two key structural features called the Z and R groups. While the Z group controls the bulk reactivity of the RAFT-agent, the R group mediates the polymerization in a controlled fashion. The latter is a good homolytic (free radical) leaving group that once dissociated from the RAFT-agent, is able to initiate polymerization. The initiator is usually an azo compound such as 2,2'-Azobis(isobutyronitrile) (AIBN). As represented Figure 2.1, the RAFT process is divided into the following 4 steps:

(i)Initiation: The polymerization starts with the reaction between the radical initiator and the monomer unit that induces a radical species. An active polymerizing chain P_n is created.

(ii) Addition-fragmentation: The active chain (P_n) reacts with the RAFT agent. The resulting unstable radical fragments and the detached leaving group (R) is now a radical. This is a reversible step, with an intermediate species capable of losing either the leaving group R or the active species P_n.

(iii) Re-initiation: The leaving group radical reacts with another monomer species, starting another active polymer chain. This active chain P_m is then able to go through the addition-fragmentation or equilibration steps.

(iv) Equilibration: This step is important. The majority of the active propagating species are trapped into the inactive RAFT agent. This limits the possibility of chain termination. The active polymer chains (P_m and P_n) are in an equilibrium between the active and inactive stages. While one polymer chain is in the inactive stage (bound to the RAFT agent), the other is active in polymerization to allow the increase of polymer chain length.

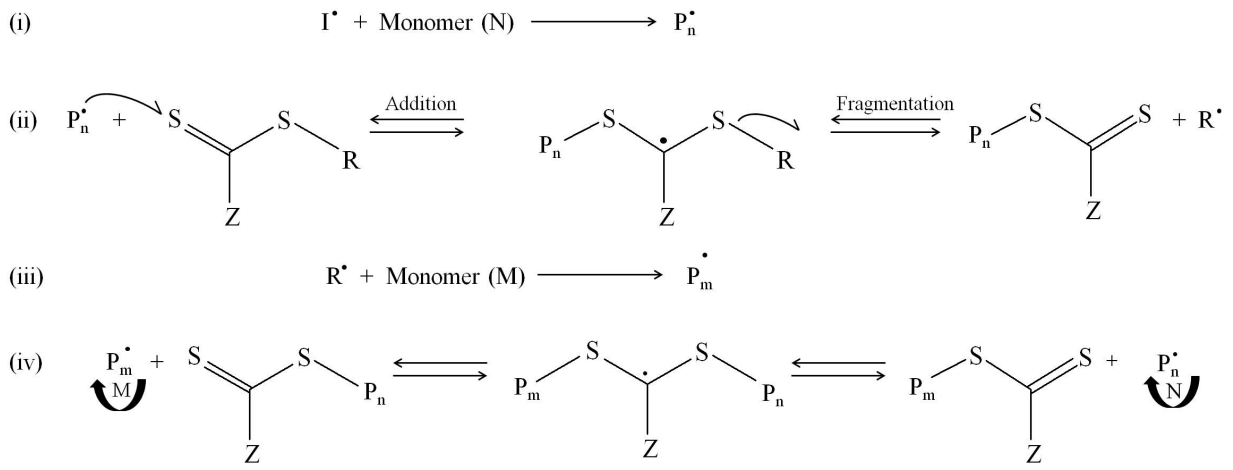

Figure 2.1: The RAFT mechanism

2.1.2 Poly(N-isopropylacrylamide) (PNIPAM)

2.1.2.1 RAFT polymerization

Cpa-PNIPAM homopolymers were synthesized by Reversible Addition-Fragmentation Chain Transfer (RAFT) polymerization using 4-cyanopentanoic acid dithiobenzoate(cpa-RAFT) as the RAFT agent and 2,2'-Azobis(isobutyronitrile) (AIBN) as the initiator [48],[49],[50]. Recrystallized NIPAM monomer, cpa-RAFT and AIBN were dissolved in distilled dioxane in a round-bottom flask equipped with a magnetic stirrer. The mixture was degassed either with N_2 flow for 45 minutes or by three freeze-pump-thaw cycles to optimize the oxygen elimination, sealed under vacuum and polymerized in a thermostated oil bath at 60°C for varying times. The polymers were precipitated in excess diethyl ether, purified by repeated precipitations and dried under vacuum. Finally, they were further purified by dialysis against water to remove oligomers. The synthesis route of the thermoresponsive Cpa-PNIPAM polymers is illustrated in Figure 2.2. The details of the RAFT polymerization reactions are collected in Table 8.1.

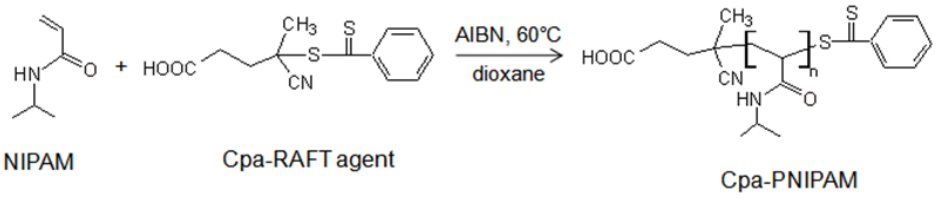

Figure 2.2: Schematic representation of reaction routes for Cpa-RAFT-PNIPAM.

2.1.2.2 Chemical characterization

The Cpa-PNIPAM homopolymer chemical composition was determined by IR and ^{1}H NMR spectrosocopies. ^{1}H NMR spectroscopy was also utilized to determine the molecular mass of the short polymer chains. Gel Permeation Chromatography (GPC) provided the molecular characteristics as well as the polydispersity index.

(i) Infra-Red Spectroscopy (IR):IR spectra were recorded in the range of 4000-650 cm^{-1} with a Perking-Elmer Spectrum One. In Figure 2.3a, the characteristic peaks assigned to NIPAM are [49]: N-H stretching (3292 cm^{-1}), C=O stretching (1640 cm^{-1}), a second amide stretching (and 1537 cm^{-1}) and deformation of the two methyl groups (1389 cm^{-1}and 1366 cm^{-1}).

(ii) ^{1}H Nulear Magnetic Resonance Spectroscopy (^{1}H NMR): These measurements were conducted with a 200 MHz Varian Gemini 2000 Specrometer. Deuterated chloroform (99.90%, Eurisotop, France) was used as solvent to dissolve the PNIPAM samples. In Figure 2.3b, the resonance at δ = 4.0 ppm is assigned to the lone proton of the N-isopropyl group [59],δ = 1.6-2.0 ppm to the CH_2 groups of the polymer main chain, and δ = 1.1 ppm to the CH_3 of the isopropyl group. The estimation of the molecular mass of shorts polymer chains is based on the integral of the resonance peak of five protons (δ = 8.0 ppm, o-ArH) of the phenyl group of the fragment of the cpa-RAFT agent present at one end of the PNIPAM chain and the other integral of the lone proton (δ = 4.0 ppm)of the N-isopropyl group in the repeating

units of PNIPAM.

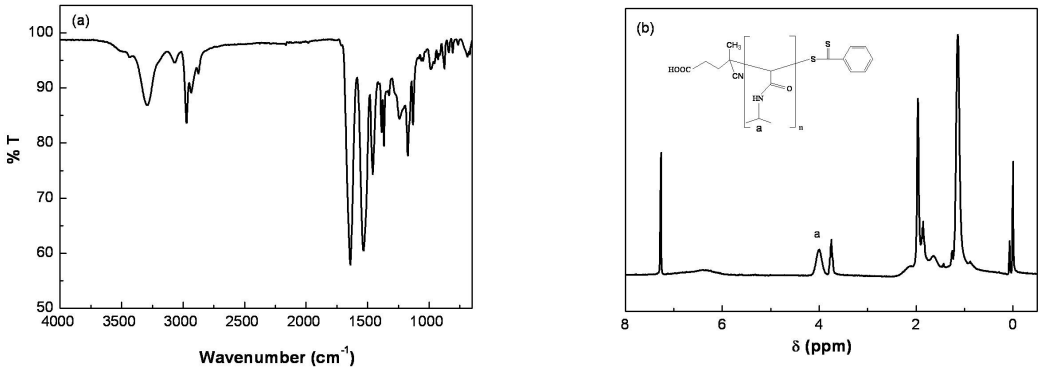

Figure 2.3: IR (a) and ^{1}H NMR (b) spectra of Cpa-RAFT-PNIPAM homopolymer.

(iii) Gel Permeation Chromatography (GPC):GPC was employed to determine the PNIPAM molar mass. PMMA standards from PSS Polymer Standards Service GmbH were used for calibration using DMF/LiBr (1mg/mL) as eluent. The molecular characteristics and the polydispersity Index (PDI) are summarized in Table 8.1.

2.1.3 Poly(N-isopropylacrylamide-co-propylacrylamide)(Poly(NIPAM-co-NPAM))

2.1.3.1 RAFT copolymerization

Statistical Cpa-PNIPAM-co-NPAM copolymers with varying NIPAM:NPAM molar ratios were prepared in a two-step synthesis. First, Poly(N-isopropylacrylamide-acryloxysuccinimide) (PNIPAM-co-NASI) was synthesized by RAFT polymerization [51] ,[52] using 4-cyanopentanoic acid dithiobenzoate(cpa-RAFT) as the RAFT agent and 2,2'-Azobis(isobutyronitrile) (AIBN) as the initiator. Re-crystallized NIPAM monomer and high-purity NASI monomer were dissolved together with cpa-RAFT and AIBN in distilled dioxane in a round-bottom flask equipped with a magnetic stirrer. The mixture was degassed with N_2 flow for 45 minutes to remove oxygen, sealed under vacuum and co-polymerized in a thermostated oil bath at 60°C for 48h. The resulting copolymers were precipitated in diethyl ether, purified by repeated precipitations, and dried under vacuum. Then, the copolymers were further purified by dialysis against water to remove oligomers. Different initial [NIPAM]:[NASI] monomer ratios were used to vary the molar ratios of NIPAM to NASI in the copolymer. The details of the RAFT copolymerization reactions are collected in Table 2.2. In a second step, once the NIPAM:NASI was determined, the Cpa-PNIPAM-co-NASI was converted to poly(N-isopropylacrylamide-co-proylacrylamide) (Cpa-PNIPAM-co-NPAM) by aminolysis of the active ester NASI units using a 1.5-fold molar excess of n-propylamine in the presence of triethylamine (TEA, catalyst) in dichloromethane. The reaction solution was stirred at room temperature for 72 h. The resulting copolymer was precipitated in diethyl ether, purified by

repeated precipitations, and dried under vacuum. Then, the copolymer was further reacted with excess TEA and isopropylacrylamide for 48h to convert any left over NASI units. The Cpa-PNIPAM-co-NPAM copolymers were then purified by dialysis against water.

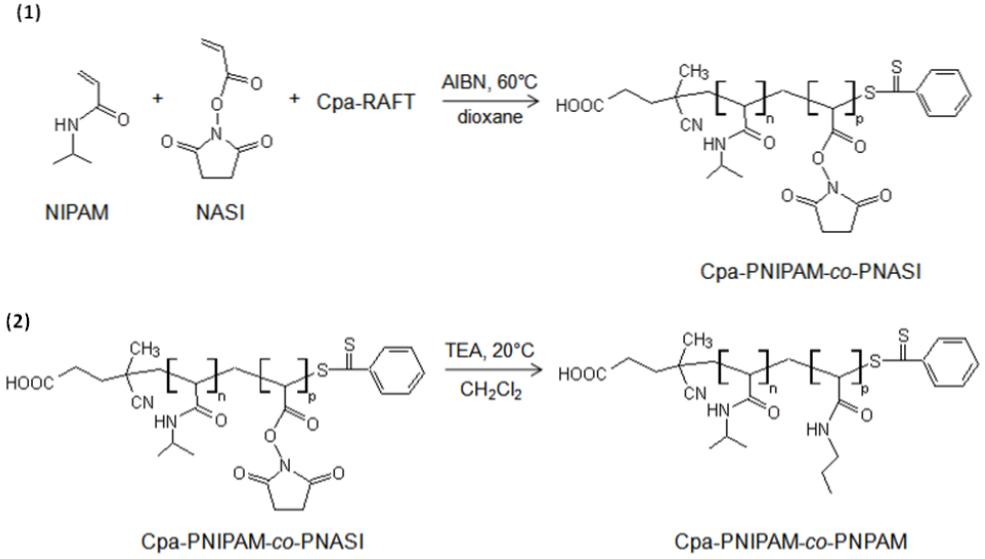

Figure 2.4: Schematic representation of reaction routes for: (1) copolymerization of Cpa-PNIPA-NASI (1) and, (2) conversion of Cpa-PNIPAM-co-NASI to Cpa-PNIPAM-co-NPAM by aminolysis using n-propylamine.

2.1.3.2 Chemical characterization

The Cpa-RAFT-PNIPAM-co-NPAM copolymer chemical composition was determined by IR and ^{1}H NMR spectroscopies. ^{1}H NMR spectroscopy was also crucial to determine the NIPAM:NPAM ratio in the copolymer chain. Gel Permeation Chromatography (GPC) study provides the molecular characteristics as well as the polydispersity index.

(i)IR spectroscopy: The IR spectrum represented in Figure 2.5a shows, in addition to the NIPAM peaks, three additional IR bands at 1811, 1781, 1737 cm^{-1} attributed to the succinimide group of NASI [60].

(ii) ^{1}H NMR spectroscopy was employed to determine both the chemical composition and the NIPAM:NASI and NIPAM:NPAM ratios of the Cpa-RAFT-PNIPAM-co-NASI and Cpa-RAFT-PNIPAM-co-NPAM, respectively. In Figure 2.5b, the resonance at δ = 2.95 ppm is attributed to the four CH_2 groups on the succinimide ring of NASI. To determine the NIPAM:NASI ratio, the integral of the resonance peak representing the lone proton on the NIPAM (at δ= 4.0 ppm), and the integral of the resonance peak of the 4 protons of the succinimide ring of NASI (δ= 2.95 ppm, divided by 4) are used as references. In the ^{1}H NMR spectrum of the Cpa-RAFT-PNIPAM-co-NPAM copolymer shown in Figure 2.6, the resonance at δ= 3.10 ppm is attributed to the CH_2 adjoining the amide group of NPAM. The resulting Cpa-RAFT-PNIPAM-co-NPAM with varying NIPAM:NPAM ratio are summarized in 2.2.

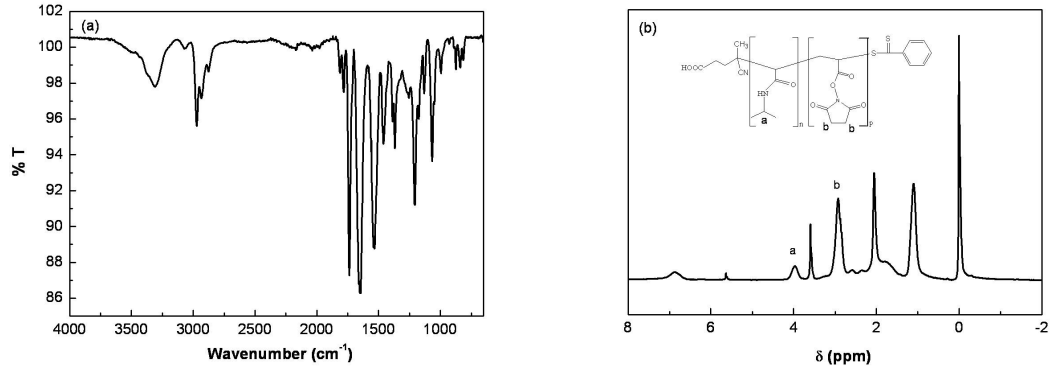

Figure 2.5: IR (a) and ^{1}H NMR (b) spectra of Cpa-RAFT-PNIPAM-co-NASI copolymer.

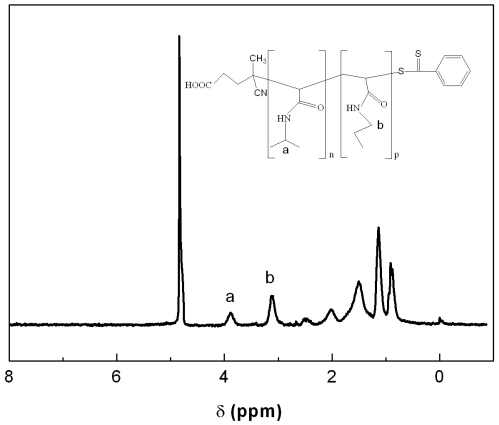

Figure 2.6: ^{1}H NMR spectrum of Cpa-RAFT-PNIPAM-co-NPAM copolymer.

(iii) Gel Permeation Chromatography (GPC)was used to determine the Cpa-PNIPAM-co-NPAM copolymers molar mass. The molecular characteristics are summarized in Table 2.2.

2.1.4 Results and discussion

In an ideal RAFT-polymerization [44], the degree of polymerization is mostly controlled by the [Monomer]:[RAFT]ratio. The RAFT-polymer and RAFT-copolymer [61] theoretical molecular masses are calculated from equation 2.1 and 2.2, respectively:

$$M_{\mathrm{n}} = \frac{[\mathrm{Monomer}] \times M_{\mathrm{Monomer}}}{[\mathrm{RAFT}]} + M_{\mathrm{RAFT}} \tag{2.1}$$

and

$$M_{\mathrm{n}} = \frac{[\mathrm{Monomer1}] \times M_{\mathrm{Monomer1}} + [\mathrm{Monomer2}] \times M_{\mathrm{Monomer2}}}{[\mathrm{RAFT}]} + M_{\mathrm{RAFT}} \tag{2.2}$$

The above equations are to be regarded as guidance only as the experimentally obtained molecular mass of the RAFT-polymer is often lower than the expected value. The following five parameters are considered to affect the resulting molecular mass:

(i) The efficiency of the oxygen removal prior to the polymerization

(ii) The initiator activity

(iii) The efficiency of the chain transfer agent (RAFT-agent)

(iv) The polymerization conditions: solvent, temperature, time

(v) The monomer activity

Since the activities of the reagents (initiator, RAFT-agent and monomer) are often less than 100%, the obtained RAFT-polymer molar mass shifts from the theoretical value. The degree of polymerization can be improved by increasing the monomer, initiator and RAFT-agent efficiency by purifying them as much as possible. Then, the oxygen removal can be optimized. However 100% conversion is not always desirable, since at high conversions termination reactions are more likely to occur and end groups might be lost, leading to higher PDI values. We noticed that RAFT-polymer with molecular mass approaching the theoretical molecular mass were obtained when the reaction mixture was degassed by freeze-thaw cycles at least three times. For the polymerizations undertaken using Shan's conditions [49], the theoretical molar mass derived from equation 2.1 gave $M_{\mathrm{n}} = 22329$ g.mol^{-1}. The obtained molar masses did not reach the calculated theoretical molar mass but vary randomly from 7861 to 17514 g.mol^{-1} independently of the polymerization duration (Table 8.1, samples 1-4). An alternative approach to control the molar mass was then adopted. The [Monomer]/[RAFT] ratio was changed by increasing [Monomer] and decreasing [RAFT] in order to increase the theoretical molar mass. The [RAFT]:[Initiator] was also varied by increasing [Initiator] to better initiate the monomer towards polymerization and decreasing [RAFT] to yield longer polymer chain (fewer number of them to terminate the end of the polymer chain). Using this new approach, the experimentally obtained molecular mass approached the theoretical value of $M_{\mathrm{w}} = 33538$ g.mol^{-1} and two different batches were obtained by controlling the reaction time. Thus, a 24h-reaction time yields polymers of 24603 to 29650 g.mol^{-1} (Table 8.1, samples 5 and 6) and a 48h-reaction time yields polymers of 48089 to 60529 g.mol^{-1} (Table 8.1, samples 7 and 8), ie two-times longer polymer chains.

Homo	[Monomer] ($mol.L^{-1}$)	[RAFT] ($mmol.L^{-1}$)	[AIBN] ($mmol.L^{-1}$)	[RAFT] /[AIBN]	t (h)	M_w ($g.mol^{-1}$)	PDI
1	1.77	8.95	0.65	13.77	48	7861	1.3
2	1.77	8.95	0.65	13.77	48	11852	1.1
3	1.77	8.95	0.65	13.77	48	14617	1.2
4	1.77	8.95	0.65	13.77	48	17514	1.2
5	1.85	5.73	1.34	4.27	24	24603	1.1
6	1.85	5.73	1.34	4.27	24	29650	1.3
7	1.85	5.73	1.34	4.27	48	48089	1.2
8	1.85	5.73	1.34	4.27	48	60529	1.2

Table 2.1: Cpa-PNIPAM homopolymers synthesized by RAFT polymerization using different [Monomer]/[RAFT] and [RAFT]/[Initiator] ratios and polymerization times at 60°C.

For the copolymerization, The resulting copolymer molecular masses (M_n = 40000-46066 $g.mol^{-1}$) were found to be close to theoretical value. Simultaneous addition of the co-monomers NIPAM and NASI in the reaction mixture produced statistical Cpa-RAFT-PNIPAM-co-NASI, as reported in literature for other NASI-based copolymers [62] . On the other hand, the final molar ratio of NIPAM to NASI on the copolymer chain did not agree with the initial NIPAM:NASI molar ratio: an initial ratio of 3:1 (and 9:1) yields a final ratio of about 2:1 (Table 2.2). This lower final content of NIPAM may be due to the higher reactivity of NASI towards the initiator. Further trials led us to the observation that by decreasing the initiator concentration, the final molar ratio approaches that of the initial value. Subsequent aminolysis with n-propylamine converts the Cpa-PNIPAM-co-NASI to Cpa-PNIPAM-co-NPAM. A similar lower final NIPAM:NPAM ratio has been reported by Mao et al [63] for copolymers prepared using a different synthesis route. In their case, starting from PNASI homopolymer, PNIPAM-co-NPAM copolymer was produced by aminolysis using different molar ratios of n-propylamine and isopropylamine. They explained the higher final ratio of NPAM by the higher nucleophilic nature of the primary amine, and where steric bulk of the isopropylamine decreased its rate of substitution of the active ester.

Copo	[NIPAM] ($mol.L^{-1}$)	[NASI] ($mol.L^{-1}$)	NIPAM:NASI molar ratio		[RAFT] ($mmol.L^{-1}$)	[AIBN] ($mol.L^{-1}$)	[RAFT] / [AIBN]	M_w ($g.mol^{-1}$)
			initial	final				
1	1.38	0.46	3:1	1:0.42	5.70	1.14	5	43066
2	1.70	0.19	9:1	1:0.55	5.81	1.14	5	46066
3	1.38	1.38	1:1	1:1	1.59	0.18	9	40000

Table 2.2: Cpa-PNIPAM-co-NPAM copolymers synthesized using different [NIPAM]/[NASI] and [RAFT]/[Initiator] ratios at T = 60°C. The PDI values are 1.5 for all copolymers.

2.1.5 Thermal properties of Cpa-PNIPAM and Cpa-PNIPAM-co-NPAM

The collapse transition behavior of the thermosensitive RAFT-polymers were characterized by transmission measurement and by Differential Scanning Calorimetry (DSC). The latter provides additional information about the thermal properties of the polymers and also the collapse process such as the cooperative nature.

(i) Transmission measurements: The absorbance of aqueous solutions of Cpa-PNIPAM and Cpa-PNIPAM-co-NPAM (C_p = 0.2 mg.mL^{-1}) at λ= 600 nm were recorded at different temperatures. The collapse temperature T_c was evaluated from the intersection of the tangents to the curves (Figure 2.7).

(ii) Differential Scanning Calorimetry (DSC):The microcalorimeter used is a MicroCal VP-DSC with a sample cell volume of 0.507 mL. Polymer solutions at concentration of 1 mg.mL^{-1} were scanned at heating/cooling rate of 1°C/min from 5-90°C under 180 kPa pressure. Two cycles of heating and cooling were performed on each sample and the latter cycle was used to determine the values of onset (T_0) and peak maximum (T_m) collapse transition. T_0 was evaluated from the intersection of the tangents of the baseline and the peak.

2.1.5.1 Transmission measurements

First of all, thermoresponsive PNIPAM homopolymer synthesized by radical polymerization using neutral initiators exhibits coil-globule transition at a critical temperature T_c = 32-33°C. [64],[65]. The Cpa-PNIPAM synthesized in this study by RAFT polymerization contains a charged carboxyl end-group that raises the transition temperature to T_c =34-38°C depending on the chain length; such terminal group effects are more important for shorter chains than longer ones [66]. For the series of Cpa-PNIPAM synthesized here, we also find a small effect of chainlength on the collpase temperature. An important aspect of thermosensitive polymers lies in the possibility to tune the expansion-collapse transition temperature.This can be achieved by screening the electrostatic charges at the polymer end chain with salt addition or by incorporating hydrophilic/hydrophobic groups on the polymer chain to obtain a copolymer with varying hydrophilic/hydrophobic balance. In this study, hydrophobic n-propylamine is introduced to increase overall hydrophobicity while keeping the same chemical functions. The resulting Cpa-RAFT-PNIPAM-co-NPAM copolymer hydrophobicity is thus controlled by a balance of isomeric primary and secondary amines. Firstly, as expected, the collpase temperature of the Cpa-PNIPAM-co-NPAM copolymer is lower than the Cpa-PNIPAM homopolymer. It is further shown that the T_c decreases approximatively linearly with NIPAM:NPAM ratio. Secondly, for both types of PNIPAM-based polymers, the T_c can be further lowered with increasing salt concentration (Figure 8.6b). The T_c values measured by transmission are given in Table 2.3.

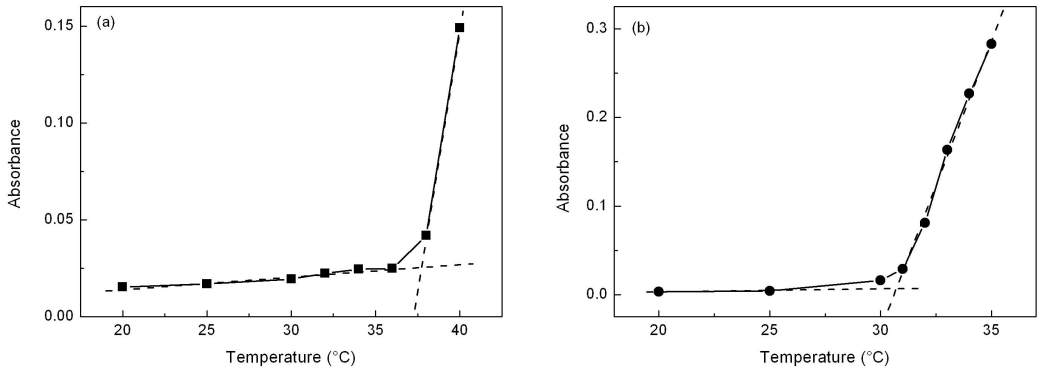

Figure 2.7: Determination of the T_c of : (a) Cpa-RAFT-PNIPAM$_{154}$ and (b) Cpa-RAFT-PNIPAM$_{176}$-co-PNPAM$_{176}$.

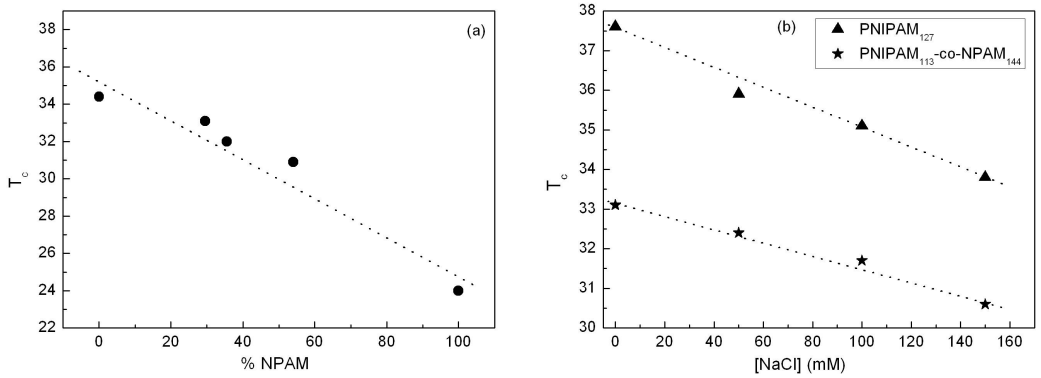

Figure 2.8: Plot of T_c as a function of % NPAM on the polymer chain for comparable chain lengths (a); and effect of NaCl on T_c (b).

Polymer	[NaCl] (mM)	T_c (°C)
$PNIPAM_{127}$	0	37.6
$PNIPAM_{127}$	50	35.9
$PNIPAM_{127}$	100	35.1
$PNIPAM_{127}$	150	33.8
$PNIPAM_{154}$	0	37.5
$PNIPAM_{265}$	0	34.4
$PNIPAM_{270}$-co-$PNPAM_{113}$	0	33.1
$PNIPAM_{270}$-co-$PNPAM_{113}$	50	32.4
$PNIPAM_{270}$-co-$PNPAM_{113}$	100	31.7
$PNIPAM_{270}$-co-$PNPAM_{113}$	150	30.6
$PNIPAM_{261}$-co-$PNPAM_{144}$	0	32
$PNIPAM_{176}$-co-$PNPAM_{176}$	0	30.6
$PNPAM_{380}$	0	24.3

Table 2.3: The critical collapse temperatures of the Cpa-RAFT-polymers measured by transmission at λ= 600 nm.

2.1.5.2 Calorimetry measurements

Figure 8.7a compares thermograms of the collapse transitions for Cpa-RAFT-PNIPAM and Cpa-RAFT-PNIPAM-co-NPAM at different NIPAM:NPAM molar ratios. These curves show that both the onset of collapse transition temperature (T_o) and the maximum enthalpy peak temperature (T_m) are shifted to lower temperatures for the copolymers, with a reduction in T_m of about 5°C for NIPAM:NPAM molar ratio 1:1. The calorimetric enthalpies evaluated from the peak areas give $\Delta H^{cal} \approx$ 5 - 7 kJ per mole monomer. These values fall within the range of values reported in the past for PNIPAM homopolymers [67],[68] and correspond to the energy required to rupture H-bonding of the amide group with solvation water molecules. Interestingly for the copolymer, the width of the enthalpy peak is significantly reduced, suggestive of a higher degree of cooperativity in the polymer collapse process. A measure of cooperative effects can be estimated from the two-state coil-to-globule van't Hoff enthalpy: [69], [70] $\Delta H^v = 4RT_m{}^2\ C_p(T_m)/\Delta H^{cal}$ where $C_p(T_m)$ is the specific heat capacity at the peak maximum temperature T_m, and ΔH^{cal} the calorimetric enthalpy mentioned above. ΔH^v represents the enthalpy per "cooperative unit", and the average size per unit is thus, m = $\Delta H^v/\Delta H^{cal}$ (number of monomer per cooperative domain) and the number of cooperative units (or domains) per macromolecule of chain length N is n = N x $\Delta H^{cal}/\Delta H^v$. The estimated enthalpies and cooperativity indices are given in Table 2.4. For Cpa-PNIPAM with chain lengths N = 154 and 265, the average size of the cooperative unit falls in the range m = 92-114, in fairly close agreement with results of Tiktopulo et al for neutral PNIPAM homopolymers with chain lengths N ≈ 100-3000. For the Cpa-PNIPAM-co-NPAM copolymers (NIPAM:NPAM molar ratios 1:0.4 to 1:1) on the other hand, a higher range is obtained with m = 144-174, suggesting an increased level of cooperativity of the more hydrophobic primary amine in the collapse transition. Therefore, for a given polymer above a critical chain length (N ≈ 100 for PNIPAM), the size of each cooperative unit in the collapse transition is almost independent of chain length (see Figure 8.7b); only the number of

cooperative units (collapse domains) per macromolecule increases. For the range of molecular weights investigated here, n ≈ 2-3. These results show that T_c measured by the more conventional transmission method falls in closer agreement with the calorimetric T_m rather than the onset of collapse transition temperature T_o.

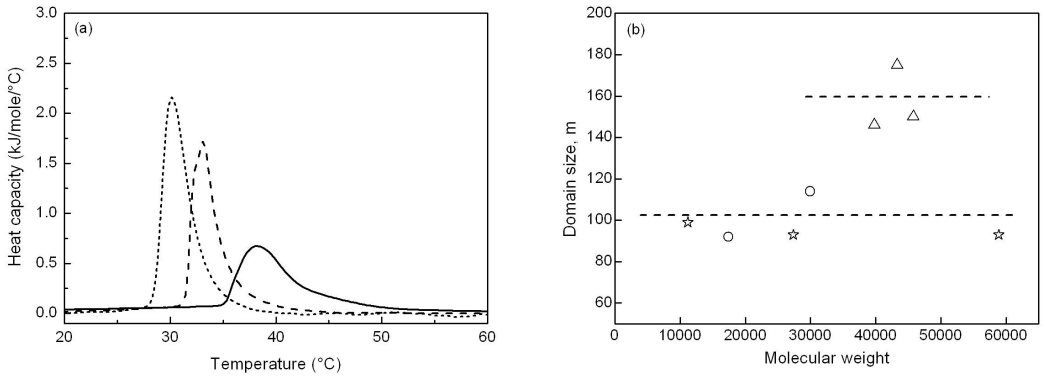

Figure 2.9: (a) Microcalorimetry endotherms of aqueous solutions of Cpa-PNIPAM$_{154}$ (solid line), Cpa-PNIPAM$_{270}$-co-PNPAM$_{113}$ (dashed line), Cpa-PNIPAM$_{176}$-co-PNPAM$_{176}$ (dotted line). C_p = 1mg/mL, scanning rate = 1°C/min. The y-axis is represented in per mole monomer. (b) Size of cooperative unit (number of monomers per collapse domain) versus molecular mass. (circles): Cpa-PNIPAM; (stars): PNIPAM from Tiktopulo and al; (triangles): Cpa-PNIPAM-co-NPAM. The horizontal lines are a guide to show the two different populations for Cpa-PNIPAM homopolymers and Cpa-PNIPAM-co-NPAM copolymers.

Polymer	N	NIPAM:NPAM molar ratio	T_o (°C)	T_m (°C)	T_c (°C)	$\Delta^a H^{cal}$ (kJ.mol^{-1})	$^b\Delta H^v$ (kJ.mol^{-1})	n	m
Homo 1	154	1:0	34.2	38.2	37.6	747 (4.9)	445	1.7	92
Homo 2	265	1:0	31	34.8	34.4	1913 (7.2)	829	2.3	114
Copo 1	383	1:0.42	30.7	33.1	33.1	2662 (7.0)	1219	2.2	174
Copo 2	405	1:0.55	30.7	32.9	32	2479 (6.1)	881	2.8	144
Copo 3	352	1:1	28.2	30.1	30.6	2365 (6.7)	982	2.4	146

Table 2.4: Microcalorimetric data of Cpa-RAFT-PNIPAM and Cpa-RAFT-PNIPAM-co-NPAM aqueous solutions. C_p = 1 mg/mL, scanning rate = 1°C/min. T_o and T_m are onset and peak transition temperatures, respectively.[a]calorimetric enthalpy obtained from peak area (kJ/mole polymer; the number in parenthesis gives kJ/mole repeating unit). [b]van't Hoff enthalpy (kJ/mole 'cooperative unit'). n = N × $\Delta H^{cal}/\Delta H^v$(average number of 'cooperative domain'). m = Δ $H^v/\Delta H^{cal}$ = N/n (size of cooperative domain), N = degree of polymerization. T_c is the critical collapse temperature measured by light absorbance at λ= 600 nm.

2.2 Synthesis of polymer-protected gold nanoparticles

This section describes the synthesis methods and the characterization of the polymer-protected gold nanoparticles. Successful synthesis routes for gold nanoparticles have been previously reported by Shan [57]. We adopt Shan's methods to stabilize the gold particles with the pre-synthesized cpa-RAFT-PNIPAM homopolymers and the cpa-RAFT-PNIPAM-co-NPAM copolymers. Two kinds of thermoresponsive and amphiphilic gold nanoparticles; Au-PNIPAM and new Au-PNIPAM-co-PNPAM, are thus prepared by "grating-to" technique via both one-step and two-step synthesis. In this work, a wider range of polymer molecular masses are used as stabilizers and the [polymer]:[gold] ratio is adjusted to obtain larger particles. The gold core size and the grafting density of the particles resulting from each method are determined. Then, comparisons between the one and two-step way synthesis are made.

2.2.1 "Grafting-to" technique

The "grafting-to" technique consists of grafting a pre-synthesized polymer at the metal surface, while in the "grafting-from" technique, monomers are polymerized from the metal surface carrying polymerization-initiating species. In this study, the RAFT-polymers is terminated with a dithioester or thiol group that possesses a sulfur atom capable of chemically binding to the gold surface. As bare gold is unstable, the particularity of our synthesis is that the grafting of the polymer chains occurs simultaneously as the growth of the gold cores. Two ways of preparation, one-step and two-step synthesis, are distinguished. Both types of reactions are carried out in a homogenous THF phase and the concentration of $HAuCl_4$ is always kept at 0.1 mmol and the molar ratio of $LiB(C_2H_5)_3H$: $HAuCl_4.xH_2O$ is 10:1. The ratio between the RAFT-polymer and $HAuCl_4$ is changed by varying the amount of RAFT-polymer used in the preparation to modulate the gold-core size of the resulting nanoparticles.

2.2.2 Experimental

2.2.2.1 "One-step" method

This method consists of directly employing the RAFT-polymer end-capped with the ditioester group without pre-hydrolysis. The strong base $LiB(C_2H_5)_3H$ simultaneously reduced $HAuCl_4$ to Au(0) and hydrolyzed the dithioester end group of the polymer to a thiol which then immediately bound the gold nanoparticles. To obtain different gold core sizes, two $HAuCl_4$:RAFT-polymer molar ratios were used: (i) 10:1 (0.1 mmol:0.01 mmol)to obtain small particles and (ii) 20:1 (0.1 mmol:0.005 mmol) to obtain larger particles. The RAFT-polymer and $HAuCl_4.xH_2O$ were dissolved in THF. A 1.0 M THF solution of $LiB(C_2H_5)_3H$ was then added drop-wise to the vigorously stirred solution. The solution immediately turned purple with a little gas evolution and was further stirred for 2h. The resulting dispersions were purified by centrifugation at 5000 rpm at 6°C for 30 min to remove big aggregates; only a small amount of precipitate was observed on the bottom of the centrifuge tube and the supernatant was collected. Gold particles from the supernatant were then precipitated in a ether: hexane (2:1) mixture and centrifuged at 5000 rpm at 6°C for 30 min (3 times 10 min)

to remove free polymers. The nanoparticles were re-dispersed in water and the dispersions further centrifuged at 30°C to remove unreacted polymers that precipitated at temperature close to their LCST. The resulting gold nanoparticles were then washed with very little cold water to remove any residual free polymers and then dried under vacuum. In a final step to ensure maximum removal of free polymers, the nanoparticles were redissolved in THF and dialyzed against water for 48 hours and finally dried under vacuum. To obtain different gold core sizes, two molar ratios of $HAuCl_4$:RAFT-polymer were used, 10:1 (0.1 mmol: 0.01 mmol) to obtain small particles and 20:1 (0.1 mmol: 0.005 mmol)to obtain larger particles. The synthesis route for polymer-protected gold nanoparticles is illustrated in Figure 2.10

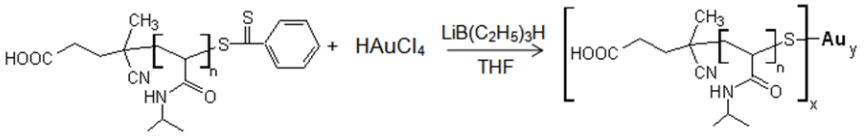

Figure 2.10: The synthesis route of Cpa-PNIPAM-protected gold nanoparticles

2.2.2.2 "Two-step" method

This method consisted of hydrolyzing the polymer grafts prior to the reaction with gold. The RAFT-PNIPAM polymers were modified into thiolated PNIPAM-SH polymers in THF by hydrolysis of the dithioester end group to a thiol using a 10 fold molar excess of $NaBH_4$. The reaction solution was stirred for 12h. The modified polymers were precipitated in diethyl ether, dried under vacuum and purified by dialysis against water to remove any side products. Then the gold particles were prepared in the same way of the gold particles prepared via the one-step technique. The pre-hydrolyzed polymer graft and $HAuCl_4.xH_2O$ were dissolved in THF. A 1.0 M THF solution of $LiB(C_2H_5)_3H$ was then added drop-wise to the vigorously stirred solution. The solution immediately turned purple with a little gas evolution and was further stirred for 2h. Unlike the dispersions from the one-step synthesis, the presence of gold aggregates was visibly detectable. The resulting dispersions were first separated from the visible aggregates before centrifugation at 5000 rpm at 6°C for 30 min to remove big particles.The gold core size was also tuned by using the same $HAuCl_4$:RAFT-polymer molar ratios. The one and two-step methods are illustrated in Figure 2.11

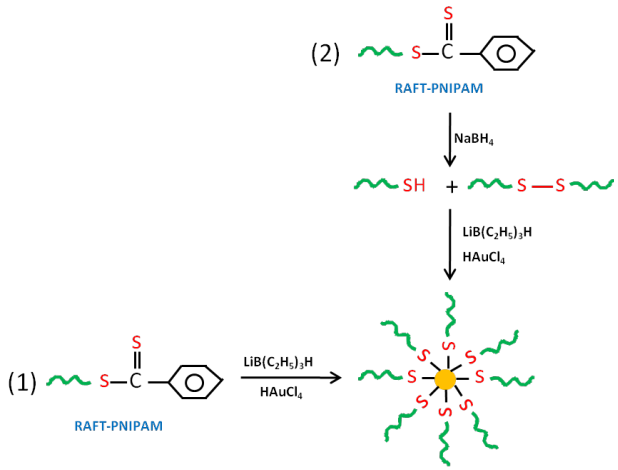

Figure 2.11: The synthetic routes for polymer-protected gold nanoparticles by a 'grafting-to' technique via (1) one-step method and (2) two-step method, employed by Shan.

2.2.3 Characterization

The mean gold core sizes were characterized by High-Resolution Transmission Electron Microscopy (HRTEM) and the total amounts of grafted polymer and residual gold were estimated with Thermogravimetric analysis (TGA). From those characterizations, we were able to calculate the number of gold atoms per gold core and the grafting density (the number of polymer chains grafted per particle).

2.2.4 Results and discussion

Using the one-step way, we successfully synthesized two populations of gold core size by controlling the $HAuCl_4$: Polymer molar used in the preparation. Particles sizes ranging from 2.9 to 5.0 nm were obtained using $HAuCl_4$: RAFT-Polymer molar ratio 10:1, and larger size particles ranging from 6.6 to 8.0 nm using molar ratio 20:1. From these results, it is clear that the gold core size increases with decreasing molar ratio of $HAuCl_4$:Polymer, that is to say with decreasing polymer concentration (Figure 8.9 and Figure 2.13). Grafting densities around 1-2 chains/nm^2 were obtained independently of the concentration and molecular mass of the RAFT-polymer . An exception was found for the sample Au-PNIPAM$_{261}$-NPAM$_{144}$ where a lower grafting density of 0.64 chain/nm^2 may be due to adsorption of the more hydrophobic polymer on the gold core, impeding accessibility of the surface to further grafting. The grafting density of the metal nanoparticle should depend on the concentration of the polymer used in the preparation and the polymer grafting efficiency. Our aim was to synthesize larger particles than Shan and that are stabilized by longer polymer grafts. As a result, the amount of polymer used was two times less than the original recipe and the protecting polymer length was up to 4 times longer. The parameters mentioned are expected to contribute in lowering the grafting density and favouring the aggregates formation. Additionally, it is expected to be more difficult for a high molar mass polymer to stabilze gold particles for steric reason. The sulfur atom capable of binding to gold may be hidden inside the chain and, as a result,

is not available. Then, if a long chain polymer succeeds to coat the particle, it occupies more space than a short chain grafts space which leaves less space for other long chain polymers to graft the nanoparticle surface. Despite all these factors, RAFT-polymers with molar masses from 7862 to 46066 g.mol^{-1} have been successfully grafted to the gold core. The characteristics of the thermoresponsive gold nanoparticles prepared via the one-step way are outlined respectively in Table 2.5.

When employing the two-step approach, particles with diameter ranging from 2.00 to 3.9 nm were successfully prepared with $HAuCl_4$:Polymer molar ratio 10:1. However, synthesis using $HAuCl_4$:Polymer molar ratio 20:1 failed and large insoluble aggregates were obtained. Therefore, unlike the one-step way method, we could not control the gold core size by tuning the $HAuCl_4$:Polymer molar ratio. The other disadvantage of this method was that it yielded more polydisperse particles. In fact, already during the synthesis, a larger amount of aggregates were visibly detectable. The TEM image in Figure 2.13 (right)shows a mixture of remaining larger aggregates and small individual particles even after centrifugation. In the two-step synthesis, the RAFT-polymer was first hydrolyzed to PNIPAM-SH prior to the reaction with the gold. Exposed to air, the thiol end of PNIPAM-SH is prone to react easily with another PNIPAM-SH to form disulphide PNIPAM-S-S-PNIPAM. Results from previous work done by Shan, showed that even if the hydrolysis is carried out under a nitrogen atmosphere, disulphides still occured. Therefore the protecting polymer used to bind to the gold cores was composed of a mixture of PNIPAM-SH with the thiol ready to react with gold and PNIPAM-S-S-PNIPAM unable to react with gold as the thiol was unavailable. As a consequence, the grafting efficiency was lowered as less polymers were effective to graft and this was even worse when preparing particles using reduced amount of polymers. Thus the grafting density was very low and gold aggregate formation was favoured leading to formation of nanoparticles with broad size distribution. From these results, we can conclude that the one-step method is more suitable to synthesize the gold nanoparticles as it yielded less polydisperse particles and the $HAuCl_4$: RAFT-Polymer molar ratio can be successfully controlled to obtain varying sizes of polymer-coated gold nanoparticles.

Au-Polymer	Formula	D (nm)	Grafting density (chains/nm^2)
Sample 1	$Au_{8863}(PNIPAM_{67})_{156}$	6.6	1.14
Sample 2	$Au_{15785}(PNIPAM_{127})_{312}$	8.0	1.55
Sample 3	$Au_{2809}(PNIPAM_{154})_{75}$	4.5	1.18
Sample 4	$Au_{2809}(PNIPAM_{265})_{127}$	4.5	2.00
Sample 5	$Au_{4590}(PNIPAM_{270}\text{-}PNPAM_{113})_{112}$	5.3	1.27
Sample 6	$Au_{752}(PNIPAM_{260}\text{-}PNPAM_{144})_{17}$	2.9	0.64
Sample 7	$Au_{459}(PNIPAM_{57})_{33}$	2.7	1.4

Table 2.5: Polymer-stabilized gold nanoparticles Au_y-$(Polymer_n)_x$ prepared via 'one-step' synthesis in THF; [$HAuCl_4$] = 0.1 mmol/L, $HAuCl_4$:$LiB(C_2H_5)_3$ = 10:1. n = degree of polymerization, x = number of chains per particle, y = number of gold atoms. Molar ratio $HAuCl_4$:Polymer = 10:1 (samples 3-6) and 20:1 (samples 1,2). Sample 7 was prepared by Shan using molar ratio $HAuCl_4$:Polymer = 10:1.

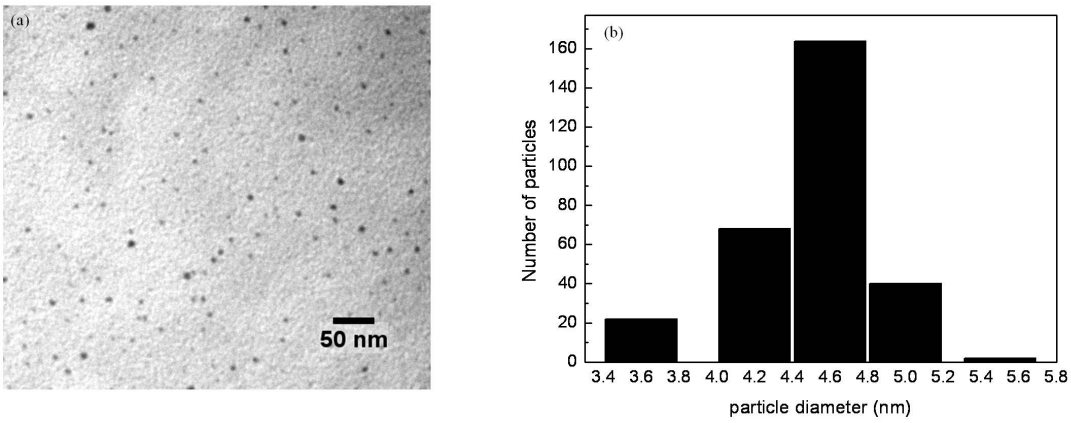

Figure 2.12: TEM image (a) and corresponding size distribution (b) of Au-PNIPAM$_{265}$ synthesized via the one-step synthesis using $HAuCl_4$:Polymer molar ratio 10:1.

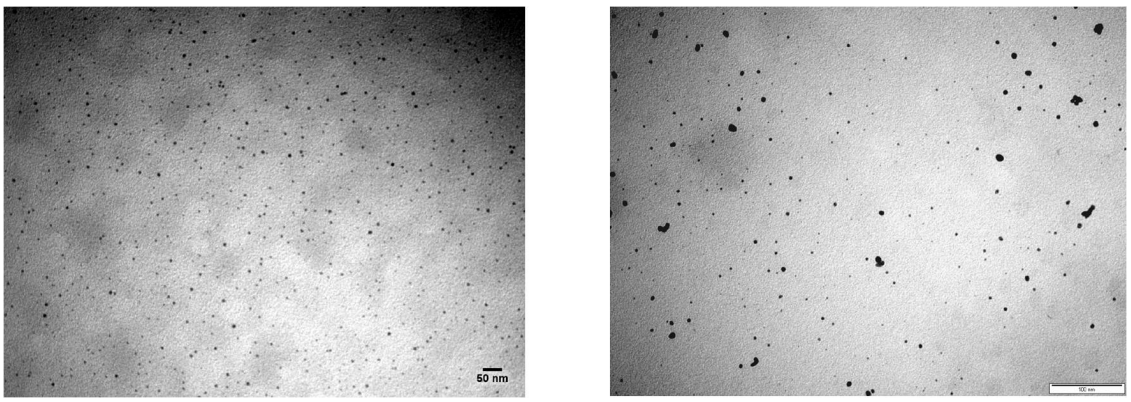

Figure 2.13: TEM images of: Au-PNIPAM$_{127}$ synthesized via the one-step synthesis using $HAuCl_4$:Polymer molar ratio 20:1 (left)and Au-PNIPAM$_{154}$ synthesized via the two-step synthesis using $HAuCl_4$:Polymer molar ratio 10:1 (right).

2.2.5 Summary

Gold nanoparticles protected with two types of PNIPAM-based thermosensitive polymers have been synthesized. The polymers were synthesized by RAFT-polymerization where molecular chain lengths were controlled by [NIPAM]/[RAFT] ratio and reaction time. An important aspect of thermosensitive polymers lies in the possibility to tune the expansion-collapse transition temperature. To this end, we have synthesized a copolymer by incorporation of n-propylamine co-monomer that is more hydrophobic than its n-isopropyl counterpart. The hydrophobicity of the resulting copolymer, while maintaining similar chemical formula along the chain, is thus controlled by a balance of the isomeric primary and secondary amines. A decrease of $\Delta T_c \approx 10^{\circ}C$ is observed from NPAM fraction from 0 to 1. The T_c values can be further reduced by addition of NaCl to screen the charged RAFT end-group. Calorimetry data also suggest a higher cooperativity effect in the collapse process of the copolymer.

Synthesis of the polymer-protected gold nanoparticles was carried out by "grafting-to" method in a "one-step" approach. This method was used by Shan [49] to synthesize very small particles (D ≈ 3 nm) grafted with short PNIPAM chains (N ≈ 50). We have adopted this approach and, by judicious modifications of Shan's recipe, we have succeeded in obtaining larger-sized particles and also much longer graft chain lengths. Thus, two types of colloidally-stable thermosensitive gold nanoparticles, Au-PNIPAM and Au-PNIPAM-co-NPAM of varying hydrophobicities have been synthesized. The wide range of particle size (D ≈ 3-8 nm) and of graft polymer chain length (N ≈ 57-400) thus facilitate our studies to understand and control their optical properties, and the available range of T_c increases the flexibility in which the thermosensitive aspect can be exploited.

Figure 2.14: Thermoresponsive gold nanoparticles synthesized by "Grafting-to" via the one-step technique:(a)Au-PNIPAM (M_w = 7861 - 29650 g.mol^{-1} and D =4.5 - 8.0 nm) and (b) Au-PNIPAM-co-NPAM (NIPAM:NPAM = 2.4:1 to 1:1 and D = 2.9 - 5.3 nm).

Chapter 3

Structural properties of polymer-protected gold nanoparticles

In this chapter, the structural properties of polymer-protected gold nanoparticles in solution are studied. The objective is to correlate these structural properties with the gold nanoparticles bulk optical properties. Small Angle Neutron Scattering (SANS) measurements were performed on gold particles stabilized by varying molecular mass of RAFT-polymer on the PACE spectrometer (Laboratoire Léon Brillouin, CEA-Saclay, France) where we have employed two configurations: (i) D= 3 m, λ = 6 Å; corresponding to a configuration for "meduim q" (t $\geq$ 30 min) and (ii) D = 5 m, λ = 13Å; corresponding to a configuration for "small q" (t $\geq$ 120 min). These two configurations allow us to study our sample in the range of q included between 0.003 and 0.12 $Å^{-1}$. The resulting scattering curves were treated and then fitted using the three following models that we are going to describe: core-shell, hairy-sphere and hard sphere.

3.1 Contrast and contrast-match

3.1.1 Contrast

To measure a significative scattered intensity, it is necessary to have a sufficient contrast between the sample and the medium. This contrast is calculated from the difference between the scattering length densities (ρ) of the sample and the medium. The ρ value of a component is derived from the coherent scattering lengths b_i of all atoms composing the sample.

$$\rho = \frac{N_A d}{M} \sum_i a_i b_i \tag{3.1}$$

d is the component density in $g.cm^{-3}$, M its molecular mass in $g.mol^{-1}$ and N_A the Avogadro number. a_i is the number of atoms of scattering length b_i in the sample. The contrast is defined as the square of the difference between the scattering length densities (ρ) of the sample and the medium : $\Delta\rho^2 = (\rho_{\text{component A}} - \rho_{\text{component B}})^2$. b_i can be positive or negative depending on whether the neutron-matter interaction is attractive or repulsive and varies from one isotope to another. These differences have an influence on the scattering

length densities values. The b values of components used in this thesis are listed in Table 3.1

Component	b (10^{-12} cm)	ρ (10^{-6})
D_2O	1.9140	6.39
H_2O	-0.1680	-0.5621
PNIPAM in H_2O	1.384	0.79
PNIPAM in D_2O	2.4257	0.90

Table 3.1: b and ρ values of different components.

The difference between the ρ value of H_2O and its deuterated equivalent D_2O (as well as for the polymer and its deuterated equivalent) is due to the difference of the scattering length b of the hydrogen (b_H = -0.374 × 10^{-12} cm) and the deuterium (b_D = 0.667 × 10^{-12} cm). This difference is the basis of the important advantage of SANS in that isotopic substitution can be mode to change the contrast without modifying the chemical properties of the molecule.

3.1.2 Contrast-match

When studying a system composed of 3 components like our gold nanoparticles (component 1) grafted with thermoresponsive polymer (component 2) in a solvent (component 3), we have three different contrasts and the scattered intensity includes the contributions of the two components compared to the solvant and between them. The resulting signal will be complex and will need to be separated. Due to the negative value of b for H_2O, it is possible to prepare a mixture of H_2O and D_2O to contrast-match the solvent with one of the components.

$$\rho_{\text{mixture}} = x\rho_{\text{solvent D}} + (1-x)\rho_{\text{solvent H}} \tag{3.2}$$

In our 3-component system, the contribution of either the gold core or the protecting polymer can be matched to give the signal of polymer or gold core, provided that their ρ is included between the ρ of H_2O and the ρ of D_2O. This technique is called contrast-match. In the case of our polymer-protect gold particles, the polymer contribution can be switched-off by a 19% H_2O and 81% D_2O (volume %) mixture and the gold-core contribution can be matched-out by a 27% H_2O and 73% D_2O (volume %) mixture. Figure 3.1 represents the polymer and gold signal extinction.

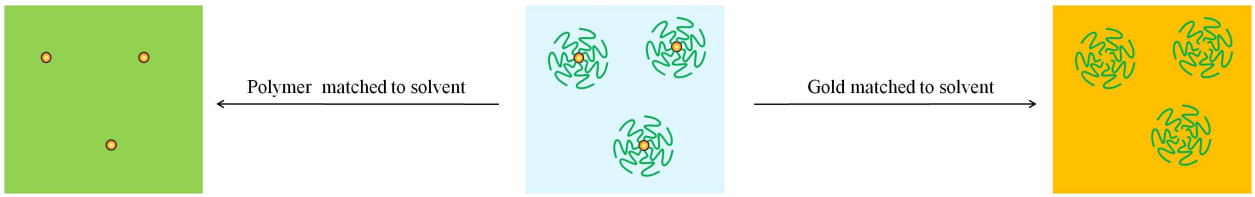

Figure 3.1: Principle of contrast-match.

In our experiments, it was necessary to work with very dilute solutions in order to be as close to the conditions used to study the optical properties. Unfortunately, under these conditions, contrast-match scattering signals were extremely weak and even very long counting times gave signals that were difficult to exploit. Since we were more interested in the structure of the polymer graft, we decided to maximize the contrast between the protecting polymer and the solvent by using pure D_2O where $\Delta\rho = \rho_{\text{polymer}} - \rho_{\text{solvent}} = (0.90 - 6.39) \times 10^{-6}$ Å^{-2} = -5.49 $\times 10^{-6}$ Å^{-2}. The gold core contributes to a much lesser extent due to its lower contrast with the solvent : $\Delta\rho = \rho_{\text{gold core}} - \rho_{\text{solvent}} = (4.50 - 6.39) \times 10^{-6}$ Å^{-2} = -1.89 $\times 10^{-6}$ Å^{-2}.

3.2 Modelling

In the past, nanoparticles grafted with polymers have been modelled with a few classic models. These include the core-shell, Pedersen (Hairy sphere) and hard sphere models. For example, Chevigny [71] used the core-shell and Pedersen models to characterize silica nanoparticles grafted with polystyrene. She found that both models worked well at small angle as they yielded comparable shell size (shell thickness for the core-shell model and R_g for the Pedersen model) for the same sample. Hourdet and al [72] have also found the Pedersen model to give good fits to their SANS data on PNIPAM-based copolymers/silica system. In our study, the three models mentioned above are employed to charaterize the protecting polymer shell. The first model is the core-shell model which represents a sphere (the core: gold) stacked in an other sphere (the shell: polymer). The second model, Pedersen (Hairy sphere) model takes into account the nature of the shell by modelling it by an infinite number of gaussian chains. The last model, hard sphere represents the core + shell forming a filled (and dense) sphere.

3.2.1 Core-shell model

This model is a combination of form factors of hard spheres: a small sphere of scattering length density ρ_{core} (the core) and a big sphere (with a hole in the middle of radius R_{core}) with scattering length density ρ_{shell} (the shell). In our case, the contrast gold core/solvent is minimal and the contrast between the polymer shell and the solvent is maximized [73]. The total scattering intensity is I(Q)= P(Q)× S(Q) where P(Q) is the form factor and S(Q) is the structure factor (interparticle interaction). But for dilute solution, S(Q)=1. The final scattered intensity is:

$$I(Q) = [\Delta\rho_{core} \times \frac{4}{3}\pi \times R_{core}^3 \times F(R_{\text{core}}) + \Delta\rho_{shell} \times \frac{4}{3}\pi \times R_{shell}^3 \times F(R_{\text{shell}})]^2 \times \frac{m}{V} \quad (3.3)$$

where $\Delta\rho_{\text{core}} = \rho_{\text{core}} - \rho_{\text{shell}}$ and $\Delta\rho_{\text{shell}} = \rho_{\text{shell}} - \rho_{\text{solvent}}$, m the number of spheres and V the total volume. F(Q,R) is the amplitude of the form factor such as:

$$F(Q,R) = 3\frac{\sin(QR) - QR\cos(QR)}{(QR)^3} \quad (3.4)$$

Another parameter of this model concerns the shell scattering length density. In fact, the chains are swollen with solvent and the ρ_{shell} will be proportional to the quantity of solvent according to the formula:

$$\rho_{shell} = x\rho_{solvent} + (1-x)\rho_{polymer} \tag{3.5}$$

x represents the solvent volume fraction in the shell. The fitting parameters for this model are the polymer shell thickness (e), the gold core radius (R_{core}), the polydispersities (polymer shell and gold core) and the scattering length densities (polymer shell, gold core and surrounding solvent).

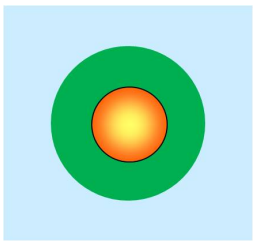

Figure 3.2: Representation of the core-shell model.

3.2.2 Pedersen model (Hairy sphere)

This model was originally developped by Pedersen [74] for block copolymers micelles. The shell is modeled by a fixed number of gaussian chains which do not interact between them. Many variations of this model are possible. For a hard sphere core, the general expression is:

$$\begin{aligned} P_{\text{Pedersen}}(Q, R_{\text{AuNPs}}, R_{\text{g}}) \;=\; & V_{core}^2 \Delta\rho_{core}^2 P_{sphere}(Q, R_{\text{AuNPs}}) \\ & + N\Delta\rho_{chain}^2 V_{chain}^2 P_{chain}(Q, R_{\text{g}}) \\ & + 2NV_{core}V_{chain}\Delta\rho_{core}\Delta\rho_{chain}S_{core-chain}(Q, R_{\text{AuNPs}}, R_{\text{g}}) \\ & + N(N-1)\Delta\rho_{chain}^2 V_{chain}^2 S_{chain-chain}(Q, R_{\text{AuNPs}}, R_{\text{g}}) \end{aligned}$$

V_{core} and V_{chains} are the volumes of gold particle and the polymer chain, P_{sphere} and P_{chain} are the form factors of the particle and the polymer chain, $\Delta\rho^2{}_{\text{core}}$ and $\Delta\rho^2{}_{\text{chain}}$ are the respective contrast between the core and the solvent and the chain and the solvent, $\text{S}_{\text{core-chain}}$ and $\text{S}_{\text{chain-chain}}$ are the crossed terms core-chain and chain-chain (interactions between the chains), and N is the number of chains per particles. The crossed terms are defined by the following expressions:

$$S_{core-chain}(Q, R_{\text{AuNPs}}, R_{\text{g}}) = F_{\text{sphere}}(Q, R_{\text{AuNPs}}) \times \frac{1-e^{-Q^2R_g^2}}{Q^2R_g^2} \times \frac{\sin(Q(R_g + R_{\text{AuNPs}})}{(Q(R_g + R_{\text{AuNPs}})} \tag{3.6}$$

For the crossed term core-chain, and:

$$S_{chain-chain}(Q, R_{\mathrm{AuNPs}}, R_{\mathrm{g}}) = \left[\frac{1 - e^{-Q^2 R_g^2}}{2Q^2 R_g^2} \times \left(\frac{\sin(Q(R_g + R_{\mathrm{AuNPs}})}{(Q(R_g + R_{\mathrm{AuNPs}})}\right)\right]^2 \tag{3.7}$$

for the crossed term inter-chains

As for the core-shell model, the core polydispersity is considered and no complementary polydispersity of the chain length is introduced. The polydisperse form factor has the following expression:

$$P_{\mathrm{Pedersen}}(Q, R_{\mathrm{AuNPs}}, R_{\mathrm{g}}) = \int p(R, R_{\mathrm{AuNPs}}, \sigma) P_{\mathrm{Pedersen}}(Q, R_{\mathrm{AuNPs}}, R_{\mathrm{g}}) dR \tag{3.8}$$

The scattered intensity with shells volume fraction ϕ and the scattering object volume $\mathrm{V_{part}}$ is then written:

$$I(Q) = (\phi / V_{\mathrm{part}}) P_{\mathrm{Pedersen}}(Q, R_{\mathrm{AuNPs}}, R_{\mathrm{g}}) \tag{3.9}$$

This model was initially developped to describe block copolymer and included an additional parameter illustrating the interdiffusion zone between two polymers and the impossibility for the chain to penetrate in the polymer core was imposed with the help of an appropriate profile for the shell. In our case, it is not necessary to use this parameter as it is physically impossible for the polymer to penetrate the gold core, and this has simplified the analytic formulation of the model.

The fit parameters for this model are the $\mathrm{R_g}$ of polymer chains, the gold core radius, the polydispersities (polymer shell and gold core) and the scattering length densities (polymer shell, gold core and surrounding solvent).

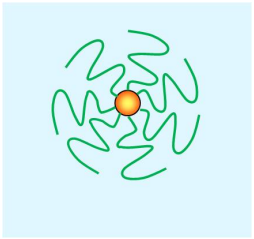

Figure 3.3: Representation of the hairy sphere model.

3.2.3 "Hard sphere" model

This model is used to characterize object composed of one component. To model the form factor of the particles, we use the form factor of a sphere:

$$P(Q,R) = \left[3\frac{\sin(QR) - QR\cos(QR)}{(QR)^3}\right]^2 \tag{3.10}$$

The measurements are realised in very dilute solution. The scattered intensity therefore allows to directly observe the form factor of the particles. However, we need to take into account that all the particles have not the same size: there is a size distribution in the solution that is characterized by the size distribution law and a polydispersity.

$$p(R,R_0,\sigma) = \frac{1}{\sqrt{2\pi}R\sigma}\exp\left(\frac{-1}{2\sigma^2}\left(\ln\frac{R}{R_0}^2\right)\right) \tag{3.11}$$

The general expression of the form factor of a solution of polydiperse sphere is expressed below:

$$P(Q) = \int p(R,R_0,\sigma)P_{sphere}(QR)dR \tag{3.12}$$

The polydispersity attenuates and smooths the oscillations on the spectrum. The fit parameters for this model are the R_g the system studied (polymer shell+gold core) and the polydispersity.

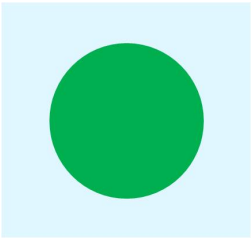

Figure 3.4: Representation of the hard sphere model.

3.3 Results

In this part we present the theoretical fits to the experimental scattering curves using the three models described above. Pasinet program (developed by Didier Lairez, LLB) is used to fit the scattering spectra. The number of parameters varies depending on the model and can be reduced by fixing some of them. In fact, some can be calculated ($\Delta\rho^2$) and other can be measured (the gold core radius by TEM, gold core volume fraction by TGA). For example, we can fix the gold core radius, while leaving the polydispersity parameter to float (as it is considered as a variable parameter). The limiting values of the adjustable parameters are kept in the range of physically realistic values. The best fit model is determined by minimization of χ^2.

3.3.1 Polymer molecular mass effect

3.3.1.1 Au-PNIPAM

Figure 3.5 represents the experimental scattering curves of gold nanoparticles with the same gold core diameter but coated with varying molecular mass of PNIPAM polymers: $PNIPAM_{154}$ and $PNIPAM_{265}$. Apart from the increase in scattering intensity at low q for particles coated with the longer PNIPAM chain, both scattering curves have about the same shape. At low q, the curve presents a plateau, commonly know as the Guinier part that is significative of objects with finite size. At high q, the scattering curve approaches a q^{-2} behavior (see Figure 3.5, inset), indicating a smooth interface between the protecting polymer shell and the surrounding solvent (as opposed to a q^{-4} for an abrupt interface). In other words, the polymer shell is well hydrated.

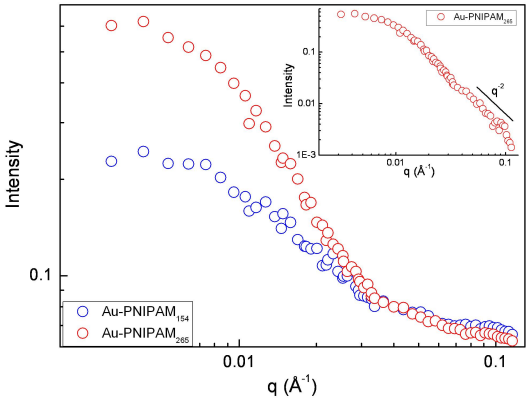

Figure 3.5: Representations of the scattering curves of $Au\text{-}PNIPAM_{154}$ (blue) and $Au\text{-}PNIPAM_{265}$ (red) particles dispersed in D_2O at 20°C. The inset shows the q^{-2} slope for the scattering curve of $Au\text{-}PNIPAM_{265}$ with background substracted.

We start by describing the adjustments made using the core-shell and the hairy-sphere models which give information about the polymer shell thickness and the R_g of polymer chains, respectively. Both models also provide information about the gold core size. The best adjustments resulting from those models are shown in Figure 3.6a and Figure 3.6b. The core-shell model yields a correct fit at low q with acceptable data for the polymer shell structural parameters. However, the quality of adjustment at high q could be further improved. As expected, the shell thickness increases with increasing polymer graft chain length. The hairy-sphere model gives a visibly better fit particularly for $Au\text{- }PNIPAM_{265}$ scattering curve. As expected, higher shell thickness and higher R_g of chain are obtained with increasing polymer molecular mass. For the case of $Au\text{-}PNIPAM_{154}$, the shell thickness and the R_g of chain are almost equal which is reasonable. As for $Au\text{-}PNIPAM_{265}$, the R_g of chain is superior to the shell thickness showing the divergence of the two models. However, for both types of fits we do not manage to correctly fit the existing oscillation at high q.

We attempted to simplify the adjustments by fixing the core radius (with TEM value, for example) and/or the thickness of shell or the R_g of chains. The scattering length densities of surrounding solvent, gold core and polymer shell were set to 6.37, 4.5 and 4 respectively. Unfortunately, this approach resulted in poorer quality fits. On the other hand, floating all parameters give the best adustments but with physically unrealistic structural data. In all cases, the shell polydispersities are always low, as expected for protecting shell build up with quite monodisperse polymer. The resulting core radii are either less than 1 nm or negative. The systematic negligeable core radii obtained are unrealistic. In our model, we estimate that the particles are grafted with about 44% polymer, corresponding to shell scattering length density of 4. This value is close to the gold core scattering length density of 4.5. It is possible therefore that the shell average scattering length density and the gold core are matched so that both are seen as being part of only one entity.

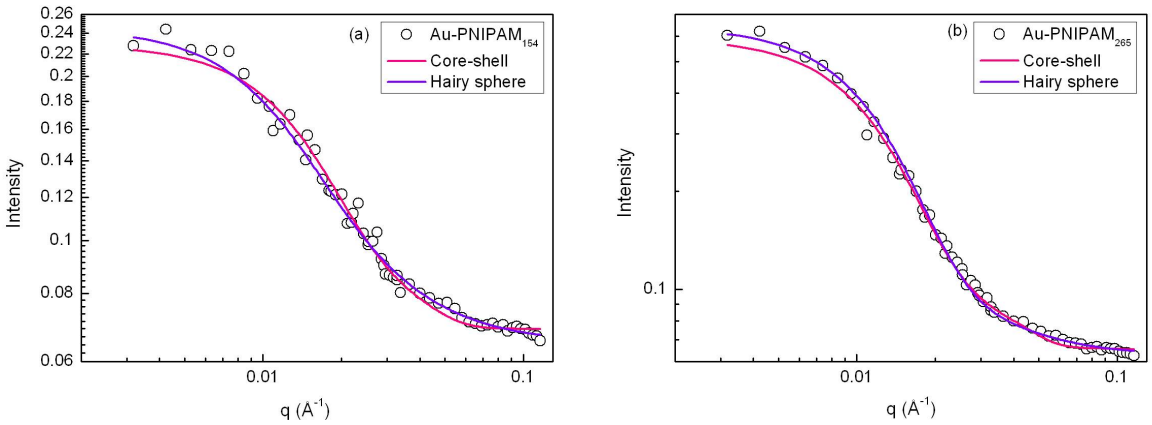

Figure 3.6: The core-shell and hairy sphere adjustments made on the: (a) Au-PNIPAM$_{154}$ (e= 5 nm and R_g= 4.8 nm) and (b) Au-PNIPAM$_{265}$ (e= 10 nm and R_g= 7 nm) scattering curves at 20°C.

We then decided to use the hard sphere model to adjust the experimental curves. The fits made using the hard sphere model are shown on Figure 3.7a for the Au- PNIPAM$_{154}$ particles and on Figure 3.7b for the Au- PNIPAM$_{165}$ particles. This model fits well the low-q region and there is a significant improvement in pinning the oscillation at high q. This is a hint that we are dealing with dense or compact gold-polymer particles with relatively low polydispersity. Furthermore, the oscillation is at 0.0520Åfor Au-PNIPAM$_{154}$ particles and at 0.047Åfor Au- PNIPAM$_{265}$ corresponding to system with a diameter of 12 and 13.3 nm (D=2π/q), respectively. We found that the resulting radii (D/2) are equal to the R_g given by the adjustment. We can thus assume that this oscillation corresponds to the signal of the compact gold-polymer particle. The hard sphere model gives us information about the radius of the whole particle (gold core + polymer shell). This enables us to evaluate the thickness of shell (e) by substracting the core radius (characterized by TEM) from the particle radius given by the fit. We notice that the polymer shell thickness e is either equal or slighlty

superior to the theoretical polymer radius of gyration R_g. The R_g of polymer chain in bulk is obtained from the following equation: $R_g = 0.12M_w^{0.59}$ [75]. For example, Au-PNIPAM$_{154}$ particles are protected by a polymer shell of 6 - 2.2= 3.8 nm and the Au-PNIPAM$_{265}$ are protected by a polymer shell of 6.6 - 2.2= 4.4 nm. The estimated R_g of PNIPAM$_{154}$ and PNIPAM$_{265}$ are 3.8 and 5.2 nm, respectively. Thus, within experimental uncertainty, we may consider acceptable the fit values, and say that the shell thickess is of order of radius of gyration of the polymer chain R_g (see Table 3.2).

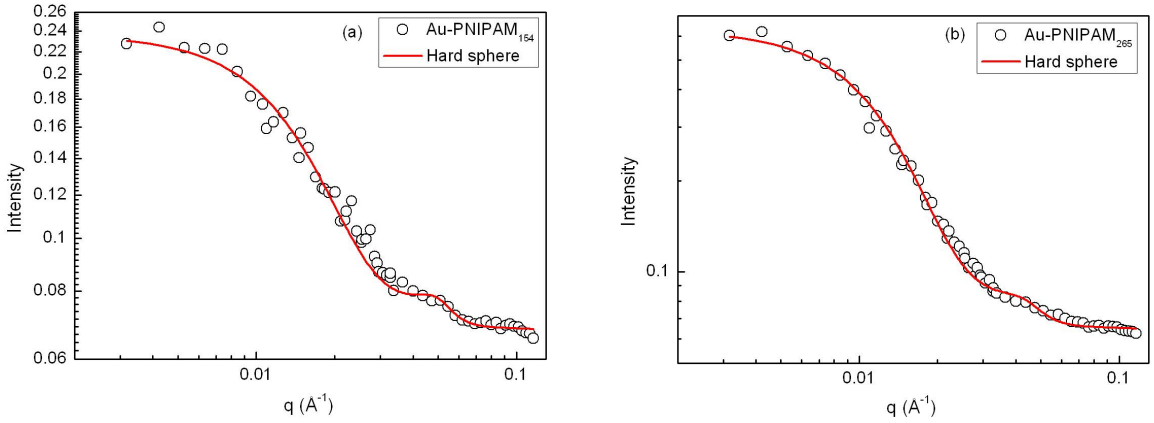

Figure 3.7: The hard sphere adjustment for: (a)Au-PNIPAM$_{154}$ (R_g = 6.0 nm) and (b) Au-PNIPAM$_{265}$ (R_g = 6.6 nm) scattering curves at 20°C.

3.3.1.2 Gold particles coated with PNIPAM-co-NPAM copolymer

In this part we study the Au-PNIPAM$_{270}$-co-NPAM$_{113}$ and Au-PNIPAM$_{261}$-co-NPAM$_{144}$ particles which are stabilized by a copolymer of 1:0.42 and 1:0.55 NIPAM:NPAM molar ratio and with molecular mass of 43066 and 46066 g/mol, respectively. Figure 3.8 shows the scattering curves of Au-PNIPAM$_{261}$-co-NPAM$_{144}$ particles in absence and presence of 150 mM NaCl at 20°C. There is visibly no difference in form and intensity betweeen the two curves which suggests no detectable change in the copolymer shell conformation and concentration with addition of salt. Like the scattering curves of the particles grafted with PNIPAM polymers, the Au-PNIPAM-co-NPAM curves presents a q^{-2} slope at high q (Figure 3.8, inset).

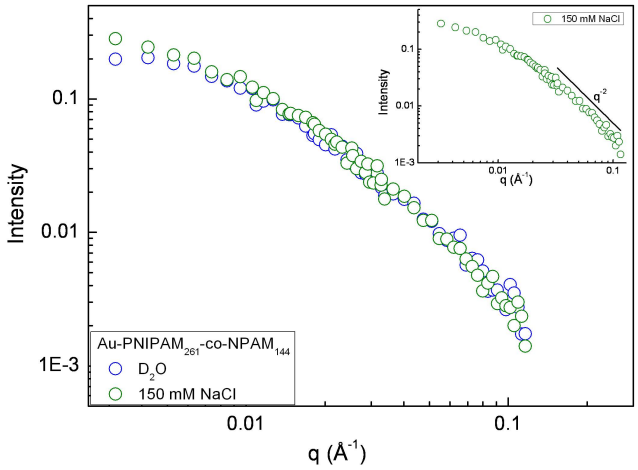

Figure 3.8: Representations of the Au-PNIPAM$_{261}$-co-NPAM$_{144}$ scattering curve in D_2O (blue) and 50 mM NaCl (green) at 20°C. the inset shows the q^{-2} slope for the scattering Au-PNIPAM$_{261}$-co-NPAM$_{144}$ curve with background substracted.

In Figure 3.9a and Figure 3.9b, we observe that, unlike the Au-PNIPAM particles, the hard sphere model is clearly not appropriate for fitting the scattering curves of the particles grafted with PNIPAM-co-NPAM copolymer.

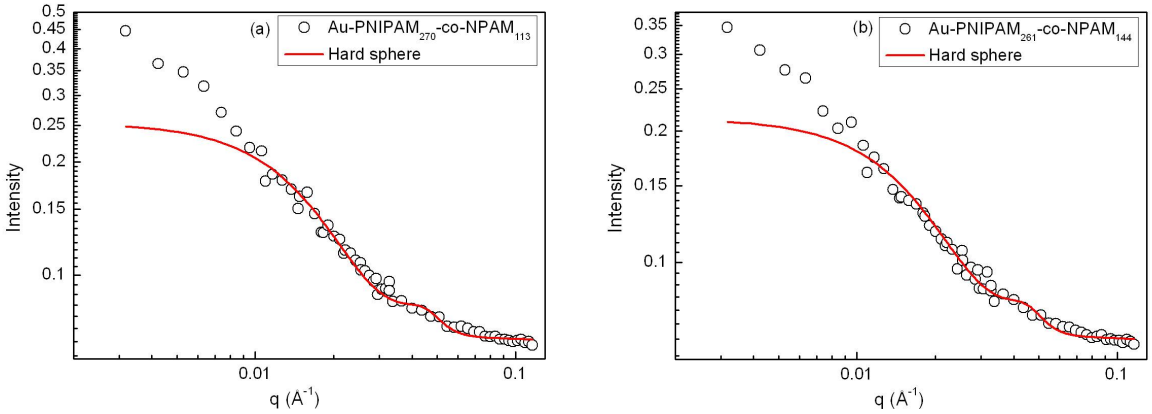

Figure 3.9: The hard sphere adjustment for: Au-PNIPAM$_{270}$-co-NPAM$_{113}$ scattering curve in D_2O and (b) Au-PNIPAM$_{261}$-co-NPAM$_{144}$ scattering curve in 50 mM NaCl at 20°C.

The core-shell model also yields a poor quality fit especially at low q. The hairy sphere model, in the other hand, gives a visibly better adjustment at both low and high q (Figure

3.10a and Figure 3.10b). But curiously, the fitted gold core diameter ≈ 0. We invoke here the same possible explanation that the core is almost matched to the average scattering length density of the polymer layer. These experimental curves are thus best fitted with the hairy-sphere model. Table 3.2 gives the values of the results for Au-PNIPAM and Au-PNIPAM-co-NPAM samples.

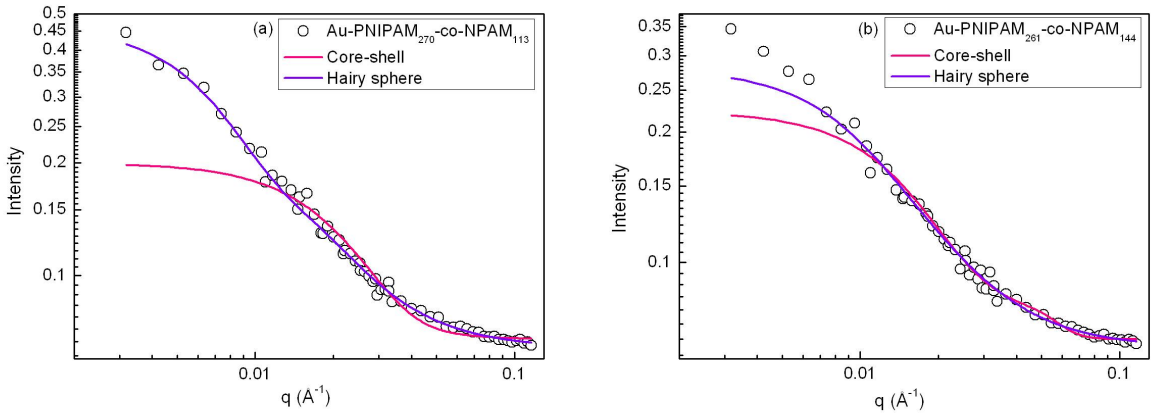

Figure 3.10: The core-shell and hairy sphere adjustments made on the: (a)Au-PNIPAM$_{270}$-co-NPAM$_{113}$ scattering curve in absence of salt (R_g = 6.8 nm) and (b) Au-PNIPAM$_{261}$-co-NPAM$_{144}$ scattering curve in presence of salt (R_g = 7.5 nm) at 20°C.

Sample	Model	d-TEM (nm)	R_g= core + shell - SANS (nm)	e = R_g - $D/2$(nm) (nm)
PNIPAM$_{67}$	hard sphere	6.6	6.5	3.2
PNIPAM$_{154}$	hard sphere	4.5	6.0	3.8
PNIPAM$_{265}$	hard sphere	4.5	6.6	4.4
PNIPAM$_{270}$-co-$_{113}$	hairy sphere	5.3	6.8	4.2
PNIPAM$_{261}$-co-$_{144}$	hairy sphere	2.9	7.5	6.1

Table 3.2: Structural properties of the polymer-protected gold nanoparticles in bulk.

3.4 Temperature effect

In this section, we seek information on the structural changes induced by temperature. We have chosen to concentrate on the copolymer sample Cpa-PNIPAM-co-NPAM due to the high chain length that facilitates observation of thermally-induced chain collapse in the polymer layer (or so we hoped). Figure 3.11 represents the scattering curves of PNIPAM-co-NPAM coated particles in absence of salt at varying temperatures. In Figure 3.11 (inset), the q^{-4} slop reveals that at elevated temperature there is now a clear interface between the surrounding solvent and the protecting shell. In other words, the protecting shell has become dehydrated. Unlike the curves at 20°C, the hard sphere model gives an excellent fit for the experimental curves at both low and high q (Figure 3.12). Unfortunately, at the moment of writing this thesis, we have not succeeded in obtaining conclusive data to demonstrate collapse of the polymer layer on an individual particle at intermediate temperatures. Instead of decreasing in size, we find, on the other hand a significant rise in scattering intensity at low q when the temperature is raised beyond the T_c. This rise is characteristic of aggregate structure, in this case formed by attraction of the collapsed (dehydrated) polymer layer. The difficulty in observing polymer collpase without interference of aggregation (even under the current dilute concentration) is partly due to the high data acquisition time (2 hours per run). These long times run facilitate interparticle encounter. New trials with an alternative approach are underway to overcome these technical challenges. Our future plans also include studying the gold-core structure at the Synchotron source, which should require infinitement shorter data acquisition times.

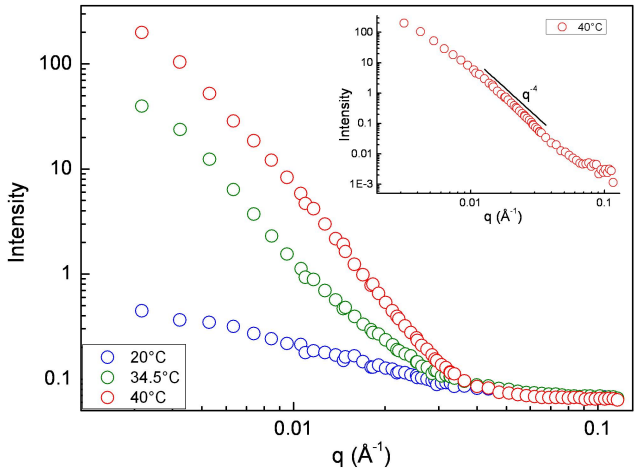

Figure 3.11: Representation of the Au-PNIPAM$_{261}$-co-NPAM$_{113}$ scattering curve in D_2O at varying temperatures. The inset shows the q^{-4} slope for the scattering curve at 40°C with background substracted.

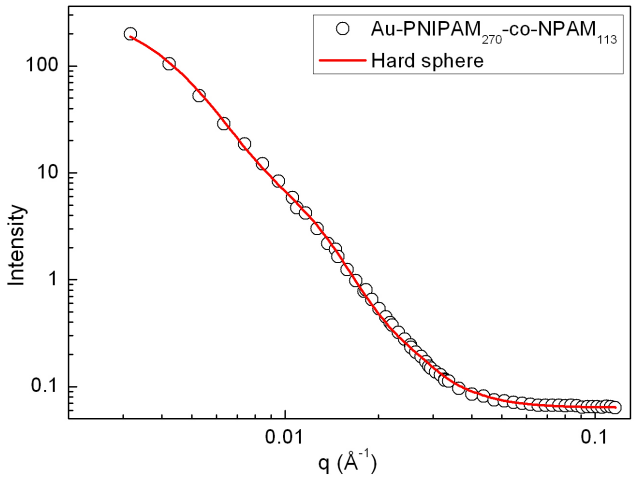

Figure 3.12: Hard sphere adjustment for Au-PNIPAM$_{270}$-co-NPAM$_{113}$ scattering curve in D_2O at 40°C (R_g = 21.5 nm).

Figure 3.13 represents the scattering curves of PNIPAM-co-NPAM coated particle in presence of salt at varying temparatures. The same appearence is observed with heating. In this case, the Guinier plateau is visible (in the same q-range) indicating smaller aggregate at lower temperature. It may also be deduced that the shell goes from partially collapsed to completely collapsed due to the NaCl screeening of the negative charges at the polymer end chains, and consequently producing more compact and well-defined larger aggregates. The size variation of the nanoparticles with temperature in absence and presence of NaCl is shown in Figure 3.15. The corresponding values are given in Table 3.3.

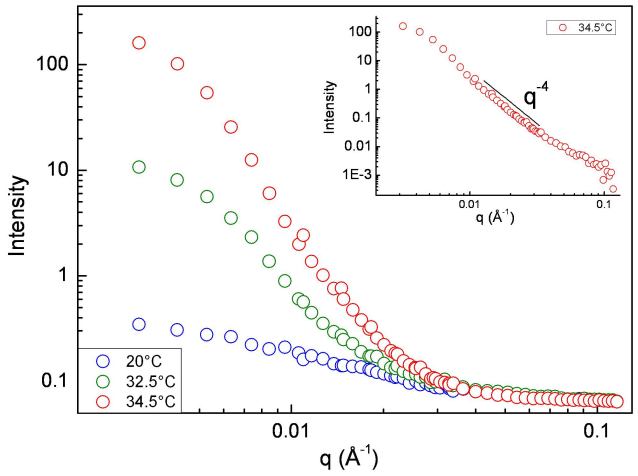

Figure 3.13: Representations of the Au-PNIPAM$_{270}$-co-NPAM$_{144}$ scattering curve in 50 mM NaCl at varying temperatures. The inset shows and the q^{-4} slope for the scattering curve at 34.5°C with background substracted.

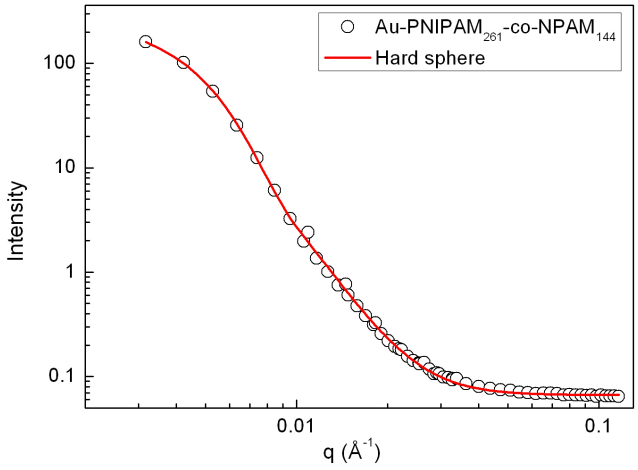

Figure 3.14: Hard sphere adjustment for Au-PNIPAM$_{261}$-co-NPAM$_{144}$ scaterring curve in 50 mM NaCl at 34.5°C (R_g = 35.5 nm)

NaCl (mM)	T (°C)	R_g (nm)
0	20	7.5
0	34.5	12.3
0	40	21.5
50	20	7.5
50	32.5	9.0
50	34.5	35.5

Table 3.3: Nanoparticles sizes evaluated from the hard sphere model for Au-PNIPAM-co-NPAM.

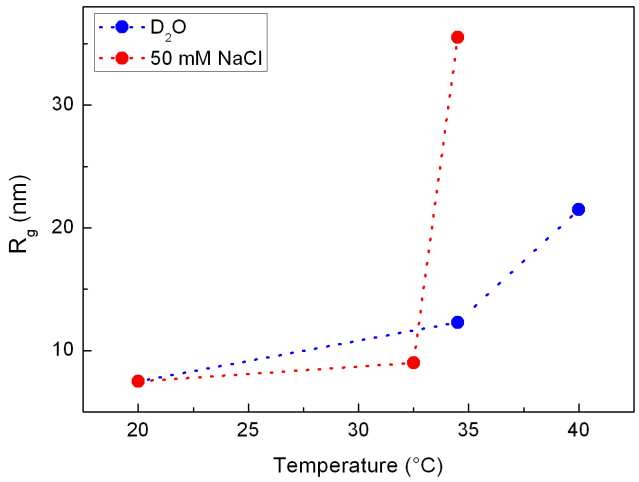

Figure 3.15: Plot of nanoparticle size versus temperature in pure D_2O (blue) and in 50 mM NaCl (red) for Au-PNIPAM-co-NPAM.

3.4.1 Summary

From the structural characterization of the polymer shell by SANS, we learn that under good solvent condition the gold particles are surrounded by a solvated polymer shell. To fit the experimental scattering curves we used the core-shell, hairy sphere and hard sphere models. We observe that stabilizing shell thickness increases with increasing polymer graft molecular mass and is of the order of the radius of gyration of the polymer chain. With increasing temperature, aggregates with well-defined sizes are formed, with apparently dehydrated polymer shell. Unfortunately at this time, we do not have conclusive data on polymer collapse on individual particles. Nevertheless, we will see in the next section that the structural properties thus obtained in this chapter furnish useful complementary information to understanding the optical properties of the polymer-coated gold nanoparticles.

Chapter 4

Thermoresponsive gold nanoparticles optical properties in solution

In this chapter, we present the optical response of polymer-coated gold nanoparticles in very dilute colloidal dispersions. The optical properties of metallic nanoparticles depend on their size and shape and their local dielectric environment that includes the surrounding solvent and the protective ligand. Past studies on ligand-protected metal nanoparticles have centered on small molecules like citrates and surfactants, where the protective layer serves mostly as a stabilizer. In this work, we study the optical properties of gold nanoparticles grafted with a thermosensitive polymer layer. The objective is to understand the structure-optical property relationship and to modulate local dielectric properties through thermally-induced structural changes in the polymer shell. The graft polymer layer thus serves a dual function as a chemical and colloidal stabilizer, as well as a local stimulus for the optical response of the nanoparticle. The gold nanoparticles are grafted with PNIPAM-based polymers of varying chainlengths and of different hydrophobicities. Here, in conjunction with a control of the physico-chemical properties of the solution, thermally-induced structural changes (and therefore dielectric constant) of the polymer shell can thus be effected over a wide range of temperatures. In this study, we concentrate on two principal aspects: (i) the effect of molecular chainlength on the optical sensitivity of the gold nanoparticle to the surrounding dielectric constant, and (ii) the SPR response to temperature-induced conformational changes in the polymer shell. The advantage of our new more hydrophobic PNIPAM-co-NPAM-stabilized particles is that we will be able to observe the temperature influence at lower temperature range.

The optical measurements were carried out on a Varian Cary100 spectrometer at LLB (Laboratoire Léon Brillouin, CEA-Saclay, France). UV-vis spectra of gold nanoparticles dispersions were recored at λ = 200-800 nm and the temperature was varied from 20 to 45°C with a heating rate of 0.5°C/min.

4.1 Uncoated particles

The optical extinction (absorption + scattering) of a homogeneous spherical metal nanoparticle embedded in a homogeneous medium has been widely modeled using the Mie theory [76] in terms of the particle complex dielectric function $\epsilon = \epsilon_1 + i\epsilon_2$ and the matrix dielectric constant ϵ_m. For particle size D much smaller than the optical wavelength λ (kD « 1, k = $2\pi/\lambda$), the extinction cross section is dominated by the lowest order dipole term and the Mie theory is reduced to:

$$\sigma(\omega) = 9\epsilon_m^{3/2} V \left(\frac{\omega}{c}\right) \frac{\epsilon_2(\omega)}{\left[\epsilon_1(\omega) + 2\epsilon_m\right]^2 + \epsilon_2^2(\omega)} \tag{4.1}$$

$\sigma_a(\omega)$ is the absorption cross section, V is the particle volume, $\omega = 2\pi c/\lambda$ the optical frequency, c the speed of light, $\epsilon_1(\omega)$ and $\epsilon_2(\omega)$ the real and imaginary parts of the frequency-dependent dielectric constant of the absorbing metal particle. The scattering cross section $\sigma_s(\omega)$ follows a $1/\lambda^4$ relationship but for nanoparticles up to about 20 nm in the frequency range of interest, $\sigma_a(\omega) \gg \sigma_s(\omega)$ and the extinction cross section $\sigma_e(\omega) \approx \sigma_a(\omega)$. From the above expression, it follows that resonance enhancement occurs when the denominator tends to zero. For small value of ϵ_2, this leads to the approximate surface plasmon resonance (SPR) condition:

$$\epsilon_1(\omega) + 2\epsilon_m = 0 \tag{4.2}$$

The resulting absorption peak at $\epsilon_1(\omega_{peak}) = -2\epsilon_m$ in the visible frequency range is the origin of intense colors displayed by gold sols. The Mie theory thus predicts the plasmon peak position to be determined mostly by $\epsilon_1(\omega)$ while the peak height and shape to be governed by $\epsilon_2(\omega)$. The negative index means that the plasmon oscillates out of phase with electric field.

4.1.1 Particle size effect

4.1.1.1 Extrinsic size effect

For gold nanoparticles in the size range D ≈ 2-25 nm [77] the dipolar approximation of the Mie theory predicts the plasmon peak position to be insensitive to particle size, the latter contributing only to the absorption intensity in the term V. In this size range, the plasmon band tends to the Frohlich frequency (≈ 520 nm) [78]. The lower size limit of 2 nm is attributed to a transition in electronic structure of the metal below this size and the optical properties can no longer be described by bulk dielectric functions. Beyond the upper limit, the condition kD « 1 is not fulfilled and the electric field around the particle cannot be taken as constant. For these larger particles, the plasmon peak shifts to lower energy (red-shift) and higher multipole terms in the Mie theory as well as scattering become important in describing the extinction spectra. In our study, the nanoparticle samples fall in the size range ≈ 3 to 8 nm and the plasmon band is therefore insensitive to this extrinsic size effect. However, although the peak position remains invariant, the shape and width of the absorption spectrum depend directly on the particle size - an intrinsic size effect.

4.1.1.2 Intrinsic size effect

This effect is due to confinement of the free electrons in low dimension. When the particle radius is smaller than the mean free path of the conduction electron, R < R_{mfp} (50 nm for Au nanoparticles) [77], 13 nm polycrystalline gold film [79], 37 nm single crystal [80] the conduction electrons are additionally scattered by the particle surface. In order to take into account this size effect, the bulk metal dielectric function needs to be modified in order to model optical features of small particles. This is carried out by decomposing the metal dielectric function into two terms: an interband contribution (IB) accounting for the 5d-electrons response and a free-electron contribution (Drude, D), where $\epsilon_1(\omega) = \epsilon_{1IB}(\omega) + \epsilon_{1D}(\omega)$ and $\epsilon_2(\omega) = \epsilon_{2IB}(\omega) + \epsilon_{2D}(\omega)$. The free electron behavior is well described by the Drude model [81] that expresses the real and imaginary parts as:

$$\epsilon_{1D}(\omega) = 1 - \frac{\omega_p^2}{\omega^2 + \omega_0^2} \tag{4.3}$$

and

$$\epsilon_{2D}(\omega) = \frac{\omega_p^2 \omega_0}{\omega(\omega^2 + \omega_0^2)} \tag{4.4}$$

ω_p is the bulk plasma frequency that is related to the metal properties by:

$$\omega_p^2 = \frac{Ne^2}{\epsilon_0 m} \tag{4.5}$$

N and e are the electron density and charge, m the effective mass and ϵ_0 the vacuum permittivity. ω_0 is the bulk scattering rate due to inelastic scattering within the metal and is related to the mean free path of the conduction electrons R_{mfp} and the Fermi velocity υ_F: $\omega_0 = \upsilon_F / R_{mfp}$. It is thus a constant that characterizes the bulk relaxation or damping frequency. Figure 4.2 shows the decomposition of the bulk gold dielectric constants taken from Johnson and Christie [79]. In this exercise, we have used $\omega_0 = 0.071$ eV (from the same authors), and $\omega_p = 9.27$ eV (Figure 4.1). The value of ω_p is deduced as follows. The complex dielectric constant is: $\epsilon = \epsilon_1 + i\epsilon_2$, where $\epsilon_1 = n^2 - k^2$ and $\epsilon_2 = 2nk$. For all our calculations in this study, we use the optical constants n and k given by Johnson and Christie [79]. The bulk plasmon wavelength, λ_p can be obtained from the Drude component of the real part:

$$\epsilon_1 = 1 - \frac{\lambda^2}{\lambda_p^2} \tag{4.6}$$

By plotting ϵ_1 versus λ^2 (Figure 4.1), the intercept yields the high-frequency offset ϵ^∞ and the slope = - $1/\lambda_p^2$. From such a plot in the region of interest from λ = 471 - 756 nm, we obtain intercept = ϵ^∞ = 10.98 and slope = -5.59 × 10^{-5} giving λ_p = 133.8 nm (ω_p = 9.27 eV).

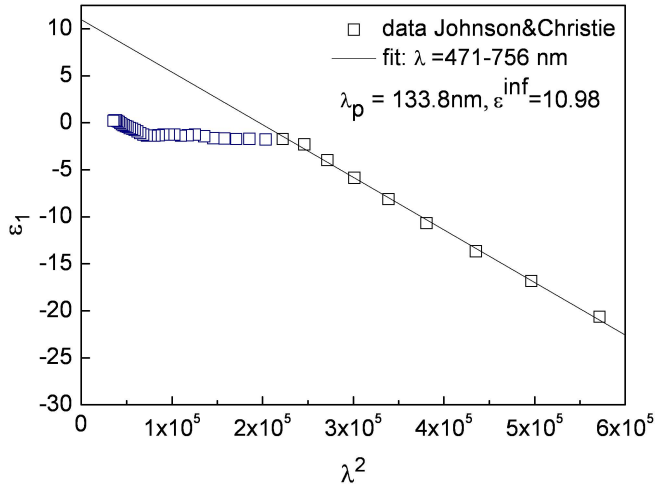

Figure 4.1: Plot of ϵ_1 versus λ^2.

It can be seen that $\epsilon_1(\omega)$ is dominated by the free electron component, with an offset by an almost-constant interband contribution (Figure 4.2a). The $\epsilon_2(\omega)$ function, on the other hand is dominated by free electron only below ≈ 1.7 eV (Figure 4.2b). Therefore, the SPR peak position is mostly determined by $\epsilon_1(\omega)$. In considering size effect, an excess surface scattering term is introduced:

$$\omega_s = 2g\upsilon_F/D \tag{4.7}$$

D is the particle diameter, $\upsilon_F = 1.4 \times 10^8$ cm/s for gold [82], and g and is a proportionality factor of the order of 1 although a wide range of values has been reported [81], [83], [84]. The total scattering rate, $\omega_t = \omega_0 + \omega_s$ is then the damping factor that controls the width of the plasmon peak. To introduce this size effect in the metal dielectric constant, the interband contribution ($\epsilon_{IB}(\omega)$) is considered to be the same as the bulk value and only the free electron part is corrected for the excess scattering. The term ω_0 is very small (< 0.1 eV, Johnson and Christy) and for nanoparticles in the current size range of interest $\omega_s \gg \omega_0$.

To illustrate the above discussion, Figure 4.3 shows calculated spectra for uncoated gold nanoparticles ranging from 3 to 8 nm in water. It can be seen that the SPR peak position remains fixed at around 520 nm with only a variation in the peak width with size. The strong broadening and damping of the SPR is caused by the surface scattering ω_s of the conduction electrons. As mentioned above, ω_s depends on 1/R so the effect of surface scattering is less important as the particle size increases and the absorption peak becomes sharper (Figure 4.3).

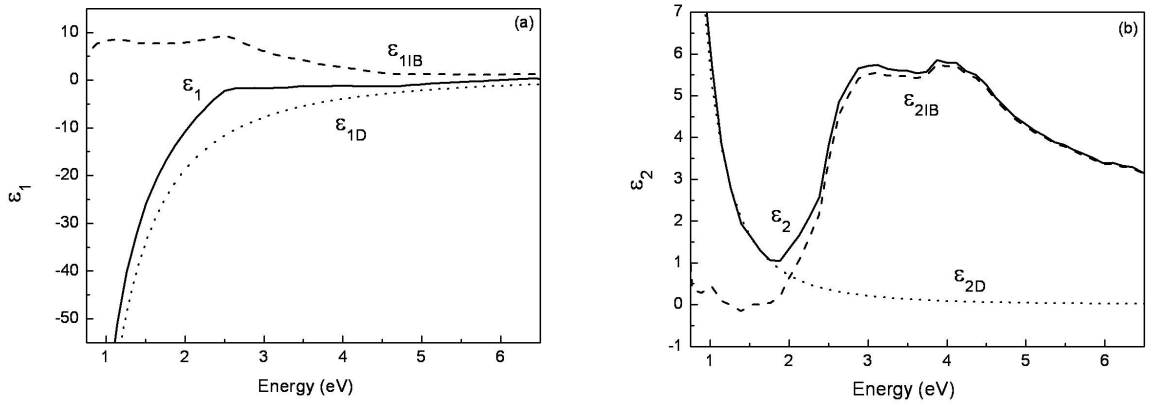

Figure 4.2: Decomposition of: (a) ϵ_1 and (b) ϵ_2 of gold dielectric functions using optical data of Johnson and Christy [79].

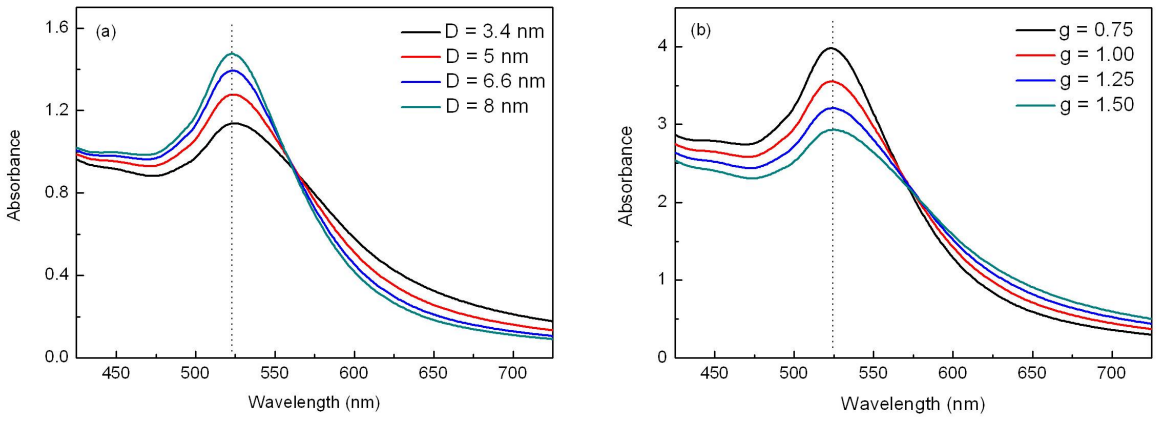

Figure 4.3: Calculated curves of uncoated gold nanoparticles in water: (a) effect of particle size ($g = 1$), the curves are normalized at 350 nm; (b) effect of g ($D = 5$ nm).

4.2 Polymer-protected gold nanoparticles

Attachment of a ligand (surfactant, polymer) to a metal particle engenders an alteration of the electronic state of the metal core that may cause either a blue-shift or a red-shift (shift to higher or lower energy, respectively) depending on how the electronic density is modified. The resulting shell further modifies the local dielectric environment. Gold nanoparticles always require stabilization of some sort to prevent colloidal instability, therefore its plasmon band rarely falls exactly where the Mie theory predicts for bare particles. Furthermore, for the PNIPAM-coated nanoparticles used in our study, the PNIPAM ligands form strong covalent bonds through π-bonding between the sulfur atom and the gold surface atoms, leading to more dampened plasmon bands. The Mie theory also predicts that the protective coating modifies the dielectric environment leading to reduced sensitivity of the plasmon mode to the embedding matrix.

4.2.1 Experimental results

4.2.1.1 Effect of polymer molecular mass

UV-vis absorption measurements of coated gold nanoparticles were carried out under very dilute concentrations (0.3 - 0.5 mg/mL). First, we present the effect of M_w on nanoparticles in a given solvent. Figure 4.4a shows the absorption spectra of Au-PNIPAM nanoparticles with varying PNIPAM chain lengths in water (n = 1.333) at T = 20°C. These results show that compared to the calculated curve for bare particle, the absorption band for polymer-coated nanoparticles are shifted to higher values, with the degree of shift increasing with M_w. The plot of SPR peak position in Figure 4.4b shows that a red-shift of about 16 nm is obtained for the highest molecular chain length. Two effects of the polymeric ligand on the nanoparticle local environment can be mentioned: an alteration of the gold core electronic property resulting from the chemical binding, and an increasing change in local dielectric environment with thickness of the polymer shell.

4.2.1.2 Effect of solvent

Figure 4.5 compares the optical response for naked (calculated) and coated gold nanoparticles in different solvents (water, chloroform, THF, pyridine) with refractive indices varying from 1.333 to 1.51. The solubility of PNIPAM in these solvents was checked by dissolving the pure polymer in the solvents; immediate dissolution of the polymer was observed in all cases. We therefore consider the PNIPAM-coated nanoparticles to be dispersed in comparable good-solvent conditions. As predicted by the Mie theory, a red-shift of the SPR peak for uncoated particle is clearly seen with increasing solvent refractive index [85]. For the Au-$PNIPAM_{154}$ on the other hand, this shift in energy becomes less marked. The experimental SPR positions of gold particles coated with varying PNIPAM molecular masses dispersed in different solvent refractive indexes are given in Table 4.1

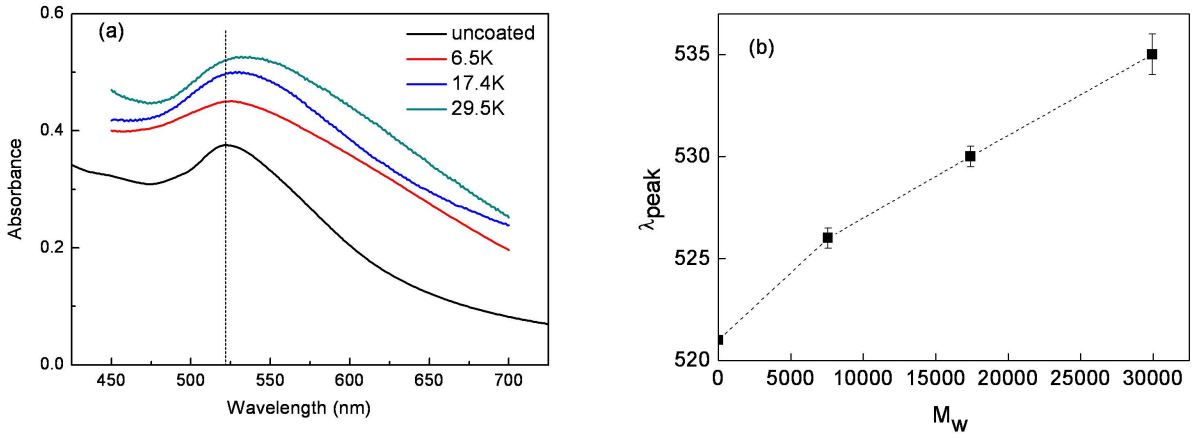

Figure 4.4: Absorption spectra of Au-PNIPAM nanoparticles coated with different molecular chain lengths in water at T = 20°C (a). Absorption peak position (in nm) versus graft polymer chain length (b); a red-shift of about 12 nm compared to (calculated) uncoated particle is obtained for the 29.5K sample.

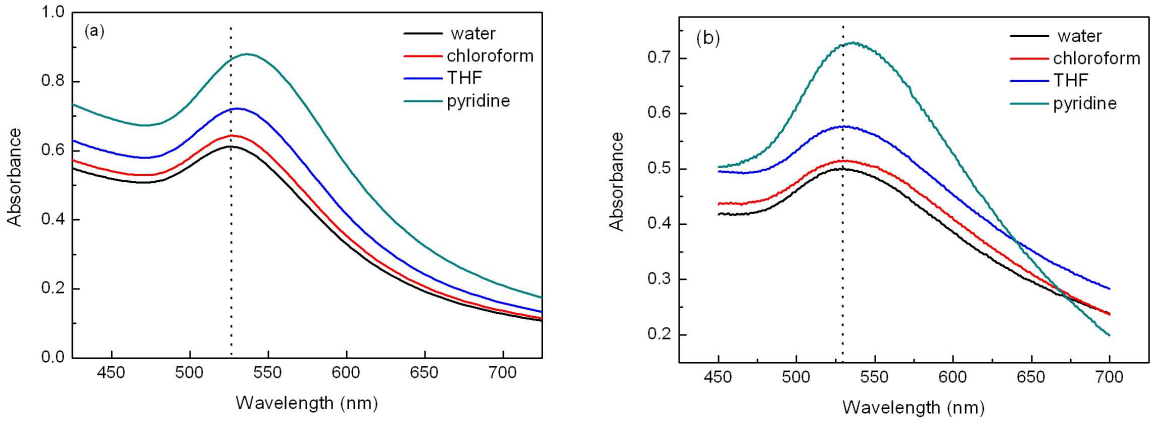

Figure 4.5: Calculated absorption spectra of uncoated nanoparticles (a) and experimental absorption spectra of nanoparticles coated with $PNIPAM_{154}$ in water (n = 1.333), chloroform (n = 1.353), THF (n = 1.408) and pyridine (n = 1.51) (b).

Solvent-n	$\lambda_{\text{Au-PNIPAM}_{67}}$ (nm) (nm)	$\lambda_{\text{Au-PNIPAM}_{154}}$ (nm)	$\lambda_{\text{Au-PNIPAM}_{265}}$ (nm)
Water-1.333	526	530	535
Chloroform-1.353	528	532	536.4
THF-1.408	531	532	536
Pyridine-1.510	537	536.8	536

Table 4.1: Experimental SPR peak positions of PNIPAM-coated particles in different solvents.

The effects of a polymer coat on the gold nanoparticle plasmon behavior may be understood by the following. As mentioned before, attaching a ligand to the particle also modifies the gold core electronic property. However, in this work, since all the nanoparticles were synthesized using the same chemical bonding (polymer-SH-Au) we therefore consider this ligand-surface effect to be approximately the same for all samples. We thus concentrate on the dominant effect of the shell dielectric and structural properties on the reduced sensitivity to the changes in solvent refractive index. For a nanoparticle enrobed in a shell, the surrounding solvent dielectric constant (ϵ_{m}) is replaced by an effective value that includes the shell dielectric constant, ϵ_{s} The resonance condition in the denominator of the absorption cross section for the composite particle becomes [86], [87] is then:

$$\epsilon_1 = -2\epsilon_s \frac{[\epsilon_s p + \epsilon_m(3-p)]}{\epsilon_s(3-2p) + 2\epsilon_m p} \tag{4.8}$$

where p is the shell volume fraction:

$$p = \frac{(D/2+e)^3 - (D/2)^3}{(D/2+e^3)} \tag{4.9}$$

e is the shell thickness.

For thin shell (p « 1), the above expression is reduced to:

$$\epsilon_1 = -2\epsilon_m - \frac{2p(\epsilon_s - \epsilon_m)}{3} \tag{4.10}$$

(for $p = 0$, ϵ_1 = -2ϵ_{m} which is the resonance condition for uncoated particle). For small core volume fraction or relatively thick shell (1 - p «1), it can be written as:

$$\epsilon_1 = -2\epsilon_s \left[1 + \frac{(1-p)(\epsilon_m - \epsilon_s)}{(\epsilon_s + 2\epsilon_m)}\right] \tag{4.11}$$

In an approximative approach proposed by Templeton et al [88] for simple metals, ϵ_1 is considered to follow the Drude behavior with a high-frequency contribution ϵ^∞ giving:

$$\epsilon_1 = \epsilon^\infty - \frac{\lambda^2}{\lambda_p^2} \tag{4.12}$$

where $\lambda_{\text{p}} = 2\pi c/\omega_{\text{p}}$. Combining the above equations, the SPR peak position λ_{peak} can be shown to depend on the solvent and shell properties as:

$$\frac{\lambda^2_{peak}}{\lambda^2_p} = \epsilon^{\infty} + 2\epsilon_m + \frac{2p(\epsilon_s - \epsilon_m)}{3} \tag{4.13}$$

for thin shell ($p \ll 1$), and as:

$$\frac{\lambda^2_{peak}}{\lambda^2_p} = \epsilon^{\infty} + 2\epsilon_s + \frac{2(1-p)\epsilon_s(\epsilon_m - \epsilon_s)}{\epsilon_s + 2\epsilon_m} \tag{4.14}$$

for thick shell (1-p «1).

These expressions show that for uncoated particle, a plot of $\lambda^2_{\mathrm{peak}}/\lambda^2_{\mathrm{p}}$ versus ϵ_{m} yields a slope of 2. In the presence of a shell layer and for $\epsilon_{\mathrm{s}}>\epsilon_{\mathrm{m}}$, the slope decreases, explaining the reduced sensitivity of the resonance peak to changes in solvent refractive index. In particular, for thick shell (1-p«1), the slope becomes very small and is dominated by the ϵ_{s} term (Equation 4.13). In this case, the surface plasmon mode "freezes" at ϵ_1 = -2ϵ_{s} and becomes insensitive to the solvent and responds only to the shell layer.

For our samples, it is important to note that the graft shell layer is not constituted of pure polymer melt; on the contrary, as already seen in the results of SANS characterization, the shell layer is highly solvated. Thus, the shell dielectric is defined as: $\epsilon_{\mathrm{s}} = \epsilon_{\mathrm{p}}\ \phi_{\mathrm{p}}$+(1-$\phi_{\mathrm{p}}$)$\epsilon_{\mathrm{m}}$ where ϵ_{p} ($\approx 1.48^2$) and ϵ_{m} are the dielectric constants of pure polymer and solvent, respectively, and ϕ_{p} is the volume fraction of polymer in the shell layer. Figure 4.6 shows a plot of $\lambda^2_{\mathrm{peak}}/\lambda^2_{\mathrm{p}}$ versus ϵ_{m} for Au-PNIPAM nanoparticles of varying core sizes (D = 2.3 nm to 8 nm) and PNIPAM chain lengths ($\mathrm{M_w}$ = 6.5K to 29.5K). First, we examine the samples with small gold cores of comparable size, $D \approx$ 2-3 nm represented in the figure by closed symbols (green squares, blue squares, red circles). For this population of samples, the slope of $\lambda^2_{\mathrm{peak}}/\lambda^2_{\mathrm{p}}$ versus ϵ_{m} is less than 2, and decreases with $\mathrm{M_w}$ of the graft polymer. This trend is as predicted by Equation 4.13 that shows a decrease in solvent sensitivity with increase in the shell volume fraction p; further, when p tends to 1, the slope becomes very slight and the plasmon behavior becomes dominated by the shell term ϵ_{s}. This last effect is clearly demonstrated in the case of Au-PNIPAM$_{265}$ (closed red circles). For this series of samples (closed symbols) therefore, the effect of $\mathrm{M_w}$ (and thus of p) is relatively clear, if we consider the concentration of polymer in the shell to be the same: constant ϕ_{p} and ϵ_{s} in each solvent for all samples.

Next, we examine the second population of particles with larger core size (D = 4.5 - 8 nm) grafted with same or comparable molecular chain length (open symbols). Interestingly, these points do not appear to follow a clear trend, and their $\lambda^2_{\mathrm{peak}}/\lambda^2_{\mathrm{p}}$ versus ϵ_{m} dependence cannot be explained by accounting only for the corresponding changes in the shell volume fraction p with the larger core sizes. Therefore, for the ensemble of our Au-PNIPAM nanoparticles of various core sizes and $\mathrm{M_w}$, it is insufficient to relate the plasmon peak-shift (decrease in sensitivity to solvent refractive index) only to the molecular chain length. The above approximative method proposed by Templeton [88] thus provides a convenient and direct description of the influence of p on SPR peak position and the subsequent sensitivity to solvent refractive index, provided ϵ_{s} is constant throughout, as in the case for solid-coated particles. This is clearly not the case for polymer-coated particles where differences in ϕ_{p} in the shell layer, due probably to different grafting density, between samples cannot be neglected. We shall show in the next section that variations in shell properties between

samples can be consolidated by considering the effective layer thickness: $e_{eff} = e.\phi_p$ where e is the hydrated thickness and e_{eff} is the equivalent polymer melt thickness.

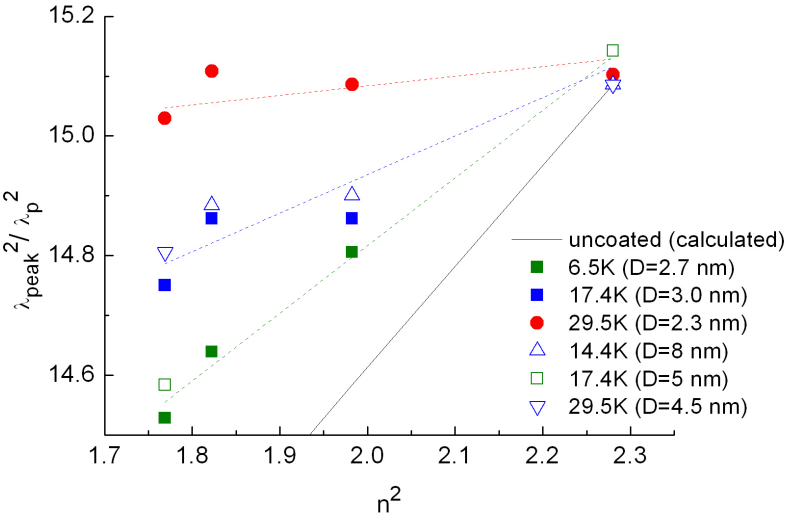

Figure 4.6: Normalized plasmon peak position versus solvent dielectric constant for of Au-PNIPAM nanoparticles. The solid line is calculated for bare particles (slope = 2).

4.2.2 Modelling extinction spectra

Our objective in modeling the absorption spectra is to gain more detailed information on the relationship between the optical and structural properties of the polymer shell, and their influence on solvent-sensitivity. Here, we attempt to model the experimental spectra by fitting λ_{peak} as well as the form of the spectra using the Mie dipolar theory. We point out that the approximation method discussed above assumes the interband term around λ_{peak} to be non-dispersive (independent of wavelength) and constant by introducing the term ϵ^{∞} which is not rigorously correct (F. Vallée, personal communication). The more correct form should be $\epsilon_{1\text{IB}}(\lambda)$ (see Figure 4.2a) that is used in the current modeling using the Mie theory. The model consists of a core-shell (Figure 4.7) configuration with a homogeneous polymer shell. In this model, similarly to what has already been discussed in the previous section, ϵ_{m} is replaced in the resonant denominator by an effective dielectric function. Adopting the methodology and terminology of Del Fatti et al [89], we have:

$$\epsilon_{\text{eff}} = \frac{\epsilon_s(1-\alpha\beta)}{(1+2\alpha\beta)} \tag{4.15}$$

where α is the gold core volume fraction:

$$\alpha = \frac{(D/2)^3}{(D/2+e)^3} \tag{4.16}$$

and

$$\beta = \frac{(\epsilon_s - \epsilon_m)}{(\epsilon_s + 2\epsilon_m)} \tag{4.17}$$

Retaining our previous designation of p = polymer volume fraction, α = 1 - p and the new resonance condition is now $\epsilon_1 + 2\epsilon_{\text{eff}}$=0. It is further shown [89] that the SPR peak dependence on shell thickness e is given by:

$$\frac{\Delta\lambda_{peak}(e)}{\Delta\lambda_{peak}^{max}} = \frac{1-\alpha}{1+2\alpha(\epsilon_s-\epsilon_m)/(\epsilon_s+\epsilon_m)} \tag{4.18}$$

where $\Delta\lambda_{\text{peak}}$(e)= λ_{peak}(e)-λ_{peak}(0). $\Delta\lambda_{peak}^{max}$ is the maximum peak shift expected when the matrix index is modified from ϵ_m to ϵ_s (corresponding to a change from a bare to a coated particle of infinitely-thick shell). For polymer, ϵ_s - $\epsilon_m > 0$ and the effect of e on $\Delta\lambda_{\text{peak}}$ depends mostly on 1 - α. It can be shown from these equations and also from the approximative method in the previous section that the influence of the bulk solvent refractive index becomes negligible when $e \approx D/2$ corresponding to shell volume fraction $p \geq 0.8$.

The modelling procedure was carried out by visual comparison of calculated and experimental curves. This visual method is adequate for our current purposes in best-fitting the spectra in the region around the resonance peak. We use a convenient program for calculating the Mie curves (SigmaMie) at the courtesy of Paolo Maioli (LASIM-University Lyon 1). The variable parameters are: D, e, ϵ_{m}, ϵ_{s} and g (proportionality factor related to surface scattering ω_s). To reduce the number of fitting parameters, D (from TEM) and e (from SANS) are held constant. For a given solvent then, ϵ_{m} is also a constant and only two fitting parameters are required: ϵ_{s} that determines the plasmon peak position, and g which

controls the plasmon band width. (D and e affect the amplitude through the volume term in Equation 4.1).

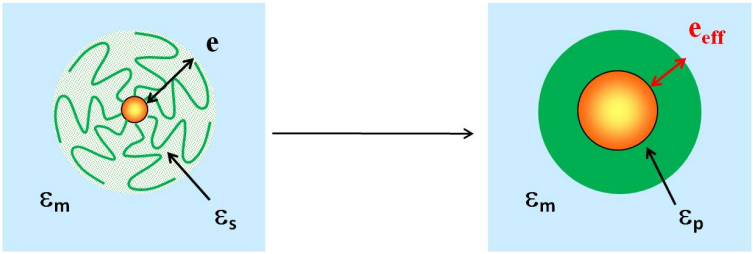

Figure 4.7: The core-shell model showing solvated polymer shell with thickness e and pure polymer shell with effective thickness e_{eff} (right).

Au-PNIPAM nanoparticles of different core sizes and grafted with varying polymer chain lengths are dispersed in different solvents: water ($\epsilon_m = 1.333^2$), chloroform ($\epsilon_m = 1.353^2$), THF ($\epsilon_m = 1.408^2$), and pyridine ($\epsilon_m = 1.510^2$). Figure 4.8 shows the experimental spectra together with the best theoretical adjustments for the smallest gold core size we work with, Au-PNIPAM$_{57}$ (D = 2.7 nm) and Au-PNIPAM$_{265}$ (s1) (D = 2.3 nm). (The corresponding polymer molecular mass are 6.5K and 29.5K).

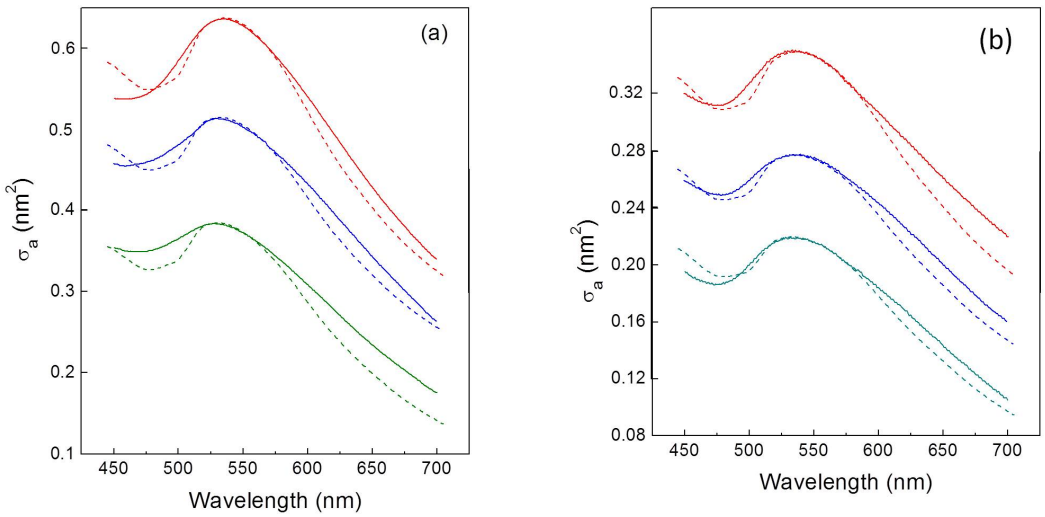

Figure 4.8: Theoretical fits of absorption spectra of Au-PNIPAM nanoparticles with small gold-core sizes in different solvents: chloroform (a) or water (b) (green lines), THF (blue lines), pyridine (red lines). (a) Au-PNIPAM$_{57}$ (D = 2.7 nm, g = 1.2 - 1.3), (b) Au-PNIPAM$_{265}$ (s1) (D = 2.3 nm, g = 1.2 - 1.4); solid line = experiment curve, dashed line = theoretical curve. The spectra are vertically-separated for better reading.

It can be seen that the general quality of fit to these curves is mediocre: only the peak position and its immediate vicinity can be fitted. The position of the peak is very sensitive to the shell refractive index, ϵ_s while the peak width is related to the surface scattering parameter, g. From the different solvents, the best-fit parameters to the peak position for Au-PNIPAM$_{57}$ are ϵ_s = 1.83 - 2.25 (value increasing from water to pyridine). Using the relation ϕ_p=(ϵ_s - ϵ_m)/(ϵ_p - ϵ_m), the corresponding polymer concentrations in the shell are evaluated to be, for $\phi_p \approx$ 0.13 - 0.19 in water, chloroform and THF; for pyridine, a much higher value of 0.33 is estimated. In the case of Au-PNIPAM$_{265}$, ϵ_s = 1.95 - 2.23, giving ϕ_p $\approx$ 0.33-0.42 in the first three solvents, and again a higher value of 0.54 in pyridine. Note that in principle for a given sample, the value of ϕ_p evaluated from all solvents should be the same. In practice, for most samples, a range of values is obtained from the results in different solvents. We consider the range of ϕ_p resulting from water, chloroform and THF to be the acceptable overall experimental uncertainty. The large deviation of the ϕ_p values deduced from pyridine with respect to the other solvents is due to the very small dielectric contrast between polymer and pyridine; from this viewpoint, due to the larger contrast between polymer and water, the ϕ_p obtained from the water fit is probably closer to the true value. We also found that a value of $\epsilon_p = 1.48^2$ for the dielectric constant of pure polymer gives the most consistent overall results, in line with literature values that report $\epsilon_p = 1.45^2$ - 1.50^2 [55]. Concerning the peak width, both the above samples are fitted with g = 1.2 - 1.4, or an average $g/D \approx 0.47$ for Au-PNIPAM$_{57}$ and an average $g/D \approx 0.56$ for Au-PNIPAM$_{265}$. Figure 4.9 compares absorption spectra for different gold core sizes, D = 3 nm (s1) and 5 nm (s2), coated with the same polymer chain length PNIPAM$_{154}$ (17.4K). For D = 3 nm, the curves are fitted with ϵ_s = 1.88 - 2.24 yielding $\phi_p \approx$ 0.18-0.25 (for the first three solvents, neglecting pyridine) and g = 1.1 - 1.4 (value increasing from pyridine to water). For D = 5 nm, the fitted values are ϵ_s = 1.92-2.25 giving corresponding polymer concentration, $\phi_p \approx$ 0.34-0.35 and g = 0.9 - 1.2 (value increasing from pyridine to water). From these Figures, it can be seen that increase in particle size from D = 3 nm (average g/D $\approx$ 0.44) to D = 5 nm (average $g/D \approx 0.21$) the quality of fit is significantly improved. For the larger particle size, the solvent-induced red-shift is also markedly higher.

In Figure 4.10, we show samples with comparable polymer concentration in the polymer shell and with relatively large core size: Au-PNIPAM$_{265}$ (s2) (D = 4.5 nm) and Au-PNIPAM$_{127}$ (D = 8 nm). The curves are fitted with ϵ_s = 2.0 - 2.22 ($\phi_p \approx$ 0.54) and ϵ_s = 2.08 - 2.22 ($\phi_p \approx$ 0.62), respectively. These two samples are thus protected with very dense polymer shell, an observation that is in agreement with the results of thermogravimetric analysis. For these spectra, $g/D \approx$ 0.31 - 0.32. From these results, we obtain a large range of ϕ_p for different samples ranging from $\approx$ 0.15 to $\approx$ 0.6. This range falls within the values reported for strongly-grafted polymer brushes [90], [91], [92], [93], [94].

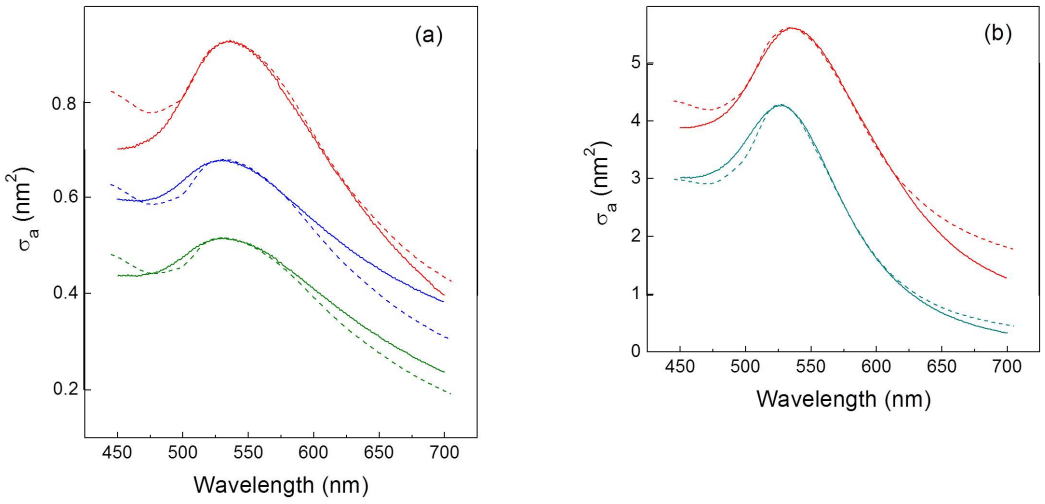

Figure 4.9: Comparison of particles with different core sizes grafted with the same polymer chain length. Best-fit curves for Au-PNIPAM$_{154}$ in different solvents: water (green lines), THF (blue lines), pyridine (red lines). (a) D = 3 nm, g = 1.2 - 1.4; (b) D = 5 nm, g = 0.9 - 1.2. Solid line = experimental curve, dotted line = calculated curve. The curves are vertically-separated for better reading.

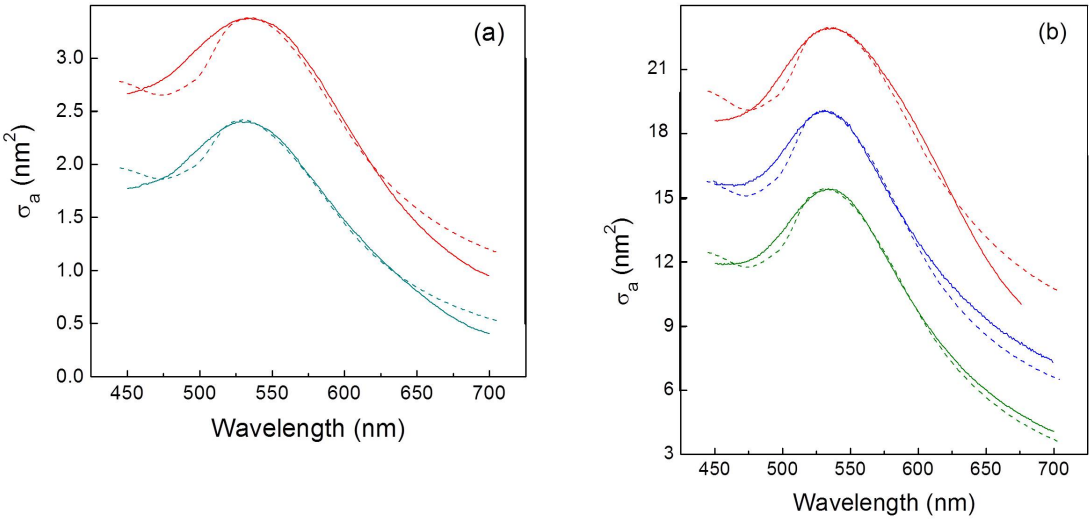

Figure 4.10: Comparison of particles with different core sizes and with comparable grafting density in different solvents: chloroform (green lines), THF (blue lines), pyridine (red lines). Best-fit curves for (a) Au-PNIPAM$_{265}$ (D = 4.5 nm, g = 1.2 - 1.4); (b) Au-PNIPAM$_{127}$(b) (D = 8 nm, g = 2.5 - 2.7). Solid line = experimental curve, dotted line = calculated curve. The curves are vertically-separated for better reading.

Sample	Solvent	λ_{peak} (nm)	ϵ_s	ϕ_p	g	g/D
Au-PNIPAM$_{57}$ (D = 2.7 nm, e = 2 nm)	Water	526	1.83	0.13	1.3	0.48
	Chloroform	528	1.9	0.19	1.3	0.48
	THF	531	2.02	0.18	1.3	0.48
	Pyridine	537	2.25	0.33	1.2	0.44
Au-PNIPAM$_{265}$ (s1) (D = 2.3 nm, e = 5.4 nm)	Water	535	1.95	0.42	1.3	0.56
	Chloroform	536.4	1.95	0.33	1.4	0.61
	THF	536	2.05	0.32	1.3	0.56
	Pyridine	536	2.23	0.54	1.2	0.52
Au-PNIPAM$_{154}$ (s1) (D = 3 nm, e = 4.5 nm)	Water	530	1.88	0.25	1.4	0.46
	Chloroform	532	1.92	0.25	1.4	0.46
	THF	532	2.02	0.18	1.4	0.46
	Pyridine	536.8	2.22	0.67	1.2	0.4
Au-PNIPAM$_{154}$ (s2) (D = 5 nm, e = 3.5 nm)	Water	527	1.92	0.34	0.9	0.18
	Pyridine	537	2.25	0.35	1.2	0.24
Au-PNIPAM$_{265}$ (s2) (D = 4.5 nm, e = 4.4 nm)	Chloroform	531	2.0	0.54	1.4	0.31
	Pyridine	536	2.22	0.56	1.4	0.31
Au-PNIPAM$_{127}$ (D = 8 nm, e = 6 nm)	Chloroform	532.4	2.08	0.32	2.5	0.31
	THF	532.7	2.1	0.57	2.5	0.31
	Pyridine	536	2.22	0.67	2.7	0.33

Table 4.2: ϵ_s and g fitting parameters used to adjust the absorption spectra of Au-PNIPAM particles dispersed in different solvents; T = 20°C.

From the ensemble of all the data of different particle sizes, chain length, and polymer concentration in the shell, the following observations can be made:

4.2.2.1 Peak position

The absorption peak position depends on ϵ_m and ϵ_s. The polymer shell screens and reduces the sensitivity of SPR to the external solvent. The extent of this screening effect depends on the shell characteristics and particle size. For comparable shell thickness at relatively low polymer concentration, the reduction in solvent-sensitivity is more marked for smaller particle ($D = 3$ nm) compared to its larger counterpart ($D = 5$ nm). For very higher polymer shell concentration, the size effect is less significant and, for small core-size, solvent sensitivity is completely suppressed. All these various shell and core size effects can be rationalized by considering the effective shell thickness $e_{eff} = e.\phi_p$ (e = solvated shell thickness) and p the corresponding shell volume fraction.

Figure 4.11 shows the plasmon peak position (λ_{peak}) versus the dielectric constant of the solvent for all the samples studied. First, consider the closed symbols: closed green squares (Au-PNIPAM$_{57}$, D = 2.7 nm), closed blue upright triangles (Au-PNIPAM$_{154}$, D = 3 nm) and closed red circles (Au-PNIPAM$_{265}$, D= 2.3 nm). The solid lines through these three sets of data are the theoretical Mie curves calculated using the average polymer concentration evaluated from the fits in different solvents ($\phi_p = 0.16, 0.23, 0.36$ respectively). Recall that these curves are exact calculations without the approximation made to the non-dispersive nature of the bound-electron component of the refractive index. (We find that approximative method used by Templeton et al [88] over-estimates the ϕ_p values). Now consider the open symbols: open green square (Au-PNIPAM$_{154}$, D = 5 nm, ϕ_p = 0.34), open blue upright triangle (Au-PNIPAM$_{127}$, D = 8 nm, ϕ_p = 0.62), open blue inverted triangle (Au-PNIPAM$_{265}$, D = 4.5 nm, ϕ_p = 0.54). These open-symbol points fall on the same curves as the closed symbols with similar corresponding polymer shell volume fraction: $p = ((D/2 + e_{eff})^3 - (D/2)^3)/(D/2 + e_{eff})^3$. Thus all the different samples with their various structural characteristics are now consolidated into three populations: $p \approx 0.6$; $p \approx 0.8$; $p>0.9$. With increasing p, the λ_{peak} versus n^2 slope decreases, indicating reduced sensitivity to the solvent refractive index. At $p > 0.9$, the slope becomes negligible; in this case, the plasmon mode is considered to be "frozen" in by the polymer shell ϵ_s and loses complete sensitivity to the external medium. This polymer shell volume fraction corresponds to $e \approx 1.3(D/2)$, a little higher than $e = D/2$ as predicted for solid impermeable shells.

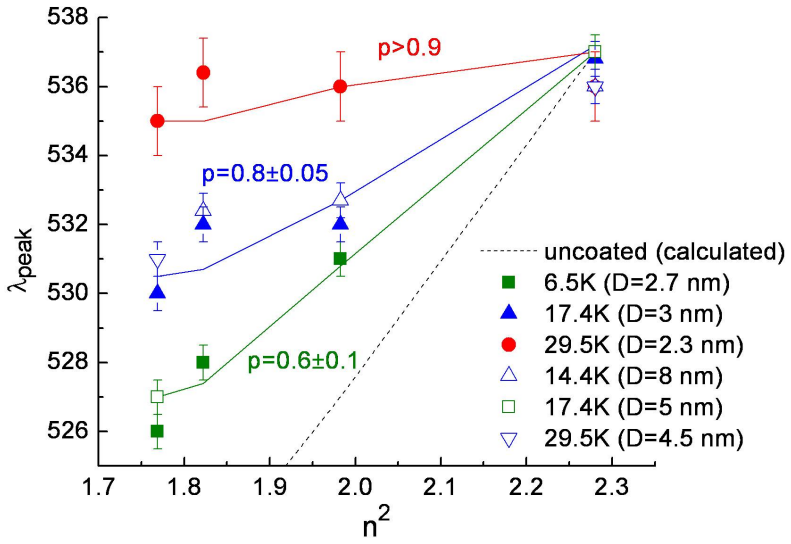

Figure 4.11: Plasmon peak position versus solvent dielectric constant for of Au-PNIPAM nanoparticles. The solid lines are theoretical curves calculated using Mie core-shell model. The dotted line is calculated for bare particles (slope = 2).

4.2.2.2 Peak width

The peak width of the SPR band is dependent on surface scattering due to the reduced size of the particle as mentioned in the beginning of the chapter (intrinsic size effect). It can be characterized by the parameter g which is an intrinsic function of D. In general therefore, the larger the particle, the smaller the value of g. Here, we consider that associated to this parameter are size-dependent imperfections in: morphology (shape, deviation from sphericity) electronic state and chemical heterogeneity (inhomogeneous grafting density for example). All these effects contribute to widen the peak width and their individual contributions are not easy to separate. One can however isolate the geometrical size effect by considering the normalized form, g/D.

Figure 8.14 shows the effect of g/D on the quality of the spectra fit for different particles in the same solvent, water. Clearly, the smaller the value of g/D, the better the quality of theoretical fit to the experimental curve. Spectra with large peak widths that are characterized by high g/D therefore indicate imperfections due to the above mentioned defects and therefore deviate more from theoretical description.

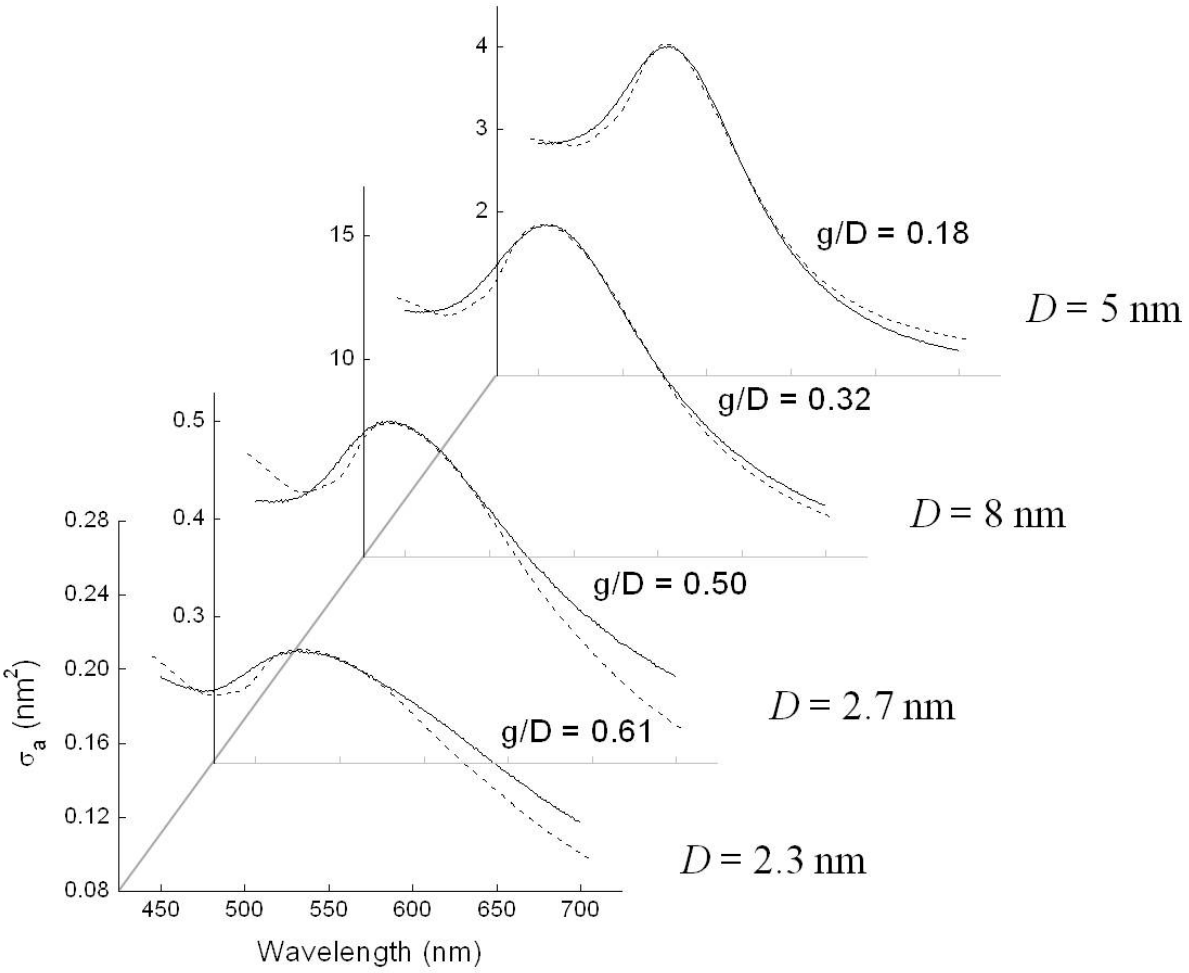

Figure 4.12: Effect of g/D on the quality of theoretical fits to absorption spectra of Au-PNIPAM nanoparticles in water at T = 20°C. Solid line = experimental curve; dashed line = fitted curve.

We have recently begun to try to improve the quality of fit by introducing core-size polydispersity and shape anisotropy effects. These calculations are less direct to perform and have been facilitated with help from Paolo Maioli and the use of his new-improved program. Figure 4.13 shows the initial results. Figure 4.13a shows the introduction of core-size polydispersity with the distribution function:

$$P(D) = \exp((-4\ln 2(D - D_{av})^2/\Delta D^2 \tag{4.19}$$

D_{av}(3 nm) is the average particle size and ΔD (2 nm) is the full-width-half-maximum (FWHM) of the probability distribution. Unfortunately, no improvement can be seen from our initial attempts. In Figure b, the original fit is already quite acceptable but we were interested in seeing if we could improve the fit in the low-wavelength region by introducing a simple anisotropy to the particle form. In this case also, we have not yet succeeded in getting better quality fit. Our future attempts aim to introduce more dispersities in D and g separately, as well as anisotropy.

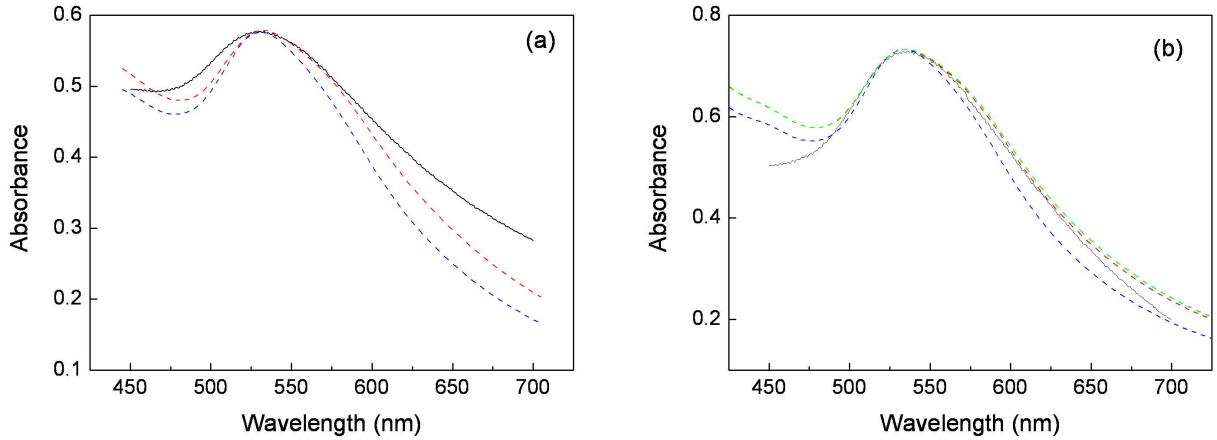

Figure 4.13: (a) Au-PNIPAM$_{154}$ in THF (D = 3 nm); polydispersity effect: red = no polydispersity, blue=size polydispersity. (b) Au-PNIPAM$_{154}$ in pyridine; anisotropy effect: red (no polydispersity), blue = size polydispersity, green = aspect ratio dispersity Δ(a/b) = 0.5. Solid line = experimental curve.

Modelling has helped us understand the origin of SPR peak-shift and how it is related to polymer shell property. We also obtain valuable information on ϵ_{s} and thus the ϕ_{p} in the polymer shell. Combining results from different techniques D (TEM), e (SANS), we are able to rationalize and consolidate the data from different samples with different gold-core sizes and polymer chain lengths. We find that the gold particles sensitivity to surrounding solvent is reduced with increasing polymer volume fraction p until it is totally screened from solvent when $p>$ 0.9 (SPR frozen by polymer shell). Figure 4.14 shows solutions of gold nanoparticles grafted with varying polymer chain length and dispersed in varying solvents. This picture clearly demonstrates the control of gold nanoparticles optical properties by the polymer shell.

Figure 4.14: Gold nanoparticles grafted with varying polymer chain lengths and dispersed in different solvents.

4.3 Temperature effect

In this section, the objective is to modulate the gold SPR by thermally inducing the polymer shell collapse. All experiments were performed on aqueous dispersions. In good solvent condition, the polymer shell is hydrated as the polymer chains are solvated and adopt a coil conformation. At temperature above the polymer graft critical temperature, the particle shell should become dehydrated as the polymer chains become hydrophobe and collapse at the gold particle surface. As a result, we expect the stabilizing shell dielectric constant ϵ_s to increase and modify the SPR.

4.3.1 Thermoresponsive gold nanoparticles dispersed in water

Figure 4.15a and Figure 4.15b represent the absorption spectra at different temperatures for Au-PNIPAM$_{127}$ and Au-PNIPAM$_{270}$-co-NPAM$_{113}$ dispersed in water, respectively. To our disappointment, in both cases, very insignificant peak-shift is registred, $\Delta\lambda \approx 2$ nm, even when the temperature is raised to beyond the T_c. This suggests a non-significant change in the stabilizing shell dielectric constant. It is hypothesized that the stabilizing shell collapses partially due to the presence of the ionizable carboxyl group at the end of RAFT-polymers. Microcalorimetry studies of Au-PNIPAM particles undertaken by Shan and co-workers [67] showed that the gold particles endotherms show two separate transition processes. It was proposed that a first transition occurs at a temperature close to the free polymer T_c and corresponds to the collapse of the shell's "inner zone". The second transition occurs at about 10°C higher and corresponds to the collapse of the "outer zone", supposedly the ionizable carboxyl end-group zone, that shows a higher phase transition temperature than neutral groups. Based on this calorimetry study, we suppose that our nanoparticle shells are only collapsed partially or insufficiently to provoke changes in ϵ_s. In spite of the insignificant peak-shift, an increase in intensity is obtained. We do not know the origin of this increase; it might be due to very small amount of aggregates (stabilized by carboxyl end groups), that contribute to the volume term in the absorption. Under this condition, the thermally-induced partial collapse of polymer shell is fully reversible. Therefore, these polymer-protected particles are stable in water.

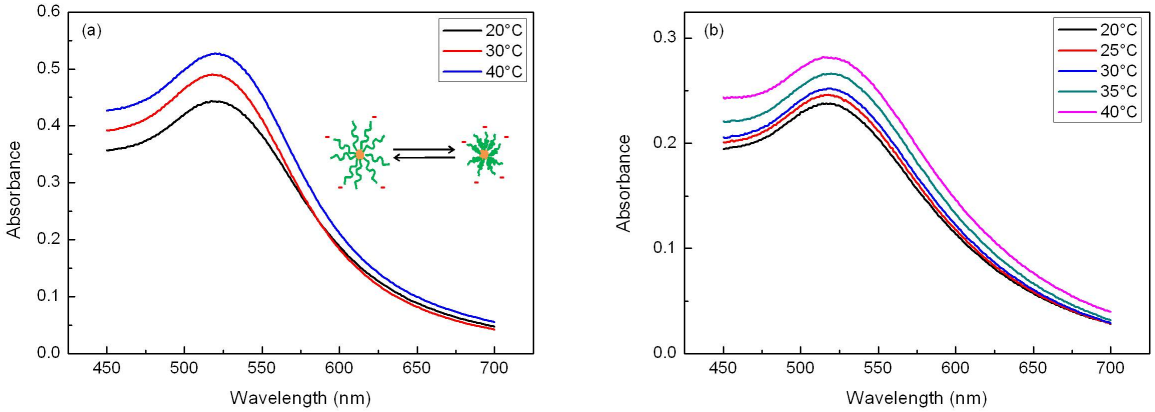

Figure 4.15: UV-vis absorption spectra as a function of temperature: (a) Au-PNIPAM$_{127}$ and (b) Au-PNIPAM$_{270}$-co-NPAM$_{113}$ dispersed in water.

4.3.2 Thermoresponsive gold nanoparticles dispersed in saline solution

The next step consists of screening the polymer graft negative charges with addition of NaCl to enable the protecting shell to completely collapse and lead to the expected increase of ϵ_s [54], [95], [96]. Figure 4.16 show the absorption spectra as a function of temperature of Au-PNIPAM$_{127}$ dispersed in 50 mM NaCl and Au-PNIPAM$_{270}$-co-NPAM$_{113}$ and Au-PNIPAM$_{261}$-co-NPAM$_{144}$ dispersed in 60 mM NaCl, respectively. In the case of Au-PNIPAM$_{127}$ particles, from T = 20 to 32°C, λ_{peak} is shifted only by a very small degree. At T = 33°C however, a very significant shift occurs and λ_{peak} increases up to about 560 nm at T = 35°C. Accompanying this very significant red-shift, is a decrease in intensity of the curve (contrary to an expected increase in intensity with red-shift). This is most probably due to some loss in material due to aggregation, although up to 34°C, the solution appears clear to the eye. We shall see in the next section from modelling the curves that, this decrease in intensity is also a consequence of peak broadening (increase in g/D), indicating an increased inhomogeneity of the aggregated particles at high temperature. As for Au-PNIPAM$_{270}$-co-NPAM$_{113}$ particles, noticeable SPR peak displacement starts at lower temperature (25°C) and λ_{peak} red-shifts up to about 550 when temperature is raised to 34°C.

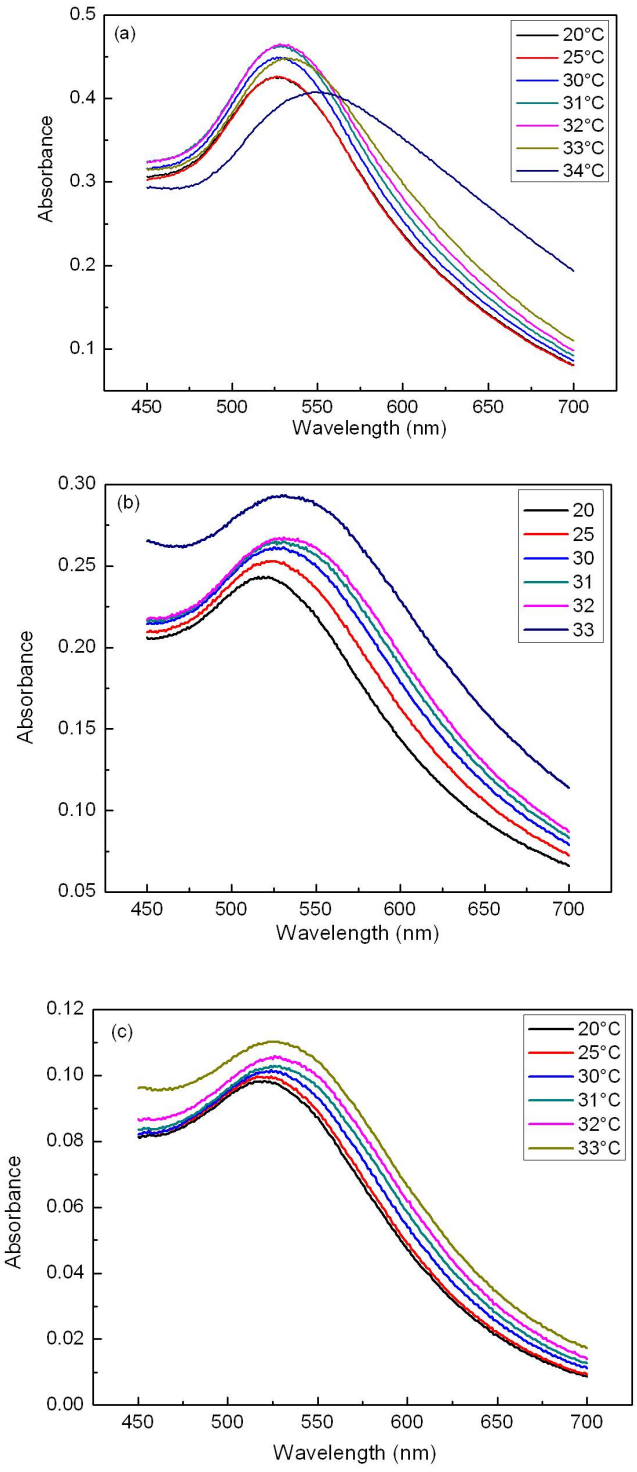

Figure 4.16: UV-vis absorption spectra as a function of temperature of : (a)Au-PNIPAM$_{127}$ dispersed in 50 mM NaCl; (b) Au-PNIPAM$_{270}$-co-NPAM$_{113}$ and (c) Au-PNIPAM$_{261}$-co-NPAM$_{144}$ dispersed in 60 mM NaCl.

Figures 4.17a and 4.17b show similar observations at higher NaCl concentration. In Figures 4.16b and 4.16c, we compare the spectra of Au-PNIPAM$_{270}$-co-NPAM$_{113}$ and Au-PNIPAM$_{261}$-co-NPAM$_{144}$; we can see that these two samples stabilized by copolymers with very similar thermal properties behave very similarly. In all cases, the significant red-shift produces a visibly detectable color change. The solutions of both types of particles have a pink color at 20°C which turn violet at 33°C and 30°C for the Au-PNIPAM$_{127}$ and the Au-PNIPAM$_{270}$-co-NPAM$_{113}$, respectively. It is interesting to note that the color change occurs at a lower temperature for the more hydrophobic particles Au-PNIPAM$_{270}$-co-NPAM$_{113}$ and Au-PNIPAM$_{261}$-co-NPAM$_{144}$, as expected from their lower T_c. For these two samples, the intensity increases at high temperature as expected, suggesting that these particles are better stabilized (no significant loss of larger aggregates). We can conclude that, unlike the particles dispersed in water, the protecting polymer shell in NaCl can undergo a more complete collapse and induces a significant increase in ϵ_s that is responsible for the SPR red-shifting. It is also important to note: (i) for the more hydrophobic particles, Au-PNIPAM$_{270}$-co-NPAM$_{113}$ and Au-PNIPAM$_{261}$-co-NPAM$_{144}$, the sensitivity of SPR to the progressive changes in the polymer shell, (ii) in all samples significant red-shift is registered at temperatures below the T_c for the free chains in solution, and (iii) the sudden departure of the high-temperature curves from the other curves. We shall show later from our modelling data that these latter curves, associated with very large and sudden λ_{peak}-shifts, are due to aggregation of the gold particles.

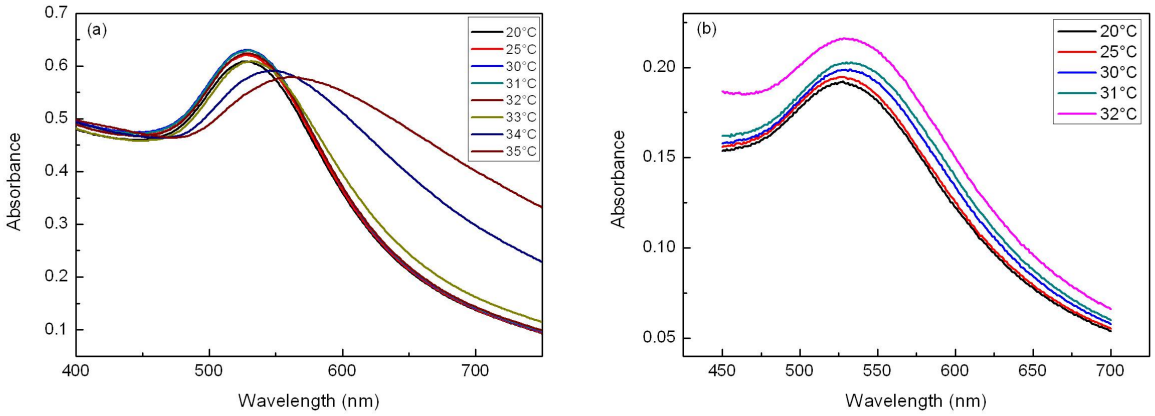

Figure 4.17: UV-vis absorption spectra as a function of temperature of : (a)Au-PNIPAM$_{127}$ and (b) Au-PNIPAM$_{270}$-co-NPAM$_{113}$ dispersed in 100 mM NaCl.

Figure 4.18a and Figure 4.18b show the plots of λ_{peak} as a function of temperature at two NaCl concentration for Au-PNIPAM$_{127}$ and Au-PNIPAM$_{270}$-co-NPAM$_{113}$, respectively. To begin with, at low NaCl concentration (10 mM), as for water, no significant SPR shift is observed when heating the Au-PNIPAM$_{127}$ and Au-PNIPAM$_{270}$-co-NPAM$_{113}$ solutions. In the case of the Au-PNIPAM$_{127}$ particles, the temperature at which a significant SPR shift occurs is lowered from 32.2 to 31.5°C as the salt concentration is increased from 50 to 150

mM. The corresponding values for Au-PNIPAM$_{270}$-co-NPAM$_{113}$ are 30 and 28.5°C at 50 to 100 mM, respectively.

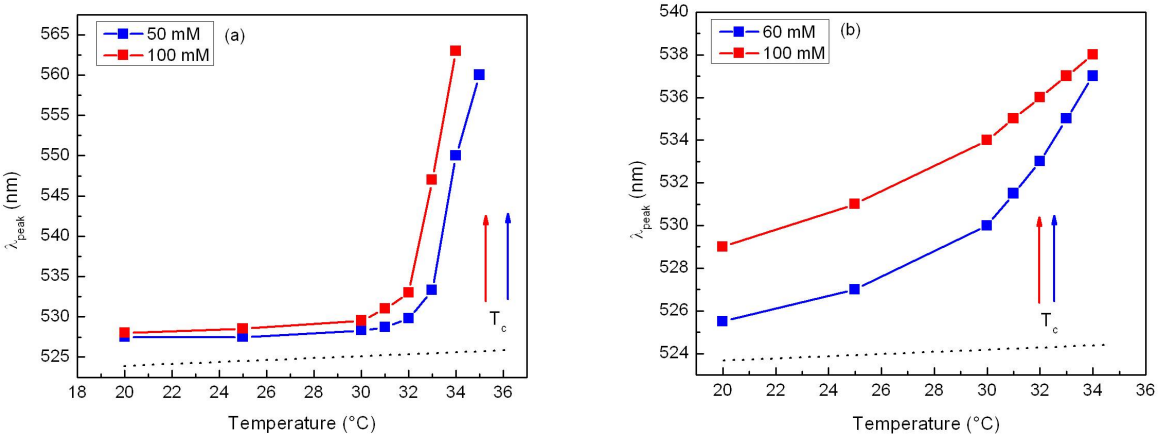

Figure 4.18: Position of SPR peak as a function of temperature for: (a) Au-PNIPAM$_{127}$ and (b) Au-PNIPAM$_{270}$-co-NPAM$_{113}$ dispersed in 50 - 60 (blue) and 100 mM (red) NaCl solutions. The T_c for free chains at the corresponding NaCl concentrations are indicated by vertical arrows. The black dotted lines represent the evolution with temperature of SPR peak position in water.

Temperature (°C)	$\lambda_{\text{Au-PNIPAM}}$ 50 mM NaCl (nm)	$\lambda_{\text{Au-PNIPAM}}$ 100 mM NaCl (nm)	$\lambda_{\text{Au-PNIPAM-co-NPAM}}$ 60 mM NaCl (nm)	$\lambda_{\text{Au-PNIPAM-co-NPAM}}$ 100 mM NaCl (nm)
20	527.5	528	525.5	529
25	527.5	528.5	527	531
30	528.3	529.5	530	534
31	528.7	531	531.5	535
32	529.8	533	533	536
33	533.3	547	535	537
34	550	563	537	538
35	560	-	-	-

Table 4.3: SPR peak positions as a function of temperature in presence of 50, 60 and 100 mM NaCl.

Note that for the more hydrophobic Au-PNIPAM$_{270}$-co-NPAM$_{113}$ at 20°C, an SPR shift is already occurring with increasing salinity. This suggests that the SPR is already sensitive to changes in the polymer shell property induced by screening of the charged end-group.

4.3.3 On the reversibility of temperature effect

In water and at low NaCl concentration, an almost insignificant peak-shift ($\approx$ 2 nm) and an increase in intensity are observed with increase in temperature (T= 20-40°C). For these situations, the absorption spectra are almost completely reversible (also in intensity) when re-cooled to 20°C. At higher NaCl concentration where significant peak-shift takes place, the thermally-induced SPR shift /color change is partially reversible. Firstly, we observe that the absorption peak does not regain its initial position when the Au-PNIPAM$_{127}$ and Au-PNIPAM$_{270}$-co-NPAM$_{113}$ dispersed in NaCl are cooled back to 20°C (Figures 4.19a, 4.19b and 4.19c). Secondly, the resulting solutions exhibit an intermediate color between pink and violet(Figure 4.19d). This partial reversibility of heat-induced SPR shift/color change is probably due to the very slow kinetics of re-hydration of the collapsed chains in the aggregates, and also to possibly some loss of colloidal stability.

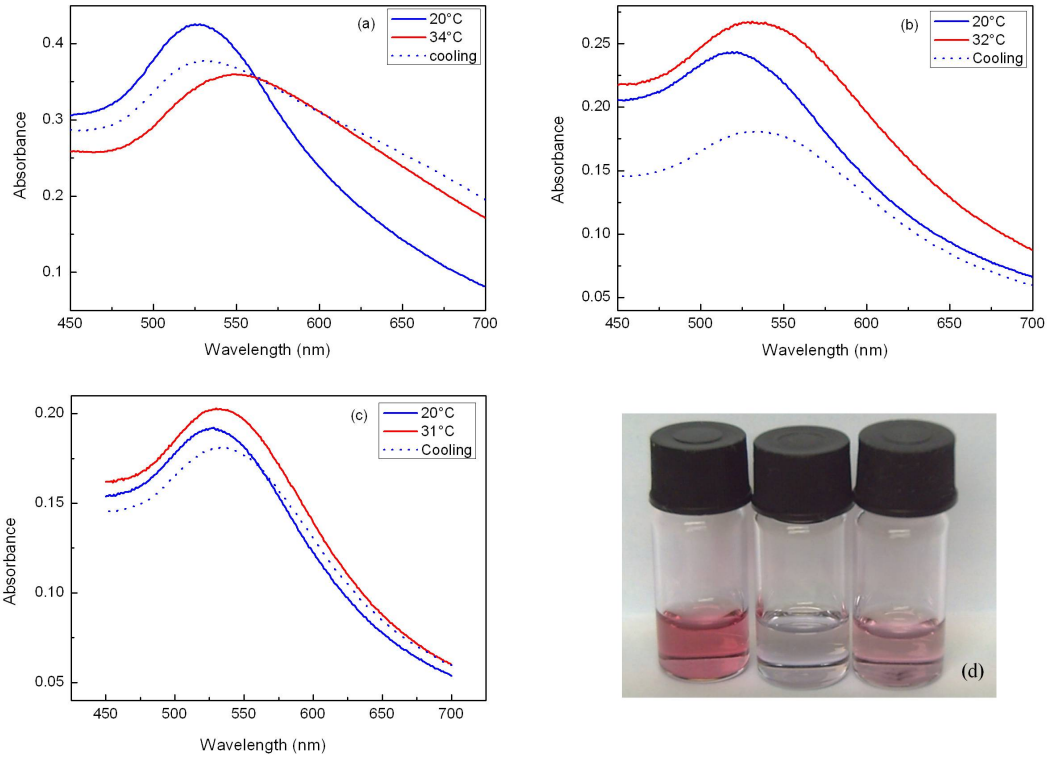

Figure 4.19: Partial reversibility of heat-induced SPR peak shift of: (a) Au-PNIPAM$_{127}$ in 50 mM NaCl; (b) Au-PNIPAM$_{270}$-NPAM$_{113}$ in 60 mM NaCl and (c) Au-PNIPAM$_{270}$-NPAM$_{113}$ in a 100 mM NaCl at T = 20°C (blue solid lines), heated to T = 31/34°C (red solid lines) and cooled to 20°C (blue dotted lines). (d) Dispersions of Au-PNIPAM$_{270}$-co-NPAM$_{113}$ in 60 mM NaCl at T = 20°C (pink solution), 30°C (violet solution) and cooled to 20°C (pale pink solution).

4.4 Modelling the extinction spectra

In the previous section, we supposed that the SPR-shift with temperature is, at first instance, due to increase of ϵ_s. By modelling the extinction spectra, we can obtain a direct relation between these two properties.

4.4.1 Au-PNIPAM

Figure 4.20 represents the extinction spectra of Au-PNIPAM$_{127}$ dispersed in a 50 mM NaCl solution at varying temperatures. These are modelled by keeping the particle size D and shell thickness e constant ($D = 8$ nm and $e = 6$ nm). It is of course expected that with dehydration/collapse of the polymer shell, e would also decrease with temperature. However, at the time of writing this thesis, we have not yet obtained conclusive experimental data to support changes in e (we are continuing to investigate this aspect with SANS). Simulations show that under these sets of conditions, variations in e only affect, to a small extent, the intensity through the volume term in the Mie equation. We therefore, for these fits, kept e constant with temperature. Similarly to the previous section, the fitting parameters are ϵ_s and g. From 20 to 25°C, no SPR shift occurs and each extinction spectra is adequately modelled with $\epsilon_s = 1.85$ and $g/D = 0.3$. From 30 to 33°C, the SPR progressively red shifts and the extinction spectra are modelled with ϵ_s value increasing from 1.9 to 2.1 and $g/D =$ 0.29 - 0.35 (Table 4.4). This confirms the direct relation between λ_{peak}-shift and increase in ϵ_s that results from the thermally-induced collapse in the polymer shell. At T $\geq$ 34°C, the broad spectra that are very highly red-shifted are not fittable (see next section).

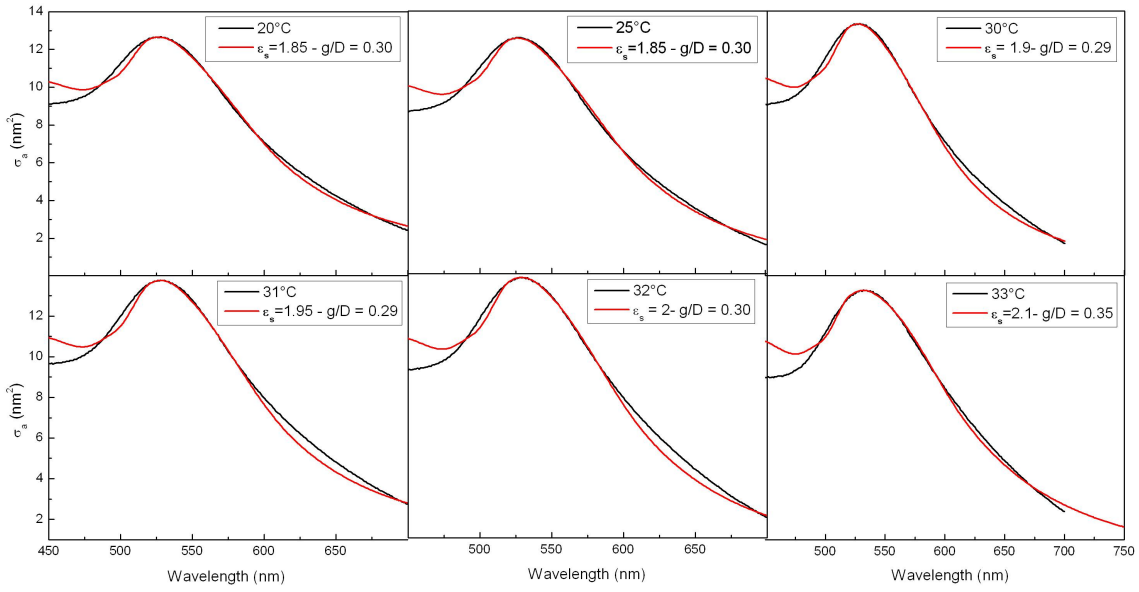

Figure 4.20: Fits of extinction spectra of Au-PNIPAM$_{127}$ particles dispersed in 50 mM naCl at varying temperature.

4.4.2 Au-PNIPAM-co-NPAM

Figure 4.21 represents the extinction spectra of Au-PNIPAM$_{270}$-co-NPAM$_{113}$ particles dispersed in a 60 mM NaCl solution at varying temperatures. The modelling parameters D and e are kept constant (D = 5.3 nm and e = 4 nm). Like the extinction spectra of Au-PNIPAM$_{127}$ particles, the curves are modelled with increasing ϵ_s when temperature is raised. In fact, from 20 to 32°C, the ϵ_s value increases from 1.80 to 2.18 (Table 4.4). Here again, we can conclude that from 20 to 32°C the SPR red-shift is due to the increase of ϵ_s. At T $\geq$ 33°C, as in the case of Au-PNIPAM$_{127}$, the broad spectra at the high λ_{peak} values could not be fitted. Since ϵ_s is already close to 2.19 (corresponding to $\phi_p \approx 1$, ie pure polymer shell), this value already pins λ_{peak} at approximatively 537 nm; the significant red-shift of $\lambda_{peak} >$ 537 nm thus cannot be explained by a further increase in ϵ_s. Furthermore, an increase in e only increases the peak intensity but does not shift the peak position to longer wavelengths. The significant red-shift close and beyond T_c should then be attributed to aggregation, as supported by SANS (see Figures 8.17 and 4.23). Note that at T = 32°C, we find a surprisingly high concentration of polymer in the collapse shell ($\phi_p \approx 1$); this almost-dry state of the PNIPAM has also been reported by Viovy et al [97] in a PNIPAM core-corona structure and for grafted PNIPAM layers [98].

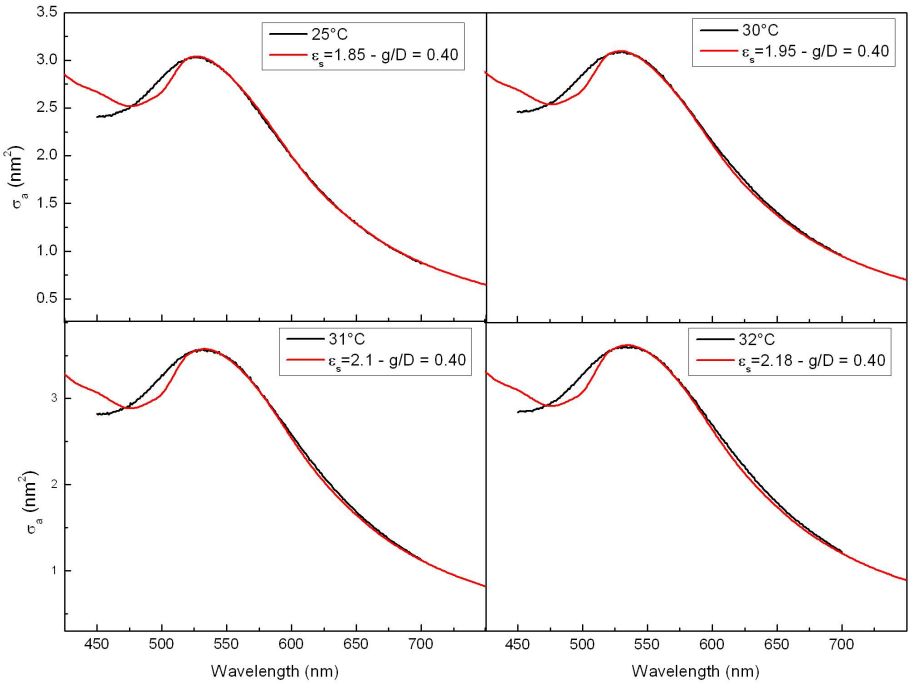

Figure 4.21: Fits of extinction spectra of Au-PNIPAM$_{270}$-co-NPAM$_{113}$ particles dispersed in 60 mM naCl at varying temperatures.

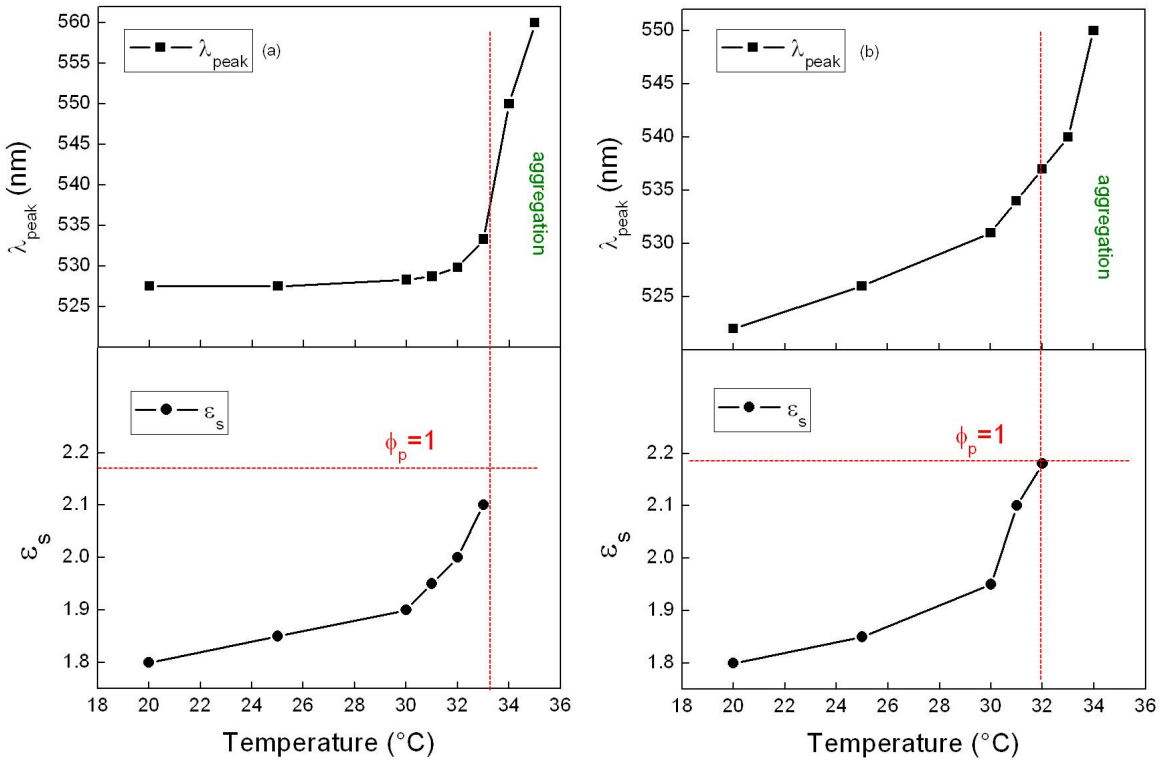

Figure 4.22: Plot of λ_{peak} position and ϵ_s as a function of temperature of: (a) Au-PNIPAM$_{127}$ dispersed in 50 mM NaCl and (b) Au-PNIPAM$_{270}$-NPAM$_{113}$ dispersed in 60 mM NaCl.

Sample	Temperature (°C)	λ_{peak} (nm)	ϵ_s	ϕ_p	g/D
Au-PNIPAM$_{127}$	20	527.5	1.85	0.18	0.30
	30	528.3	1.9	0.30	0.29
	31	528.7	1.95	0.42	0.29
	32	529.8	2	0.54	0.30
	33	533.3	2.1	0.78	0.35
Au-PNIPAM$_{270}$-co-NPAM$_{113}$	20	522	1.80	0.06	0.40
	25	526	1.85	0.18	0.40
	30	531	1.95	0.42	0.40
	31	534	2.1	0.78	0.40
	32	537	2.18	0.97	0.40

Table 4.4: ϵ_s and g fitting parameters as a function of temperature used to adjust the absorption spectra of Au-PNIPAM$_{127}$ and Au-PNIPAM$_{270}$-co-NPAM$_{113}$ particles dispersed in 50 and 60 mM NaCl solution; respectively. The spectra could not be fitted satisfactorily at T$\geq$ 34°C and T$\geq$ 33°C for Au-PNIPAM$_{127}$ and Au-PNIPAM$_{270}$-co-NPAM$_{113}$; respectively.

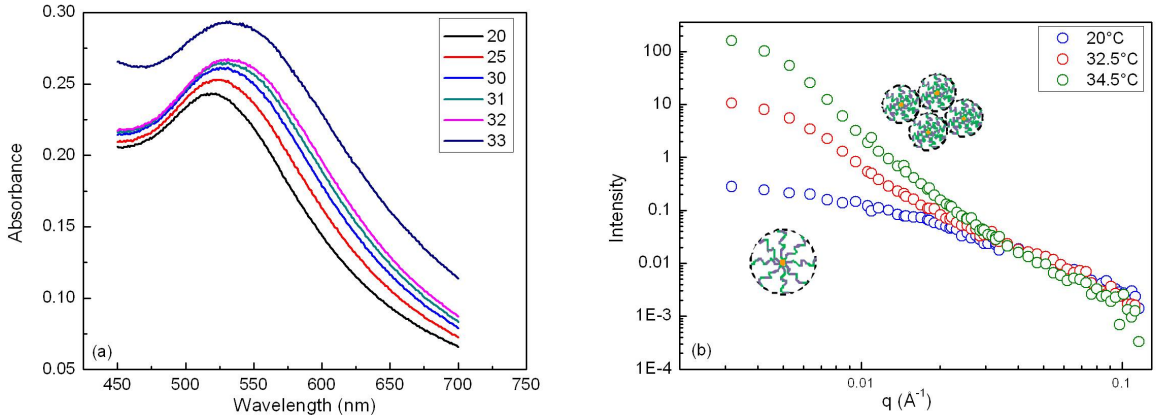

Figure 4.23: Representations of: (a) extinction spectra and (b) scaterring curves accompagnied with schematic representation of particles of Au-PNIPAM-co-NPAM particles dispersed in a saline solution at varying temperature.

4.5 Summary

We have studied the optical properties of gold nanoparticles of various sizes and that are coated with polymers of varying chain lengths. First, we have analyzed the effect of the graft polymer to external solvent. We observe that the polymer shell screens and reduces the sensitivity of SPR to the external solvent. The experimental spectra are modelled by fitting $\lambda_{\mathbf{peak}}$ and the form of the spectra with a core-shell model in the Mie dipolar theory. This enables us to gain information on the direct relationship between the optical properties and the structural properties of the polymer shell, and their influence on solvent-sensitivity. By fitting $\lambda_{\mathbf{peak}}$, we obtain $\epsilon_{\mathbf{s}}$ from which we deduce the polymer volume fraction in the shell $\phi_{\mathbf{s}}$. Combining results from different techniques D (TEM), e (SANS), we are able to rationalize and consolidate data from the different samples with different characteristics. We show that the gold nanoparticle sensitivity to external solvent is reduced with increasing polymer volume fraction p. Furthermore, when $p > 0.9$, the SPR is frozen by polymer shell.

The SPR peak width is fitted with a surface scattering parameter g which is an intrinsic function of D. This parameter depends on the size-dependent imperfections in morphology, electronic state and chemical heterogeneity that contribute to the peak broadening. To isolate the geometrical size effect, we consider the normalized form g/D. We observe that the lower the g/D value, the better is the quality of theoretical fit. Spectra with large peak widths that are characterized by high g/D therefore indicate higher surface imperfections.

In a second part, we focused on SPR response to temperature-induced conformational changes in the polymer shell. We observe that only in the presence in presence of salt, the SPR is significantly red-shifted (clear visible color change

occurs).The extent of the red-shift is controlled by the graft polymer hydrophobicity and the salt concentration. Modelling the spectra revealed two reasons for the red-shift: the initial is due to an increase in ϵ_s caused by the polymer shell collapse; however, the significant red-shift close to and beyond T_c is attributed to aggregation, as supported by SANS. It is interesting to note the partial reversibility of the temperature effect; this particularity can have potential applications in detection. We thus conclude that the gold nanoparticle SPR can be tuned by the polymer shell layer. Gold nanoparticles are thus sensitive probes for changes in local environment.

Chapter 5

Polymer-protected gold nanoparticles interfacial properties

PNIPAM is among the most surface-active water-soluble polymers. It adsorbs spontaneously at the water-air interface, reducing the interfacial tension to about 40 mNm^1. Gold nanoparticles protected by graft PNIPAM chains are therefore rendered colloidally stable and amphiphilic. These Au-PNIPAM nanoparticles can therefore be spread on the water surface to form Langmuir monolayers, the structural properties of which can be manipulated by compression and by temperature. We are interested in the interfacial phenomena of our nanoparticles such as their adsorption and monolayer behavior because these are aspects pertinent to templating building blocks and self-assembly, and to interactions of nanoparticles with biological membranes. For example, a recent study on Langmuir monolayers of magnetic nanoparticles [99] showed that packing and stability of the monolayer affect the ability of the nanoparticles to cross cellular membranes, a process that is important for potential applications in enhancement of magnetic response of biological cells.

Past studies on Au-PNIPAM-PS nanoparticle surface layers have been reported to exhibit SPR [100]. In these studies, a blue-shift was observed upon compression, contrary to an expected red-shift [101] if the interparticle distance is sufficiently reduced for dipole-coupling to occur. This unexpected compression-induced blue-shift was hypothesized to be closely related to conformational changes in the polymer shell. A follow-up to this hypothesis was undertaken by Lee et al [102] using contrast-matched neutron reflectivity to study the structure of the composite nanoparticle layer, and where the system studied was simplified to Au-PNIPAM (without the polystyrene chains). Very detailed studies and analyses of the data revealed clear compression- and temperature-induced conformational changes in the polymer shell layer. It is shown that upon isothermal compression, the adsorbed polymer layer thickens with partial desorption of polymer chains to form brush-like structures. Two distinct polymer conformations thus co-exist: adsorbed conformation that ensures stability of the monolayer, and brush structures that dangle in the subphase. Such structural changes may qualitatively support the argument for a blue-shift due to the resulting higher exposure of the gold-core to the aqueous medium of lower dielectric constant. However, the degree of conformational changes and the accompanying modification of the local dielectric constant do not appear sufficiently large to explain the extent of blue-shift that is measured. Increase in temperature to near-collapse temperature results in contractions of both adsorbed and

brush-like layers. These contractions were invoked to explain the observed red-shift upon increase in temperature whereby dipole coupling was promoted by a decrease in interparticle distance.

In the above past neutron reflectivity studies, although very detailed structural information on the polymer layer were revealed, the gold-core organization was less well-characterized due to the low surface concentration, lower contrast with the polymer-matched solvent, and to the small particle size for which the Q-range of the spectrometer was not well-adapted. In this part of the thesis work, we wish to explore in more detail the interfacial properties of our new thermosensitive nanoparticles by a combination of isothermal compression studies using the Langmuir balance and neutron and X-ray reflectivities. We cover the entire compression isotherm from the low compression (2-dimensional) regime (structural properties not measureable by reflectivity) up to very high compression (3-dimensional) regime. Our aim is to control interparticle distance in the monolayer using the soft polymer shell and by their temperature-sensitive expansion-collapse. Neutron and X-ray reflectivities are performed to characterize the polymer conformation and the gold-core organization, respectively. But since a lot of detailed information has already been revealed from past studies on the polymer conformational changes, we shall invest more effort in the characterization of the gold-core organization using X-ray reflectivity. We then address the problem of stability of the nanoparticle layers in the high compression regime in order to identify optimal conditions for subsequent studies of their optical properties.

5.1 Compression isotherms

We first present the compression isotherms of the polymer layer alone [103] (without gold core) in order to determine the role of these polymer layers on the 2-dimensional organization of the gold nanoparticle monolayers.

5.1.1 Polymers monolayers

5.1.1.1 Compression effect

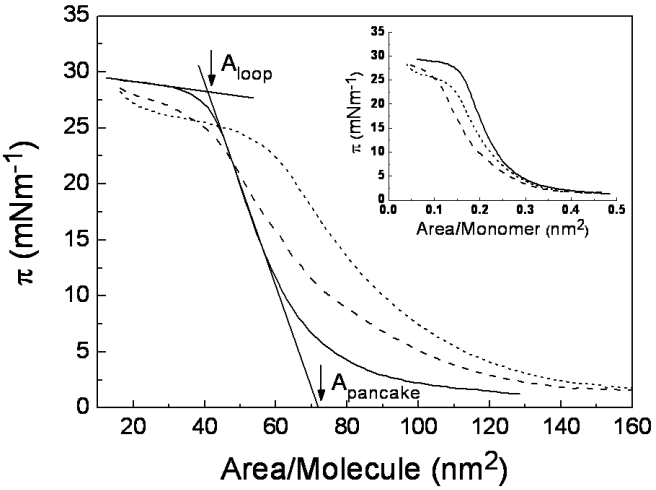

Figure 5.1: Compression isotherms of Cpa-PNIPAM$_{265}$ (solid line), Cpa-PNIPAM$_{270}$-co-NPAM$_{113}$ (dash line) and Cpa-PNIPAM$_{261}$-co-NPAM$_{144}$ (dotted line) at T = 20°C. The inset shows the normalized curves (π versus area per monomer).

In Figure 5.1, the compression isotherms at T = 20°C for Cpa-PNIPAM and Cpa-PNIPAM-co-NPAM polymers show typical distinguishable regions: very low-pressure region (2-D ideal gas) followed by a rise in pressure and a leveling off to a "pseudo-plateau". The rise in pressure, in the so-called "pancake" region, is attributed to 2-dimensional segmental interactions [104] and extrapolation of this region of the isotherm to π= 0 yields the limiting "pancake area", $A_{pancake}$. This area occupied by the molecule depends on molecular chain length and, for a homologous series of polymers, converges when normalized by the degree of polymerization. For the Cpa-PNIPAM$_{265}$ and copolymers Cpa-PNIPAM$_{270}$-co-NPAM$_{113}$ and Cpa-PNIPAM$_{261}$-co-NPAM$_{144}$, extrapolations of these normalized curves yield $A_{monomer}$ = 0.24 to 0.27 nm^2. These values are in agreement with typical values of $\approx$ 0.25 nm^2 per monomer found for neutral PNIPAM and PEO [104], [105], [106] in good solvents. With further compression beyond a critical surface concentration (denoted here as A_{loop}) the surface pressure increase is slowed down and a pseudo-plateau is reached. In this region, monomer-monomer steric repulsion exceeds monomer-surface attractions and the polymer segments gradually desorb from the interface forming loops that immerse in the water subphase. Onset of this "pancake-to-loop" transition corresponds closely to the surface coverage attained

by freely adsorbed chains, that is, the surface density of a polymer layer formed by spontaneous adsorption from a dilute polymer solution. The structure of the monolayer beyond this point approaches 3-dimensional and the surface coverage can be evaluated from A_{loop} by: $\Gamma = M_w/(N_A\ A_{loop})$ where M_w is the molar mass of the polymer and N_A the Avogadro's number. A_{loop} is estimated from the intersection of the extrapolations of the pseudo-plateau and pancake regions. For Cpa-PNIPAM, the calculated surface density is $\approx$ 1.2 mg/m^2, in fairly close agreement with results evaluated by neutron reflectivity for neutral PNIPAM layers physically adsorbed from a dilute solution [65]. For the Cpa-PNIPAM-co-NPAM copolymers, only a small increase is registered, with $\Gamma \approx$ 1.4-1.7 mg/m^2. Thus, at T = 20°C, there appears to be no significant difference in the surface density between the homopolymer and copolymers. However, the gradual rise in pressure in the pseudo-plateau region is more significant for Cpa-PNIPAM-co-NPAM than for Cpa-PNIPAM. This slow pressure change is indicative of continual conformational changes at high compression. It appears therefore that presence of the more hydrophobic NPAM segments prevents complete dissolution of the molecule into the subphase at high compression, thus increasing the compressibility and stability of the monolayer.

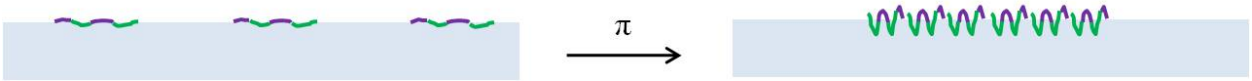

Figure 5.2: Representation of the compression-induced pancake-to-loop transition of Cpa-PNIPAM$_{270}$-co-NPAM$_{113}$ monolayer.

5.1.1.2 Temperature effect

We find that the compression isotherms performed too close to the bulk collapse-transition temperature (T_c which we take here as the calorimetry T_m) gave poor reproducibility due most probably to surface aggregation. Therefore, in this section we only present the results obtained under near-theta conditions, taken to be approximately 2-3°C lower than the T_c [107]. Figure 5.3 compares the thermal response of the Cpa-PNIPAM and Cpa-PNIPAM-co-NPAM monolayers. For Cpa-PNIPAM, when the temperature is increased from T = 20°C to T = 33 °C ($T_c \approx$ 34.8°C), no significant change in the pancake region is registered; only a small increase in the pseudo-plateau region is observed. For the copolymers under a similar change in solvent quality, when the temperature is raised from T = 20 °C to T $\approx$ 30°C ($T_c \approx$ 33°C), the curves are shifted to lower molecular areas: $A_{pancake}$ decreases from 92 nm^2 to 72 nm^2 per molecule for Cpa-PNIPAM$_{270}$-co-NPAM$_{113}$ (Figure 5.3b) and from 110 nm^2 to 87 nm^2 per molecule for Cpa-PNIPAM$_{261}$-co-NPAM$_{144}$ (Figure 5.3c). These decreases correspond to about 25-30% contraction in their 2-dimensional areas. Inspection of the form of pressure-rise in the low-pressure pancake regime provides further insight to the 2-dimensional nature of the monolayers. For interfacial layers, the surface pressure due to segmental interactions can be considered as the 2-dimensional equivalent of the bulk osmotic pressure. It is predicted to depend on the surface coverage (c) as $\approx c^y$ where $y = d\nu/(d\nu - 1)$, d is the dimensionality and ν the critical exponent that takes the theoretical value of $\nu = 3/5$ for $d = 3$, and $\nu = 3/4$ for $d = 2$, in good solvents [108], [109], [110]. For a polymer

molecule in a 2-D self-avoiding walk conformation therefore, $d = 2$, $\nu = 3/4$ and y= 3 (y = 2.25 for $d = 3$). Under theta-condition [111], $\nu = 4/7$ and y = 8. The insets in Figure 5.3 show corresponding double logarithmic plots of the π-A isotherms (since A = 1/c, $\pi \approx A^{-y}$). Due to the limited range of the linear region of the curves, rather than performing a theoretical fit to the data, we have superposed calculated lines on the experimental curves for visual comparison. It can be seen that at T= 20°, both the Cpa-PNIPAM and the Cpa-PNIPAM-co-NPAM experimental curves compare relatively well with the theoretical line with slope -3, supporting the 2-dimensional conformation of the polymer layers. When the temperature is increased to near-theta condition, no detectable change in slope can be seen for Cpa-PNIPAM (inset, Figure 5.3a). For the Cpa-PNIPAM-co-NPAM isotherms on the other hand, the slope increases to about -4 (insets, Figure 5.3b and Figure 5.3c), an increase that does not meet the theoretical value of -8 for theta-solvent. This weaker dependence, also observed in the past for elastic modulus measurements of neutral PNIPAM [75] and protein systems[112] might suggest that under these experimental conditions, the monolayer exists between good and theta solvent conditions. (Incidentally, the value of y = 4 corresponds to $\nu = 2/3$ as originally predicted by the theory of Flory but was contested and corrected by others [111] leading to the commonly accepted value of $\nu = 4/7$). For all polymers, the thermally-induced reduction in molecular area is accompanied by a delay in onset of the pseudo-plateau region (decrease in A_{loop}), consistent with a more compact surface layer at the onset of the pancake-to-loop transition. The values for $A_{pancake}$ and $A_{loop}$and are given in Table 5.1.

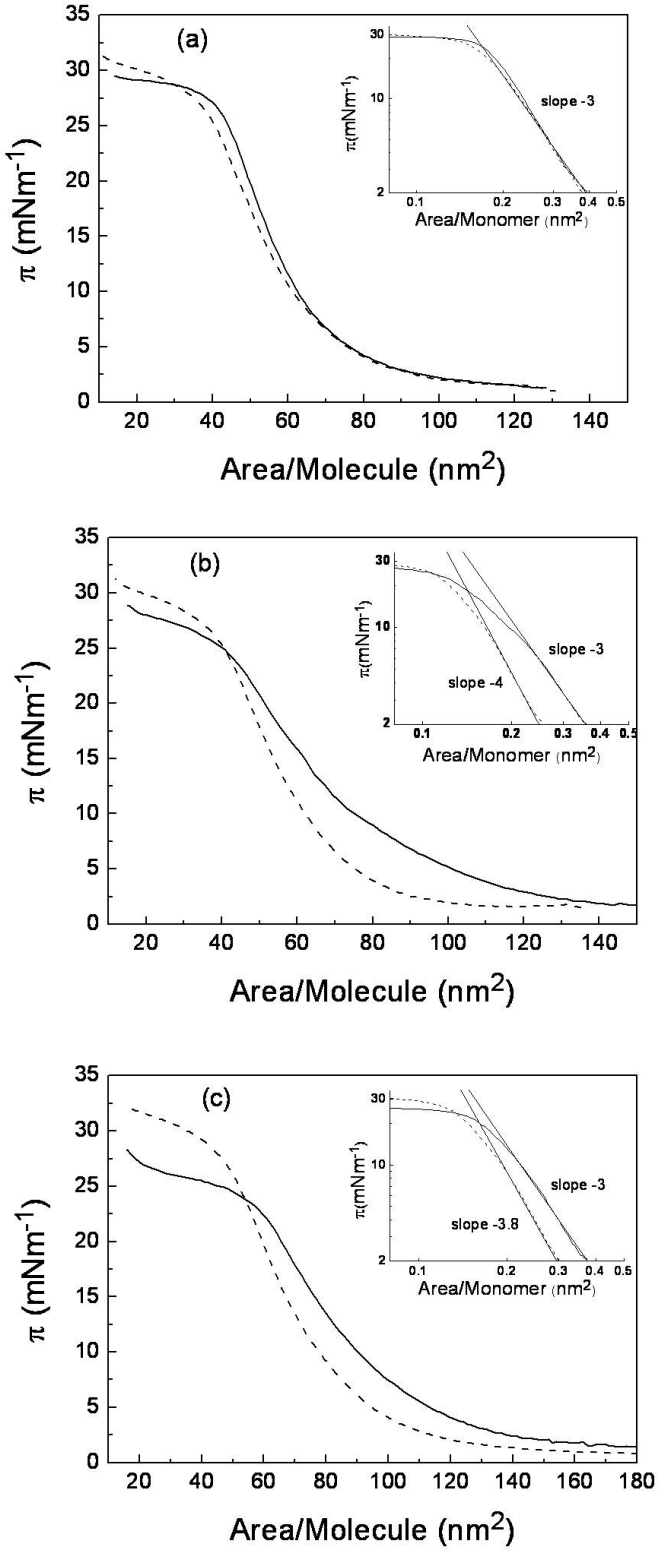

Figure 5.3: Compression isotherms of (a) Cpa-PNIPAM$_{265}$ at T= 20°C(solid line), T= 33°C (dashed line); (b) Cpa-PNIPAM$_{270}$-co-NPAM$_{113}$ at T= 20°C (solid line), T= 30°C (dashed line); (c) Cpa-PNIPAM$_{261}$-co-NPAM$_{144}$ at T= 20°C (solid line), T= 29°C (dashed line). The insets show double logarithmic plots with calculated slopes for comparison (straight lines).

Polymer	T(°C)	$A_{pancake}(nm^2)$	A_{loop} (nm^2)	Γ (mg/m^2)
$PNIPAM_{265}$	30	72 (0.27)	41	1.21
$PNIPAM_{265}$	33	70 (0.26)	37	1.34
$PNIPAM_{270}$-co-$PNPAM_{113}$	20	92 (0.24)	42	1.71
$PNIPAM_{270}$-co-$PNPAM_{113}$	30	72 (0.19)	38	1.89
$PNIPAM_{261}$-co-$PNPAM_{144}$	20	109 (0.27)	56	1.36
$PNIPAM_{261}$-co-$PNPAM_{144}$	29	87 (0.21)	46	1.65

Table 5.1: Area/molecule for Cpa-RAFT-PNIPAM and Cpa-RAFT-PNIPAM-co-NPAM polymers. $A_{pancake}$ and A_{loop} are the limiting molecular areas evaluated from the respective regimes. The area per monomer in the pancake regime is given in parenthesis. Γ is the surface coverage evaluated from A_{loop}.

The above results show that thermally-induced molecular contraction is enhanced when the hydrophobicity of the polymer is increased. It is important to note that these compression measurements of spread monolayers reveal thermally-induced 2-D lateral contraction within a true monomolecular layer. In contrast, for a surface layer formed by spontaneous adsorption from a polymer solution, this type of monomolecular collapse, whether lateral or perpendicular to the surface, might be detectable only for a monolayer formed at infinitely dilute solution ($\phi_p \approx 10^{-7} - 10^{-6}$) that would require prohibitively long adsorption time. Normal polymer adsorption measurements are usually carried out at higher concentrations ($\phi_p \approx 10^{-5} - 10^{-3}$) and under these conditions, monolayer collapse is not observable within the time-frame of the measurement; instead, an abrupt increase in adsorbed layer thickness is obtained with increase in temperature [102]. This increase is attributed to multilayer build-up as the temperature approaches the critical temperature.

5.1.2 Polymer-protected gold particles monolayers: Low compression regime

As seen earlier, amphiphilic Cpa-PNIPAM and the new copolymer Cpa-PNIPAM-co-NPAM exhibit interfacial stability where the molecular structure in the monolayer depends on molecular chain length and can be controlled by the degree of hydrophobicity and temperature. Therefore when adsorbed or grafted onto nanoparticles, these amphiphilic polymers provide colloidal stability and also confer surface-activity to the nanoparticles.

5.1.2.1 Compression effect

Figure 5.4 shows compression isotherms at T = 20 °C (π versus area per nanoparticle) for gold nanoparticles grafted with Cpa-PNIPAM homopolymers of chain lengths varying from about 6500-30000 $g.mol^{-1}$ (N = 55-265). These isotherms show characteristics similar to those for polymer monolayers, exhibiting a pancake region (low compression regime) and a pseudo-plateau with comparable surface pressure characteristic of a loop region (high compression regime). The driving force for the formation of the nanoparticle monolayer can thus be considered to be derived from the interfacial behavior of the graft polymer

chains. The strong dependence on polymer chain length is clearly shown by the shift of the isotherms towards larger particle areas with increase in M_w. The limiting nanoparticle area A_p(gold core + polymer shell layer) are obtained from pancake ($A_{p\text{-pancake}}$) and loop ($A_{p\text{-loop}}$) regimes (Figure 5.4, inset), the interparticle distance deduced from $d_p = 2(A_p/\pi)^{1/2}$ and the graft polymer (in-plane) layer thickness from $L = (A_p/\pi\ )^{1/2}$ - $D_p/2$ where D_p is the gold core diameter. The values of A_p and d_p are given in Table 5.2. It can be seen that A_p » $A_{molecule}$ where $A_{molecule}$ is the 2-D molecular area of the unattached polymer chain evaluated from the polymer compression isotherm. Thus, L » R_g where and $R_g = (A_{molecule}/\pi\ )^{1/2}$ indicating stretched conformation of the graft polymer chains; for Au-PNIPAM$_{265}$ the degree of stretching is found to be $L/R_g \approx 10$. In this stretched regime, the chains may be considered as brush-like (in 2-D) and one expects L ≈ N. The interparticle distance that is modulated by this graft polymer layer can thus also be expected to vary with molecular weight as d_p ≈ N. Figure 5.4a and Figure 5.4b show logarithmic plots of d_p versus M_w for interparticle distance deduced from $A_{p\text{-loop}}$and $A_{p\text{-pancake}}$ for the series of Au-PNIPAM samples. In both cases, linear fits to the experimental points yield a slope of ≈ 0.8. Two possible reasons may explain this weaker dependence. First, the degree of stretching, although high, may not have reached the very strongly-stretched regime required to observe the theoretical linear dependence. Second, the non-identical grafting density, and therefore different degree of stretching for each sample may also contribute to the dispersion of the experimental points. Nevertheless, a clear and strong dependence of the 2-D interparticle distance with the graft chain length can be attested. The polymer chains thus adopt an extended conformation in 2-D that tethers the nanoparticles to the interface and also controls the interparticle distance in a predictable manner with chain length.

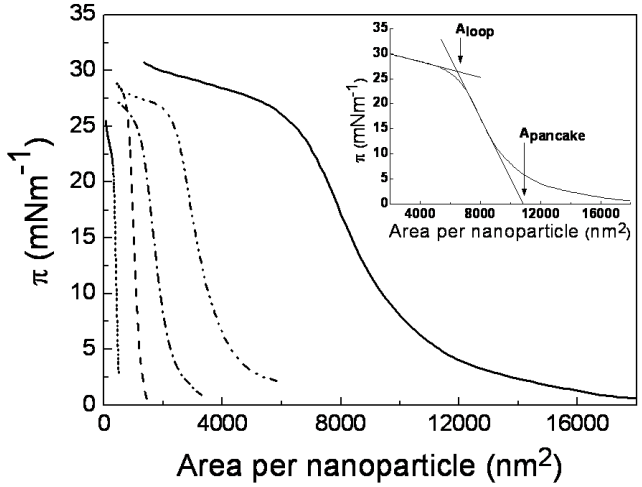

Figure 5.4: Compression isotherms of Au-PNIPAM nanoparticle monolayers at the air-water interface at T = 20°C. From left to right: Au-PNIPAM$_{55}$, Au-PNIPAM$_{67}$, Au-PNIPAM$_{118}$, Au-PNIPAM$_{165}$, Au-PNIPAM$_{265}$. Inset: extrapolations to $A_{p\text{-pancake}}$ and $A_{p\text{-loop}}$.

We note that a high degree of stretched conformation is achieved only at high grafting density which in this case falls in the range σ = 1-2 chains/nm^2. At low grafting density, reduced steric repulsions between neighboring chains and possibly re-adsorption of polymer segments on the particle surface decrease chain stretching and thus lower the nanoparticle area. For example, for nanoparticles grafted with polymers of comparable hydrophobicity and chain length, a six-fold decrease in A_p is obtained when the grafting density is reduced from $\sigma \approx 1.3$ to $\sigma \approx 0.6$ chains per nm^2 (Figure 5.5).

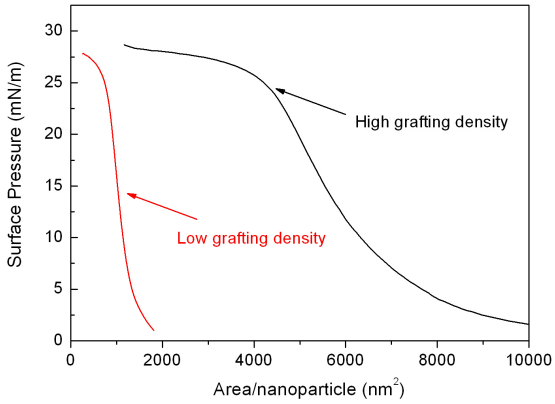

Figure 5.5: Effect of grafting density. Compression isotherms of Au-PNIPAM-co-NPAM nanoparticle monolayers at the air-water interface at T = 20°C. From left to right: $\sigma \approx 0.6$ and $\sigma \approx 1.3$ chains/nm^2.

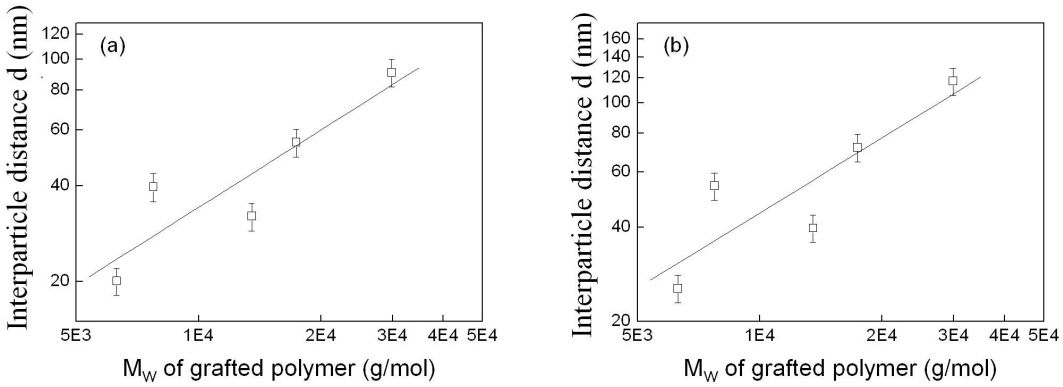

Figure 5.6: Interparticle distance versus graft polymer chain length evaluated from: (a) $A_{\text{p-loop}}$ and (b) $A_{\text{p-pancake}}$; the solid lines are best-fit curves with slopes of 0.80 and 0.81, respectively.

5.1.2.2 Temperature effect

The thermal response of the polymer-protected nanoparticles follows closely the response of the pure polymer monolayers. For the Au-PNIPAM$_{265}$ (as already seen for Au-PNIPAM$_{265}$), little change in the compression isotherm occurs when the temperature is raised from T = 20°Cto T = 33°C. A small increase in slope in the pseudo-plateau region can again be noted, suggesting a higher degree of structural changes and enhanced stability in the loop (3-D) region. The area per nanoparticle thus remains invariant within this range of temperature due to the insensitivity of the 2-D conformation of the polymer shell layer (Figure 5.7a). For the copolymer, the thermal response is more marked and its thermally-induced lateral contraction clearly decreases the nanoparticle area (Figure 5.7b). For the PNIPAM$_{270}$-co-PNPAM$_{113}$, when temperature is increased from 20°C to 30°C, $A_{p\text{-}pancake}$ decreases from 8506 to 6710 nm^2 and $A_{p\text{-}loop}$ from 4784 to 3698 nm^2 ie a reduction of 30% for both areas.

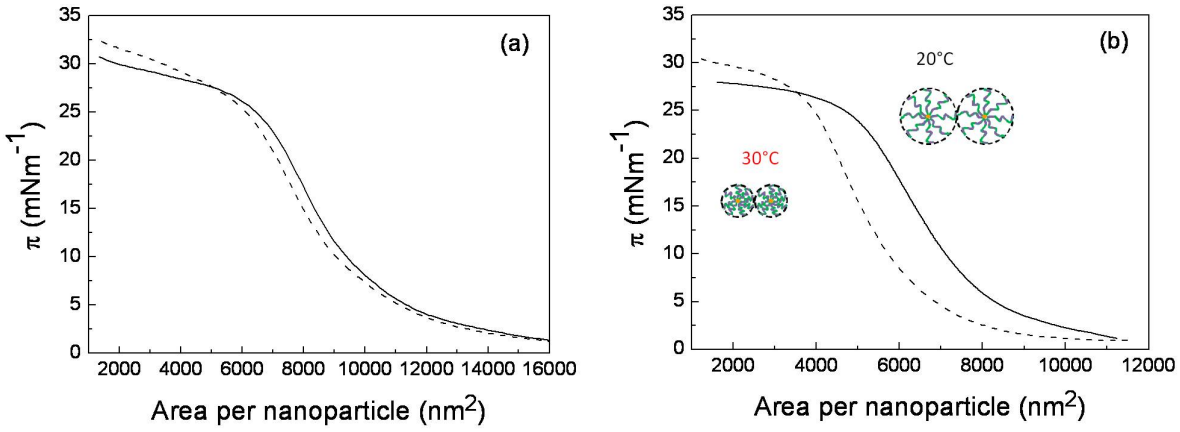

Figure 5.7: Effect of temperature on compression isotherms on: Au-PNIPAM$_{265}$ (solid line: T = 20°C, dashed line: T = 33°C)and (b) Au-PNIPAM$_{270}$-co-PNPAM$_{113}$ (solid line: T = 20°C, dashed line: T = 30°C).

To summarize, nanoparticles grafted with the RAFT-polymers exhibit excellent colloidal stability and amphiphilicity that facilitates their formation of stable Langmuir monolayers. Under moderate compression below the critical surface pressure, it is inferred that the graft polymer chains adopt an extended conformation that tethers the nanoparticles to the interface. In this 2-dimensional monolayer, the nanoparticle cores are isolated by the polymer shell and the limiting interparticle distance is controlled in a predictable manner by the polymer chain length. Furthermore, for the Au-PNIPAM-co-NPAM, the interparticle distance can be modulated by temperature (see Figure 5.8). An increase in temperature up to near-theta condition suffices to decrease the interparticle distance through lateral collapse of the polymer layer. This thermally-induced collapse in 2-D, not detectable for the Au-PNIPAM samples, is an unusual and novel observation that may be attributed to enhanced cooperative effects of the collapse transition of the new copolymer PNIPAM-co-NPAM.

AuNP-Polymer	T (°C)	$A_{p\text{-}pancake}$ (nm^2)	$A_{p\text{-}loop}$ (nm^2)	$d_{pancake}$ (nm)	d_{loop} (nm)
$PNIPAM_{57}$ ($\sigma \approx 1.4$)	20	510	316	25	20
$PNIPAM_{67}$ ($\sigma \approx 1.1$)	20	2312	1235	54	40
$PNIPAM_{118}$ ($\sigma \approx 1.4$)	20	1240	807	40	32
$PNIPAM_{154}$ ($\sigma \approx 1.2$)	20	4076	2358	72	55
	34	3994	2162	71	52
$PNIPAM_{265}$ ($\sigma \approx 2.0$)	20	10793	6482	117	91
	33	10453	6081	115	88
$PNIPAM_{270}$-co-$PNPAM_{113}$ ($\sigma \approx 1.3$)	20	8506	4784	104	78
	30	6710	3698	92	69
$PNIPAM_{261}$-co-$PNPAM_{144}$ ($\sigma \approx 0.6$)	20	1355	776	42	31
	29	1341	762	41	31

Table 5.2: Area/nanoparticle for Au-PNIPAM and Au-PNIPAM-co-NPAM for different chain lengths and temperatures. Ap-pancake and Ap-loop are the limiting nanoparticle areas evaluated from the respective regimes, and $d_{pancake}$ and d_{loop} their corresponding interparticle distances.

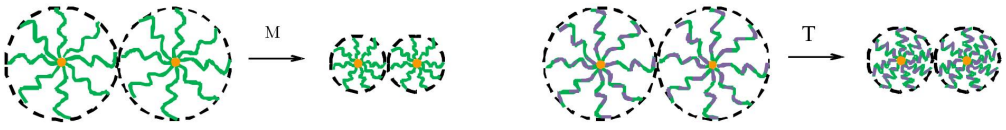

(a) Long and short chain spacers (b) Swollen and collapsed chain spacers

Figure 5.8: Control of interparticle distance d in: (a) Au-PNIPAM monolayer with PNIPAM molecular mass and (b) Au-PNIPAM-co-NPAM monolayer with temperature.

5.2 Structural studies of polymer-protected gold monolayers

At low compression regime, the Langmuir isotherm provides us with a lot of information about the 2-dimensional nanocomposite monolayer behaviour. The surface concentration is low and reflectivity is not sensitive for probing molecular structure. Specular reflectivity is used to characterize interfacial layers perpendicular to the surface (in 3D), thus adapted to studying our surface layer in the high compression regime, that is to say, beyond the pseudo-plateau regime where the surface concentration is high and the graft polymer is assumed to undergo compression-induced conformational transition from 3-D loop-to-brush structure. We employ neutron and X-ray reflectivities to characterize in detail the compression and temperature-induced changes in polymer layer conformation and gold organization, respectively . Neutron and X-ray reflectivities are non-destructive techniques generally used in complementarity to investigate the structural properties of thin films with a depth resolution from less than one nanometer up to several hundred nanometers. They characterize the thickness, chemical composition and roughness of the layer(s) at the surface. Both methods are employed in the specular mode ($\theta_{\text{in}} = \theta_{\text{out}}$) and in a horizontal liquid configuration.

5.2.1 Neutron reflectivity: Polymer conformation

Many optical phenomena observed in classical optics such as reflection, refraction and interference are also observed with slow neutrons [113], [114]. Information on interfacial properties described by a refractive index profile can therefore be extracted from reflectivity measurements. The particularity about neutron is its interaction with the nucleus (instead of electrons as in the case of X-ray). The refractive index is therefore related to the neutron scattering length density, a parameter that describes neutron-matter interaction. The advantage here is the variation of the neutron scattering length from one element to another. Of particular interest to soft-matter science is the large variation both in amplitude and sign between hydrogen and deuterium, making it possible to vary the refractive index of a molecule while keeping the same chemical composition. This distinct advantage makes neutron reflectivity a unique tool to probe light elements in low density molecules such as surfactants, polymers, proteins, and multi-component systems where one component can be contrast-matched to the solvent while the structure of the other component can be measured. Due to this neutron-nucleus interaction, it is appropriate to define a neutron refractive index (for non-magnetic material, neglecting absorption) [115]:

$$n = 1 - \frac{Nb}{2\pi}\lambda^2 \tag{5.1}$$

Nb is the scattering length density given by:

$$Nb = \sum_i b_i n_i \tag{5.2}$$

where b_i is the scattering length and n_i the number density of the atomic species i.

To study the polymer conformation in the polymer-gold composite monolayer, it is possible to contrast-match the gold to the solvent and obtain reflectivity signal from the polymer

only. This gold-core contrast-matched solvent would give a polymer-solvent contrast of ΔNb = Nb_p - Nb_s = (0.90 - 4.50) $\times$ 10^{-6} Å^2 = -3.60 $\times$ 10^{-6}Å^{-2}. For a pure D_2O solvent, the contrast is ΔNb = Nb_p - Nb_s = (0.90 - 6.39) $\times$ 10^{-6} Å^2 = -5.49 $\times$ 10^{-6} Å^{-2}. For the experiments performed here, we have decided to maximize the contrast between the polymer and the solvent to give higher signal. Therefore we have chosen to use pure D_2O as the subphase. Here, although the gold core signal is not masked out, it contributes to a much lesser extent than the polymer due to its lower contrast with the solvent, ΔNb = Nb_{gc} - Nb_s = (4.50 - 6.39) $\times$ 10^{-6} Å^2 = -1.89 x 10^{-6} Å^{-2} compared to -5.49 $\times$ 10^{-6} Å^{-2} for the polymer. In this polymer/D_2O mixture, $Nb_p < Nb_{D_2O}$, the reflectivity of a surface containing a polymer layer is therefore lower than that for pure D_2O.

Neutron reflectivity experiments were carried out on the time-of-flight reflectometer EROS (θ fixed, polychromatic beam) (Laboratoire Léon Brillouin, CEA-Saclay, France). The spectra were acquired on the Langmuir monolayers in a compression trough (Kibron MicroTroughX trough, 208 mm $\times$ 52 mm). The plastic cover of the trough was specially fitted with quartz windows to allow the neutron beam to enter and exit the trough with minimal absorption. Special care was taken to seal the trough to minimize the exchange of water vapor with the deuterated subphase. The grazing incident angle, θ = 1.545° and the angular solution, $\delta\theta \approx 3\%$. The wavelengths range from $\lambda \approx$ 2.5-25 Å, corresponding to wave vector, k = $2\pi/\lambda$ ranging from 0.068 to 0.0068. The nanoparticles were spread from a chloroform dispersion onto the D_2O surface that is pre-cleaned by compression-aspiration process. After about 20 minutes, the monolayer was compressed to the desired surface pressure, and neutron reflectivity spectra were acquired. Several two-hour spectra were acquired and compared, and in all cases, no kinetics effects were observed; all the spectra were then summed for improved statistics. The reflectivity spectra were analyzed using the n-layer model (Refit program, LLB). The theoretical reflectivity curve calculated using a given model was fitted to the experimental curve and the best-fit was determined by χ^2 minimization.

In the next sections, we show an example of each effect; compression, M_w of graft polymer and temperature, on polymer layer conformation. Note that for a given compression area, we define the theoretical amount of particles from the volume of particles deposited (1/area = NPs/nm^2)

5.2.1.1 Compression effect

An example of compression effect is shown in Figure 5.9. This figure shows the neutron reflectivity curves of the Au-$PNIPAM_{270}$-co-$PNPAM_{113}$ monolayer at two surface compressions at 150 mM NaCl and T = 20°C. The curve representing the lower surface compression is best fitted with a two-layer model. In this n-layer model, the scattering length density profile is defined by:

$$Nb(z) = \sum_{0}^{n} \left(\frac{Nb_i - Nb_{i+1}}{2} \right) \left(1 - \mathrm{erf} \frac{z - z_i}{\sigma_i} \right) \tag{5.3}$$

Nb_i is the scattering length density in layer i with corresponding thickness L_i= z_i - z_{i+1}, and σ_i is the interfacial roughness at each layer defined by an error-function. The corresponding volume fraction ϕ_p is defined by:

$$\phi_p = \frac{Nb_{\text{fit}} - Nb_{\text{s}}}{Nb_{\text{p}} - Nb_{\text{s}}} \tag{5.4}$$

and

$$\Gamma_{\text{p}} = \phi_{\text{p}} L \rho_{\text{p}} \tag{5.5}$$

Nb_{fit}, Nb_{s} and Nb_{p} are the scattering length densities of the fitted layer, solvent and polymer respectively. L is the layer thickness and ρ_{p} the polymer density.

The first layer L_1 is polymer-rich and thin so we believe this layer characterizes the adsorbed polymer segments that anchor the nanoparticle to the surface. The second layer L_2 is polymer-poor and thick therefore it consists of the immersed polymer segments with a loop conformation in the subphase. We note that the L_2 thickness is close to the gold core diameter characterized by TEM. We can thus add that the gold core resides in this last layer. The curve representing the higher compression exhibits more signals which indicates an increase in polymer concentration (Γ_{p} increases from 1.65 to 1.95 mg/m^2). This latter curve is now best fitted with a three-layer model. Therefore a change in polymer conformation occurs with compression. L_1 is still polymer-concentrated but its thickness increases slightly due to the lateral contraction of adsorbed polymer. Some polymer segments are also pushed out of L_2 and, as a result, a third layer L_3 is formed. This very low-polymer concentration last layer possesses a significantly larger thickness (it is twice the L_2 layer), so it is thought that the chains in this region adopt a brush-like structure. We notice that with compression, the increase in adsorption density is not very significant. This suggests a loss of material at high compression.

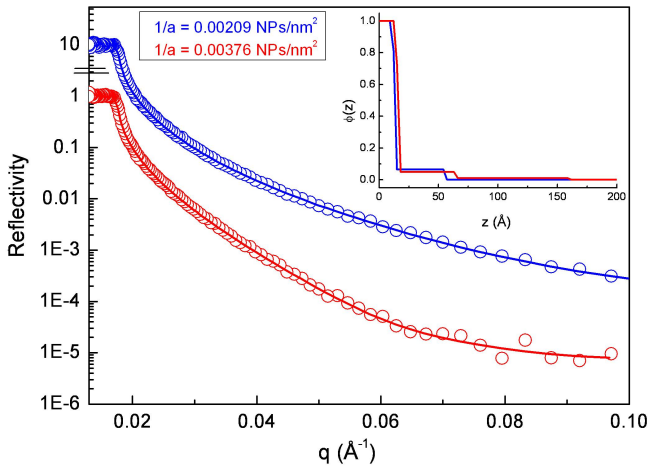

Figure 5.9: Neutron reflectivity curves of Au-PNIPAM$_{270}$-co-PNPAM$_{113}$ monolayer at two different surface compressions (curves are separated vertically for better visualization). The solid lines are theoretical best-fit curves with corresponding polymer concentration profiles shown in the inset.

1/area (NPs/nm^2) (NPs/nm^2)	Layer	Thickness (nm)	Roughness (nm)	ϕ_p	Γ_p (mg/m^2)
0.00209	L_1	1.26	0.78	1	1.35
	L_2	4.32	0.1	0.065	0.3
					Total = 1.65
0.00376	L_1	1.54	0.76	1	1.65
	L_2	4.94	0.1	0.05	0.26
	L_3	9.58	0.1	0.01	0.04
					Total = 1.95

Table 5.3: Neutron reflectivity fit data of Au-PNIPAM$_{270}$-co-PNPAM$_{113}$ monolayer the air-water interface at different surface compressions (150 mM NaCl, T = 20°C).

5.2.1.2 Polymer chain length effect

The chain length effect is better emphasized with the fit data listed in Table 5.4. The reflectivity curves of Au-PNIPAM$_{67}$ and Au-PNIPAM$_{127}$ monolayers are fitted with a three-layer model (the description of this model have already been defined earlier). The respective L_1 and L_2 layers are almost identical. The interesting difference resides in the thickness of L_3. In fact, the particles grafted with the longer PNIPAM$_{127}$ chains possess the larger L_3 layer as expected.

Au-PNIPAM	1/area (NPs/nm^2)	Layer	Thickness (nm)	Roughness (nm)	ϕ_p	Γ_p (mg/m^2)
Au-PNIPAM$_{67}$	0.01347	L_1	1.32	0.74	1	1.41
		L_2	4.62	0.1	0.084	0.39
		L_3	12.68	0.1	0.011	0.15
						Total= 1.95
Au-PNIPAM$_{127}$	0.00524	L_1	1.2	0.46	1	1.28
		L_2	4.7	0.1	0.071	0.36
		L_3	14.56	0.1	0.011	0.17
						Total= 1.81

Table 5.4: Neutron reflectivity fit data of Au-PNIPAM$_{67}$ and Au-PNIPAM$_{127}$ monolayers at the air-water interface (150 mM NaCl, T = 20°C).

5.2.1.3 Temperature effect

Here, the samples are heated to 32°C before compression. Figure 5.10a shows the neutron reflectivity curves of Au-PNIPAM$_{127}$ monolayer at the end of compression at 20 and 32°C. Both experimental curves are ajusted with a three-layer model. Under good solvent condition, L_1 consists of the adsorbed polymer segments and L_2 and L_3 comprise the immersed brush-like polymer segments. When the temperature is raised to near-theta condition, the brush L_3 layer decreases in thickness indicating a measurable degree of chain contraction.

The adsorbed L_1 layer thus increases significantly as a consequence of this L_3 contraction, and possibly also to horizontal contraction. We notice that the polymer concentration is well optimized: Γ_p increases from 1.81 to 3.96 mg/m^2. Thus with decrease in solvent quality, the polymer chains (particles) are more stable. (If the temperature is raised after compression at 20°C, the same increase is registered: particles previously lost in the subphase return to the interface.)

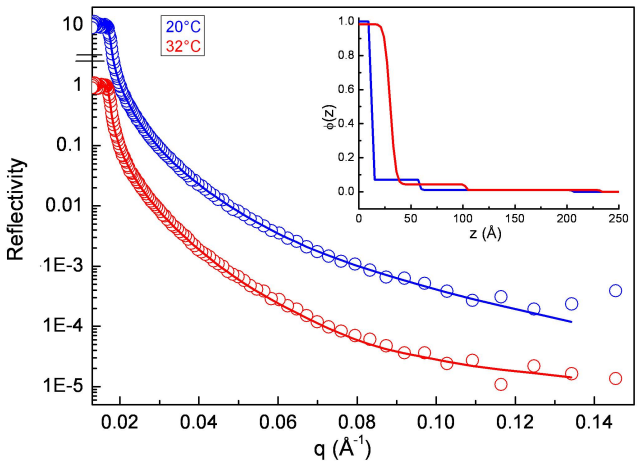

Figure 5.10: Temperature effect on Au-PNIPAM$_{127}$ monolayer: (a) neutron reflectivity curves at 20 (blue) and 32°C (red) (1/area= 0.00524 NPs/nm^2).The solid lines are theoretical best-fit curves with corresponding polymer concentration profiles shown in the inset.

Temperature (°C)	Layer	Thickness (nm)	Roughness (nm)	ϕ_p	Γ_p (mg/Nm^2)
20	L_1	1.2	0.46	1	1.28
	L_2	4.7	0.1	0.071	0.36
	L_3	14.56	0.1	0.011	0.17
					Total= 1.81
32	L_1	3.42	0.1	0.98	3.14
	L_2	8	0.6	0.044	0.34
	L_3	11.46	0.12	0.011	0.15
					Total= 3.96

Table 5.5: Neutron reflectivity fit data of Au-PNIPAM$_{127}$ monolayer at 20 and 32°C (1/area= 0.00524 NPs/nm^2).

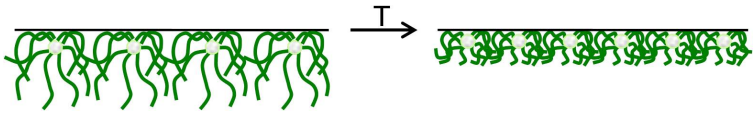

Figure 5.11: Temperature effect on polymer layer conformation revealed by neutron reflectivity.

5.2.2 X-Ray reflectivity: Gold cores organization

Unlike neutron reflectivity, X-ray reflectivity probes the electron density. Thus, in our case, these measurements allow us to study the gold core organization in the monolayer as it has a higher electron density compared to the grafted polymer. The optical index n is given by:

$$n = 1 - \delta = 1 - \frac{\lambda^2}{2\pi}\rho r_e f \tag{5.6}$$

ρ is the atomic number density (m^{-3}), r_e is the classical electron radius $r_e = 2.810\times10^{-5}$ Å, and f is the X-ray scattering length (scattering length density; SLD = $\rho r_e f$).

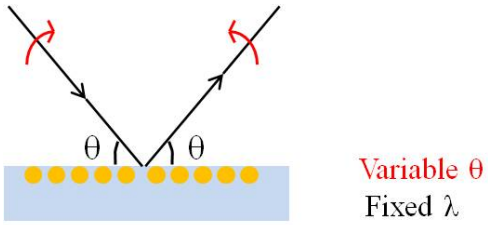

Figure 5.12: Specular X-ray reflectivity

$sld_{gold} > sld_{H_2O}$ (Nb = ρf), therefore the X-ray reflected intensity of a surface containing a layer of gold core is higher than the reflected intensity of pure solvent ($R_{gold\ core}/R_{water} > 1$). X-ray reflectivity experiments were carried out on a reflectometer conceived by J. J. Benattar in collaboration with Microcontrole (U = 40 kV, I = 20 mA, λ fixed; monochromatic beam) at SPEC (Service de Physique de l'Etat Condensé, CEA-Saclay, France). A conventional, fine-focus copper tube was used as an X-ray source. The monochromator was LiF (200) which selected the Cu Kα_1 line (λ = 1.54 Å). A low divergence of the X-ray beam is obtained by placing vertical slits in front of the X-ray source and in front of the detector. The spectra were acquired on the Langmuir monolayers in the same compression trough (Kibron MicroTroughX trough, 208 mm × 52 mm) as for the neutron reflectivity measurements. Instead of the quartz windows, the plastic cover of the trough was fitted with 50 μm mylar films to allow the X-ray beam to enter and exit the trough with minimal absorption. The grazing incident angles range from, $\theta \approx 0.15$ to 3.5°. The nanoparticles were spread from a chloroform dispersion onto the H_2O surface that is pre-cleaned by compression-aspiration process. After about 20 minutes, the monolayer was compressed to the desired surface pressure, and X-ray reflectivity spectra were acquired. The acquisition time was 5 to 60 s

per point, from low to high θ. The data are collected as function of θ (or equivalently Q $=(4\pi/\lambda)\sin\theta$) and then analyzed with a multilayer model using SimulReflec (LLB software) that incorporates several variable fit parameters : thickness, density and roughness of film. From the fit data, the density and the volume fraction profiles can also be calculated and plotted as a function of the depth z. The adequate n-layer model for fitting the experimental data is determined by minimization of χ^2 value. Then we can evaluate the gold core concentration Γ_{gc} from:

$$\Gamma_{gc} = \phi_{gc} L \rho_{Au} \tag{5.7}$$

where L is the layer thickness, ϕ_{gc} the gold core volume fraction and ρ_{Au} the gold density.

Component	f	sld ($\times 10^{-6}$Å^{-2})
Au	75	124.3
NIPAM	63	10.1
H_2O	10	9.4

Table 5.6: X-ray scattering length f and sld values of different components.

5.2.2.1 Compression effect

Figure 5.13a shows the X-ray reflectivity curves of the Au-PNIPAM$_{270}$-co-PNPAM$_{113}$ layer at two surface compressions. The curve representing the lower surface compression is best fitted with a one-layer model. The layer thickness is about the diameter of the gold core evaluated by TEM. The curve representative of the higher surface compression is best adjusted with a with a two-layer model. We notice that the sum of the two layers thickness corresponds to the thickness of the single layer characterized at lower surface compression. This might suggest that the gold particles do not form a bilayer but most likely adopt a staggered conformation in the monolayer. We conclude that when the gold particles are spread at the interface, they self-assemble as a monolayer. Upon compression, the gold cores adopt a staggered organization but are still self-assembled as a monolayer (Figure 5.14). We observe that there is not much change in Γ_{gc}. This insignificant increase is also coherent with the data of neutron reflectivity suggesting particle loss.

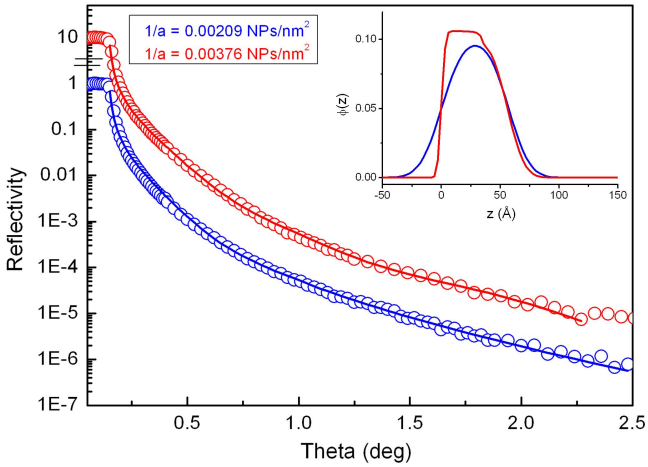

Figure 5.13: X-ray reflectivity curves of Au-PNIPAM$_{270}$-co-PNPAM$_{113}$ monolayer at the air-water interface at two different surface compressions (curves are separated vertically for better visualization)(150 mM NaCl, T = 20°C). The solid lines are theoretical best-fit curves with corresponding gold core concentration profiles shown in the inset.

1/area (NPs/nm^2)	Layer	Thickness (nm)	Roughness (nm)	ϕ_{gc}	Γ_{gc} (mg/m^2)
0.00209	L_1	5.72	0.29	0.1	11
					Total= 11
0.00376	L_1	3.42	0.36	0.106	4.25
	L_2	2.2	0.2	0.1	7.05
					Total= 11.3

Table 5.7: X-ray reflectivity fit data of PNIPAM$_{270}$-co-PNPAM$_{113}$ monolayer at lower compression.

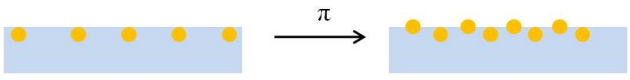

Figure 5.14: Compression effect on gold organization in the monolayer.

5.2.2.2 Temperature effect

Figure 5.15 shows the X-ray reflectivity curves of Au-PNIPAM$_{127}$ monolayer at the end of compression at 20 and 32°C. A noticeable variation in form and intensity (especially at low

θ) is observed between the curves which is suggestive of a change in the gold concentration and organization. However, all curves are adjusted with a two-layer model. At 20°C, the fit data indicate that the gold core are organized as a staggered monolayer (for the same reason cited before for a staggered organization). With elevation of temperature, the gold core are still self-assembled as a staggered monolayer. As the total film thickness increases by 1 nm, it is concluded that the degree of staggering increases. The particles maybe approach a bilayer organization. Additionally, we note that Γ_{gc} significantly increases from 13.33 to 19.74 mg/m^2. This goes in accordance with data of neutron reflectivity indicating increased stability of the surface layer.

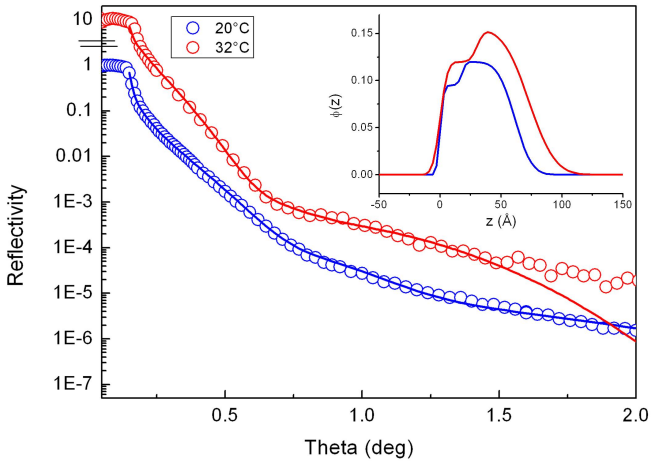

Figure 5.15: X-ray reflectivity curves of Au-PNIPAM$_{127}$ monolayer (curves are separated vertically for better visualization) at 1/area= 0.00524 NPs/nm^2 at 20 (blue) and 32°C (red). The solid lines are theoretical best-fit curves with corresponding gold core concentration profiles shown in the inset.

Temperature °C	Layer	Thickness (nm)	Roughness (nm)	ϕ_p	Γ_{gc} (mg/m^2)
20	L_1	1.79	0.33	0.095	3.28
	L_2	4.33	0.4	0.12	10.05
					Total= 13.33
32	L_1	3.05	0.67	0.12	6.98
	L_2	4.24	0.64	0.156	12.76
					Total= 19.74

Table 5.8: X-ray reflectivity fit data of PNIPAM$_{127}$ monolayer (1/area= 0.00524 NPs/nm^2).

5.3 Stability of surface layer

We gather all the results obtained from neutron (polymer concentration) and X-ray (gold core concentration) reflectivity measurements to calculate the total surface concentration $\Gamma_{\text{Au-Polymer}}$ ($\Gamma_{\text{Au}}=\Gamma_{\text{gc}}+\Gamma_{\text{p}}$) under three experimental conditions: (i)0 mM NaCl at 20°C, (ii) 150 mM NaCl at 20°C and (iii) 150 mM NaCl at 28 or 32°C (depending of the nature of the polymer graft). The percentage of particles that remain at the interface is calculated from the theoretical amount deposited in order to evaluate the thin film stability with hydrophobicity, compression and temperature. Our objective is to identify stable regimes of the gold nanoparticles monolayer for the study of their optical properties at the interface.

5.3.1 PNIPAM-protected gold nanoparticles monolayer

In Figure 5.16a, we compare the experimental surface concentrations of the Au-PNIPAM$_{127}$ monolayer at different surface compressions with the initial amount of particles deposited. For all experimental conditions, we observe an increase in surface concentration with compression. However, it is clear that the monolayer concentration progressively differs from the theoretical concentration which suggests a loss of stability with compression. When we spread the particles on a water surface at 20°C and compress the resulting monolayer to the first high compression, it is estimated that 69% of particles deposited form the monolayer. At this stage, we can say the film has a reasonable concentration. When the monolayer is further compressed, the percentage of particles remaining at the interface falls drastically to 35.5% until reaching the low value of 17% at the end of compression. This monolayer instability upon compression is mainly due to two reasons: (i) the amphiphilic character of the polymer chains makes the soluble segments desorbing from the interface and (ii) the negative charges present at the end of the polymer chains makes the nanoparticles electrostatically repulse each other. By screening the negative charges with addition of salt, the gold monolayer concentration is noticeably improved at the equivalent surface compressions (88, 47 and 23% of the deposited particles formed the monolayer at specific surface area).

When the temperature is increased to near-T_c condition, the polymer becomes less soluble and more surface-active. A the first compression, the monolayer is estimated to be composed of 100% of particles initially spread. It is evident that we managed to further optimize the monolayer stability as no particles are lost during compression. At the end of compression, the monolayer concentration is more than doubled compared to 20°C (from 17 to 37.5%). Thus by increasing the monolayer stability by addition of NaCl and by temperature, the interparticle distance (d) can be better manipulated, as shown in Figure 5.16b - that is to say, better control is achieved by improvement of the monolayer stability rather than by change in polymer conformation. For example, at T = 20°C, with addition of 150 mM NaCl, the interparticle distance at the end of compression decreases from 20 nm to 16 nm. In this case, no measurable change in polymer conformation was registered at this high end of compression. The increase in monolayer stability due to screening of the charged RAFT end-group enhances surface activity and thus enables a more compact layer to be formed, resulting in a gain in interparticle approach of 3.4 nm. The same remark can be made for the monolayer at high temperature: at the end of compression at T = 32°C, the interparticle distance is 13.6 nm, 3 nm lower compared to 20°C. But since the particle concentration is

also much higher, the decrease in interparticle distance cannot be attributed only to thermal contraction of the polymer layer - stability is key to this control in distance.

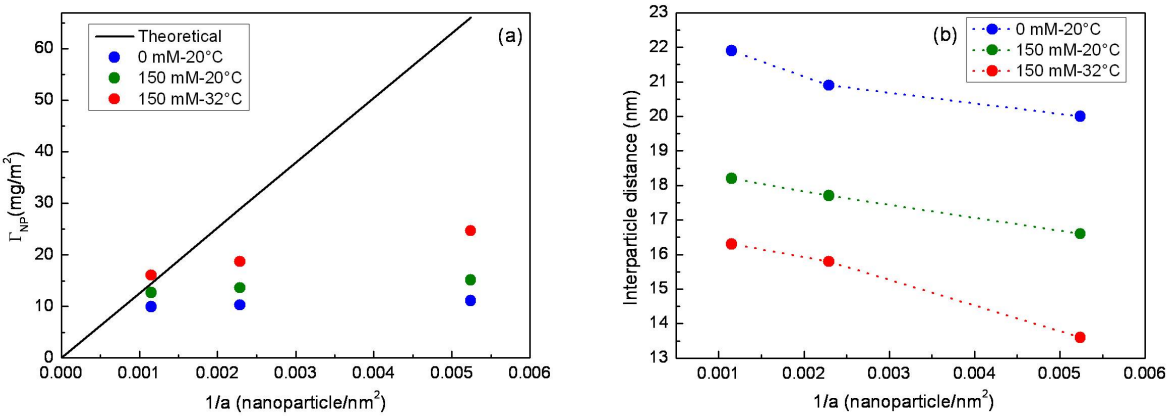

Figure 5.16: Comparison of the Au-PNIPAM$_{127}$: (a) surface density (gold core + grafted polymer layer) evaluated from X-ray and neutron reflectivities (coloured symbols) with the amount deposited (solid lines) and (b) the interparticle distance.

Temperature (°C)	[NaCl] (mM)	1/area (NPs/nm^2)	Γ_{NP} (mg/m^2)	$\Gamma_{theoretical}$ (mg/m^2)	%NPs (%)	d (nm)
20	0	0.00115	9.98	14.47	69	21.9
		0.00229	10.29	28.95	35.5	20.9
		0.00524	11.14	66.1	17	20
20	150	0.00115	12.72	14.47	88	18.2
		0.00229	13.6	28.95	47	17.7
		0.00524	15.14	66.1	23	16.6
32	150	0.00115	16	14.47	>100	16.3
		0.00229	18.7	28.95	64.6	15.8
		0.00524	24.68	66.1	37.5	13.6

Table 5.9: Characteristics of the Au-PNIPAM$_{127}$ monolayer at varying experimental conditions: (i)0 mM, T = 20°C; (ii) 150 mM NaCl, 20°C; (iii) 150 mM NaCl, 32°C. (D = 8.0 nm). 1/area and $\Gamma_{theoretical}$ are theoretical values; Γ_{NP}, $\%NPs$ and d (interparticle distance) are experimental values.

The influence of the polymer molecular mass on nanoparticle monolayer stability can be observed at T = 20°C. In fact, at each compression area, the particle concentration in monolayer formed by Au-PNIPAM$_{67}$ is a little higher than that formed by Au-PNIPAM$_{127}$, with an overall interparticle distance that is about 2 to 2.7 nm lower. This reduction might be attributed to the lower footprint of the Au-PNIPAM$_{67}$.

Au-PNIPAM	[NaCl] (mM)	1/area (NPs/nm^2)	Γ_{NP} (mg/m^2)	$\Gamma_{theoretical}$ (mg/m^2)	%NPs (%)	d (nm)
Au-PNIPAM$_{67}$	150	0.0033	15.59	16.17	96.4	16.2
		0.00659	18.19	32.34	56.2	15
		0.01347	20.92	66.1	31.6	13.9
Au-PNIPAM$_{127}$	150	0.00115	12.72	14.47	88	18.2
		0.00229	13.6	28.95	47	17.7
		0.00524	15.14	66.1	23	16.6

Table 5.10: Characterisctics of the Au-PNIPAM$_{67}$ and Au-PNIPAM$_{127}$ monolayers at 20°C (150 mM NaCl, T = 20°C;D = 5.3 and 8.0 nm, respectively). 1/area and $\Gamma_{theoretical}$ are theoretical values; Γ_{NP}, $\%NPs$ and d are experimental values.

5.3.2 PNIPAM-co-NPAM-protected gold nanoparticles monolayer

We can attempt to further optimize gold nanoparticle monolayer stability using particles coated with the more hydrophobic copolymer PNIPAM-co-NPAM. As mentioned earlier, this copolymer exhibits a lower collapse temperature and also appears to possess a higher degree of cooperativity in the collapse process compared to PNIPAM homopolymer. Therefore, we can also expect to increase its monolayer stability at lower temperature. Figure 5.17a shows the surface concentrations versus compression for Au-PNIPAM$_{270}$-co-NPAM$_{113}$. Improved stability can already be seen at T = 20°C from the higher amount of particles that remains in the surface layer at first compression (96%). At the end of compression, this value falls to 38% (compared to 17% for Au-PNIPAM$_{127}$). When temperature is raised to T = 28°C, the monolayer stability can be seen to be significantly improved. Here, we note that for the second compression, 91.5% of the particles remains at the surface. Thus, the rate of displacement of the copolymer-coated nanoparticles is also reduced. The corresponding interparticle distances decrease from 13.8 nm to 12.6 nm at 20°C and from 12 nm to 10.2 nm at 28°C. Thus, as expected, a lower temperature is required to change the solvent quality for the copolymer and to enhance its surface activity.

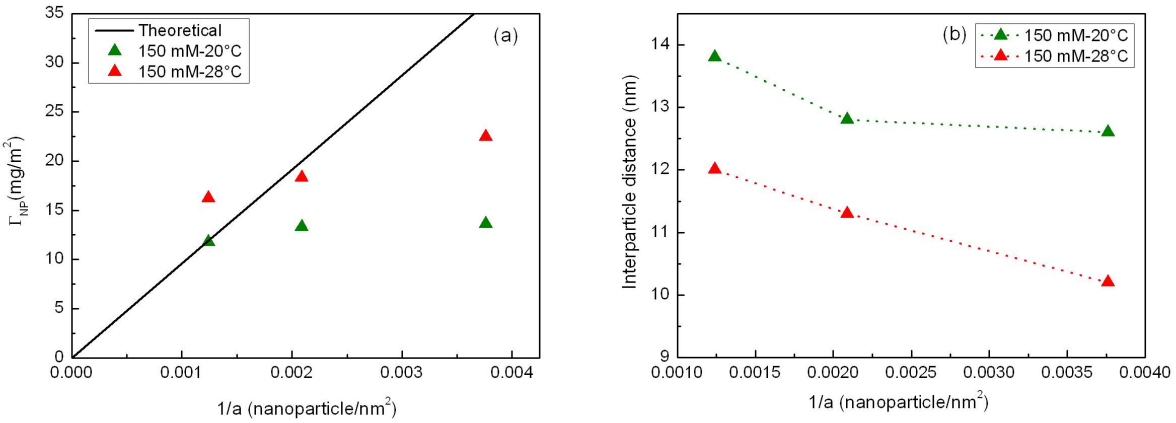

Figure 5.17: Comparison of the Au-PNIPAM$_{270}$-co-NPAM$_{113}$: (a) surface density (gold core + grafted polymer layer) evaluated from X-ray and neutron reflectivities (coloured symbols) with the amount deposited (solid lines) and (b) the interparticle distance.

Figure 5.18 compares the interparticle distances for Au-PNIPAM$_{67}$, Au-PNIPAM$_{127}$ and Au-PNIPAM$_{270}$-co-NPAM$_{113}$. At T = 20°C, for the PNIPAM-coated particles, a possible effect of the smaller footprint of Au-PNIPAM $_{67}$ and the consequent higher compressibility of the monolayer can be noticed. The significantly lower distances obtained for Au-PNIPAM$_{270}$-co-NPAM$_{113}$ compared to the Au-PNIPAM particles are also very clearly shown in both good solvent and in near-theta solvent conditions. All these samples have different gold-core sizes, therefore in order to compare the degree of closeness of the particles, the interparticle distance d is normalized to their gold-core diameter D. The plot of this normalized distance d/D versus compression is shown in Figure 8.22. Surprisingly, we find that at T = 20°C,

the normalized distances for all three samples tend towards d/D ≈ 2.1 - 2.2. The gold-cores therefore do not touch each other but are separated but the protective polymer shell, the lateral thickness of which does not appear to depend on the molecular chain length. This latter observation is reasonable, considering the relatively high polymer concentration in this interfacial zone at maximal compression. At T = 28°C - 32°C (depending on sample), the degree of particle proximity tends towards d/D ≈ 1.7, thus a small but convincing reduction (Table 5.12)

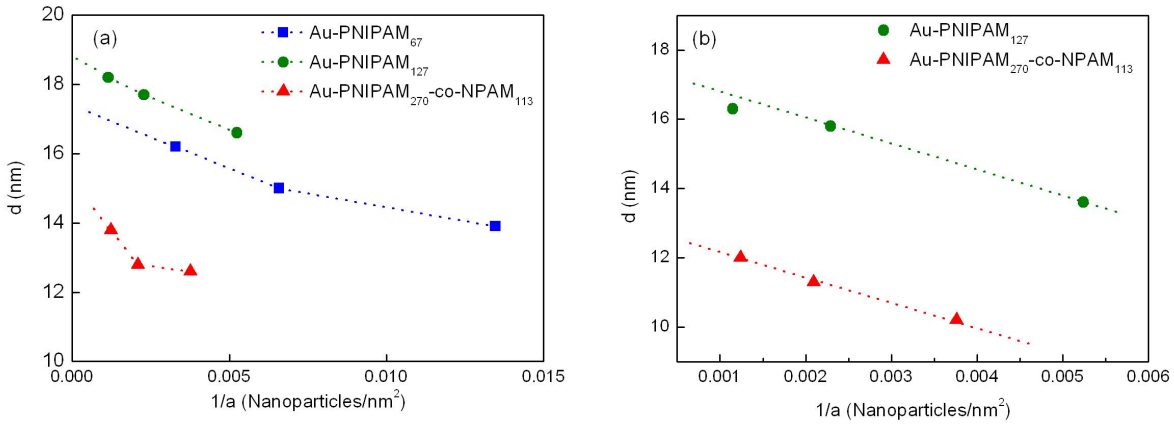

Figure 5.18: Interparticle distances of Au-polymer nanoparticles versus compression at: (a) T = 20°C, and (b) T = 32°C (for Au-PNIPAM$_{127}$) and T = 28°C (for Au-PNIPAM$_{270}$-co-NPAM$_{113}$).

Temperature (°C)	[NaCl] (mM)	1/area (NPs/nm^2)	Γ_{NP} (mg/m^2)	$\Gamma_{theoretical}$ (mg/m^2)	%NPs (%)	d (nm)
20	150	0.00124	11.47	11.93	96	13.8
		0.00209	13.3	20	66.5	12.8
		0.00376	13.62	36	38	12.6
28	150	0.00124	16	11.93	>100	12
		0.00209	18.3	20	91.5	11.3
		0.00376	22.46	36	62.5	10.2

Table 5.11: Characteristics of the Au-PNIPAM$_{270}$-co-NPAM$_{113}$ monolayer (150 mM NaCl, T = 20 and 28°C - D = 5.3 nm). 1/area and $\Gamma_{theoretical}$ are theoretical values - Γ_{NP}, $\%NPs$ and d are experimental values.

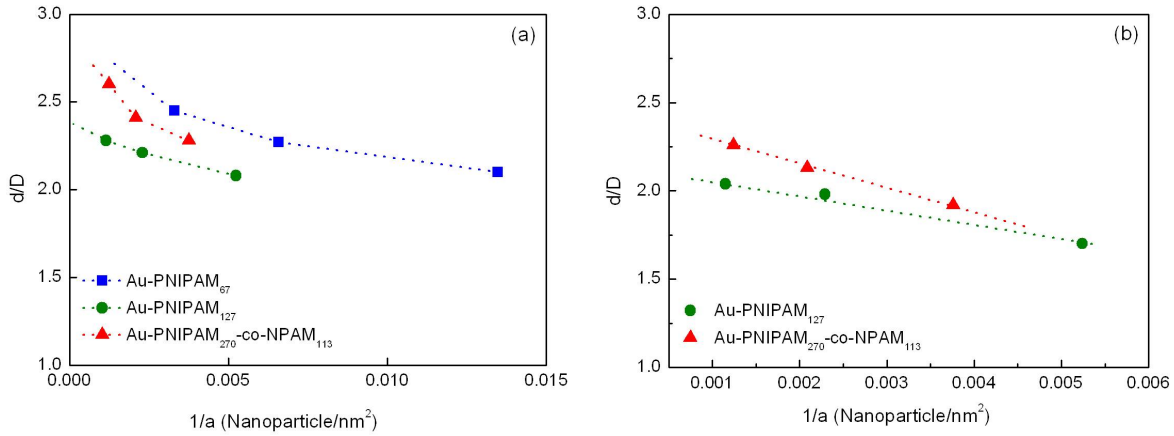

Figure 5.19: Normalized interparticle distances of Au-polymer nanoparticles versus compression at: (a) T = 20°C, and (b) T = 32°C (for Au-PNIPAM$_{127}$) and T = 28°C (for Au-PNIPAM$_{270}$-co-NPAM$_{113}$).

Au-Polymer	T (°C)	d (nm)	d/D
Au-PNIPAM$_{67}$	20	16.2	2.45
		15.0	2.27
		13.9	2.1
Au-PNIPAM$_{127}$	20	18.2	2.28
		17.7	2.21
		16.6	2.08
	32	16.3	2.04
		15.8	1.98
		13.6	1.70
Au-PNIPAM$_{270}$-co-NPAM$_{113}$	20	13.8	2.6
		12.8	2.41
		12.6	2.38
	28	12.0	2.26
		11.3	2.13
		10.2	1.92

Table 5.12: Interparticle distances and normalized interparticle distances of Au-PNIPAM$_{67}$, Au-PNIPAM$_{127}$ and Au-PNIPAM$_{270}$-co-NPAM$_{113}$ at varying temperatures.

We have established that increasing the coating shell hydrophobicity enables us to form more dense monolayers that are stable upon compression. We then wish to further optimize the thin film stability in order to build multilayers, by spreading even more hydrophobic gold nanoparticle: Au-PS-PNIPAM.

5.4 Effect of Polystyrene (PS)

A third type of thermosensitive gold nanoparticles was provided to us by Shan: Au-PNIPAM-PS. These particles are the most hydrophobic as, in addition in being grafted with the usual amphiphilic PNIPAM polymer, they are also grafted with the water-insoluble polystyrene (PS). So when they are spread on an aqueous subphase, they can form even more stable film as the totally hydrophobic PS chains serve as a more efficient buoy to anchor the particles to the interface. We have at our disposition two samples of this type: Au-PNIPAM$_{24}$-PS$_{28}$ ($D \approx 3$ nm) and Au-PNIPAM$_{118}$-PS$_{28}$ ($D \approx 2.3$ nm). The first one is grafted with a short PNIPAM chain and therefore is thought to have more stability at the interface. The second one is protected with a longer PNIPAM chain that is almost the same length as the PNIPAM polymer that stabilizes our Au-PNIPAM$_{127}$ particles. Thus we will be able to make comparisons between the two latter samples in order to better emphasize the PS effect on the gold particles interfacial properties.

5.4.1 Au-PNIPAM$_{24}$-PS$_{28}$

We deposit Au-PNIPAM$_{24}$-PS$_{28}$ particles on a D_2O subphase at 20°C. Figure 5.20a represents the neutron reflectivity curves of the Au-PNIPAM$_{24}$-PS$_{28}$ thin film at different surface compressions. First, we notice that the curves representing the lower surface compression already shows higher signal than the reflectivity curves for the Au-PNIPAM and Au-PNIPAM-co-NPAM monolayers which suggests a larger amount of polymer at the interface. The curve is best adjusted with a single-layer model. We can therefore assume that all the short PNIPAM chains are adsorbed at the interface. Furthermore, the dense polymer layer thickness is more than three times compared to the L_1 region of PNIPAM and PNIPAM-co-NPAM layers, which leads us to think that it comprises both the PNIPAM and the PS chains. Therefore we cannot distinguish between the PS and PNIPAM signals. With surface compression, a clear change in the reflectivity curve occurs and the signal is much intensified. The curve is now fitted with a two-layer model. L_1 keeps about the same thickness but decreases in density suggesting some displacement of PNIPAM chains from L_1 to form L_2 (Figure 5.20b). We also note a relatively high thickness of L_2, surprising for the short PNIPAM$_{24}$ chains. Furthermore, this thickness is of same order as the gold core diameter characterized by TEM so we can add that the gold core may reside in this same layer. It is interesting to note that the polymer volume fraction is high compared to the volume fraction calculated for a usual second layer in the case of the Au-PNIPAM and Au-PNIPAM-co-NPAM particles. Later, the X-ray study will reveal that at high compression, the Au-PNIPAM$_{24}$-PS$_{28}$ particles form a bilayer. This explains the important concentration in this second polymer layer. The polymer concentration Γ_p increases from 3.48 to 4.66 mg/nm^2 with compression.

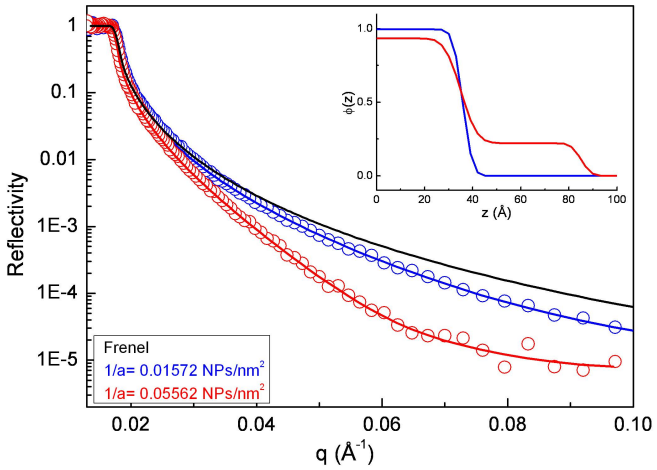

Figure 5.20: Neutron reflectivity curves of Au-PNIPAM$_{24}$-PS$_{28}$ thin film at two different surface compressions (D_2O, T = 20°C).The solid lines are theoretical best-fit curves with corresponding polymer concentration profiles shown in the inset.

1/area (NPs/nm^2)	Layer	Thickness (nm)	Roughness (nm)	ϕ_p	Γ_p (mg/nm^2)
0.01572	L_1	3.58	0.12	0.996	3.82
					Total= 3.82
0.05562	L_1	3.5	0.18	0.93	3.48
	L_2	5	0.74	0.22	1.18
					Total= 4.66

Table 5.13: Neutron data fit of Au-PNIPAM$_{24}$-PS$_{28}$ surface layer at different surface compressions (0 NaCl, T = 20°C) - $D \approx 3$ nm).

Figure 5.21 shows the X-ray reflectivity curves of the Au-PNIPAM$_{24}$-PS$_{28}$ monolayer at different surface compressions. We can distinguish a clear difference in the curves pattern with compression. At lower compression, the experimental data are fitted with a two-layer model. In that case again, we conclude that the gold core adopt a staggered conformation in a single layer as the sum of the two layers is approximatively the same as the gold core diameter. The gold core concentration profile is shown in Figure 5.21, inset. At higher compression, the experimental curve is also adjusted with a two-layer model. However, this time, each layer thickness is approximatively equal to the gold core diameter (the total film thickness is twice the gold core diameter) and each has a significant surface concentration (12.67 and 10 mg/m^2). This indicated that the gold cores are self-assembled as a bilayer. It further provides strong evidence that, even in absence of NaCl and in good solvent condition

for PNIPAM, PS confers such interfacial stability to the particles that they form a multilayer with compression with little loss of material from surface.

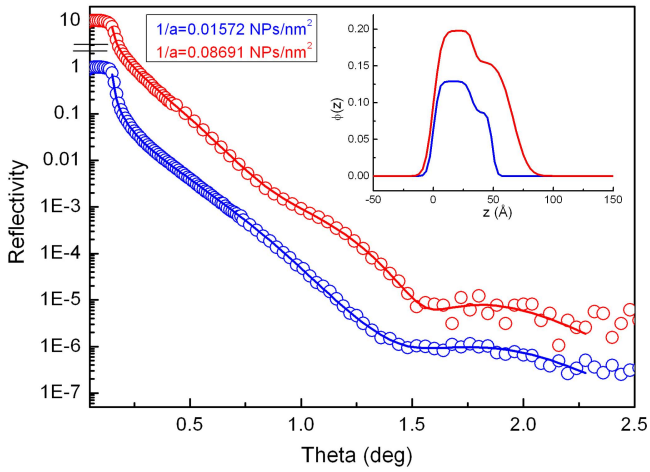

Figure 5.21: X-ray reflectivity curves of Au-PNIPAM$_{24}$-PS$_{28}$ surface layer at two different surface compressions (curves are separated vertically for better visualization) (H_2O, T = 20°C). The solid lines are theoretical best-fit curves with corresponding gold core concentration profiles shown in the inset.

1/area (NPs/nm^2)	Layer	Thickness (nm)	Roughness (nm)	ϕ_{gc}	Γ_{gc} (mg/m^2)
0.01572	L_1	3.14	0.52	0.129	7.8
	L_2	1.75	0.51	0.0864	2.92
					Total= 10.72
0.08691	L_1	3.31	0.77	0.198	12.67
	L_2	3.33	0.44	0.156	10.02
					Total= 22.69

Table 5.14: X-ray data fit of Au-PNIPAM$_{24}$-PS$_{28}$ surface layer (0 NaCl, T = 20°C); $D \approx 3$ nm).

5.4.2 Au-PNIPAM$_{118}$-PS$_{28}$

These particles are deposited on 150 mM NaCl subphase in order to make comparison with Au-PNIPAM$_{127}$. Since in both cases the PNIPAM chain length is about the same, the effect of PS can directly be seen. Figure 5.22 represents the reflectivity curves of the Au-PNIPAM$_{118}$-PS$_{28}$ surface layer at different surface compressions. Both curves are fitted with a two-layer model. We observe with much interest that even at lower compression the

particles are already forming a bilayer. In fact, both layer thickness are approximatively equivalent to the gold core diameter. The film consist of a layer of 2.25 nm and a layer of 2.75 nm, both with slightly different surface concentration (3.9 and 4.9 mg/m^2)(see Figure 5.22, inset). At higher compression, the gold core are still self-assembled as a bilayer. Each layer keeps almost the same thickness (3.08 and 2.15 nm) only the surface concentration increases from 8.8 to 9.7 mg/m^2 with compression. These results clearly demonstrate the stability brought by the presence of PS. In contrast, the Au-PNIPAM$_{127}$ particles always form monolayer due to particle loss during compression. With addition of PS polymers, the particles are better anchored at the interface and self-assemble as a bilayer with compression.

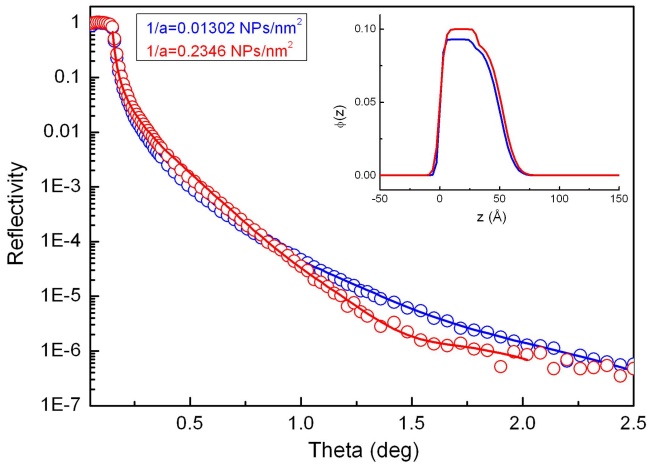

Figure 5.22: X-ray reflectivity curves of Au-PNIPAM$_{118}$-PS$_{28}$ thin film at two different surface compressions (150 mM NaCl, T = 20°C); the solid lines are theoretical best-fit curves with corresponding gold core concentration profiles shown in the inset.

1/area (NPs/nm^2)	Layer	Thickness (nm)	Roughness (nm)	ϕ_{gc}	Γ_{gc} (mg/m^2)
0.01302	L_1	2.75	0.32	0.093	4.947
	L_2	2.25	0.2	0.088	3.86
					Total= 8.8
0.02346	L_1	3.08	0.48	0.1	5.94
	L_2	2.15	0.2	0.09	3.73
					Total= 9.67

Table 5.15: X-ray data fit of Au-PNIPAM$_{118}$-PS$_{28}$ at different surface compressions (150 mM NaCl, T = 20°C, $D \approx 2.3$ nm).

We then decided to render the Au-PNIPAM$_{118}$-PS$_{28}$ particles even more hydrophobic

by elevating the temperature to near the PNIPAM T_c. In Figure 5.23a, we plot the X-ray reflectivity curves of the Au-PNIPAM$_{118}$-PS$_{28}$ film at 20 and 32°C . At 32°C, the curve presents oscillations which indicates thick and well-defined film. The x-ray relectivity curve is now more complicated to fit; a four-to-five-layer model is required. At elevated temperature, the difference in the Au-PNIPAM$_{127}$ and Au-PNIPAM$_{118}$-PS$_{28}$ particle organization in the thin film (as a monolyer and a multilayer, respectively) is clearly observable in the pattern of their respective relectivity curves in Figure 5.23b. Finally, we show the X-ray reflectivity curves of Au-PNIPAM$_{118}$-PS$_{28}$ with compression (Figure 5.24). These curves show very clear Kiessig fringes, indicating dense, well-defined multilayers formed by the gold cores.

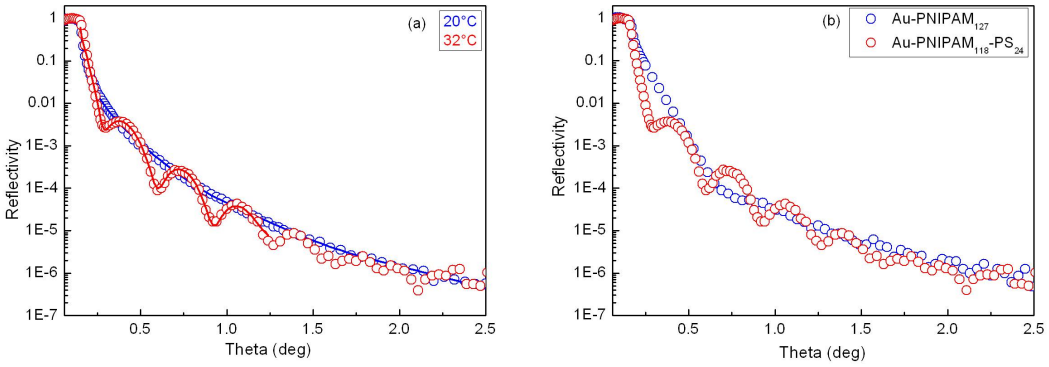

Figure 5.23: X-ray reflectivity curves of: (a) Au-PNIPAM$_{118}$-PS$_{28}$ thin film at 20°C (blue) and 32°C (red); the solid lines are theoretical best-fit curves and (b) Au-PNIPAM$_{127}$ monolayer and Au-PNIPAM$_{118}$-PS$_{28}$ multilayer at 32°C (150 mM NaCl).

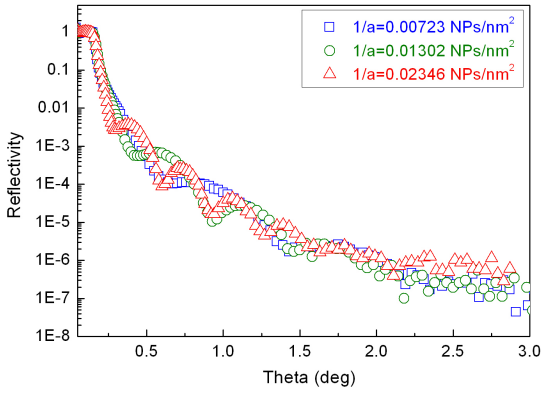

Figure 5.24: X-ray reflectivity curves of Au-PNIPAM$_{118}$-PS$_{28}$ surface layers at 32°C (150 mM NaCl): compression effects.

5.4.3 Stability

(i) Au-PNIPAM$_{24}$-PS$_{28}$

At lower compression, 89% of Au-PNIPAM$_{24}$-PS$_{28}$ form the surface film. Under non-optimal condition for surface stability of the PNIPAM chains (T = 20°C, 0 NaCl), stability is greatly improved by the non-soluble PS chains. With compression, some loss nevertheless takes place (Figure 5.25a), until at the highest compression, a bilayer structure is obtained. The thin film instability is mostly due to the PNIPAM polymer interfacial behavior. To improve the mulilayer stabilty, it is then necessary to improve the PNIPAM graft stability at the interface. Finally, at the monolayer regime, the interparticle distance is manipulated to lower distances (Figure 5.25b) and varies slowly from 9.4 to 8.88 nm.

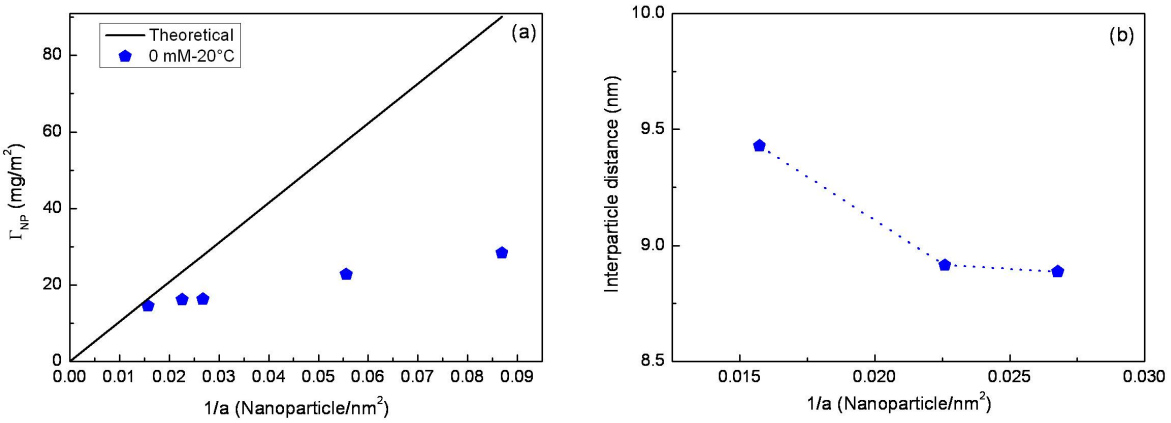

Figure 5.25: Comparison of the Au-PNIPAM$_{24}$-PS$_{28}$ thin film: (a) surface density (gold core + grafted polymer layer) evaluated from X-ray and neutron reflectivities (coloured symbols) with the amount deposited (solid lines) and (b) the interparticle distance (only for the monolayer regime) (T = 20°C, 0 NaCl).

Temperature (°C)	[NaCl] (mM)	1/area (NPs/nm^2)	Γ_{NP} (mg/m^2)	$\Gamma_{theoretical}$ (mg/m^2)	%NPs (%)	d (nm)
20	0	0.01572	14.54	16.4	89	9.4
		0.0226	16.22	23.44	69.2	8.9
		0.02678	16.3	27.78	58.7	8.8
		0.05562	22.78	57.7	39.5	
		0.08691	28.36	90.16	31.5	

Table 5.16: Characteristics of the Au-PNIPAM$_{24}$-PS$_{28}$ surface film (T = 20°C, 0 NaCl).

(ii) Au-PNIPAM$_{118}$-PS$_{28}$

We have seen the effect of PS on the monolayer stability. This Au-PNIPAM$_{118}$-PS$_{28}$ sample allows us to make a more direct comparison with Au-PNIPAM$_{127}$ by keeping the PNIPAM molecular mass constant. Figure 5.26a shows the experimental surface concentrations of the Au-PNIPAM$_{118}$-PS$_{28}$ film at different compressions and the theoretical surface concentrations calculated from the initial amount of particles deposited. For each compression, the surface concentration is noticeably optimized at 20 and 32°C. At 20°C, we again invoke the particles instability upon compression due to the presence of PNIPAM (since the ratio of PNIPAM to PS chainlength is over 4). At 32°C, the PNIPAM interfacial stability is increased and the particles gain even more stability as 100% of them are still at the interface. Furthermore, at the end of compression, only 11% of them are lost (may be due to steric reason or limited multilayer compressability, aggregate going into bulk phase) (Figure 5.26). Here, the PS effect is confirmed: we can build dense and stable multilayer film. We emphasised the fact that, to achieve this structure, both PS and PNIPAM graft interfacial behavior are important for the thin film stability. Figure 5.27 compares the surface layer stability (% NPs left at surface) for Au-PNIPAM$_{127}$ and Au-PNIPAM$_{118}$-PS$_{28}$ samples.

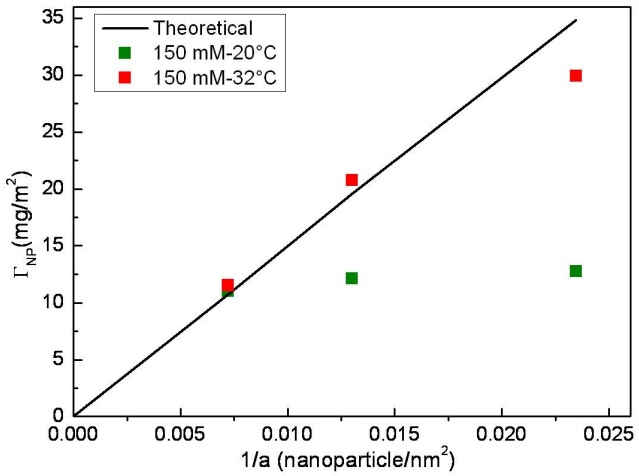

Figure 5.26: Comparison of the Au-PNIPAM$_{118}$-PS$_{28}$ multilayer surface density (gold core + grafted polymer layer) evaluated from X-ray and neutron reflectivities (coloured symbols) with the amount deposited (solid lines).

Temperature (°C)	[NaCl] (mM)	1/area (NPs/nm^2)	Γ_{NP} (mg/m^2)	$\Gamma_{theoretical}$ (mg/nm^2)	%NPs (%)
20	150	0.00723	11	10.74	>100
		0.01302	12.1	19.6	62
		0.02346	12.75	34.86	36.5
32	150	0.00723	11.5	10.74	>100
		0.01302	20.77	19.6	>100
		0.02346	29.9	34.86	86

Table 5.17: Characteristics of the Au-PNIPAM$_{118}$-PS$_{28}$ multilayer (150 mM naCl, $D \approx 2.3$ nm).

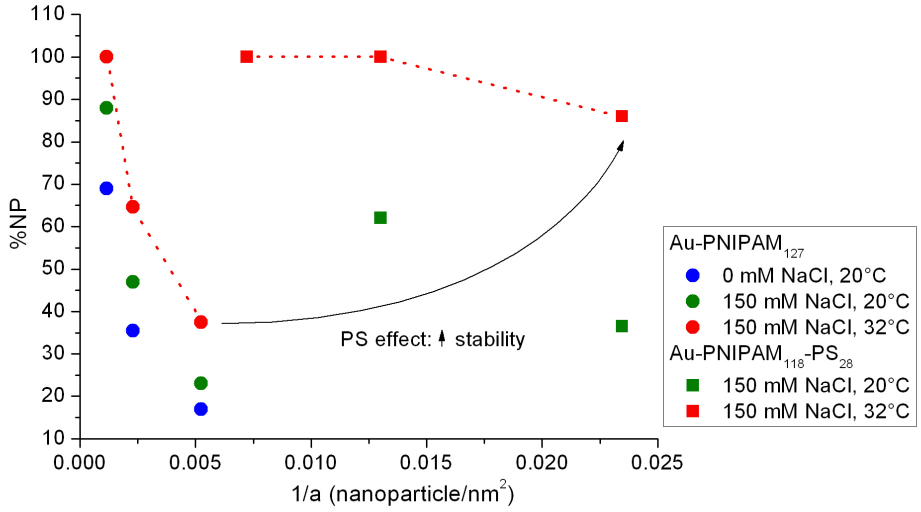

Figure 5.27: Effect of the PS polymer on the thin film stability.

5.5 Summary

Using a combination of the Langmuir balance and reflectivity techniques, we have explored and characterized the surface properties (water-air interface) of amphiphilic and thermosensitive gold nanoparticles. These two techniques allowed us to characterize their structural properties over the entire range of the compression isotherm. Gold nanoparticles coated with a large range of polymer chain length and hydrophobicities have been studied (Au-PNIPAM and Au-PNIPAM-co-NPAM).

By very careful and meticulous experimental practice, the two-dimensional structures of the interfacial particles have been evaluated from the isotherms. In this pancake region, we find the gold cores to be isolated by the (2-dimensional) polymer shell, with limiting interparticle distance that varies predictably with polymer chain length. A novel observation of 2-dimensional polymer collapse is also evidenced at near-theta condition for the new copolymer that we synthesized.

At high compression, we were interested in assessing how far the surface layer can be compressed. The aim here is to optimize the interfacial layer concentration and stability and to manipulate interparticle distance, for eventual optical studies. In this high compression regime, the use of complementary neutron and X-ray reflectivities was essential in obtaining a comprehensive picture. Indeed, the monolayers, although stable at low compression, lose stability at high compression through loss in the bulk phase. We show that the monolayer stability can be improved by addition of NaCl to screen out charge end-groups, increased hydrophobicity of the polymer chain and by temperature. Furthermore, temperature-enhancement of hydrophobic nature and surface-activity can be effected at a lower temperature for the new copolymer. Interestingly, we find that at maximal compression, the degree of proximity of the nanoparticles, expressed as the normalized interparticle distance, tends towards a common value irrespective of polymer chain length: $d/D \approx 2.1$-2.2 in good solvent and 1.7 in near-theta solvent. Core-core contact ($d/D = 1$) is not reached and the particles are therefore still well protected by the polymer shell. For all these particles coated with soluble amphiphilic polymers therefore, we always have a monolayer structure.

Finally, a third type of amphiphilic particles containing a fraction of non-soluble chains has also been investigated (Au-PNIPAM-PS). Due to the insoluble PS, the nanoparticles are anchored to the surface more efficiently. As a result, bilayer structures are formed at high compression. Very interestingly, by further enhancing the surface stability of the PNIPAM component, displacement of particles from the surface is minimized. In this case, we succeeded in building dense and well-defined multilayers.

Chapter 6

Polymer-protected gold nanoparticles interfacial optical properties

In this chapter, we study the optical properties of the polymer-protected gold nanoparticles interfacial layers. At low compression regime, we could not record any optical signals by transmission measurements because the surface layers are not sufficiently concentrated. We thus work at high compression regime. We wish to study the optical properties of concentrated surface layers, the structure of which have already been characterized and described in the previous section. Our aim is to understand and control the surface layer SPR by compression and temperature. Here, two aspects are to be considered: (i) when the particles are sufficiently close to each other for a strong interparticle coupling to occur ($d/D = 1$), a red-shift is usually expected and (ii) change in the interparticle distance in polymeric system is usually also accompanied by polymer conformational changes that can also lead to change in surrounding medium dielectric constant leading to possible SPR shift. The optical measurements were carried out at SPEC (Service de Physique de l'Etat Condensé, CEA-Saclay, France) using the set-up of G.Zalczer. Spectra aquisitions were performed on monolayers spread on the Langmuir trough. The bottom of the trough is fitted with a glass window in the middle and the trough is mounted on an antivibration table. Light from a halogen bulb transmitted through a 600 μm core silica fiber and made parrallel by a convergent lens directed from the bottom of the cell across the aqueous interphase at normal incidence. It is focused on another fiber above the sample surface and delivered to a multichannel spectrometer (Ocean Optics). Absorption is evaluated from 1-I/I_0 where I_0 and I are the intensities of transmitted light in pure water or NaCl solution and in the presence of a monolayer, respectively.

6.1 Polymer-protected gold nanoparticles monolayer

At 20°C, Au-PNIPAM$_{127}$ interfacial layer formed in absence of NaCl does not exihibit surface plasmon resonance (we make the same observation for all the polymer-protected gold nanoparticles interfacial layers). In absence of salt, the particle loss upon compression is significant so that we end up with low concentration of particles in the monolayer at the end of compression (17% of deposited particles). In the presence of NaCl, the particle con-

centration in the monolayer under equivalent degree of surface compression is increased and we observe a SPR peak at about 517 nm (Figure 8.25). Interestingly, we note that the absorption peak is shifted to lower wavelength compared to the absorption peak recorded in the bulk solution (525 nm). To explain this blue-shift, which is also observed under other conditions, we invoke the substrate effect, explained below.

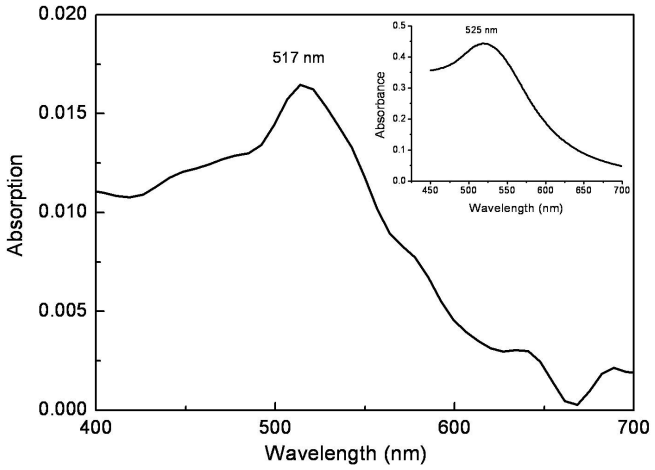

Figure 6.1: Absorption of the Au-PNIPAM$_{127}$ monolayer at 20°C. The inset shows the absorption peak in bulk water.

6.2 Substrate effect

In bulk, the gold particles see a homogeneous surrounding medium with a refractive index of 1.333 ($\epsilon_s = 1.77$). When the particles are deposited at the air-water interface, the particles are partially exposed to air with a lower refractive index of 1 ($\epsilon = 1$). This decrease in the surrounding medium dielectric constant is probably responsible for the blue shift. Kelly and co-workers [116] have studied the effect of the substrate refractive index on the metal nanoparticles optical properties by making Discrete Dipole Approximation (DDA) calculations that model a silver nanophere totally exposed to air ($\epsilon = 1$) and then progressively embedded in a thick mica shell ($\epsilon = 2.43$). The results showed that as the percentage of mica surrounding the metal core increased, the SPR peak red-shifts drastically (representation taken from Kelly's article Figure 6.2) because it is progressively subjected to a medium with increasing refractive index. Our X-ray reflectivity measurements revealed that the gold cores adopt a stagerred conformation with compression (Figure 6.3; this may suggest a partial exposure of the particles to the air-phase. In our case, the refractive index of the particles environment decreases ($n_{water} > n_{air}$) with compression. As a result, the polymer-protected gold nanoparticles monolayer SPR is blue-shifted.

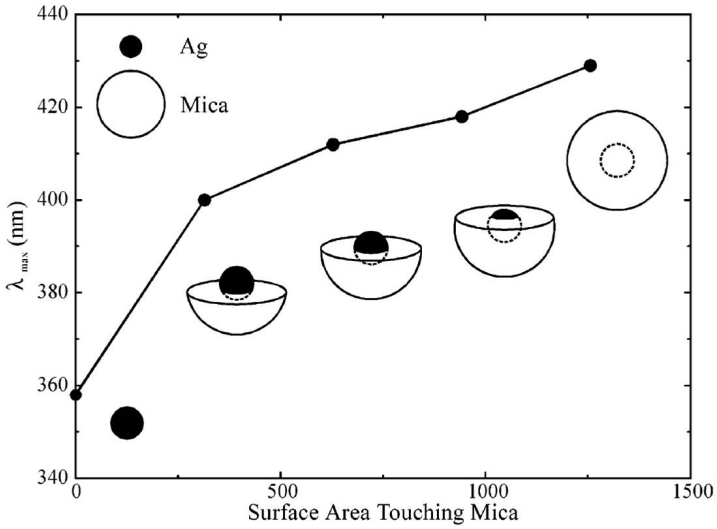

Figure 6.2: DDA results of Kelly and al [116] showing the substrate effect: Plot of peak wavelength versus surface area (in nm^2) of an Ag sphere progressively embedded into a mica shell ($\epsilon = 2.43$).

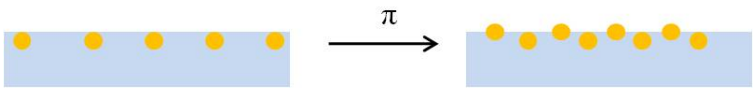

Figure 6.3: Compression effect on gold organization in the monolayer as revealed by X-ray reflectivity.

6.3 Temperature effect

At 32°C, at the same degree of surface compression as 20°C, the SPR of Au-$PNIPAM_{127}$ interfacial layer is very slighlty red-shifted from ≈ 517 to ≈ 519 nm (Figure 6.4). Futhermore, the absorption signal is significantly ameliorated. In the previous chapter, we have observed that the monolayer concentration optimization with temperature has led to an interparticle distance decrease of 2 nm. Here, the interparticle distance diminution being unsufficient to create a strong interparticle coupling ($d/D \approx 1.7$), we think that polymer collapse-induced increase of the shell dielectric constant (ϵ_s) is most likely at the origin of this small red-shift. As for the increase in absorption peak intensity it is, of course, caused by the higher surface concentration.

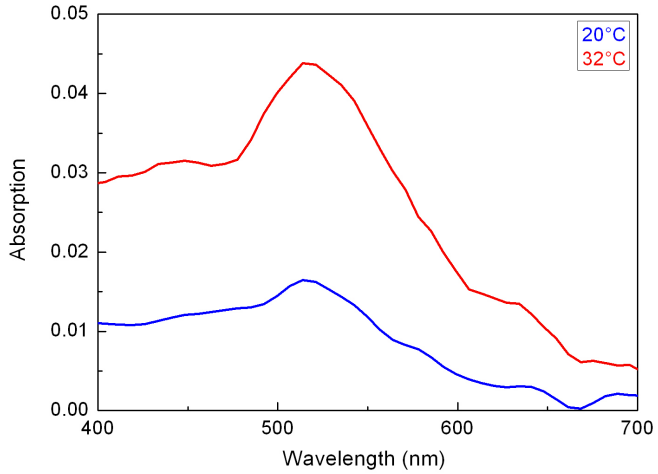

Figure 6.4: Absorption of Au-PNIPAM$_{127}$ monolayer at 20 and 32°C.

At high temperature, the Au-PNIPAM$_{270}$-co-NIPAM$_{113}$ monolayer also exhibits SPR (Figure 6.5). The absorption peak is close to that for Au-PNIPAM$_{127}$ so we can say that there is no difference in optical properties between the two types of surface layers. However, the Au-PNIPAM$_{270}$-co-NIPAM$_{113}$ SPR peak is broader and has a lower intensity than the one for Au-PNIPAM$_{127}$ monolayer as it is composed of smaller particles (D = 5.3 and 8.0 nm, respectively).

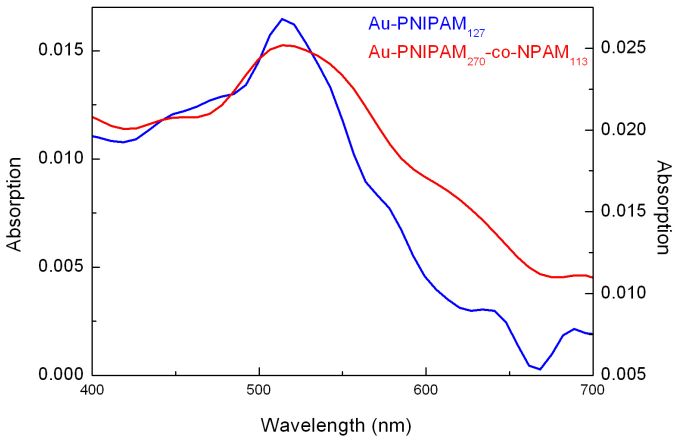

Figure 6.5: Absorption of Au-PNIPAM$_{127}$ at 32°C (blue) and Au-PNIPAM$_{270}$-co-NIPAM$_{113}$ at 28°C (red) monolayers at final compression. The y-axis for Au-PNIPAM$_{270}$-co-NIPAM$_{113}$ is vertically shifted for better comparison.

6.3.1 Compression effect at high temperature

Unlike the monolayer at 20°C, a SPR signal is also recordable at lower surface compressions at 32°C (Figure 6.6). As mentioned before, the interfacial layer concentration is increased at each surface compression as it is at its optimum stability. However, no SPR shift is observed with compression. Firstly, even at high surface coverage, the particles are still not sufficiently close to each other to provoke a strong interparticle coupling and cause a red shift. Secondly, no change in polymer layer conformation is registred. In fact, from the start to the end of compression, the polymer graft keeps a collapsed conformation around the gold core.

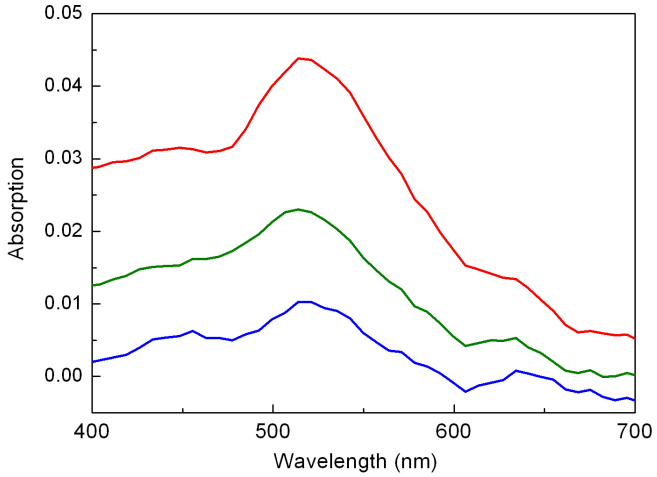

Figure 6.6: Absorption of the Au-PNIPAM$_{127}$ monolayer at different surface compressions at 32°C.

Shan has studied compression effects of Au-PNIPAM$_{24}$-PS$_{28}$ film [100]. He observed a blue shift with compression but at a lower degree of compression compared to our current study and in absence of NaCl. He proposed that this blue shift is due to the polymer conformational change. Compression-induced polymer layer conformational changes were later revealed by a detailed neutron reflectivity study undertaken by Lee and co-workers [102]. The hypothesis of polymer conformational changes leading to blue-shift was reasoned (similarly to the bulk situation), by the Mie-Drude theory:

$$\lambda_{peak} = \lambda_p \sqrt{\epsilon^{\infty} + 2\epsilon_m + \frac{2p(\epsilon_s - \epsilon_m)}{3}} \tag{6.1}$$

where λ_{peak} is the absorption peak position for the nanoparticle and λ_{p} the bulk plasma wavelength, ϵ^{∞}, ϵ_{s}, and ϵ_{m} are dielectric functions of the bulk metal, polymer shell layer and medium, respectively; p is the volume fraction of the polymer shell layer.Two points can be noted from the above equation: (i) since $\epsilon_{\mathrm{s}} > \epsilon_{\mathrm{m}}$ for most polymers in aqueous medium, the presence of a polymer shell layer increases λ_{peak} with respect to the naked nanoparticle ($p = 0$), and (ii) since (ϵ_{s} - ϵ_{m}) is concentration dependent, λ_{peak} is therefore also sensitive to the

polymer conformation. In this case, changes in conformation due to compression (pancake to brush, for example) was thought to decrease the polymer surrounding the gold-core and thus decreasing (ϵ_s - ϵ_m).

6.4 Optical properties of polymer-protected gold nanoparticles multilayer

At 20°C, contrary to the Au-PNIPAM and Au-PNIPAM-co-NPAM interfacial layers, Au-PNIPAM$_{24}$-PS$_{28}$ interfacial layer exhibits a SPR signal in absence of salt (Figure 6.7). The SPR peak is at 527-529 nm. As the absorption peak is broad ($D \approx 3$ nm), it is not evident to determine the exact peak position and observe any displacement with compression. It is though, interesting to note that the absorption peak position occurs at higher wavelength compared to the Au-PNIPAM and Au-PNIPAM-co-NPAM monolayers ($\Delta\lambda \geq 10$ nm). This red-shift compared to the Au-PNIPAM and Au-PNIPAM-co-NPAM interfacial layers may be due to bilayer organization and possible PS-shielding (due to its insoluble nature, the PS does not spread at the water-air interface and expose the gold core to air, Figure 6.8).

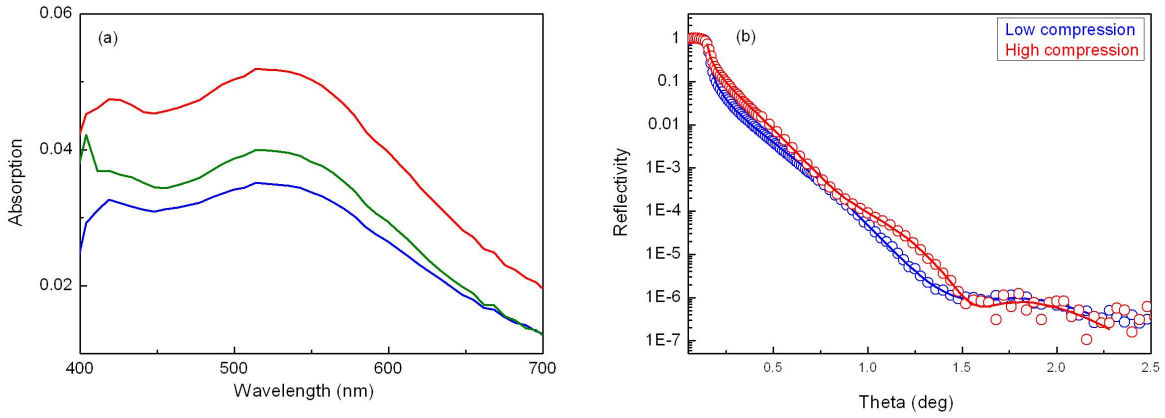

Figure 6.7: Absorption spectra of Au-PNIPAM$_{24}$-PS$_{28}$ film at 20°C at different surface compressions (a) the X-ray reflectivity curves.

Figure 6.8: Representation of Au-PNIPAM-PS surface layer.

Au-PNIPAM$_{118}$-PS$_{28}$ multilayer displays very weak SPR peak at 20°C despite the good stability shown by the reflectivity study; this is because the surface layer is composed of very small particles (D $\approx$ 2.3 nm). At 32°C and at minimal surface area, however, a very

pronounced SPR peak is obtained at 546 nm (Figure 6.9). From X-ray data we know that the particles form multilayers at the interface. Figure 8.27 compares the absorption spectra of the Au-PNIPAM$_{127}$ monolayer and the Au-PNIPAM$_{118}$-PS$_{28}$ multilayer at the end of compression. We put in evidence that from the monolayer to the multilayer formation, the SPR peak significantly red-shifts with $\Delta\lambda \approx 546\text{-}517 \approx 30$ nm. Furthermore, we note that the Au-PNIPAM$_{24}$-PS$_{28}$ bilayer SPR peak (≈ 528 nm) is situated between the two peaks determined above. These results clearly demonstrate that the SPR peak significantly red-shifts at the onset of multilayer formation (or surface aggregation). This observation parallels that of bulk studies where occurrence of comparable large red-shifts are correlated to temperature-induced aggregation. Thus, as shown by reflectivity studies, Au-PNIPAM-PS nanoparticles under controlled conditions where the anchoring PS chains efficiency is further complemented by increased hydrophobicity of PNIPAM chains, very compact and well-defined multilayers are formed that show intense SPR peaks. The strongly red-shifted peaks can only be explained by dielectric dipole-coupling of the nanoparticles within the three-dimensional multilayer structure.

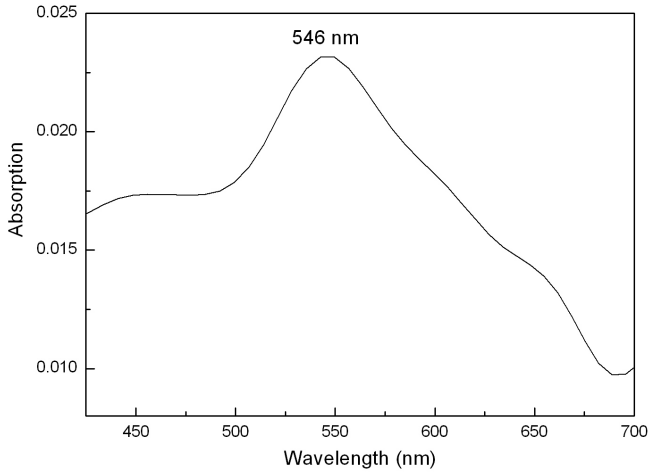

Figure 6.9: Absorption of Au-PNIPAM$_{118}$-PS$_{28}$ monolayer at 32°C.

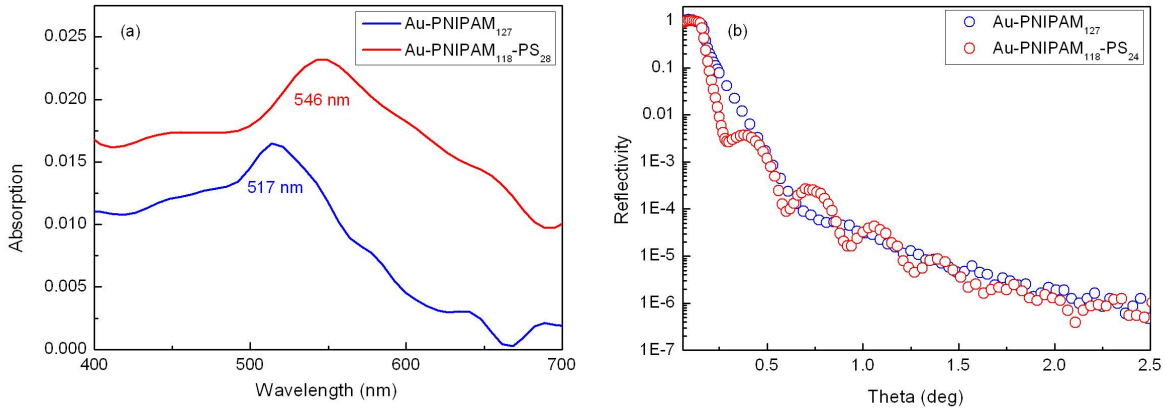

Figure 6.10: Comparison of the: (a) absorption spectra and (b) X-ray reflectivity curves of Au-PNIPAM$_{127}$ (blue) and Au-PNIPAM$_{118}$-PS$_{28}$ (red) monolayers at 32°C.

6.4.1 Summary

Neutron and X-ray reflectivity studies show that Au-PNIPAM and the Au-PNIPAM-co-NPAM particles deposited at the air-water interface always form a monolayer. Under good solvent condition, these monolayers are rather unstable upon high compression and optical signals are too weak to be registred. Working under optimized conditions identified from structural studies, the enhanced stability of these monolayers (by NaCl, temperature) facilitates increased degree of compression (and thus concentration) of the nanoparticles giving rise to detectable SPR signals. Interestingly, the SPR peak shows a significant blue-shift compared to bulk due to anisotropy substrate effect. On the other hand, increased stability conferred to the surface layer by insoluble PS chains, when further enhanced by temperature-induced collapse of the PNIPAM chains, leads to formation of dense, well-defined multilayers. These multilayers exhibit intense SPR peaks that are significantly red-shifted by $\approx$ 30 nm compared to monolayer. Thus, the three-dimensional multilayer organization, probably coupled to increased degree of interparticle proximity (at high temperature, Au-PNIPAM monolayer d$/D \approx 1.7$), strongly suggests dielectric dipole-coupling. We are thus able to form stable gold nanoparticles monolayers as well as well-controlled gold nanoparticles multilayers at the air-water interface that exhibit SPR. These different nanoparticle organizations should guide our future perspectives on studies of optical properties of gold nanoparticles deposited on solid substrates, and on their interactions with other interfaces, like biomembranes.

Chapter 7

Conclusions and perspectives

Our motivation was to control the gold nanoparticles surface plasmon resonance with a thermoresponsive polymer shell. The starting point consisted of preparing gold nanoparticles of varying sizes (D = 2.9 - 8.0 nm) that are coated with polymer of different chain lengths and degrees of hydrophobicity. Using RAFT-polymerization, we managed to synthesize the classical Cpa-PNIPAM homopolymer with various molecular masses (M_w = 7781 - 29 650 g.mol^{-1}) by controlling [NIPAM]/[RAFT] ratio and reaction time. We have also synthesized a new copolymer of Cpa-PNIPAM-co-NPAM by incorporation of n-propylamine co-monomer that is more hydrophobic than its n-isopropyl counterpart. The hydrophobicity of the resulting copolymer is controlled by [NIPAM]/[NPAM] ratio. A decrease of $\Delta T_c \approx 10°C$ is observed from NPAM fraction from 0 to 1. The T_c values can be further reduced by addition of NaCl to screen the charged RAFT end-group. Calorimetry data also suggest a higher cooperativity effect in the collapse process of the copolymer. Synthesis of the polymer-protected gold nanoparticles was successfully carried out by "grafting-to" method in a "one-step" approach. Two types of colloidally-stable thermosensitive gold nanoparticles, Au-PNIPAM and Au-PNIPAM-co-NPAM of varying sizes were obtained by controlling the [Au]:[Polymer] ratio. The wide ranges of particle size (D $\approx$ 3-8 nm) and of graft polymer chain length (N $\approx$ 57-400) thus facilitate our studies to understand and control their optical properties, and the available range of T_c increases the flexibility in which the thermosensitive aspect can be exploited.

SANS was employed to characterize the polymer shell structural properties. Modelling the scattering curves with the hard sphere model or hairy sphere model yields valuable information about the shell thickness e. Above T_c, scattering curves characteristic of interparticle association are obtained and modelled with colloidally stable well-defined particle sizes.

Study of the optical properties of the different batches of gold nanoparticles (by UV-vis spectroscopy) revealed that coating the gold particle with a polymer shell screens and reduces the sensitivity of SPR to the external solvent. Modelling the extinction spectra with the core-shell model using the Mie dipolar theory enables us to gain more detailed information on the relationship between the optical and structural properties of the polymer shell, and their influence on solvent-sensitivity . We obtain valuable information about ϵ_s and subsequently ϕ_p. Combining results obtained from different techniques D (TEM), e (SANS), we are able to rationalize and consolidate the the data from the different samples with different characteristics. We find that the gold nanoparticles sensitivity to external solvent is reduced

with increasing polymer volume fraction p(evaluated from e_{eff}). Furthermore, when $p > 0.9$, the SPR is frozen by polymer shell and loses total sensitivity to the embedding solvent medium. Apart from the SPR peak position, we have also attempted to fit the form of the absorption curve. This is characterized by the size-dependent factor that is related to surface scattering. We find that the lower the normalized scattering factor g/D, the better the quality of the theoretical fit, thus allowing us to assess the relative effects of the surfaces due to form and chemical heterogeneity. We have also analyzed the SPR response to temperature-induced conformational changes in the polymer shell. In the presence in presence of salt, the SPR is significantly red-shifted (and a clear color change occurs). The extent of the red-shift is controlled by the graft polymer hydrophobicity and the salt concentration. Modelling the spectra revealed that the control of the SPR is, at first instance, due to polymer-shell collapse-induced increase of ϵ_s. Then, following total polymer shell collapse ($\phi_p \approx 1$), the SPR peak displacement to even longer wavelength is provoked by the interparticle aggregation as supported by SANS. This thermal effect results in a red-shift of about 25 nm. The thermal effect on the optical properties is partially reversible. This is an interesting aspect that can be expoited for detection applications. (For example to detect if milk or meat has experienced transient high temperature exposure during transportation.) We conclude that the gold SPR response is very sensitive to the polymer layer property and that we succeeded in tuning SPR with variation of shell structural properties. Gold nanoparticles are therefore efficient probes for changes in local environment.

We have used a combination of the Langmuir balance and reflectivity techniques to explore and characterize the surface properties (water-air interface) of these amphiphilic and thermosensitive gold nanoparticles. The two-dimensional structures of the interfacial particles have been evaluated from the isotherms. In the low compression region, we find the gold cores to be isolated by the (2-dimensional) polymer shell, with limiting interparticle distance that varies predictably with polymer chain length. A novel observation of 2-dimensional polymer collapse is also evidenced at near-theta condition for the new copolymer that we synthesized. At high compression, we assessed by both neutron and X-ray reflectivities how far the surface layer can be compressed. The aim was to optimize the interfacial layer concentration and stability and to manipulate interparticle distance, for optical studies. We observe that the monolayers, although stable at low compression, lose stability at high compression through loss in the bulk phase. We showed that the monolayer stability can be improved by addition of NaCl to screen out charge end-groups, increased hydrophobicity of the polymer chain and by temperature. Furthermore, temperature-enhancement of hydrophobic nature and surface-activity can be effected at a lower temperature for the new copolymer. Interestingly, we find that at maximal compression, the degree of proximity of the nanoparticles, expressed as the normalized interparticle distance, tends towards a common value irrespective of gore-core size and polymer chain length: $d/D \approx 2.1$ - 2.2 in good solvent and 1.7 in near-theta solvent. Core-core contact ($d/D = 1$) is not reached and the particles are therefore still well protected by the polymer shell. For all these particles coated with soluble amphiphilic polymers therefore, we always have a monolayer structure. Finally, a third type of amphiphilic particles containing a fraction of non-soluble chains has also been investigated (Au-PNIPAM-PS). Due to the insoluble PS, the nanoparticles are anchored to the surface more efficiently. As a result, bilayer structures are formed at high compression. Very interestingly, by further enhancing the surface stability of the PNIPAM component, dis-

placement of particles from the surface is minimized. In this case, we succeeded in building dense and well-defined multilayers.

When the surface layer is sufficiently concentrated, SPR signal can be recorded. The SPR of the highly-compressed layer is shifted to lower wavelength compared to bulk particles possibly due to partial exposure of the gold core to air. At high temperature when the monolayer is the most stable, the intensity of the SPR signal increases with surface compressions. However, the SPR peak position shift with compression is insignificant. It is interesting to note that for the Au-PS-PNIPAM multilayers, SPR is very significantly red-shifted. It is clearly observed that the SPR progressively red-shifts as the number of layers composing the thin film increases. We can thus control the interfacial optical properties by controlling the gold nanoparticle assembly and interfacial organization.

Perspectives

In the future, we would like to graft the PNPAM homopolymer (T_c = 24°C) onto gold nanoparticles in order to extend the range of polymer shell collapse temperature. Thus, the gold optical properties can be controlled by tuning the protecting shell structural properties at significantly lower temperature range.

We are also interested in bio-functionalizing the RAFT-polymer. Thus, the resulting gold nanoparticles coated with the bio-fuctionalized polymer can have potential applications such as detection, drug delivery and diagnostic in the biomedical field. For example, when the biomolecule (DNA, proteins, carbohyrate) conjugated a gold nanoparticle recognizes a biological function (membrane) or target molecule (antibody) a variation in the gold particle surrounding environment occurs and a color change can be expected. We are interested in interactions of the functionalized particles with membranes, and across membranes.

We have dedicated our study to improve the polymer-gold monolayer stability. As mentioned in chapter 5, interfacial properties of functionalized gold nanoparticles are aspects pertinent to templating building blocks and self-assembly and to interactions of nanoparticles with biological membranes. Another interesting development is depositing the interfacial layers on a substrate for multilayer construction (Metamaterial). The most common way to deposit the interfacial layers in an well-organized fashion is by Langmuir-Blodgett deposition. The optical properties of the assembly of gold nanoparticles (Metamaterial) can thus be tuned with, beside the interparticle distance, the particle size by inducing particle aggregation. This can have potential applications in optics, microelectronics devices.

Chapter 8

Appendix

8.1 Small Angle Neutron Scattering (SANS)

SANS experiment consists of illuminating on a sample with a collimated beam of monochromatic neutrons, of wavelength λ, and analyzing the variation of the number of scattered neutrons (the intensity) as a function of their diffusion angle, using a detector. The neutron-matter interaction [117], [118] is explained by taking into account that the neutrons is considered to be both a wave and a particle. The incident neutron beam, of wavelength λ, is considred as a plane wave which propagation is written in the following form (ν is the wave frequency):

$$\Psi = e^{i(kz-2\pi\nu t)} \tag{8.1}$$

Once the plane wave interacts with the sample, the wave is scattered in all directions and becomes spherical:

$$\Psi_{\text{diff}} = -f(\vec{k}, \vec{k'})\frac{e^{i(kz-2\pi\nu t)}}{r} \tag{8.2}$$

-f($\vec{k}$, $\vec{k'}$) is the scattering amplitude, $\vec{k}$ and $\vec{k'}$ are the incident and scattered wave vectors. The scattering vector $\vec{Q}$ is then defined as (Figure 8.1)

$$\vec{Q} = \vec{k} - \vec{k'} \tag{8.3}$$

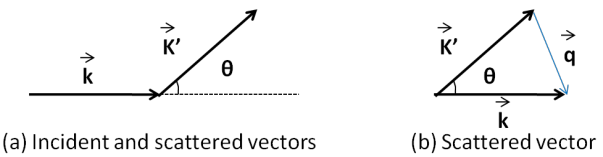

Figure 8.1: Definition of scattering vector $\vec{Q}$

The scattering vector $\vec{Q}$ has an amplitude noted q, defined as:

$$q = \frac{4\pi}{\lambda}\sin(\frac{\theta}{2}) \tag{8.4}$$

The parameter q is the most important. Its dimension is the inverse of a length. The range of Q values must be in the same order of magnitude as the inverse of the measured sample characteristics sizes.

We now consider a neutron beam,$\phi(\lambda)$ ($cm^{-2}.s^{-1}$) arriving on the sample, which diffuses a number of neutrons I(ϕ) (s^{-1}), on a plane surface S situated at a distance r (corresponding at an angle $\Delta\Omega = S/r^2$) (Figure 8.2)

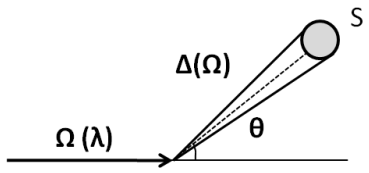

Figure 8.2: Scattering cross section.

The intensity can be written as:

$$I(\phi) = \phi(\lambda)\frac{d\sigma(\theta)}{d\Omega}\Delta\Omega \tag{8.5}$$

$d\sigma/d\Omega$,differential scattering cross section, represents the total number of scattered neutrons per second in the angle $\Delta\Omega$. σ has the dimension of a surface. It is possible to re-write the expression $d\sigma/d\Omega$ by considering the scattering amplitude A(q)(equation 7.6), which is the Fourier transform of the density ρ(r) of the system of n atoms $\rho(r) = 1/V \sum^{n}_{i} b_i \delta(r - r_i)$, the volume V containing n nuclei of scattering length b_i:

$$A(Q) = \int \rho(r) e^{iQr} dr \tag{8.6}$$

$$\frac{1}{V}\frac{d\sigma}{d\Omega} = \langle A(Q)A(-Q)\rangle = \sum_{i,j}^{n,n} \langle \rho_i \rho_j \rangle \left\langle e^{iQ(r_i - r_j)} \right\rangle \tag{8.7}$$

The square bracket indicate an average on the whole sample. This expression can finallly be written as the following formula [119], [120]:

$$\frac{d\sigma}{d\Omega} = n b_{inc}^2 + b^2 \sum_{i,j}^{n,n} \left\langle e^{iQ(r_i - r_j)} \right\rangle \tag{8.8}$$

where:

$$b_{inc}^2 = \left\langle b_i^2 \right\rangle - \left\langle b_i \right\rangle^2, b = b_i \tag{8.9}$$

The scattered intensity will be the sum of one term of incoherent scattering and one term of coherent scattering. The latter is close to the spacial correlations between nuclei

and allow to have acces to the information about the structure of the objects. It is this term that we are interested in. The term of incoherent scattering comes from the lack of correlation between the considered position and the spin state or the isotope of the nucleus that occupies it. The incoherent scattering is used to obtain informations about the sample dynamics. In our case, the incoherent scattering will be considered as flat background noise that we will need to substract from our signal.

8.1.1 Measurements and treatments

8.1.1.1 Measurements

A SANS measurement is realised by sending a beam of monochromatic neutrons, of wavelength λ, on a sample. The neutrons are then scattered and arrive on a detector where they are counted depending on their position to the center of the detector (which corresponds to the incident beam). The position depends on the scattering vector Q (which depends on the scattering angle and wavelength). Figure 8.3 represents a SANS spectrometer.

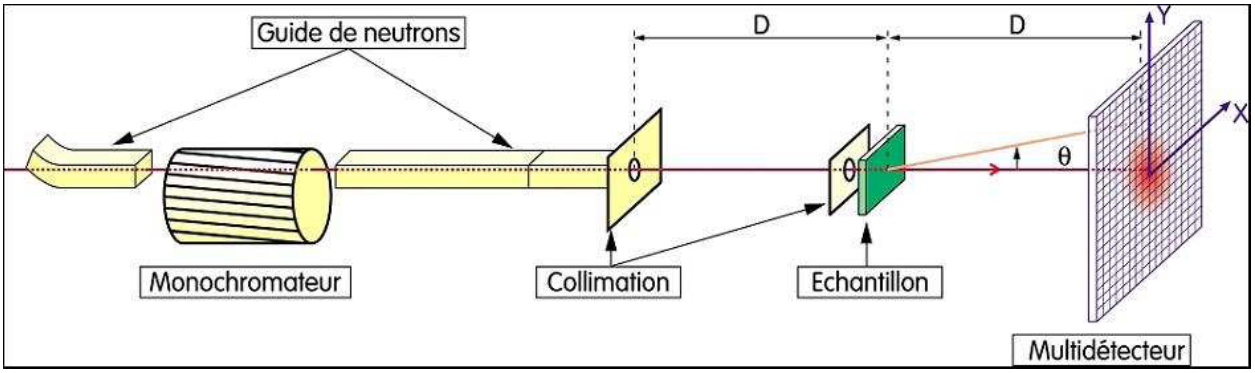

Figure 8.3: Representation of a Small Angle Neutron Scattering spectrometer.

To obtain the scattered intensity as a fonction of scattered vector, the scattered intensities are gathered at equal distance to the centre of the detector (This is accurate for isotropic samples). All information about the sample are given by the curve of intensity as a function of the wave vector q. So, it is necessary to adapt the range of q to the characteristic distances of the sample ($R \approx 1/q$). To achieve it, we can either vary the sample-detector distance or the wavelength (λ). These two parameters remain constant during a measurement. The combination of a wavelength and a distance is called configuration. Depending on the dimensions we wish to observe, we will need a more or less large range of q. We run our experiments on PACE where we have employed two configurations: (i) D= 3 m, $\lambda = 6$ Åcorresponding to a configuration for 'meduim angle' and (ii) D= 5 m, $\lambda = 13$Åcorresponding to a configuration for "'small angle". These two configurations allow us to study our sample in the range of q included between 0.003 and 0.12 $Å^{-1}$.

8.1.1.2 Data treatment

Once the measurement is performed, it is necessary to treat the crude scattered intensity to obtain the absolute intensity. First, we substract the contribution from the empty cell (cellule vide, cv). The crude intensity is also normalized by the thickness of the sample (e) and by the transmission (T) corresponding to the attenuation of the direct beam passing through the sample. The detector efficiency is then corrected by measuring the totally incoherent signal of H_2O. The incoherent signal is theoretically flat because the sample scatters in all directions in a random manner. This measure also enables us to calculate the factor of re-normalisation (F). The absolute intensity is expressed by:

$$I_{abs} = F \times \frac{\frac{I_{ech}}{T_{ech}e_{ech}} - \frac{I_{cv}}{T_{cv}e_{cv}}}{\frac{I_{H_2O}}{T_{H_2O}e_{H_2O}} - \frac{I_{cv}}{T_{cv}e_{cv}}} \tag{8.10}$$

Finally, it is possible to withdraw the electronic background noise of the detector by measuring the spectrum of Cd which is a strong neutron absorbant. When all this procedure is done, it remains to substract the incoherent part of the signal which corresponds approximatively to the solvent signal.

8.1.2 Scattered intensity

Once the treatment of the crude data is finished, we have the absolute scattered intensity curve as a function of q. This intensity only comes from the coherent scattering. This will allow us to obtain information about the structure and form of the scattering objects in solution. The scattered intensity is defined by a form factor P(q), describing the size of the particles and a structure factor S(q),which describes the correlations between the particles in the system. In the case of centrosymmetrical objects, the scattered intensity is expressed with the following equation:

$$I(q) = \Phi V_{\text{object}} (\Delta\rho)^2 P(q) S(q) \tag{8.11}$$

Φ is the volumic fraction of the scattering objects, $(\Delta\ \rho)^2$ the contrast between object/solvent, V the volume of an object.

8.1.2.1 Form factor P(q)

The form factor is a function of the form of an individual object. For simple geometrical objects, it can be analytically calculated. For sufficiently diluted solutions, the structure factor is equal to 1 and therefore the signal depends only on the form factor. It is then possible to determine the form and caracteristic dimensions of the scattering object.

8.1.2.2 Stucture factor S(q)

The structure factor represents the correlations between the objects. It allows to verify if the system is attractive or repulsive and to observe the intensity of interactions. As mention ealier, it is considered to be equal to 1 for sufficiently diluted solution. Therefore we work in diluted regime in order to disgard the correlations between the objects.

8.2 Neutron reflectivity

The neutron refractive index is defined as a change in vector between phases:

$$n = \frac{k_1}{k_0} \tag{8.12}$$

where $k_0 = (2\pi/\lambda)\sin\theta$ and $k_i = (k_0^2 - 4\pi Nb)^{1/2}$ are the wave vectors outside and inside the medium, respectively, λ is the neutron wavelength and θ the grazing incident angle. Nb is the neutron scattering length density (represented by ρ in SANS).

Specular reflectivity from an ideal interface (bare surface in absence of adsorbed layer) is referred to as the Fresnel reflectivity, R_F. It is defined as [113]:

$$R_F(k) = \left[\frac{(k_0 - k_i)}{(k_0 + k_i)}\right]^2 \tag{8.13}$$

Alternatively, in the kinetic approximation, it can be expressed as [121]:

$$R_F(k) = \frac{\pi^2}{k^4} |\Delta\rho| \tag{8.14}$$

where $\Delta\rho$ is difference in scattering length density across the interface. It can be seen from this expression that the reflectivity decreases asymptotically with k^4. In the presence of a surface layer, the reflectivity deviates from R_F and this deviation can be related to the Fresnel reflectivity by [122]:

$$\frac{R(F)}{R_F(k)} = \left(\int \rho'(z)\exp(2ikz)dz\right)^2 \tag{8.15}$$

where $\rho(z)'$ is the gradient of the scattering length density. Nb is the scattering length density that is related to the chemical composition of the adsorbed layer. Thus, when the reflectivity is represented in this reduced form, all deviations of R/R_F from unity are due only to interfacial features such as roughness and adsorbed layers. When R_F is convoluted with instrumental resolutions and surface roughness of the pure substrate, R/R_F is then attributed directly to the composition profile of the adsorbed layer. For a given model of the structure normal to the interface, it is possible to calculate exactly the reflectivity function. For a multilayer structure, the optical matrix method [113] [123] is used, where the interfacial structure is divided into different discrete layers and the sum reflectance at each interface is calculated to give the final reflectivity function.

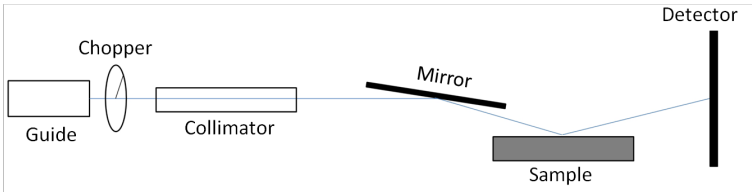

Figure 8.4: Neutron time-of-flight reflectometer

8.3 Résumé

L'objective de cette thèse est de contrôler les propriétés optiques des nanoparticules d'or par la modulation de la constante diélectrique de la couche protectrice ϵ_s. ϵ_s peut être moduler en variant les propriétés structurales de la couche protectrice. Nous avons choisi de stabiliser les nanoparticules avec un polymère thermosensible dans le but d'induire avec la température un changement de conformation de la couche de polymère pouvant résulter en une variation significative de ϵ_s. Un polymère thermosensible subit une transition pelote-globule à une température critique T_c. Notre approche est de greffer sur les nanoparticules d'or des polymères possédant une large gamme de masse moléculaire et différent degré d'hydrophobicité afin d'obtenir des particules stabilisées avec une couche protectrice d'épaisseur et hydrophobicité variables.

Des nanoparticules d'or greffées de deux types de polymères thermosensibles variant en masse molaire et en degré d'hydrophobicité sont synthétisées. La polymérisation de RAFT est employée pour d'abord synthétiser le polymère thermosensible classique Poly(N-isopropylacrylamide) (PNIPAM) de différentes masses molaires en controllant le rapport [NIPAM]/[RAFT] et le temps de réaction (Figure 8.5a). Ensuite, un nouveau copolymère Poly(N-isopropylacrylamide-propylacrylamide) (PNIPAM-co-NPAM) est synthétisé par incorporation d'un co-monomère plus hydrophobe n-propylamine (NPAM); de même composition chimique que le n-isopropylamine (NIPAM) mais variant en fonction isomérique (Figures 8.5c). La composition chimique et la masse molaire des polymères sont caractérisées par IR, RMN et GPC.

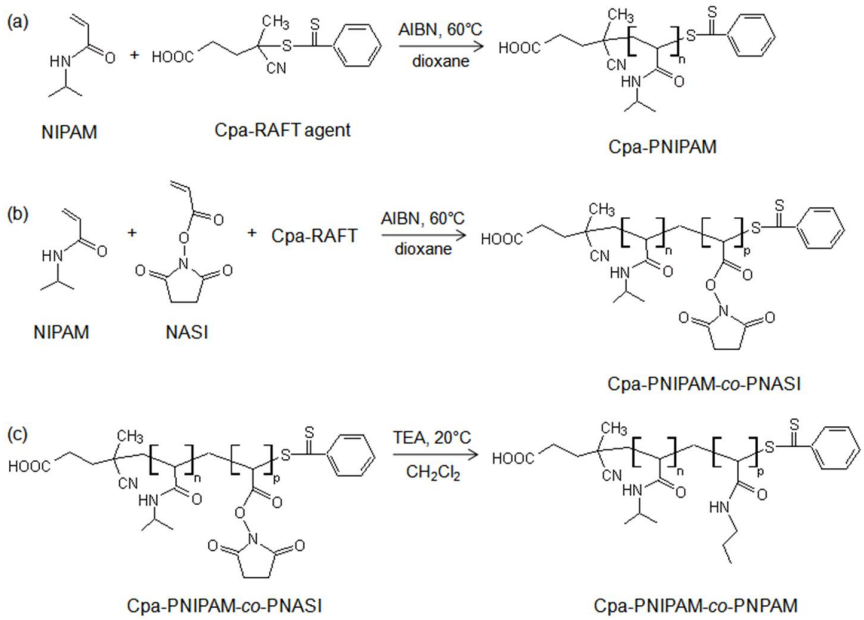

Figure 8.5: (a) Synthèse du Cpa-RAFT-PNIPAM (n = 67-265). Synthèse du copolymère Cpa-PNIPAM-co-NPAM: (b) copolymérisation du Cpa-PNIPA-NASI et (c) conversion du Cpa-PNIPAM-co-NASI en Cpa-PNIPAM-co-NPAM par aminolyse en utilisant n-propylamine (NIPAM:NPAM = 2.4:1 à 1:1).

Les propriétés thermales des polymères thermosensibles sont déterminées par mesures d'absorption et de microcalorimétrie. Les résultats ont démontré que la température de collapse (T_c) peut être diminué en augmentant la concentration de NPAM dans la chaîne (Figure 8.6a) et par l'écrantage des charges présentes en bout de chaîne de polymère par l'addition de NaCl (Figure 8.6b). La DSC a également révélé que le nouveau copolymère Cpa-PNIPAM-co-NPPAM présente un degré de coopérativité plus élevé que l'homopolymère Cpa-PNIPAM (Figure 8.7).

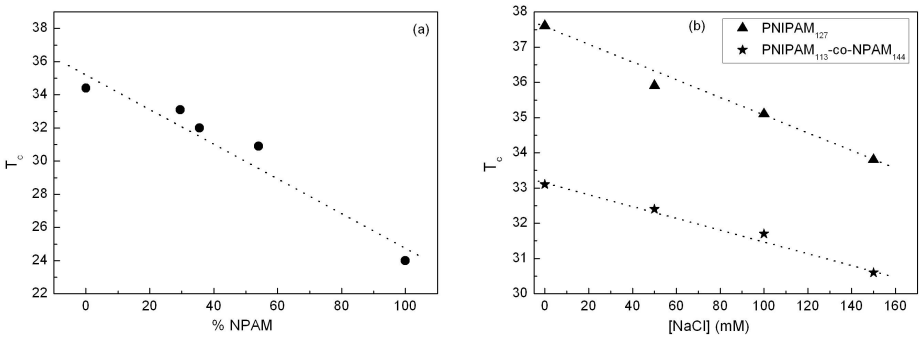

Figure 8.6: Effet de la concentration en NPAM (a) et de la salinité (b) sur la T_c(T_c = 24.3-37.6°C).

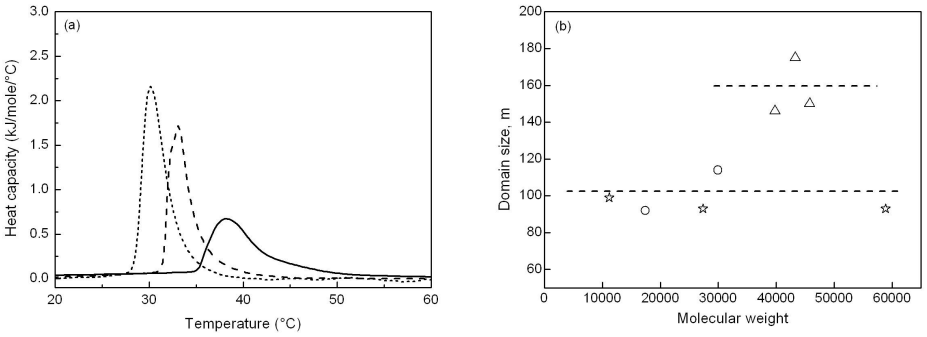

Figure 8.7: (a) Endothermes de microcalorimétrie des solutions aqueuses de Cpa-PNIPAM$_{154}$ (ligne continue), Cpa-PNIPAM$_{270}$-co-PNPAM$_{113}$ (ligne en tiret)et Cpa-PNIPAM$_{176}$-co-PNPAM$_{176}$ (ligne pointillée). (b) Taille de domaine coopératif m (= nombre de monomères par domaine collapsé) en fonction de la masse molaire. (cercles): Cpa-PNIPAM (m = 92-114); (étoiles): PNIPAM de Tiktopulo et al; (triangles): Cpa-PNIPAM-co-NPAM (m = 146-175).

Les nanoparticules d'or sont synthétisées par la méthode de "grafting-to" (Figure 8.8). Durant la synthèse, le greffage de polymère et la croissance de l'or sont simultanés. Deux techniques sont employées: (i) "one-step" où le polymère n'est pas modifié avant sa réaction avec le précurseur de l'or en présence du super-hydride et (ii) "two-step" où le polymère est d'abord pré-hydrolysé avant la préparation des nanoparticules d'or. Le "one-step" s'est révélé la méthode la plus effective pour la préparation des nanoparticules d'or. Des particules de tailles assez monodisperses sont obtenues (Figure 8.9) et la taille des nanoparticules peut être contrôlée avec le rapport [$HAuCl_4$]/[Polymère]. La taille des nanoparticules et la quantité de polymère greffée sont respectivement caractérisées par TEM et ATG. Des nanoparticules d'or de D = 2.9 à 8.0 nm stabilisées par des polymères de M_w = 7741 à 29650 g/mol et de densité de greffage $\sigma \approx$ 1-2 chaînes/nm sont obtenues (Tableau 8.1).

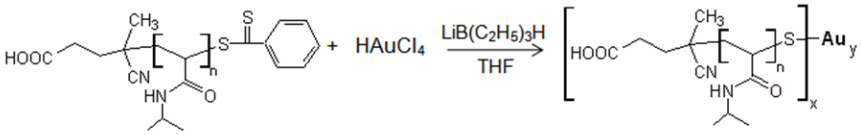

Figure 8.8: Synthèse des nanoparticules d'or Au-PNIPAM.

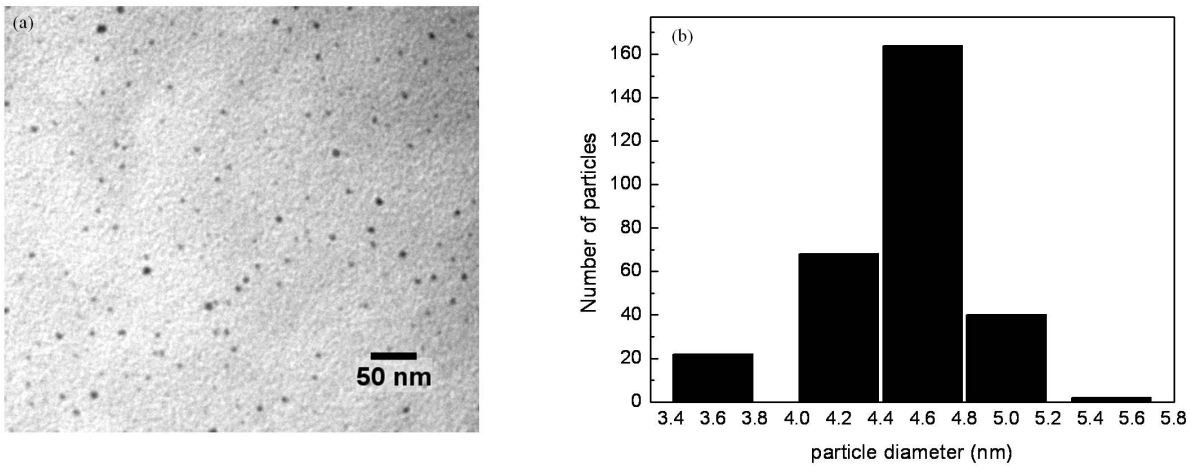

Figure 8.9: Image TEM (a) et la distribution correspondante (b) des nanoparticules de Au-$PNIPAM_{265}$ synthétisées par la méthode du "one-step" en utilisant le rapport $HAuCl_4$:Polymère = 10:1.

Au-Polymère	Formule	D (nm)	Densité de greffage (chaînes/nm^2)
échantillon 1	$Au_{8863}(PNIPAM_{67})_{156}$	6.6	1.14
échantillon 2	$Au_{15785}(PNIPAM_{127})_{312}$	8.0	1.55
échantillon 3	$Au_{2809}(PNIPAM_{154})_{75}$	4.5	1.18
échantillon 4	$Au_{2809}(PNIPAM_{265})_{127}$	4.5	2.00
échantillon 5	$Au_{4590}(PNIPAM_{270}\text{-}PNPAM_{113})_{112}$	5.3	1.27
échantillon 6	$Au_{752}(PNIPAM_{260}\text{-}PNPAM_{144})_{17}$	2.9	0.64
échantillon 7	$Au_{459}(PNIPAM_{57})_{33}$	2.7	1.4

Table 8.1: Nanoparticules d'or Au_y-$(Polymère_n)_x$ préparées avec la méthode du "one-step"; $[HAuCl_4]$ = 0.1 mmol/L, $HAuCl_4$:$LiB(C_2H_5)_3$ = 10:1. n = degré de polymérisation, x = nombre de chaînes par particule, y = nombre d'atomes d'or. $HAuCl_4$:Polymère = 10:1 (échantillons 3-6) et 20:1 (échantillons 1,2). L'échantillon 7 a été préparé par Shan avec le rapport $HAuCl_4$:Polymère = 10:1.

Les propriétés structurales de la couche de polymère sont étudiées par DNPA. Les mesures sont effectuées dans le D_2O afin de maximiser le contraste entre la couche de polymère et le solvant. En condition de bon solvant, les nanoparticules sont stabilisées par une couche de polymère hydratée (Figure 8.10). Les courbes de diffusion sont fittées avec 3 modèles classiques (Figure 8.11) utilisés au LLB pour modéliser les systèmes de nanocomposites: core-shell, hairy sphere et hard sphere. Nous observons que l'épaisseur de la couche protectrice augmente avec la masse molaire du polymère greffé et est de l'ordre du rayon de giration de la chaîne de polymère.

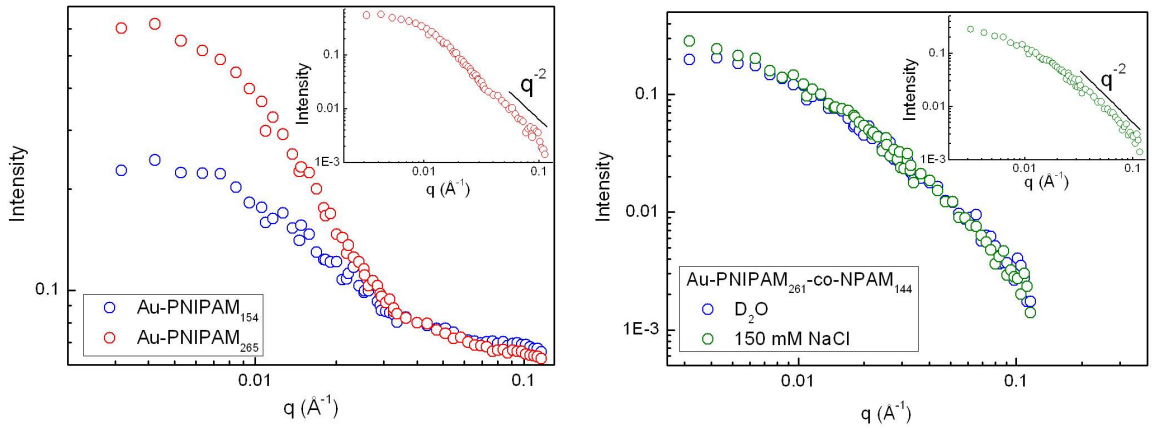

Figure 8.10: Courbes de diffusion des nanoparticules de (a) Au-$PNIPAM_{154}$ (bleu) et Au-$PNIPAM_{265}$ (rouge) dispersées dans le D_2O et (b) Au-$PNIPAM_{261}$-co-$NPAM_{144}$ dispersées le D_2O en absence (bleu) et présence de NaCl (vert) (T = 20°C. Insets: pente en q^{-2} pour les courbes de diffusion après soustraction du bruit de fond).

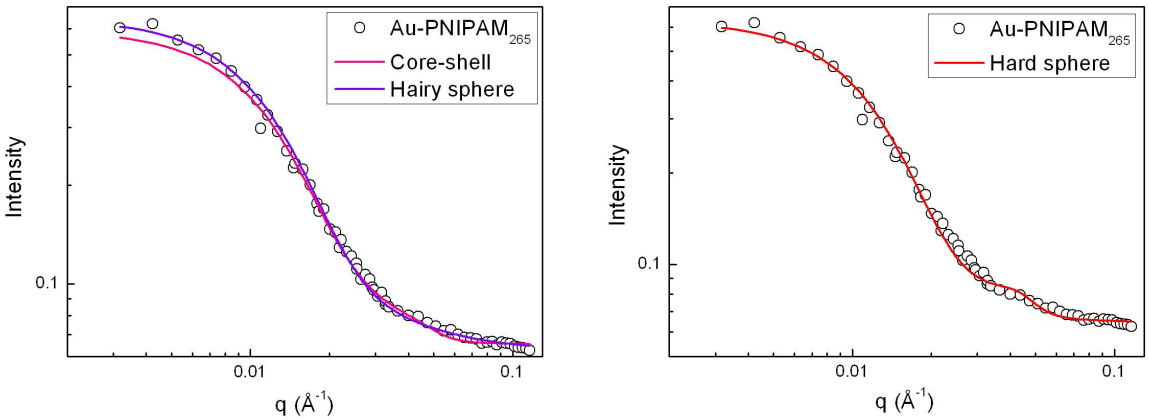

Figure 8.11: Ajustements avec les modèles de core-shell, hairy sphere (a) et hard sphere (b) réalisés sur les courbes de diffusion des nanoparticules de Au-PNIPAM$_{265}$ (e= 5 nm, R_g= 4.8 nm and R_{sphere} = 6.6 nm; respectivement.

Lorsque la température augmente, la couche de polymère devient déshydratée. Des agrégats de tailles définies se forment (Figure 8.12). Malheureusement, nous n'avons pas pu caractériser la collapse de la couche de polymère sur une particule individuelle.

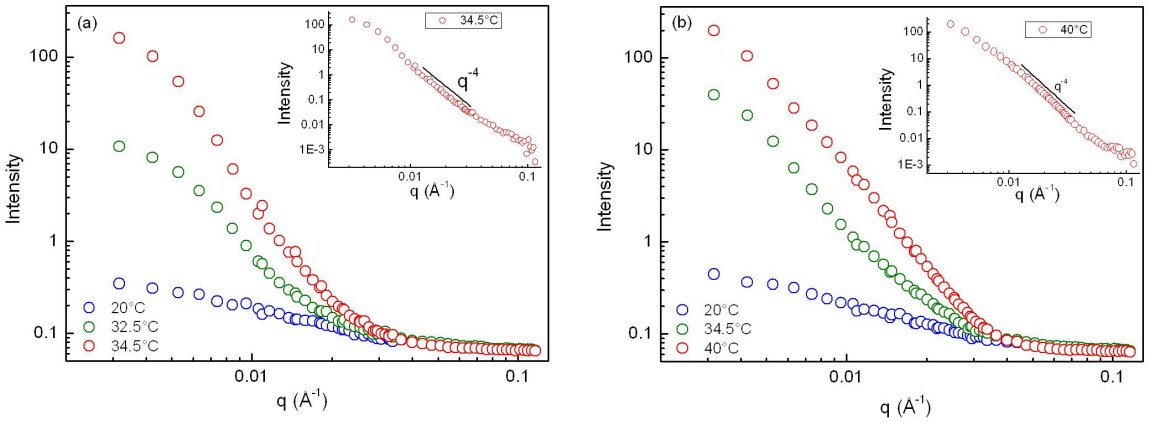

Figure 8.12: Effet de la température sur les nanoparticules de Au-PNIPAM-co-NPAM en absence de sel (a) et en présence de sel (b). Inset: pente en q^{-4} pour les courbes à haute température après soustraction du bruit de fond.

Nous avons étudié les propriétés optiques des nanoparticules d'or de taille variable et stabilisées avec des polymères de différentes masses molaires. Dans un premier temps, nous nous sommes intéressés à l'influence de la couche de polymère sur la sensibilité de la SPR au solvant environnant. Nous observons que la couche de polymère réduit la sensibilité de la SPR au solvant. Les spectres d'absorption expérimentaux sont modélisés en fittant la position et la largeur du pic d'absorption avec le modèle de core-shell qui repose sur la théorie de Mie. Cela nous permet de déterminer quantitativement la relation entre les propriétés optiques et les propriétés structurales de la couche de polymère, et leur influence sur la sensibilité au solvant. En fittant la position du pic λ_{peak}, nous obtenons la constante diélectrique de la couche protectrice ϵ_{s} à partir de laquelle on en déduit la concentration de polymère dans la couche protectrice ϕ_{p}. En combinant les résultats obtenus à partir des différentes techniques de caractérisation (D (TEM), e (DNPA)), nous sommes en mesure de rationnaliser et consolider les données des différents échantillons avec différentes caractéristiques. Nous démontrons que la sensibilité de la SPR de la nanoparticule d'or à la propriété diélectrique du solvant est progressivement atténuée lorsque la fraction volumique de la couche de polymère p augmente jusqu'à devenir quasi-nulle; dans ce dernier cas de figure, la SPR est dite "gelée" par la couche de polymère.

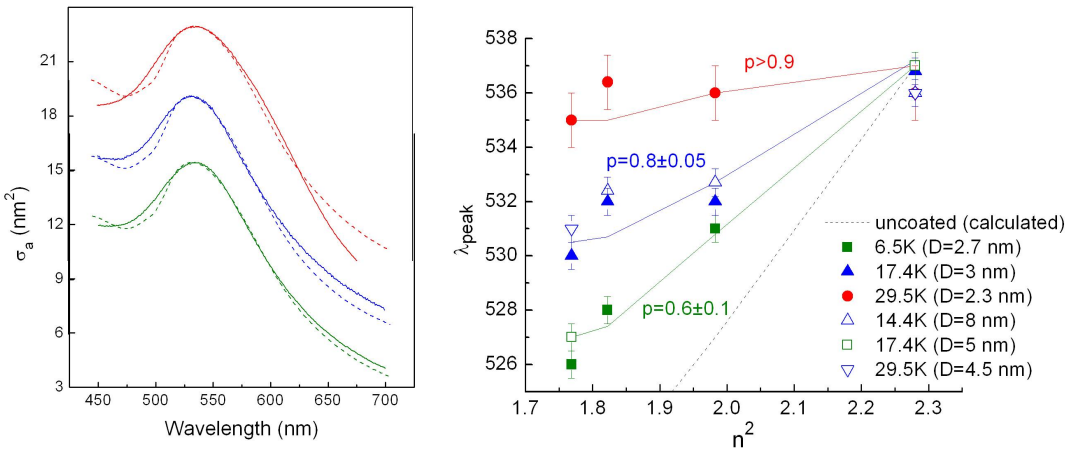

Figure 8.13: (a) Modélisation de courbes d'absorption des nanoparticules de Au-PNIPAM$_{127}$ dispersées dans différents solvants: eau (lignes vertes), THF (lignes blues), pyridine (lignes rouges). D = 8 nm, ϵ_{s} = 2.08-2.22 et g = 2.5 - 2.7. Ligne continue = courbe expérimentale, ligne pointillée = courbe théorique. Les spectres sont séparés verticalement pour une meilleure visualisation. (b) Position du pic de la SPR en fonction de la constante diélectrique du solvant pour les nanoparticules Au-PNIPAM. Les lignes continues sont les courbes théoriques calculées en utilisant le modèle de Mie core-shell. La ligne pointillée correspond aux valeurs calculées pour la particule nue (pente = 2).

La largeur du pic est modélisée par le facteur de surface g qui regroupe tous les effets de surface liés à la taille telle que la géométrie, l'inhomogénéité de forme et chimique. Pour comparer la qualité de fit, nous considérons la forme normalisée g/D pour prendre en compte

la géométrie de taille. Nous observons que lorsque le rapport g/D diminue, la qualité de fit est meilleure. Les valeurs de g/D élevées caractérisent donc une inhomogénéité de surface.

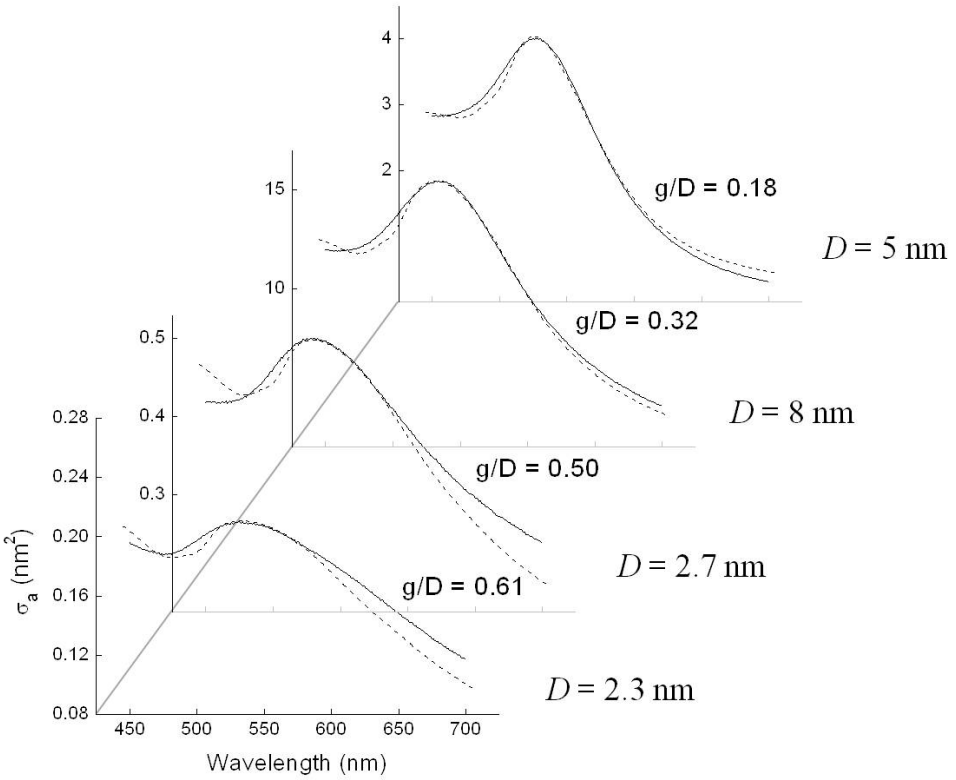

Figure 8.14: Effet de g/D sur la qualité du fit théorique des courbes d'absorption des nanoparticules Au-PNIPAM dans l'eau à T = 20°C. Ligne continue = courbe expérimentale; ligne pointillée = fit.

Un déplacement significatif de la bande de SPR vers le rouge est également induit avec la température en présence de sel (accompagné d'un changement visible de couleur). La modélisation des spectres d'absorption démontrent que ce déplacement est dû à une transition de collapse de la couche de polymère suivi d'une agrégation des nanoparticules. En effet, dans un premier temps il est provoqué par a une augmentation de ϵ_s puis au delà de 537 nm; correspondant à la couche de polymère sèche (ϕ_p=1), le déplacement rouge est due à l'agrégation comme le montrent les résultats de DNPA. Dans l'agrégat, un couplage de dipôle entre les particules se produit et cela est responsable du déplacement significatif vers le rouge. Différentes gammes de températures peuvent être employées pour induire ce déplacement optique selon le degré d'hydrophobicité du polymère et la salinité. Le changement de couleur est partiellement réversible et pourrait donc être exploité dans la détection de changement thermique de l'environnement. Nous concluons donc que la SPR des nanoparticules d'or peut être contrôlée par la modulation des propriétés structurales de la couche de polymère. Les nanoparticules sont donc sensibles pour détecter les changements de l'environnement local.

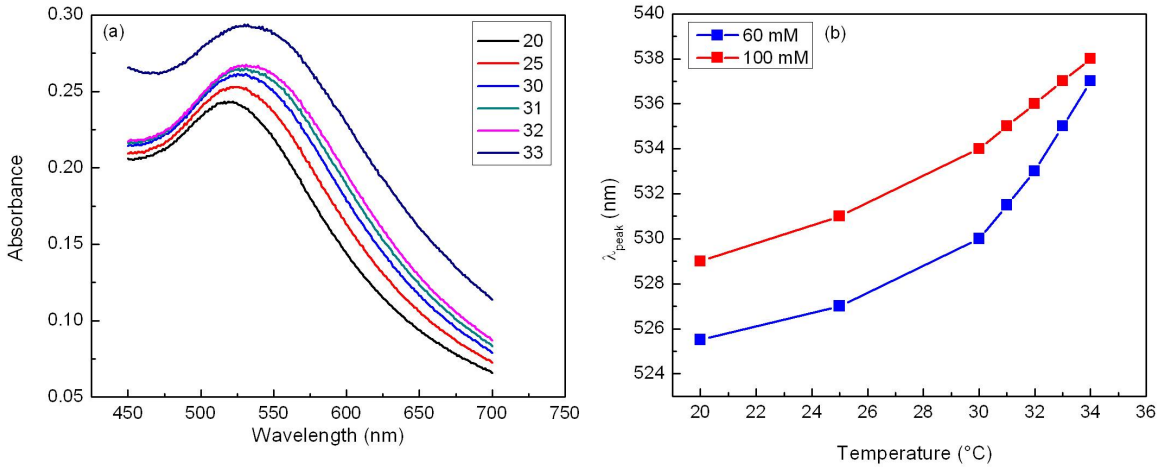

Figure 8.15: Au-PNIPAM$_{270}$-co-NPAM$_{113}$: (a) spectres d'absorption des nanoparticules dispersées dans 60 mM NaCl à différentes températures et (b) position de la SPR à différentes températures en fonction de la concentration en NaCl (60 mM (bleu) et 100 mM (rouge)).

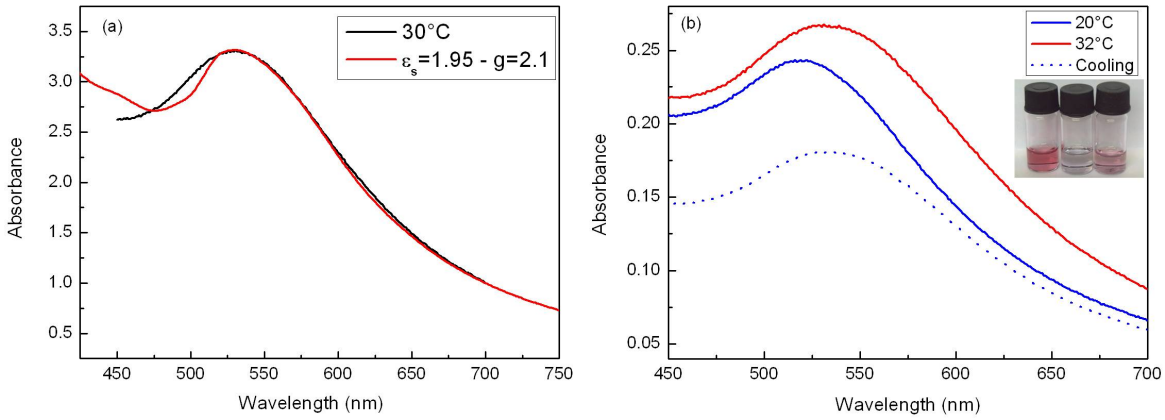

Figure 8.16: Modélisation des spectres d'absorption des nanoparticules de Au-PNIPAM$_{270}$-co-NPAM$_{113}$ dispersées dans 60 mM NaCl à T = 30°C et (b) réversibilité partielle de l'effet de température (T = 20°C (ligne continue bleue), T = 32°C (ligne continue rouge) et refroidissement à 20°C (ligne pointillée bleue)) et photo des dispersions à T = 20°C (solution rose), 30°C (solution violette) et refroidissement à 20°C (solution rose pâle).

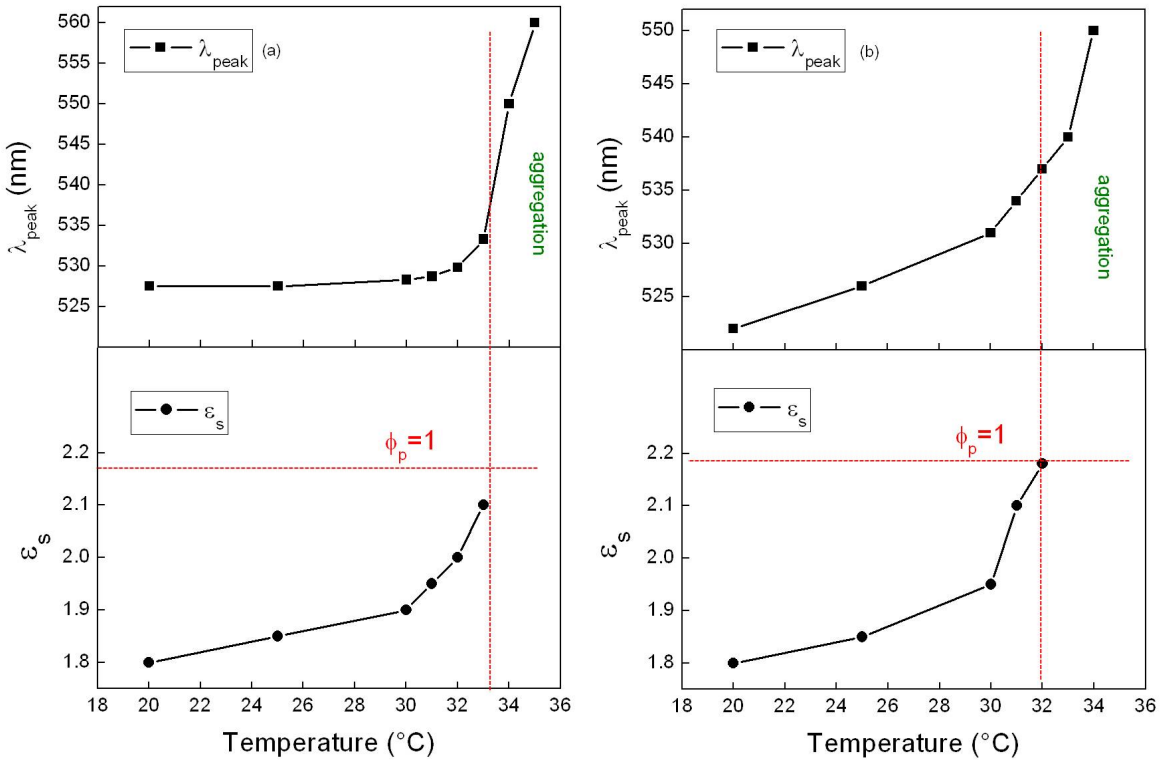

Figure 8.17: Position du pic d'absorption λ_{peak} position et ϵ_{s} en fonction de la température des nanoparticules de: (a) Au-PNIPAM$_{127}$ dispersées dans 50 mM NaCl (ϵ_{s} = 1.85-2.1 et ϕ_{p} = 0.18-0.78)et (b) Au-PNIPAM$_{270}$-NPAM$_{113}$ dispersées dans 60 mM NaCl (ϵ_{s} = 1.80-2.18 et ϕ_{p} = 0.06-0.97).

Les nanoparticules d'or Au-PNIPAM et Au-PNIPAM-co-NPAM sont amphiphiles. Nous les avons donc déposé à l'interface air-eau pour former des monocouches de Langmuir stables dont les propriétés structurales peuvent être manipulées avec la compression et la température. A partir des isothermes de compression, nous avons obtenus des informations sur la structure en 2D des nanoparticules en régime de basse compression. Dans la région pancake, nous trouvons que le coeur de l'or est bien isolé par une la couche de polymère et que la distance entre particule d dépend donc de la masse molaire du polymère greffé. Un effet de température est également observé pour la monocouche de Au-PNIPAM-co-NPAM. En condition de theta-solvant, une collapse de la couche de polymère se produit dû au degré élévé de coopérativité du copolymère PNIPAM-co-NPAM. Nous avons donc déduis qu'en régime de basse compression, la distance entre particule d peut être également variée avec la température.

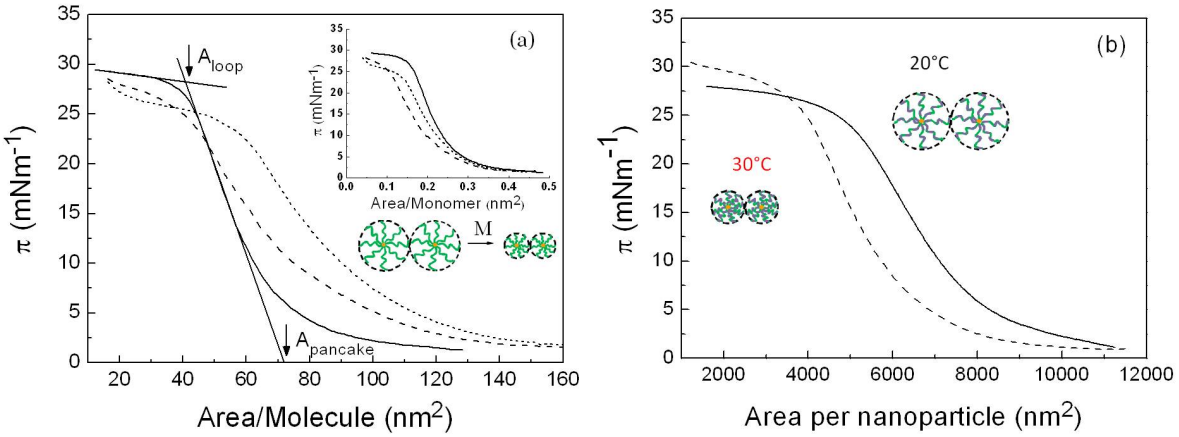

Figure 8.18: (a) isothermes de compression des monocouches de Au-PNIPAM à l'interface air-eau T = 20°C. De gauche à droite: Au-PNIPAM$_{55}$, Au-PNIPAM$_{67}$, Au-PNIPAM$_{118}$, Au-PNIPAM$_{165}$, Au-PNIPAM$_{265}$. Inset: extrapolations à $A_{\text{p-pancake}}$ and $A_{\text{p-loop}}$.(b) Effet de la température sur les isothermes de compression de la monocouche de Au-PNIPAM$_{270}$-co-PNPAM$_{113}$ (ligne continue: T = 20°C, ligne pointillée: T = 30°C).

En régime de haute compression, nous nous sommes intéressés à évaluer la compressibilité des monocouches dans le but d'optimiser la concentration et la stabilité des nanoparticules à l'interface et de mieux manipuler la distance entre particule d pour des études optiques. Nous avons employé les méthodes complémentaires de réflectivités de neutron et de rayon X pour caractériser la conformation de la couche de polymère et l'organisation du coeur de l'or respectivement.

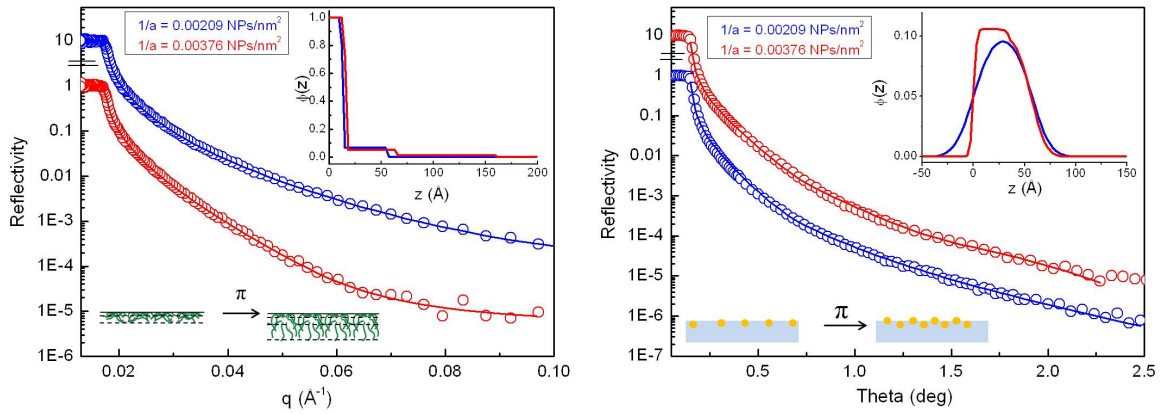

Figure 8.19: Effet de compression sur la monocouche de Au-PNIPAM$_{270}$-co-PNPAM$_{113}$: (a) courbes de réflectivité de neutron et (b) courbes de réflectivité de X à deux aires de compression différentes surface compressions (150 mM NaCl, T = 20°C) (les courbes sont séparées verticalement pour une meilleure visualisation). Ligne continue = fit, insets = profiles de concentration correspondants.

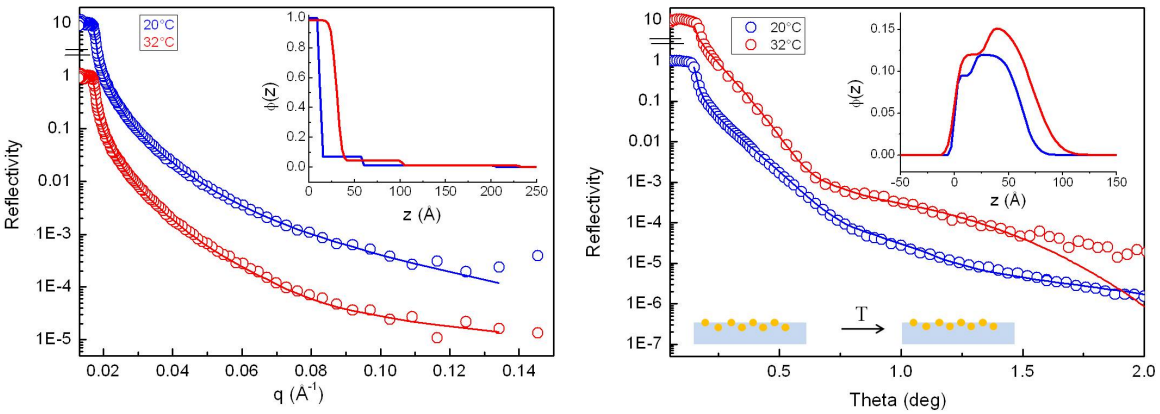

Figure 8.20: Effet de température sur la monocouche de Au-PNIPAM$_{127}$: (a) courbes de réflectivité de neutron et (b) courbes de réflectivité de X à T = 20°C (bleu) et T = 32°C (rouge) (1/area= 0.00524 NPs/nm^2, 150 mM NaCl) (les courbes sont séparées verticalement pour une meilleure visualisation). Ligne continue = fit, insets = profiles de concentration correspondants.

Ces études mettent en évidence qu'à haute compression, la monocouche perd en stabilité. Nous avons démontré que nous sommes en mesures d'améliorer la stabilité des nanoparticules à l'interface par l'ajout de sel pour écranter les charges en bout de chaînes de polymère, en augmentant le degré d'hydrophobicité du polymère greffé et par la température (Figure 8.21) . Nous observons également qu'à compression maximale, le degré de proximité exprimé par la distance entre particule normalisée d/D, tend vers une valeur commune indépendamment de la longueur de chaîne du polymère greffé: d/D = 2.1-2.2 en condition de bon solvant et 1.7 en condition de theta-solvant. Nous en déduisons qu'il n'y a pas de contact entre les coeurs de l'or et donc que les particules sont toujours protégées par une couche de polymère. Donc lorsque nous déposons ces nanoparticules amphiphiles, nous formons donc toujours des monocouches.

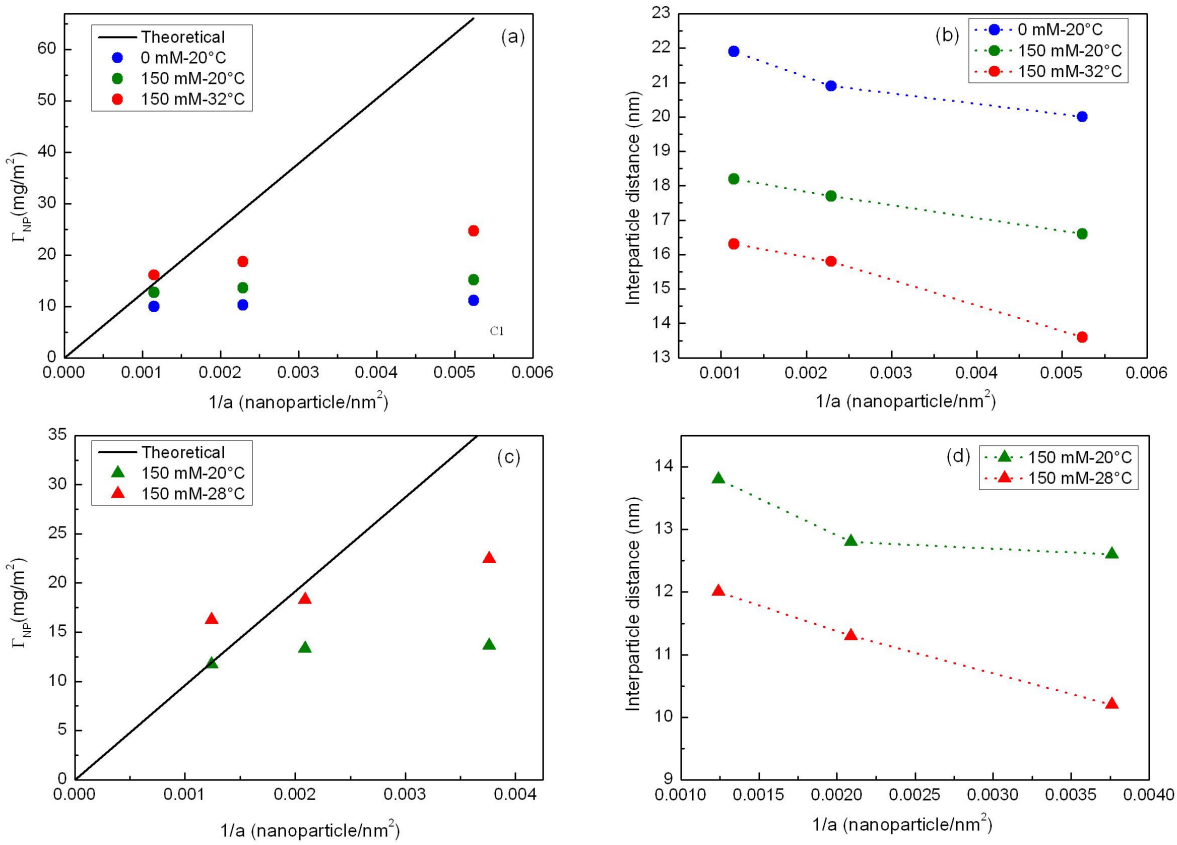

Figure 8.21: Comparaison de la concentration totale à l'interface (or + polymère greffé) évaluée à partir des résultats de réflectivités de X et de neutron (symboles colorés) avec la quantité déposée (ligne continue) pour les monocouches de Au-PNIPAM$_{127}$ (a) et Au-PNIPAM$_{270}$-co-NPAM$_{113}$ et la distance entre particules correspondante pour Au-PNIPAM$_{127}$ (c) et Au-PNIPAM$_{270}$-co-NPAM$_{113}$ (d).

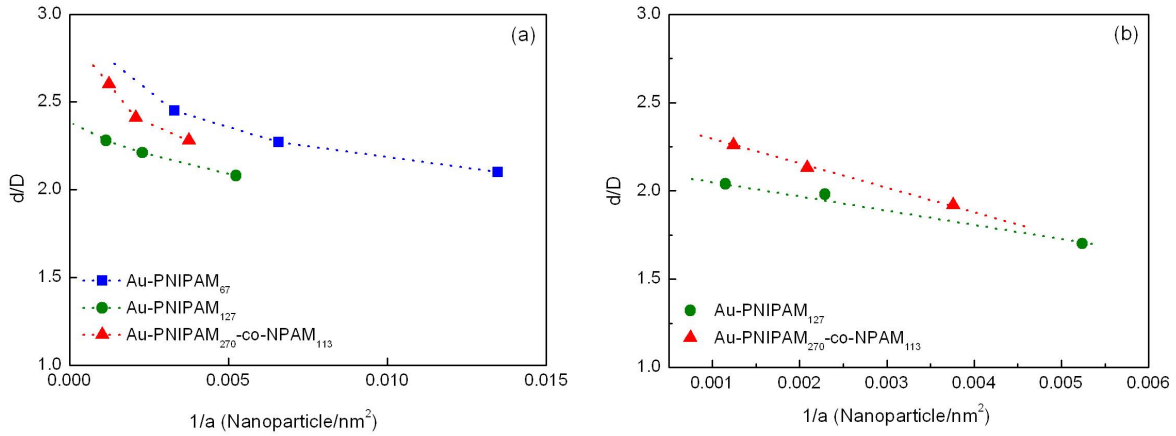

Figure 8.22: Distance entre particules normalisée en fonction de la compression à: (a) T = 20°C, et (b) T = 32°C (pour la monocouche de Au-PNIPAM$_{127}$) et T = 28°C (pour la monocouche de Au-PNIPAM$_{270}$-co-NPAM$_{113}$).

Un troisième type de nanoparticules amphiphiles contenant du polystyrène est étudié (Au-PNIPAM-PS). Le PS étant insoluble dans l'eau, les nanoparticules sont plus ancrées à l'interface. Par conséquent, à haute compression, des bicouches se forment. En augmentant la stabilité du PNIPAM, ces nanoparticules sont encore plus stables et nous réussissons à former de multicouches denses et bien définies.

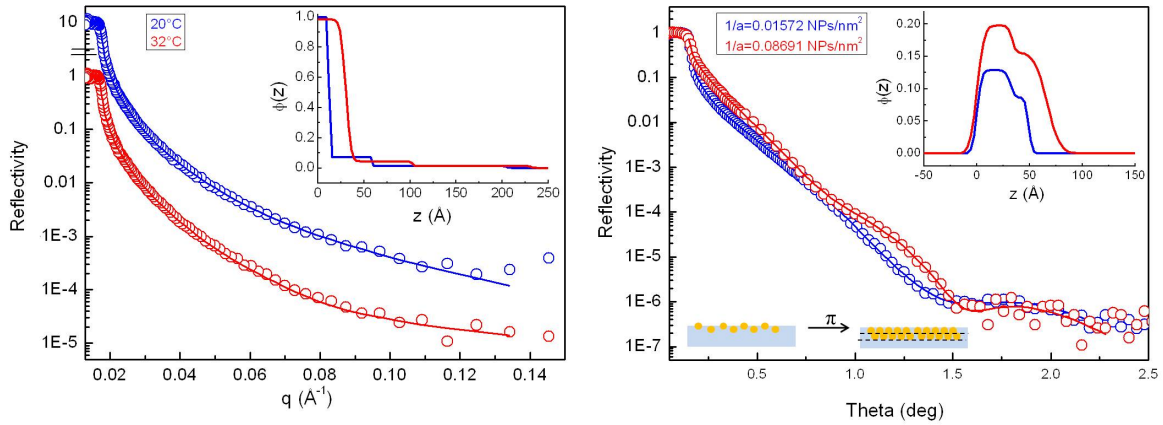

Figure 8.23: Effet de compression sur la couche de Au-PNIPAM$_{24}$PS$_{28}$: (a) courbes de réflectivité de neutron et (b) courbes de réflectivité de X à deux aires de compression différentes (0 mM NaCl, T = 20°C). Ligne continue = fit, insets = profiles de concentration correspondants.

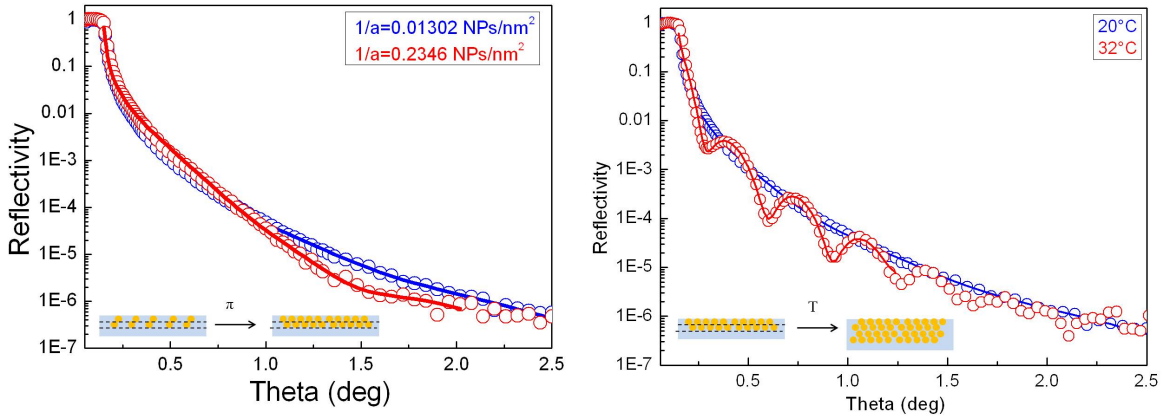

Figure 8.24: Courbes de réflectivité de X de la couche de Au-PNIPAM$_{118}$PS$_{28}$: (a) effet de compression (150 mM NaCl, T = 20°C) et (b) effet de température (150 mM NaCl, T = 20°C (bleu) et T = 32°C (rouge)). Ligne continue = fit.

Lorsque les couches à la surface sont suffisamment concentrées, une SPR peut être enregistrée (Figure 8.25). La position de la SPR est déplacée vers le bleu par rapport au signal enregistré en volume dû à l'exposition partielle des nanoparticules à l'air (effet de substrat).

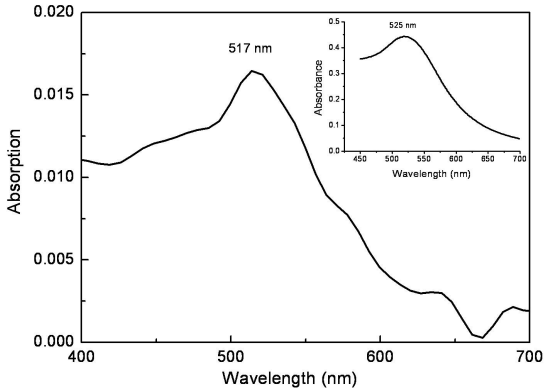

Figure 8.25: Absorption de la monocouche de Au-PNIPAM$_{127}$ à 20°C. Inset : spectre d'absorption dans l'eau.

A haute température, lorsque la monocouche est la plus stable, l'intensité de la SPR est augmentée avec la compression. Cependant, le déplacement de la position du pic est minime (Figure 8.26). Bien que la distance entre particules est diminuée, nous pensons que les nanoparticules ne sont pas suffisamment proches pour provoquer un fort couplage de dipôles et entraîner un déplacement vers le rouge.

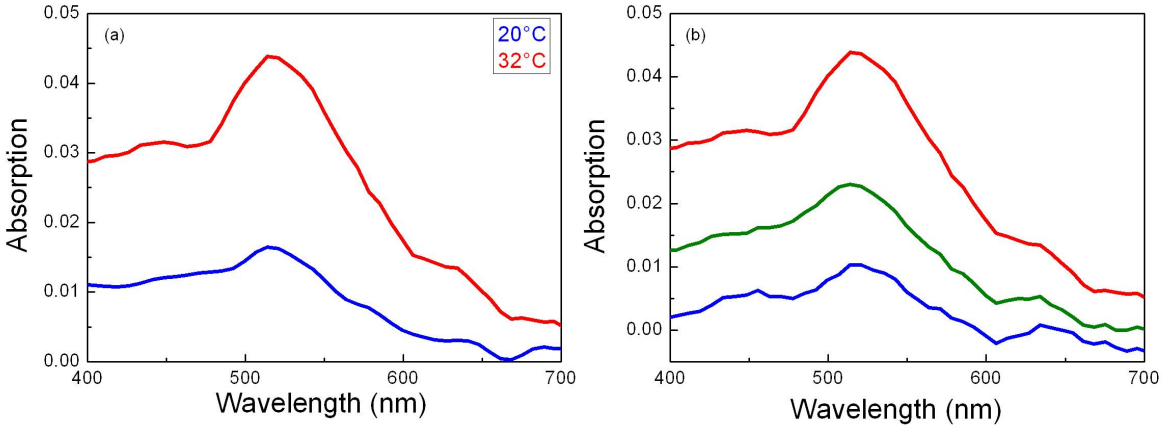

Figure 8.26: Monocouche de Au-PNIPAM$_{127}$:(a) effet de la température et (b) effet de la compression à haute température (150 mM NaCl).

C'est en comparant les propriétés optiques de la monocouche de Au-PNIPAM et la multicouche de Au-PNIPAM-PS, que nous notons un déplacement rouge significatif ($\Delta\lambda$ = 30 nm, Figure 8.27). Il est clairement observé que la position de la SPR se déplace progressivement vers le rouge lorsque le nombre de couche augmente. Dans la multicouche en 3D, ce déplacement rouge significatif est induit par un couplage dipolaire vertical et latéral. Nous pouvons donc contrôler les propriétés optiques à l'interface en contrôlant l'assemblage et l'organisation des nanoparticules à l'interface.

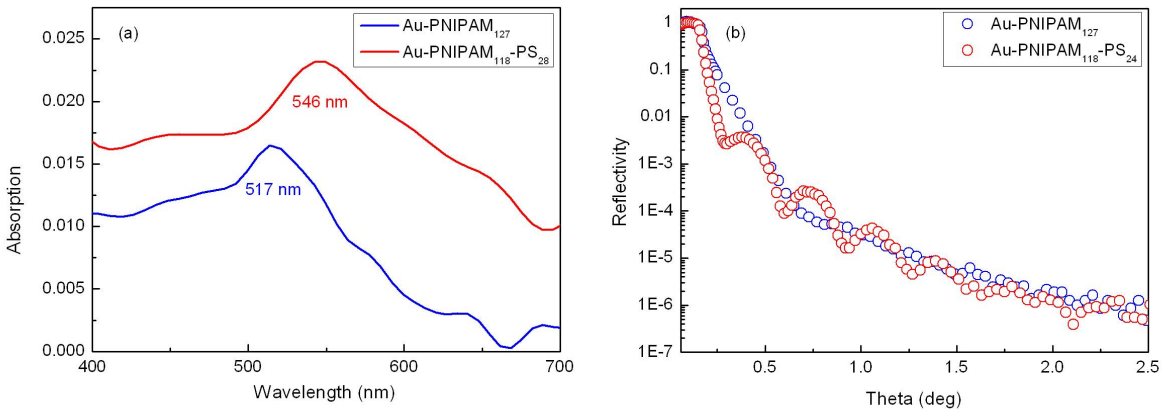

Figure 8.27: Comparaison de: (a)Absorption de la monocouche de Au-PNIPAM$_{127}$ (bleu) et de la multicouche de Au-PNIPAM$_{118}$-PS$_{28}$ (rouge) et (b) courbes de réflectivité de X correspondantes (150 mM NaCl, T = 32°C).

Nous avons préparé des nanoparticules d'or de différentes tailles qui sont stabilisées par une couche de polymère d'épaisseur et hydrophobicité variables. La modélisation des spectres d'absorption de ces nanoparticules démontre que les propriétés optiques de la nanoparticule d'or peuvent être contrôlées par la structure de la couche de polymère thermosensible. Deux résultats sont marquants: (i) une atténuation progressive de la sensibilité de la SPR à la propriété diélectrique du solvant avec la masse molaire du polymère greffé jusqu'à devenir quasi-nulle; dans ce dernier cas de figure, la SPR est dite "gelée" par la couche de polymère, (ii) un déplacement significative de la bande de SPR vers le rouge avec la température en présence de sel dû à une transition de collapse de la couche de polymère suivi d'une agrégation des nanoparticules. Les nanoparticules d'or peuvent donc être employées pour détecter les changements des propriétés diélectriques de l'environnement local. Lorsque les nanoparticules d'or sont déposées à l'interface air-eau, elles peuvent former des monocouches de Langmuir stables dont les propriétés structurales, et par conséquent la distance entre particule, peuvent être modulées avec la compression et la température. Les mesures de réflectivité de neutron et X montrent que la stabilité de la monocouche peut être optimisée avec l'addition de sel et la température. L'étude des nanoparticules de Au-PNIPAM-PS démontre que l'effet du PS combiné à l'amélioration de la stabilité du PNIPAM avec le sel et la température entraîne la formation d'une multicouche stable et bien définie dont le nombre de couches composantes peut être contrôlée par la compression. Nous avons pu enregistrer une SPR pour les monocouches concentrées par mesures de transmission. Nous ne constatons pas de déplacement significatif de la SPR de la monocouche avec la compression et la température, seulement une augmentation du signal d'absorption. Une variation des propriétés optiques est observé pour la multicouche: la SPR est progressivement déplacer vers le rouge lorsque le nombre de couche augmente. Le contrôle des propriétés optiques dans le film mince (Metamaterial) est un aspect important pouvant être exploité dans les applications optiques et micro-électroniques.

Bibliography

[1] R. L. Johnson. *Atomic molecular cluster*. Taylor & Francis: London, 2002.

[2] U.; Vollmer M. Kreibig. *Optical properties of metal clusters*. Springer: Berlin, 1995.

[3] A. N. Shipway, E. Katz, and I. Willner. Nanoparticle arrays on surfaces for electronic, optical, and sensor applications. *Chemphyschem*, 1(1):18–52, August 2000.

[4] Christopher E. D. Chidsey Stephen Creager Carol Creutz Cherie R. Kagan Prashant V. Kamat Marya Lieberman O Stuart Lindsay Rudolph A. Marcus rRobert M. Metzger M. E. Michel-Beyerle John R. Miller Marshall D. Newton Debra R. Rolison Otto Sankey Kirk S. Schanze James Yardley David M. Adams, Louis Brus and Xiaoyang Zhu. Charge transfer on the nanoscale: Current status. *J. Phys. Chem. B.*, 107:6668–6697, 2003.

[5] M. C. Daniel and D. Astruc. Gold nanoparticles: Assembly, supramolecular chemistry, quantum-size-related properties, and applications toward biology, catalysis, and nanotechnology. *Chemical Reviews*, 104(1):293–346, January 2004.

[6] J. E. Warner, M. G.; Hutchinson. *In synthesis, functionalization and surface treatment of nanoparticles*. American Scientific Publishers: California, 2003.

[7] B. Palpant, B. Prevel, J. Lerme, E. Cottancin, M. Pellarin, M. Treilleux, A. Perez, J. L. Vialle, and M. Broyer. Optical properties of gold clusters in the size range 2-4 nm. *Physical Review B*, 57(3):1963–1970, January 1998.

[8] R. C. Jin, Y. W. Cao, C. A. Mirkin, K. L. Kelly, G. C. Schatz, and J. G. Zheng. Photoinduced conversion of silver nanospheres to nanoprisms. *Science*, 294(5548):1901–1903, November 2001.

[9] S. UNDERWOOD and P. MULVANEY. Effect of the solution refractive-index on the color of gold colloids. *Langmuir*, 10(10):3427–3430, October 1994.

[10] Michael Giersig Luis M. Liz-Marzan and Paul Mulvaney. Synthesis of nanosized gold-silica core-shell particles. *Langmuir*, 12:4329–4335, 1996.

[11] George C. Schatz Michelle Duval Malinsky, K. Lance Kelly and Richard P. Van Duyne. Chain length dependence and sensing capabilities of the localized surface plasmon resonance of silver nanoparticles chemically modified with alkanethiol self-assembled monolayers. *J. Am. Chem. Soc.*, 123:1471–1482, 2001.

[12] M. Yamada and H. Nishihara. Large solvent and potential effects on the collective surface plasmon band of gold nanoparticle films. *Chemphyschem*, 5(4):555–559, April 2004.

[13] David Dunstan Thearith Ung, Michael Giersig and Paul Mulvaney. Spectroelectrochemistry of colloidal silver. *Langmuir*, 13:1773–1782, 1997.

[14] G. Mie. *Ann. Phys*, 25:377–445, 1908.

[15] M. L. Liz-Marzan. Nanometals: Formation and colors. *Materials Today*, 7:26–31, 2004.

[16] M. Faraday. *Philos. Trans.*, 147:145–181, 1857.

[17] John M. Thomas. Colloidal metals: past, present and future. *Pure and Appl. Chem*, 60:1517–1528, 1988.

[18] J. TURKEVICH, P. C. STEVENSON, and J. HILLIER. A study of the nucleation and growth processes in the synthesis of colloidal gold. *Discussions of the Faraday Society*, (11):55–&, 1951.

[19] G. Fens. *Nature: Phys. Sci.*, 241:20–22, 1973.

[20] Benjamin Abécassis. *Suivi in situ de la nucléation-croissance de nanoparticules d'or*. PhD thesis, Ecole Polytechnique, 2006.

[21] D. Bethell D.J. Schiffrin R. Whyman. M. Brust, M. Walker. *J. Chem. Soc. Chem. Commun*, page 801, 1994.

[22] J. M. de la Fuente, A. G. Barrientos, T. C. Rojas, J. Rojo, J. Canada, A. Fernandez, and S. Penades. Gold glyconanoparticles as water-soluble polyvalent models to study carbohydrate interactions. *Angewandte Chemie-international Edition*, 40(12):2258–+, 2001.

[23] J. J. Storhoff, A. A. Lazarides, R. C. Mucic, C. A. Mirkin, R. L. Letsinger, and G. C. Schatz. What controls the optical properties of dna-linked gold nanoparticle assemblies? *Journal of the American Chemical Society*, 122(19):4640–4650, May 2000.

[24] Y. W. Cao, R. Jin, and C. A. Mirkin. Dna-modified core-shell ag/au nanoparticles. *Journal of the American Chemical Society*, 123(32):7961–7962, August 2001.

[25] Z. Li, R. C. Jin, C. A. Mirkin, and R. L. Letsinger. Multiple thiol-anchor capped dna-gold nanoparticle conjugates. *Nucleic Acids Research*, 30(7):1558–1562, April 2002.

[26] S. Bidault, F. J. G. de Abajo, and A. Polman. Plasmon-based nanolenses assembled on a well-defined dna template. *Journal of the American Chemical Society*, 130(9):2750–+, March 2008.

[27] Ji-Young Kim and Jae-Seung Lee. Synthesis and thermally reversible assembly of dna-gold nanoparticle cluster conjugates. *Nano Lett*, 9(12):4564–9, December 2009.

[28] I. Y. Galaev and B. Mattiasson. 'smart' polymers and what they could do in biotechnology and medicine. *Trends In Biotechnology*, 17(8):335–340, August 1999.

[29] Y. J. Kang and T. A. Taton. Core/shell gold nanoparticles by self-assembly and crosslinking of micellar, block-copolymer shells. *Angewandte Chemie-international Edition*, 44(3):409–412, 2005.

[30] M. Karg, I. Pastoriza-Santos, L. M. Liz-Marzan, and T. Hellweg. A versatile approach for the preparation of thermosensitive pnipam core-shell microgels with nanoparticle cores. *Chemphyschem*, 7(11):2298–2301, November 2006.

[31] J. D. Gibson, B. P. Khanal, and E. R. Zubarev. Paclitaxel-functionalized gold nanoparticles. *Journal of the American Chemical Society*, 129(37):11653–11661, September 2007.

[32] P. Ghosh, G. Han, M. De, C. K. Kim, and V. M. Rotello. Gold nanoparticles in delivery applications. *Advanced Drug Delivery Reviews*, 60(11):1307–1315, August 2008.

[33] Y. Y. Yuan, X. Q. Liu, Y. C. Wang, and J. Wang. Gold nanoparticles stabilized by thermosensitive diblock copolymers of poly(ethylene glycol) and polyphosphoester. *Langmuir*, 25(17):10298–10304, September 2009.

[34] Deon T. Miles W. Peter Wuelfing, Stephen M. Gross and Royce W. Murray. Nanometer gold clusters protected by surface-bound monolayers of thiolated poly(ethylene glycol) polymer electrolyte. *J. Am. Chem. Soc.*, 120:12696–12697, 1998.

[35] M. K. Corbierre, N. S. Cameron, and R. B. Lennox. Polymer-stabilized gold nanoparticles with high grafting densities. *Langmuir*, 20(7):2867–2873, March 2004.

[36] F. Seker, P. R. L. Malenfant, M. Larsen, A. Alizadeh, K. Conway, A. M. Kulkarni, G. Goddard, and R. Garaas. On-demand control of optoelectronic coupling in gold nanoparticle arrays. *Advanced Materials*, 17(16):1941–+, August 2005.

[37] A. B. Lowe, B. S. Sumerlin, M. S. Donovan, and C. L. McCormick. Facile preparation of transition metal nanoparticles stabilized by well-defined (co)polymers synthesized via aqueous reversible addition-fragmentation chain transfer polymerization. *Journal of the American Chemical Society*, 124(39):11562–11563, October 2002.

[38] C. Mangeney, F. Ferrage, I. Aujard, V. Marchi-Artzner, L. Jullien, O. Ouari, E. D. Rekai, A. Laschewsky, I. Vikholm, and J. W. Sadowski. Synthesis and properties of water-soluble gold colloids covalently derivatized with neutral polymer monolayers. *Journal of the American Chemical Society*, 124(20):5811–5821, May 2002.

[39] I. Hussain, S. Graham, Z. X. Wang, B. Tan, D. C. Sherrington, S. P. Rannard, A. I. Cooper, and M. Brust. Size-controlled synthesis of near-monodisperse gold nanoparticles in the 1-4 nm range using polymeric stabilizers. *Journal of the American Chemical Society*, 127(47):16398–16399, November 2005.

[40] F. Gal. PhD thesis, Université Paris 6, 2010.

[41] J. Oberdisse J. Jestin G. Carrot, A. El Harrak and F. Boue. Polymer grafting from 10-nm individual particles : proving control by neutron scattering. *Soft Matter*, 2:1043–1047, 2006.

[42] K. Ohno, K. Koh, Y. Tsujii, and T. Fukuda. Synthesis of gold nanoparticles coated with well-defined, high-density polymer brushes by surface-initiated living radical polymerization. *Macromolecules*, 35(24):8989–8993, November 2002.

[43] H. Y. Zhao, X. L. Kang, and L. Liu. Comb-coil polymer brushes on the surface of silica nanoparticles. *Macromolecules*, 38(26):10619–10622, December 2005.

[44] A. B. Lowe and C. L. McCormick. Reversible addition-fragmentation chain transfer (raft) radical polymerization and the synthesis of water-soluble (co)polymers under homogeneous conditions in organic and aqueous media. *Progress In Polymer Science*, 32(3):283–351, March 2007.

[45] J. Chiefari, Y. K. Chong, F. Ercole, J. Krstina, J. Jeffery, T. P. T. Le, R. T. A. Mayadunne, G. F. Meijs, C. L. Moad, G. Moad, E. Rizzardo, and S. H. Thang. Living free-radical polymerization by reversible addition-fragmentation chain transfer: The raft process. *Macromolecules*, 31(16):5559–5562, 1998.

[46] G. Moad, J. Chiefari, Y. K. Chong, J. Krstina, R. T. A. Mayadunne, A. Postma, E. Rizzardo, and S. H. Thang. Living free radical polymerization with reversible addition-fragmentation chain transfer (the life of raft). *Polymer International*, 49(9):993–1001, September 2000.

[47] S. Perrier, P. Takolpuckdee, and C. A. Mars. Reversible addition-fragmentation chain transfer polymerization: End group modification for functionalized polymers and chain transfer agent recovery. *Macromolecules*, 38(6):2033–2036, March 2005.

[48] F. Ganachaud, M. J. Monteiro, R. G. Gilbert, M. A. Dourges, S. H. Thang, and E. Rizzardo. Molecular weight characterization of poly(n-isopropylacrylamide) prepared by living free-radical polymerization. *Macromolecules*, 33(18):6738–6745, 2000.

[49] J. Shan, M. Nuopponen, H. Jiang, T. Viitala, E. Kauppinen, K. Kontturi, and H. Tenhu. Amphiphilic gold nanoparticles grafted with poly(n-isopropylacrylamide) and polystyrene. *Macromolecules*, 38(7):2918–2926, 2005.

[50] M. Nuopponen, J. Ojala, and H. Tenhu. Aggregation behaviour of well defined amphiphilic diblock copolymers with poly (n-isopropylacrylamide) and hydrophobic blocks. *Polymer*, 45(11):3643–3650, 2004.

[51] B. S. Lokitz Y. Li and C. L. McCormick. Raft synthesis of a thermally responsive abc triblock copolymer incorporating n-acryloxysuccinimide for facile in situ formation of shell cross-linked micelles in aqueous media. *Macromolecules*, 39:81–89, 2006.

[52] Y. K. Chong, T. P. T. Le, G. Moad, E. Rizzardo, and S. H. Thang. A more versatile route to block copolymers and other polymers of complex architecture by living radical polymerization: The raft process. *Macromolecules*, 32(6):2071–2074, March 1999.

[53] M. Q. Zhu, L. Q. Wang, G. J. Exarhos, and A. D. Q. Li. Thermosensitive gold nanoparticles. *Journal of the American Chemical Society*, 126(9):2656–2657, March 2004.

[54] K.; Yamamoto T.; Iwasaki Y.; Watanabe A.; Akiyoshi K.; Moroshima Y. L. Yusa, S.; Fukuda. *Langmuir*, 23:12842–12848, 2007.

[55] J. R. Morones and W. Frey. Environmentally sensitive silver nanoparticles of controlled size synthesized with pnipam as a nucleating and capping agent. *Langmuir*, 23(15):8180–8186, July 2007.

[56] J. Shan and H. Tenhu. Recent advances in polymer protected gold nanoparticles: synthesis, properties and applications. *Chemical Communications*, (44):4580–4598, 2007.

[57] J. Shan. *Polymer protected gold nanoparticles*. PhD thesis, University of Helsinki, 2006.

[58] J. Chiefari, R. T. A. Mayadunne, C. L. Moad, G. Moad, E. Rizzardo, A. Postma, M. A. Skidmore, and S. H. Thang. Thiocarbonylthio compounds (s=c(z)s-r) in free radical polymerization with reversible addition-fragmentation chain transfer (raft polymerization). effect of the activating group z. *Macromolecules*, 36(7):2273–2283, April 2003.

[59] F. Zeng, Z. Tong, and H. Q. Feng. Nmr investigation of phase separation in poly(n-isopropyl acrylamide)/water solutions. *Polymer*, 38(22):5539–5544, 1997.

[60] G. Burillo A. Ortega, E. Bucio. *Polymer Bulletin*, 60:524, 2008.

[61] P. Relogio, M. T. Charreyre, J. P. S. Farinha, J. M. G. Martinho, and C. Pichot. Well-defined polymer precursors synthesized by raft polymerization of n,n-dimethylacrylamide/n-acryloxysuccinimide: random and block copolymers. *Polymer*, 45(26):8639–8649, December 2004.

[62] A. Favier, F. D'Agosto, M. T. Charreyre, and C. Pichot. Synthesis of n-acryloxysuccinimide copolymers by raft polymerization, as reactive building blocks with full control of composition and molecular weights. *Polymer*, 45(23):7821–7830, October 2004.

[63] H. B. Mao, C. M. Li, Y. J. Zhang, S. Furyk, P. S. Cremer, and D. E. Bergbreiter. High-throughput studies of the effects of polymer structure and solution components on the phase separation of thermoresponsive polymers. *Macromolecules*, 37(3):1031–1036, February 2004.

[64] H. G. SCHILD and D. A. TIRRELL. Microcalorimetric detection of lower critical solution temperatures in aqueous polymer-solutions. *Journal of Physical Chemistry*, 94(10):4352–4356, 1990.

[65] L. T. Lee, B. Jean, and A. Menelle. Effect of temperature on the adsorption of poly(n-isopropylacrylamide) at the air-solution interface. *Langmuir*, 15(9):3267–3272, April 1999.

[66] J. Shan, Y. M. Zhao, N. Granqvist, and H. Tenhu. Thermoresponsive properties of n-isopropylacrylamide oligomer brushes grafted to gold nanoparticles: Effects of molar mass and gold core size. *Macromolecules*, 42(7):2696–2701, April 2009.

[67] J. Shan, J. Chen, M. Nuopponen, and H. Tenhu. Two phase transitions of poly(n-isopropylacrylamide) brushes bound to gold nanoparticles. *Langmuir*, 20(11):4671–4676, May 2004.

[68] V. Aseyev, S. Hietala, A. Laukkanen, M. Nuopponen, O. Confortini, F. E. Du Prez, and H. Tenhu. Mesoglobules of thermoresponsive polymers in dilute aqueous solutions above the lcst. *Polymer*, 46(18):7118–7131, August 2005.

[69] P. L. Privalov. Stability of proteins: small globular proteins. *Adv Protein Chem*, 33:167–241, 1979.

[70] E. I. TIKTOPULO, V. N. UVERSKY, V. B. LUSHCHIK, S. I. KLENIN, V. E. BYCHKOVA, and O. B. PTITSYN. Domain coil-globule transition in homopolymers. *Macromolecules*, 28(22):7519–7524, October 1995.

[71] C. Chevigny. PhD thesis, Université Paris-Sud XI, 2009.

[72] A. Brulet F Lafuma L. Petit, L. Bouteiller and D. Hourdet. Responsive hybrid self-assemblies in aqueous media. *Langmuir*, 23:147–158, 2007.

[73] J. S. Pedersen. Analysis of small-angle scattering data from colloids and polymer solutions : modeling and least-squares fitting. *Advances in Colloid and Interface Science*, page 171Ũ210, 1997.

[74] J. S. Pedersen and M. C. Gerstenberg. Scattering form factor of block copolymer micelles. *Macromolecules*, 29(4):1363–1365, February 1996.

[75] B. Jean. PhD thesis, Université Paris 6, Paris, 2000.

[76] D.; Del Fatti N.; Vallée F. Muskens, O.; Christofilos. *J. Opt. A : Pure A*, 8:264–272, 2006.

[77] S. Link and M. A. El-Sayed. Size and temperature dependence of the plasmon absorption of colloidal gold nanoparticles. *Journal of Physical Chemistry B*, 103(21):4212–4217, May 1999.

[78] L. B. Scaffardi and J. O. Tocho. Absorption spectra of tiny gold and silver objects. *Journal of Luminescence*, 128(5-6):828–830, May 2008.

[79] P. B. Johnson and R. W. Christy. Optical constants of the noble metals. *Phys. Rev. B*, 6:4370–4379, 1972.

[80] J. H. Krafka J. Weaver. *Optical properties of metals*. Physics Data Series, 1981.

[81] T. Gregory Schaaff Marat N. Shafigullin Igor Vezmar Marcos M. Alvarez, Joseph T. Khoury and Robert L. Whetten. Optical absorption spectra of nanocrystal gold molecules. *J. Phys. Chem. B*, 101:3706–3712, 1997.

[82] R. H. Doremus. *J. Appl. Phys.*, 36:2853, 1965.

[83] L. Kreibig, U.; Genzel. *Surf. Sci.*, 156:678, 1985.

[84] A. H.; Kreibig U.; Vollmer M. Phys. ReV. Hovel, H. S.; Fritz. *Phys. ReV.*, B48:18178, 1993.

[85] S. K. Ghosh, S. Nath, S. Kundu, K. Esumi, and T. Pal. Solvent and ligand effects on the localized surface plasmon resonance (lspr) of gold colloids. *Journal of Physical Chemistry B*, 108(37):13963–13971, September 2004.

[86] P. Mulvaney. Surface plasmon spectroscopy of nanosized metal particles. *Langmuir*, 12(3):788–800, February 1996.

[87] D. R. Huffman C. F. Bohren. *Absorption and Scattering of Light by Small Particles*. Wiley, 2004.

[88] A. C. Templeton, J. J. Pietron, R. W. Murray, and P. Mulvaney. Solvent refractive index and core charge influences on the surface plasmon absorbance of alkanethiolate monolayer-protected gold clusters. *Journal of Physical Chemistry B*, 104(3):564–570, January 2000.

[89] P.; Broyer M. ; Del Fatti N.; Vallée F. Muskens, O.; Billaud. *Phys. Rev. B*, 78:205410, 2008.

[90] L. Auvray P. Auroy and L. Leger. *Macromolecules*, 24:5158–5166, 1991.

[91] L. Auvray P. Auroy and L. Leger. *Macromolecules*, 2523-2528:24, 1991.

[92] L. Auvray P. Auroy and L. Leger. *Phys. Rev. Lett.*, pages 719–722, 1991.

[93] P. Auroy Y. Tran and L-T. Lee. *Macromolecules*, 32:8952–8964, 1999.

[94] S. Satija S. S. Balamurugan G. P. Lopez H. Yim, M. S. Kent. *J. Polym. Sci. Part B: Polym. Phys*, 42:3302, 2004.

[95] K.; Yamago S.; Sugara M.; Morikawa S.; Yamamoto T.; Moroshima Y. Yusa, S.; Fukuda. *Macromolecules*, 40:5907 –5915, 2007.

[96] Y. Lui; W. Tu; D. Cao. *Ind. Eng. Chem. Res.*, 49:2707–2715, 2010.

[97] J. Sudor A.Brulet D. Hourdet V. Barbier, M. Herve and J-L. Viovy. Thermally induced gelation of poly(acrylamide) grafted with poly(n-isopropylacrylamide): A small-angle neutron scattering study. *Macromolecules*, 37:5682–5691, 2004.

[98] S. Mendez G. P. Lopez S. Satija Y. Seo H. Yim, M. S. Kent. *Macromolecules*, 39:3420, 2006.

[99] C. Stefaniu, M. Chanana, D. Y. Wang, D. V. Novikov, G. Brezesinski, and H. Mohwald. Biocompatible magnetite nanoparticles trapped at the air/water interface. *Chemphyschem*, 11(17):3585–3588, December 2010.

[100] J. Shan, H. Chen, M. Nuopponen, T. Viitala, H. Jiang, J. Peltonen, E. Kauppinen, and H. Tenhu. Optical properties of thermally responsive amphiphilic gold nanoparticles protected with polymers. *Langmuir*, 22(2):794–801, January 2006.

[101] R. Contreras-Caceres, A. Sanchez-Iglesias, M. Karg, I. Pastoriza-Santos, J. Perez-Juste, J. Pacifico, T. Hellweg, A. Fernandez-Barbero, and L. M. Liz-Marzan. Encapsulation and growth of gold nanoparticles in thermoresponsive microgels. *Advanced Materials*, 20(9):1666–+, May 2008.

[102] C. A. Rezende, J. Shan, L. T. Lee, G. Zalczer, and H. Tenhu. Tuning the structure of thermosensitive gold nanoparticle monolayers. *Journal of Physical Chemistry B*, 113(29):9786–9794, July 2009.

[103] G. M. Liu, S. H. Yang, and G. Z. Zhang. Conformational changes of poly(n-isopropylacrylamide) chains at air/water interface: Effects of temperature, compression rate, and packing density rid a-6986-2010. *Journal of Physical Chemistry B*, 111(14):3633–3639, April 2007.

[104] H. D. BIJSTERBOSCH, V. O. DEHAAN, A. W. DEGRAAF, M. MELLEMA, F. A. M. LEERMAKERS, M. A. C. STUART, and A. A. VANWELL. Tethered adsorbing chains - neutron reflectivity and surface pressure of spread diblock copolymer monolayers. *Langmuir*, 11(11):4467–4473, November 1995.

[105] A. M. G. daSilva, E. J. M. Filipe, J. M. R. dOliveira, and J. M. G. Martinho. Interfacial behavior of poly(styrene)-poly(ethylene oxide) diblock copolymer monolayers at the air-water interface. hydrophilic block chain length and temperature influence. *Langmuir*, 12(26):6547–6553, December 1996.

[106] D. H. Xie, C. A. Rezende, G. M. Liu, S. Pispas, G. Z. Zhang, and L. T. Lee. Effect of hydrogen-bonding complexation on the interfacial behavior of poly(isoprene)-b-poly(ethylene oxide) and poly(isoprene)-b-poly(acrylic acid) langmuir monolayers. *Journal of Physical Chemistry B*, 113(3):739–744, January 2009.

[107] K. KUBOTA, S. FUJISHIGE, and I. ANDO. Solution properties of poly(n-isopropylacrylamide) in water. *Polymer Journal*, 22(1):15–20, 1990.

[108] P.J. Flory. *Principles of Polymer Chemistry* . Cornell University Press, 1971.

[109] R. VILANOVE and F. RONDELEZ. Scaling description of two-dimensional chain conformations in polymer monolayers. *Physical Review Letters*, 45(18):1502–1505, 1980.

[110] V. Aguie-Beghin, E. Leclerc, M. Daoud, and R. Douillard. Asymmetric multiblock copolymers at the gas-liquid interface: Phase diagram and surface pressure. *Journal of Colloid and Interface Science*, 214(2):143–155, June 1999.

[111] B. DUPLANTIER and H. SALEUR. Exact tricritical exponents for polymers at the theta-point in 2 dimensions. *Physical Review Letters*, 59(5):539–542, August 1987.

[112] N. Puff, A. Cagna, V. Aguie-Beghin, and R. Douillard. Effect of ethanol on the structure and properties of beta-casein adsorption layers at the air/buffer interface. *Journal of Colloid and Interface Science*, 208(2):405–414, December 1998.

[113] E. Wolf M. Born. Principles of optics. *Pergmon Press, Oxford*, 1970.

[114] V. F. Sears. *Neutron Optics*. Oxford University Press, 1989.

[115] G. A. Werner A. G. Klein. *Rep. Prog. Phys.*, 46, 1983.

[116] L. Zhao K. L. Kelly, E. Coronado and G. C. Schatz. The optical properties of metal nanoparticles: The influence of size, shape, and dielectric environment. *J. Phys. Chem. B*, 107:668–677, 2003.

[117] J.P. Cotton and F. Nallet. Diffusion de neutrons aux petits angles. *Journal de Physique IV*, 09, 1998.

[118] P.Lindler and T.Zemb. In neutrons, x-ray and light scattering methods applied to soft condensed matter. *North-Holland Delta Series*, 2002.

[119] J. P. Cotton. Small-angle neutron scattering: Introduction and variations on contrast. *Journal De Physique Iv*, 9(P1):21–49, February 1999.

[120] J.Higgins and H. Benoit. *Polymer and Neutron Scattering*. Oxford Science Publications, 1994.

[121] E.M.; Simister E.A.; Thomas R.K.; Penfold J.; Rennie A.R. Crowley, T.L.; Lee. *Colloids Surf.*, 52:85, 1990.

[122] J. Als-Nielsen. *Z. Phys. B*, 61:411, 1985.

[123] F. Abeles. *Ann. Phys.*, 3:504, 1948.

Contents